KOBELCO TECHNOLOGY REVIEW

No. 43 Nov. 2025

Feature- Ⅰ: Digital Transformation to Embody KOBELCO's Unique Value
Feature- Ⅱ: Materials and Technologies for Automobiles

Contents

Feature- Ⅰ Digital Transformation to Embody KOBELCO's Unique Value

Feature- Ⅱ Materials and Technologies for Automobiles

Published by

Technical Development Group
Kobe Steel, Ltd.

5-5, Takatsukadai 1-chome,
Nishi-ku, Kobe, HYOGO 651-2271, JAPAN
https://www.kobelco.co.jp

Editorial Office: **Kobelco Business Partners Co., Ltd.**
2-4, Wakinohama-Kaigandori 2-chome,
Chuo-ku, Kobe, HYOGO 651-0073,
JAPAN
Fax: +81-78-261-7843
E-mail: rd-office@kobelco.com

KOBELCO's Perspective on Digital Transformation (DX)

Nobumitsu NAMBA*1
*1 IT Planning Department

Abstract

The distinctive strengths of the KOBELCO Group lie in its diverse technological and business assets accumulated through engaging in various businesses. Additionally, the group possesses interactions and touchpoints with customers in diverse fields of demand, enabling the group to understand industry trends and customer needs. KOBELCO's concept of digital transformation (DX) involves combining digital technology and data with these unique assets to solve societal challenges and create new value. This article introduces the concept of and approach taken by KOBELCO's DX.

Introduction

The "DX Report"[1] published in 2018 by the Ministry of Economy, Trade and Industry sparked Japan's interest in DX (digital transformation). This drove the KOBELCO Group to declare DX as one of its management strategies within the KOBELCO Group Medium-Term Management Plan (FY2021-FY2023).[2]

The Ministry of Economy, Trade and Industry defines DX as the use of data and digital technology to transform not only products, services, and business models, but also the business itself, organization, business process, and corporate culture, by responding to changes in the business environment to meet customer and societal needs and establish a competitive advantage. However, each individual company is to define its specific DX initiatives, objectives, and scope in line with its management strategy.

This paper defines KOBELCO's perspective on DX and the company's plan of action toward DX initiatives.

1. KOBELCO's unique approach to DX

The KOBELCO Group will drive sustainability management in line with the KOBELCO Group's corporate philosophy to create added value. The DX component of our management strategy stipulates the use of digital technology and data to the fullest extent to achieve KOBELCO's View of the Future per the KOBELCO Group's corporate philosophy: a world in which people, now and in the future, can fulfill their hopes and dreams while enjoying safe, secure, and prosperous lives.

Further, KOBELCO's unique approach to DX includes the use of digital technology and data to foster KOBELCO's View of the Future as we carry out KOBELCO's Mission per the KOBELCO Group's corporate philosophy. Specifically, our Mission is to provide solutions that meet the needs of society by making the best use of the talents of our employees and our technologies. Such talents and technologies include diverse technological and business assets accumulated through engagement in various businesses including materials (steel and aluminum, advanced materials, welding), machinery (machinery, engineering, construction machinery), and electric power. Additionally, the group maintains relationships and touchpoints with customers in diverse fields, enabling the company to keep abreast of industry trends and customer needs. Digitizing information related to these distinctive assets and the needs of society and our customers makes it possible to utilize data throughout the group. Analyzing these data using AI and other tools reveals insights that could not be discovered within a single business. Combining the new value added following the discovery of these insights with Kobe Steel's distinctive technologies will foster the ultimate intention behind KOBELCO's unique approach to DX, which is to solve the challenges presented to society and our customers, including carbon neutrality and labor shortages.

2. DX implementation plan

We devised a DX implementation plan to bring to life KOBELCO's unique approach to DX. **Fig. 1** depicts this three-step medium- to long-term strategy.

2.1 STEP 1: Promote aggressive and bold digitization

Although Step 1 can be broadly referred to as digitization, the full phrase "promote aggressive and bold digitization" drives the involvement of all employees. Digitization can refer to the conversion of analog data into digital form or the automation or optimization of manual tasks via digital tools.

Specifically, this means all employees will use digital tools such as RPA (robotic process automation/automation of repetitive tasks), no-

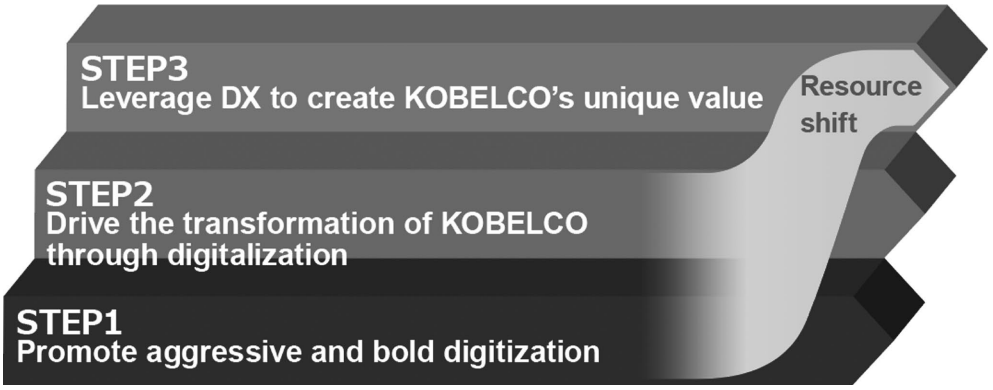

Fig. 1 Promotion strategy for digital transformation

code/low-code platforms (system development without programming languages), BI tools (business intelligence tools/data visualization), and electronic contract software to optimize processes.

Step 1 improves efficiency directly and sets the foundation for the data utilization and transformation that will occur in Step 2.

2.2 Step 2: Drive the transformation of KOBELCO through digitalization

One can broadly think of Step 2 as the digitalization stage, the purpose of which is to drive the transformation of KOBELCO through digitalization. This step involves digitalizing (systematizing) operations, connecting operations through upstream and downstream data, using data to define optimal protocols, and automating processing and decision making. These measures will transform operational processes and greatly improve efficiency.

This step also includes managing, visualizing, and analyzing integrated data for a decision-making process that is faster and more advanced due to insights that humans cannot detect.

Materials informatics (MI) provides a concrete example of data visualization and analysis. MI is the use of big data and machine learning in materials development to increase the efficiency of the development process and to discover material formulations that conventional knowledge and experience alone generally could not uncover.[3)]

Production sites are also using Internet of Things (IoT) technology to digitalize and aggregate data surrounding processes and equipment. The intention behind this is to drive the transformation toward data-driven manufacturing, which unites historical operating expertise with big data analysis (see "Building and Utilizing Company-wide Data Analytics Platform, DataLab®," pp.6-8 of this issue).

2.3 Step 3: Leverage DX to create KOBELCO's unique value

Step 3 involves implementing KOBELCO's unique approach to DX as described in Section 1 and making use of the resources (time) and aggregated assets (data) from Steps 1 and 2. This is how we will leverage DX to create KOBELCO's unique value to ultimately establish new value and solve societal challenges.

K-DIVE® (trademark of Kobelco Construction Machinery Co., Ltd.) is one example of KOBELCO's unique DX solutions. This system for remote construction equipment operation uses operating data to improve efficiency at construction sites and transform how operators work. As such, this system improves safety and addresses the societal challenge of labor shortages in the construction industry.[4)]

We are also furthering innovation in manufacturing by actively contributing to a carbon-neutral society through such products as AI Souro, an automatic blast furnace control system that uses AI to reduce CO_2 via high-volume charging of hot briquetted iron (HBI) in blast furnaces.[5)]

3. Infrastructure in support of DX

To accelerate Steps 1 through 3, every employee must support the transformation by using digital technology and data. The entire company must also hone its ability to implement, accelerate, and enhance this transformation (hereafter, the driving force for DX).

Three elements make up the driving force for DX: (1) a workforce that promotes the transformation and the use of digital technology and data; (2) an environment that facilitates employees' use of digital tools and data; and (3) an employee mindset and company culture of support and praise. Bolstering all of these elements in turn fortifies the driving force of DX.

These three elements are respectively deemed "employee development toward DX," "environment for data utilization," and "fostering a culture conducive to DX."

3.1 Employee development toward DX

We are cultivating two roles in support of DX. The first is that of technology evangelists, who will lead business improvements and the transformation through the use of digital technology in each department. The second comprises data scientists, who will use statistical methods and analytical techniques to solve problems and uncover new information from data accumulated through digitalization.

Employees in these roles must continuously incorporate DX into their work. These specialists will receive ongoing training regarding digital tools and will participate in community activities.

3.2 Environment for data utilization

We are enhancing outdated systems to ensure that our processes can respond swiftly and flexibly to internal and external changes and to support the effective storage and utilization of data generated by our processes.

We have also introduced IoT technology to collect operating data from equipment both in our plants as well as supplied to customers. Further, we are adapting our environment to support data utilization via new technologies through developments in cloud data storage and advanced data analysis software (see "Building and Utilizing Company-wide Data Analytics Platform, DataLab®," pp.4-7 of this issue).

3.3 Fostering a culture conducive to DX

We must foster a corporate culture in which all employees regard themselves as responsible for using digital technology and data, proactively inducing transformation, and taking on new challenges, wherein the cumulative actions of all employees are meaningful.

Efforts to cultivate the necessary culture have centered around sharing best practices through the intranet and internal events. However, this has not proven sufficient.

As such, we will provide training and support to improve DX literacy and foster a DX mindset, and we will establish a merit system to recognize and honor achievements.

Conclusions

This paper describes KOBELCO's perspective and implementation plan regarding digital transformation. Step 1 of the plan is to promote DX to set the stage for Step 2, the transformation of KOBELCO, which in turn supports Step 3 as the final stage of creating value through DX.

The latest Medium-Term Management Plan defines KOBELCO's unique transformation via KOBELCO-X as a means to accelerate these efforts. The relationship between KOBELCO-X and KOBELCO's perspective on DX is described next.

Step 2, driving the transformation of KOBELCO through digitalization, involves using digital technology and data to implement, accelerate, and enhance the four transformations of KOBELCO-X: business transformation (BX), customer experience transformation (CX^2), employee experience (EX), and factory transformation (FX).

Step 3, leveraging DX to create KOBELCO's unique value, involves using digital technology and data to bring to fruition the two prongs of our business strategy: ambidexterity (AX) and green transformation (GX).

Driving these initiatives forward supports our corporate philosophy of achieving KOBELCO's View of the Future as we carry out KOBELCO's Mission.

References

1) Ministry of Economy, Trade and Industry. DX Report - Overcoming the 2025 Digital Cliff and Pursuing Full-Scale DX Development. https://www.meti.go.jp/shingikai/mono_info_service/digital_transformation/20180907_report.html. Accessed 2024-03-15.
2) Kobe Steel. Kobelco Group Medium-Term Management Plan (FY2021-FY2023). https://www.kobelco.co.jp/releases/1209072_15541.html. Accessed 2024-03-15.
3) G. Taniguchi et al. R&D Kobe Steel Engineering Reports. 2023, Vol.72, No.1, pp.91-96.
4) Kobelco Construction Machinery Co., Ltd. K-DIVE®. https://www.kobelco-kenki.co.jp/dx/kdive.html?221205. Accessed 2024-3-15.
5) Kobe Steel, Ltd. Press Release. September 2020. https://www.kobelco.co.jp/releases/1205231_15541.html. Accessed 2024-03-15.

Building and Utilizing Company-wide Data Analytics Platform, DataLab®

Kazuo MINAMI*1・Masanobu FUJIHIRA*2・Taketsugu OSAKA*2

*1 IT Planning Department
*2 Digital Innovation Technology Center, Technical Development Group

Abstract

The utilization of data is becoming increasingly important in the art of manufacturing. Kobe Steel is an early adopter of IoT and big data, which has contributed to product development and service improvement, but lacked a unified platform for efficiently utilizing data across the company. To meet this challenge, a data analysis platform, DataLab®, has been established. This platform enables efficient collection and analysis of large amounts of data and leverages advanced analytical tools to provide new insights. The purpose of DataLab® is to provide centralized data management, flexible infrastructure, advanced analytical capabilities, strict security, and user-friendly operability. This paper introduces the DataLab® initiative through material development and equipment diagnosis examples.

Introduction

To increase competitiveness in today's business environment, companies must make progress in technological areas such as telecommunications and AI. Operating and product data are particularly critical to the growth of a company in numerous areas, including new product development, product improvement, market strategy, and customer experience.[1), 2)]

The importance of IoT and big data became apparent around 2014, when Kobe Steel's businesses started using them for product development, manufacturing kaizen initiatives, and customer service improvements. At the time, however, we did not yet have a platform for company-wide data storage and analysis. As such, each of these activities occurred in a silo, leading to individualized systems for analyzing data and expertise-backed information.

This led to a collaboration between the IT Planning Department and the Technical Development Group beginning in 2016, as set out in Kobe Steel's medium-term management plan. The objective of the collaboration was to support the development of data scientists and the analysis of operating and product data. Additionally, advances in digital technology have drastically increased the processing power of computers and networks. Cloud services are another area that has seen strong development. This has facilitated the previously difficult tasks of collecting, transmitting, and processing large amounts of data.

This backdrop is what led Kobe Steel to develop DataLab® [Note 1)], a data analysis platform for data storage, preprocessing, and analysis. This platform is the foundation for the unified management of data and expertise-backed information and for the systematic use of data across the company.

DataLab® was designed to provide the entire company with a platform that can facilitate the use of large amounts of unfavorably structured data, such as R&D data and time series data of equipment. This platform makes it possible to quickly and flexibly incorporate resources as needed and collect, store, and access vast amounts of data. We also incorporated advanced data analysis tools and AI algorithms to efficiently extract insights from the data and accelerate the creation of new value.

Section 1 of this paper presents the concept of DataLab®; Section 2 details the materials development and equipment diagnosis projects comprising the initial DataLab® use cases.

1. Concept of DataLab®

A data analysis platform must have data integration and management capabilities, infrastructure that responds flexibly to changes in computing resources, and advanced analysis tools and technologies, while supporting data security and ease of operation.

Data integration and management are particularly critical to guaranteeing the accuracy, completeness, and reliability of data and to ensuring that data can be analyzed effectively. Data collected from multiple sources, such as equipment and business-related systems, may have inconsistencies or exist in multiple formats. The quality of the data must therefore be improved through data cleansing (elimination of inconsistencies and multiple formats), data conversion (conversion to a standard format), and data preservation (storage for later use by business logic and analysis models).

The next requirement is to establish a scalable infrastructure that can respond flexibly to increased

Note 1) DataLab® is a trademark of Kobe Steel.

volumes of data and computational processing needs. Cloud services achieve such scalability very well.

Advanced analytical tools and technologies enable the extraction of insights from data through targeted analytical methods such as statistical analysis, machine learning, and deep learning. Encryption and the strict control of access rights guarantee data security.

Basic data visualization tools make data analysis accessible to a larger group of people and ensure that stakeholders can quickly and intuitively comprehend the data and take action.

The DataLab® platform has two main layers to provide all functions necessary for data analysis: a database layer for storing data and a solution layer for data analysis and solution development (**Fig. 1**). The following sections provide an overview of each layer.

1.1 Database layer

One of the main challenges in data management is that data are stored in multiple locations, including individuals' machines, computers inside equipment, and shared file servers. In addition, the lack of rules for associating data means that great effort is required to convert data into a format suitable for analysis and to align data created by different people for the same issue. A further challenge is the limited storage capacity of equipment controllers, meaning that key data are lost a few months after recording.

Additionally, to support efficient analysis, raw data must be converted to a specific format suitable for the issue being studied and stored in an appropriate database.

To overcome these challenges, the database layer of DataLab® makes it possible to store and manage raw data centrally in one data aggregation area. This functionality even supports differing formats, including structured data such as Excel and CSV file types, semi-structured data such as XML, and unstructured data such as image and audio files.

The process from data collection to storage in the database layer is standardized to facilitate data collection and storage, while the data association function significantly reduces the time and effort required to prepare data for analysis. Raw data are automatically stored in unprocessed form to accommodate future analysis needs. Storing data in the cloud enables indefinite data storage.

Data formatted and stored in the database layer via the process detailed above are used by the models and tools created in the downstream solution layer.

1.2 Solution layer

Accumulated data can be used for the development of purpose-built business solutions via the solution layer. This layer also serves as the environment for developing and analyzing applications using Kobe Steel's original analysis software, third-party analysis software, and visualization tools such as BI (business intelligence) tools.

Our proprietary analysis tools can perform advanced data analysis in the database, owing to models Kobe Steel's data scientists have fine-tuned for each object of analysis using machine learning.

Visualization tools support the user's decision-

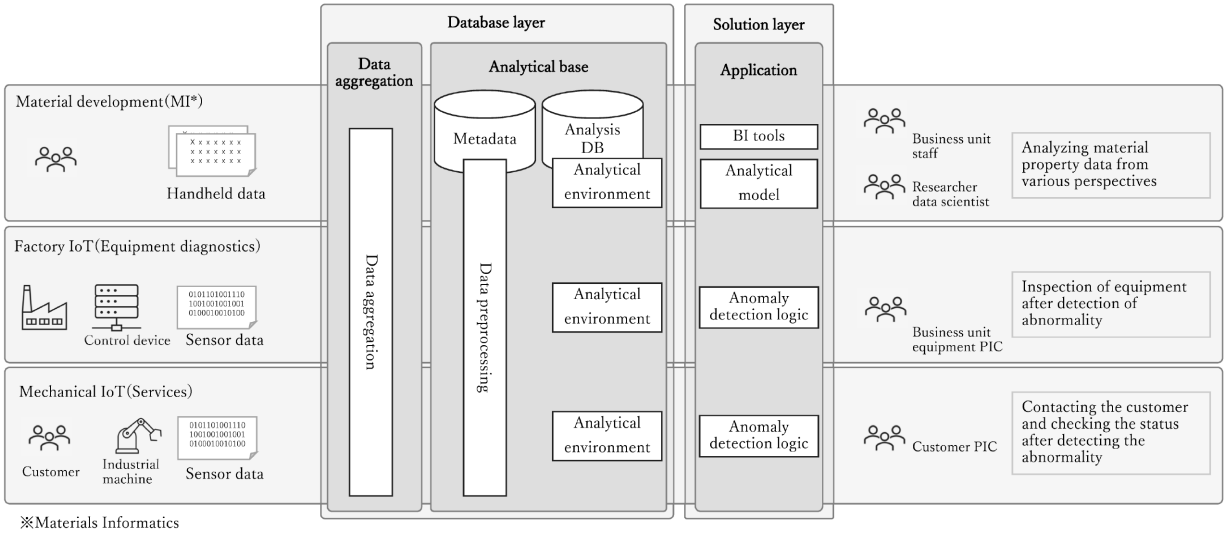

Fig. 1 Concept of DataLab®

making process by accessing the database to retrieve and visualize data.

Furthermore, the ability to securely transfer data to and from external data analysis services enables the use of third-party data analysis models. This makes it easy to perform data analysis and prediction without the need for development manpower and expertise required for AI.

2. Use cases

It is difficult to design any one system for all analysis needs. As such, the optimal configuration for each main object of analysis, such as materials development or equipment diagnosis, must be devised. Data for materials development is scant and exists in varying formats, whereas data for equipment diagnosis is abundant and has well-defined formats. These parameters lead to differences in the optimal data structures and protocols for data organization.

Materials development and equipment diagnosis served as initial use cases in developing DataLab®, as we anticipate the widespread use of such applications throughout Kobe Steel. This section provides an overview of our data analysis platform in terms of these use cases (see "MI Technology in Developing and Utilizing Materials," pp.35, and "Establishment of Condition Monitoring and Predictive Anomaly Detection System in No.2 Bloom Mill at Kakogawa Works," p.9, in this issue).

2.1 Materials development

The materials development process generally yields a broad array of research data, whether the project at hand involves developing new materials or improving existing materials. Research data include physical properties, chemical reactions, and durability test results, each of which is recorded in a different format. There is often no standard format for data regarding a given object of analysis because of differing project or team leaders, scopes, and research periods. Organizing data for analysis can be challenging because data points with the same designation may have different content, and data points with the same content may have different designations.

To organize these data, we incorporated functionality to automatically analyze accumulated data, group related data, and store data based on relationships in a database for analysis.

Research data for materials development are allocated to file formats such as CSV based on specific rules for storage in the data aggregation area. Data are then classified, tables are created, and relationships among the tables are extracted based on key fields and organized into a reverse star schema. Data are stored in a relational database, where tables can be arranged at will to extract data for analysis (**Fig. 2**).

Fit-for-purpose data tables are analyzed via commercial spreadsheet software, visualization tools such as BI tools, or our original software. Data scientists at Kobe Steel developed this software by fine-tuning machine learning output based on numerous models. To use the tool, the analyst chooses a model, enters parameters, and executes calculations to predict material properties and search for the most appropriate target material design. Cloud computing can be used for advanced calculations, negating potential speed limitations

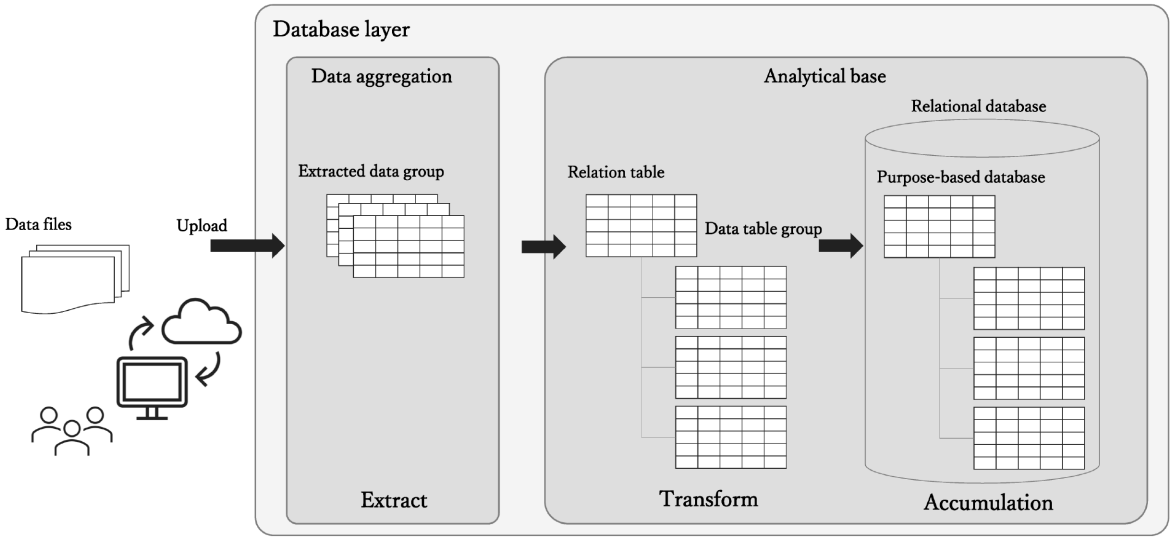

Fig. 2 Data processing image in the database

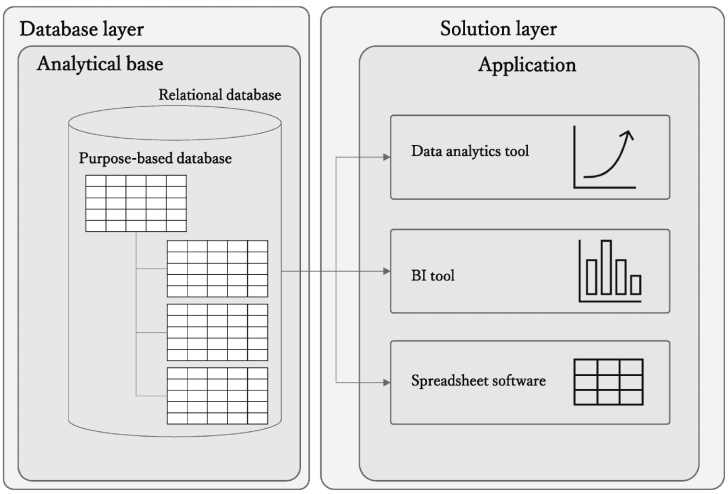

Fig. 3 System architecture of DataLab®

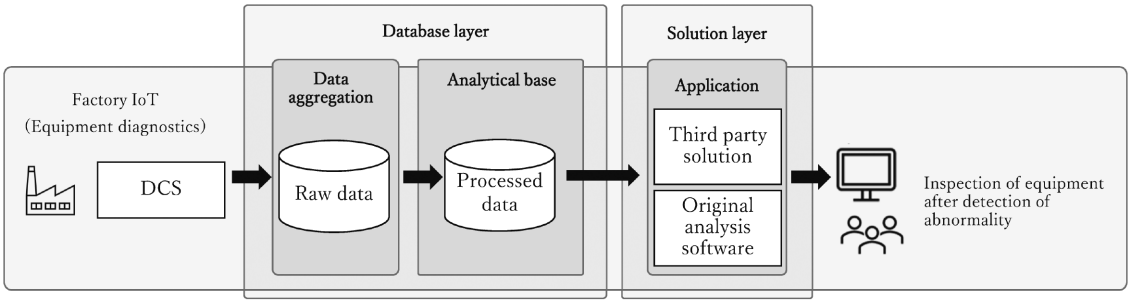

Fig. 4 Diagram of equipment diagnosis system

imposed by on-premises machines (**Fig. 3**).

2.2 Equipment diagnosis

Sensors in factory equipment provide real-time data to improve equipment availability and ensure safety; these applications fall under the field of equipment diagnosis. Data collected can include temperature, pressure, vibration levels, and equipment activity, all of which can be used to monitor equipment health and efficiency, predict faults, and set preventive maintenance intervals.

The many sensors and short acquisition cycles result in the generation of a very large amount of data. However, once a data collection mechanism is established, it can easily be deployed in other equipment since the data to be acquired is standardized. Third-party development tools for equipment diagnosis can be combined with our original software for a tailor-made analysis system.

Fig. 4 depicts all equipment diagnosis needs from data collection to analysis.

A gateway with software for transmitting data to DataLab® is used to collect the data. This device transmits data from a controller (DCS or PLC) to DataLab® for storage in the data aggregation area as raw data in a predetermined format. Data are processed and stored in a format conducive to utilization by analysis models and solutions.

In the case of equipment diagnosis, equipment sensors collect a variety of data, resulting in a large number of categories of data (i.e., columns). However, anomaly detection models only make use of data related to the anomaly being detected. In our use case, we built an analysis database by dividing time series data for equipment diagnosis at fixed intervals and storing them in a columnar database, thereby achieving both ease of analysis and high performance.

Our analysis solution uses the algorithms and functionalities of third-party tools to detect anomalies based on normal operating data. However, our data scientists can also build and implement custom analysis software using Python or programs for statistical analysis. Our system also features a data visualization tool for equipment monitoring.

3. Future prospects

Our materials development and equipment diagnosis solutions are being used only within a subset of our divisions. We plan to expand these systems to other divisions and add new

functionalities, including support for image data, which is often requested for inspection and materials development.

Additionally, it is notable that data with the potential to create value added exists in a variety of places, such as computers within equipment as well as individuals' machines. As such, we will foster data aggregation to support the sharing of data among our businesses.

We will also strive to make data analysis more accessible through the accumulation and sharing of expertise by capitalizing on the data being collected and promoting data visualization via DataLab®.

Conclusions

This paper introduces DataLab® for data utilization within an organization and presents select use cases. We believe data utilization is essential for improving manufacturing capabilities. As such, we will strengthen Kobe Steel's manufacturing capabilities by using DataLab® to accumulate and analyze data from various plants, equipment, and research projects.

References

1) N. Morita et al. Mitsubishi Electric Technical Reports. 2022, Vol.96, No.5, pp.40-43.
2) F. Taya et al. JFE Technical Report. 2022, No.50, pp.44-49.

Establishment of Condition Monitoring and Predictive Anomaly Detection System in No.2 Bloom Mill at Kakogawa Works

Takashi HAGIWARA*1 · Yoshitaka INOUE*1 · Kazuhiro MORII*2 · Hisafumi UNO*3 · Tsutomu ANDO*4

*1 Wire Rod Production Department, Kakogawa Works, Steel & Aluminum Business
*2 Digital Innovation Technology Center, Technical Development Group
*3 Process Control Department, Kakogawa Works, Steel & Aluminum Business
*4 Equipment Department, Kakogawa Works, Steel & Aluminum Business

Abstract

To ensure the stable operation of the No.2 Bloom Mill at the Kakogawa Works, a data acquisition apparatus has been introduced to develop a system for detecting signs of equipment abnormalities. To accurately capture the signs of abnormalities in the No.2 Bloom Mill, where diverse operating conditions and patterns exist, a method has been adopted that enhances the versatility of models by extracting, learning, and analyzing data at suitable intervals for evaluation. This has led to the development of a system, Mode Oriented Novel Anomaly Detector (MONAD), which enables the steps from data preprocessing to model creation without the need for programming. Standardization of the flow from the model creation to maintenance work using MONAD has enabled the set-up of a system that can be operated by technicians and operators without expertise in machine learning. Efforts to improve the accuracy of the model are being made through its operation at the manufacturing sites.

Introduction

The Kakogawa Works No.2 Bloom Mill (hereafter, No.2 Bloom Mill), which began operation in 1970, produces steel billets destined for the rolling mills that produce our steel wire rod and bar products. In 2017, we implemented a major expansion in conjunction with the consolidation of upstream processes[1] to increase the production capacity to a level unparalleled throughout the world, at 300,000 tons per month. The No.2 Bloom Mill supplies almost all the steel billets used in Kobe Steel's steel wire rod and bar products. As such, ensuring the stable operation of the No.2 Bloom Mill is critical for ensuring the stable supply of the entirety of the company's steel wire rod and bar products.

Maintenance plans have conventionally been driven by time-based maintenance (TBM) and condition-based maintenance (CBM) approaches, which are based on past experience as well as daily inspections that reveal equipment condition. There was no option other than to apply provisional TBM and CBM standards to the new equipment introduced as part of the 2017 expansion. However, we knew we needed to introduce methods that could more reliably prevent sudden equipment failure. This paper details the initiative that spurred at Kobe Steel in 2018 to develop the information infrastructure and system for continuous condition monitoring and predictive anomaly detection for a wide variety of equipment at the No.2 Bloom Mill.

1. Guidance for developing an anomaly detection system

1.1 Overall system concept

A common method of using machine learning for anomaly detection is to learn the regular patterns in data and regard deviations from these regular patterns as predictive signs of an anomaly.[2), 3)] Many anecdotes report the implementation of anomaly detection based on multivariate analysis of data aggregated from individual plants that are in continuous operation. This method has attracted attention because it can uncover signs of anomalies that are based on unexpected relationships in the data that could not be discerned by humans.[4)]

However, there is a particularly wide variety of operating conditions and operating patterns at the No.2 Bloom Mill. This is because certain circumstances call for manual operation and because parameters such as steel grade and dimensions affect motor loads and the processes executed. In contrast to a plant that is in continuous operation, data across this operation lack regular patterns; therefore, the conditions flagged by machine learning as deviations may be false positives rather than predictive signs of anomalies.

One potential solution is to train individual models for each operating condition and operating pattern. However, this would require a prohibitively large number of models. It would also be impossible to apply these models to new operating conditions and operating patterns. Therefore, we set out to develop a method to increase the model's versatility. We abandoned the focus on operating conditions and operating patterns, instead applying

machine learning to subsets of data suitable for evaluation, such as those in which the load is constant. Determining the conditions for data extraction requires considerations beyond operating conditions and operating patterns. Critical as well are equipment structure and conditions related to automatic operation, making the expertise of operators and maintenance technicians essential. Even with the data extraction method described above, exceptional circumstances could lead to false positives. This makes it challenging to define absolute standards for what should occur when an anomaly is detected, such as immediately shutting down equipment without human intervention - a human must ultimately decide the proper action.

We therefore devised the plan below to develop a model creation system for operators, maintenance technicians, and shop floor workers who do not have expertise in machine learning.

- Models should be optimized based on individual equipment rather than multivariate analysis of aggregated data for the entire plant.
- The system's tools for data preprocessing and model creation must not require programming.
- The maximum number of variables should be limited to two so the user can visually comprehend the model's behavior and the relationship between the data and actual events.

1.2 Identifying which equipment to monitor

The No.2 Bloom Mill has several thousand pieces of equipment; it is unrealistic to create anomaly detection models for all of them. With stable operation of the No.2 Bloom Mill as the objective, we narrowed our focus to equipment expected to cause production line downtime of 24 hours or more following malfunction. We put our efforts toward creating a model for predictive anomaly detection and collecting data in support of continuous monitoring.

Continuous monitoring data required for such a model include motor speeds and currents, control signals, and other data acquired by conventional control networks.

2. Implementing a data acquisition apparatus

2.1 Requirements for a data acquisition apparatus

The No.2 Bloom Mill has a complicated control system, with equipment from a variety of manufacturers due to the plant's expansion and iterations of piecemeal upgrades to the control system. Data acquisition apparatuses differ by manufacturer, and data for some signals could not be collected. Together, these issues made it impossible to collect all data synchronously and in a central repository - two criteria that are critical because they make it possible to monitor correlations within data and to detect deviations, which in turn are critical for anomaly detection.

We established the five stipulations below for the data acquisition apparatus to support the development of an anomaly detection system.

(1) The apparatus must communicate with the control networks of major Japanese PLC (programmable logic controller) manufacturers to facilitate deployment at other Kobe Steel factories.
(2) The implementation of requirement (1) must enable synchronized data acquisition and centralized data storage.
(3) Data must be available as a text file to ensure universal data utilization.
(4) Collected data must be accessible via any computer on the network to facilitate data utilization.
(5) Scaling up and the addition of new functionalities must be possible to accommodate potential future needs.

To meet these stipulations, we chose the data acquisition apparatus ibaPDA, which is manufactured by iba AG (hereafter, iba).

2.2 Features of iba's data acquisition apparatus

iba's data acquisition apparatus can connect to the networks of many PLC manufacturers (requirement (1)) and can perform synchronized, central data collection (requirement (2)). It also provides numerous methods for integrating data with higher-level systems, and packaged data can be transferred via a text file (requirement (3)). Collected data can also be viewed via analysis software from any terminal on the company network for utilization (requirement (4)). Functionalities such as vibration analysis and image processing are easy to add to the software, making it highly scalable (requirement (5)). iba's software proved extremely useful in this project, as it processed numerous signals and visualized the correlations (**Fig. 1**), making it easy to conduct preliminary modeling studies.

2.3 Introducing iba's data acquisition apparatus

Connection to a Japanese PLC manufacturer's network was not guaranteed when the system was introduced. Therefore, we conducted a small-scale demonstration to verify that the system could

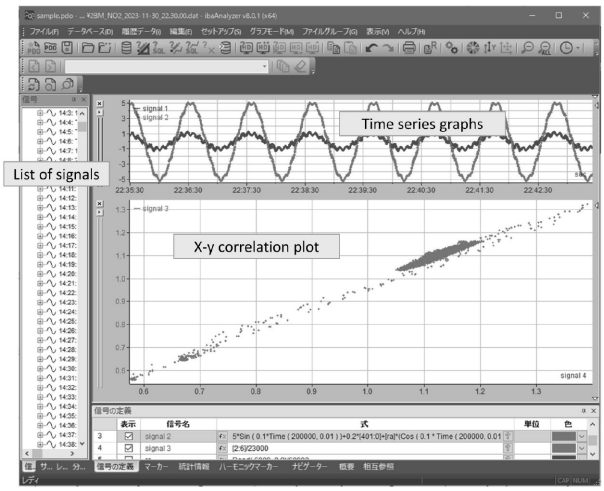

Fig. 1 Sample screen image of analysis software

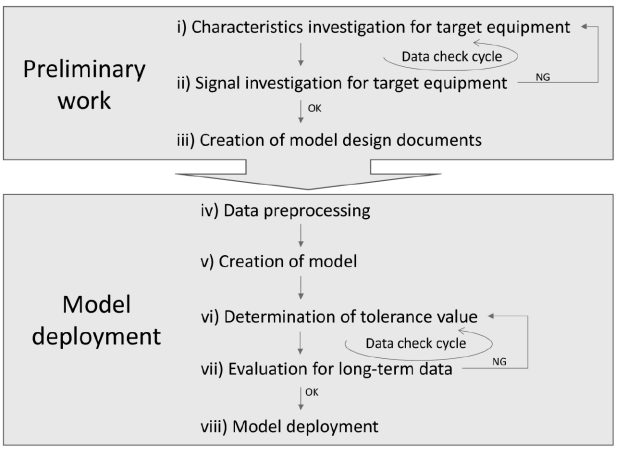

Fig. 2 Workflow for model creation

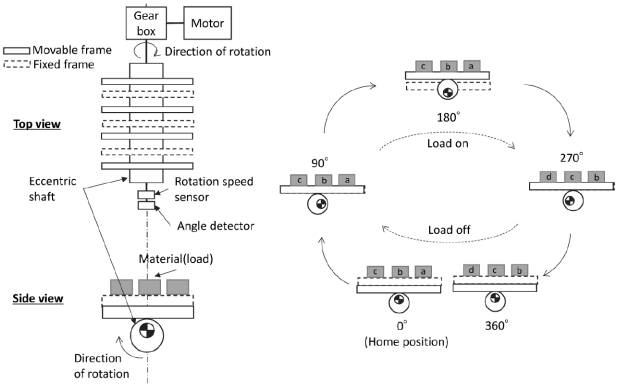

Fig. 3 Schematic diagram of equipment

perform stable data collection and central storage.

In addition, to make it easy to link collected data with Kobe Steel's other systems for complete utilization, we tagged each piece of equipment with a standardized ID as a universal key. We appended variable names and units of measure to important data to facilitate data utilization.

In addition, we developed a standard based on the No.2 Bloom Mill to guarantee that the system would be of equal quality when deployed at other plants.

3. Establishing a method for model creation

3.1 Process flow of anomaly detection model creation

Since the operators and maintenance technicians will spearhead the creation of optimized models for each piece of equipment according to the concept described in Section 1.1, we defined a standard workflow to ensure that each model would be of equal quality and developed with equal efficiency.

There is often little or no data on anomalies for training machine learning. Therefore, a model that allows for a certain degree of false positives is created, and then it is refined by trial and error until the rate of false positives is reduced to an acceptable level. This is why we created the workflow shown in **Fig. 2**, which is based on the "Conceptual Diagram of the Mixed-Standard Learning Lifecycle".[5] In this workflow, the model creation process is divided into a preprocessing phase and a deployment phase. Each phase has a data check cycle to incorporate the concept of agile development, a method that anticipates changes and additions during the development process. The preprocessing phase, which involves characteristic selection and data extraction, is particularly important for improving the accuracy of the model; the next section details this phase by way of example.

3.2 Example-guided explanation of the model creation process

Fig. 3 depicts the model creation process as it was applied to actual conveying equipment. This equipment has a movable frame connected to an eccentric shaft that picks up steel billets and advances them forward. We created the model based on a failure of the eccentric shaft to rotate, which is one of the possible failures of this equipment.

(i) Characteristics investigation for the target equipment

The first step is to select up to two characteristics for detecting rotational failure, in line with the development concept. Motor current can serve as the first characteristic because a failure of the eccentric shaft to rotate results in increased motor torque. This equipment repeatedly starts and stops during operation. Because the current constantly fluctuates alongside changes in speed, we selected motor speed as the second characteristic. The correlation between these two characteristics can be assumed to be constant when the conveying equipment is

unloaded. However, while the steel billet is being lifted, factors such as the weight of the steel billet cause variation in the motor current, changing the correlation between the two characteristics. Changes caused by operating conditions, such as the weight of the steel billet, can lead to false positives. As such, the equipment drawings and control circuit schematics must first be consulted so that only no-load data will be extracted. Per Fig. 3, the no-load condition exists when the eccentric shaft angle is between 0° and 90° or between 270° and 360°.

(ii) Characteristic investigation via analysis software

The next step is to use analysis software to review the data distribution from the investigation in (i) for a potential correlation between the two characteristics. The time series data of the two selected characteristics and the angle of the eccentric shaft as the condition for data extraction are displayed to reveal key aspects of the data (**Fig. 4** (a)). In this example, in addition to the expected "with load" section, spikes with low reproducibility occurred immediately after the motor started and immediately before it stopped. Therefore, in addition to the "with load" angle condition, we also excluded the angle range in which these spikes occurred from the scope of data extraction. We used the analysis software to create a scatter plot of the two characteristics extracted under the applicable eccentric shaft angle condition (Fig. 4 (b)). If the data points are clustered, this means the extracted data are highly reproducible, and a model can be created. Conversely, if the points are highly diffuse, reproducibility is low, and it is not possible to create a model. In the latter case, extracted data must be reviewed. These steps constitute the most critical process in model creation. It is important to systematically record the approaches taken and the results of trials run as part of this process.

(iii) Devising a model design specification

Upon data validation, the content of the investigation should be recorded as a set of model design specifications. This makes it possible for people other than the model's creator to verify the model's design concept and validity, which is useful for long-term management of the model and application to maintenance activities.

We used Airtable (trademark Formagrid Inc.) web service to create the model design specification (**Fig. 5**). This service can store information related to the model in the form of text and images, including design information, equipment structure, operating plans, sensor signal information, correlation study results, and model evaluation results. It can also store comments and revision history information, making it easy to keep a record of the model creation process and changes made.

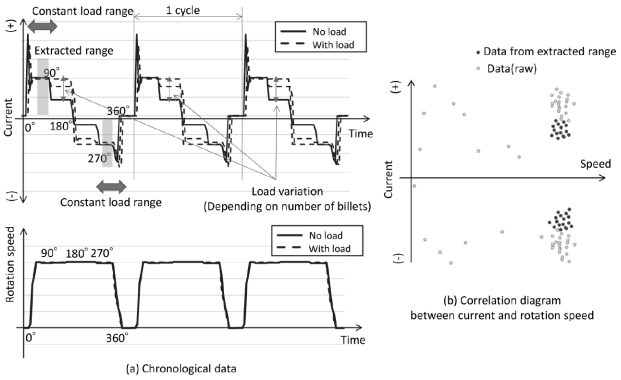

Fig. 4 Example of summary data

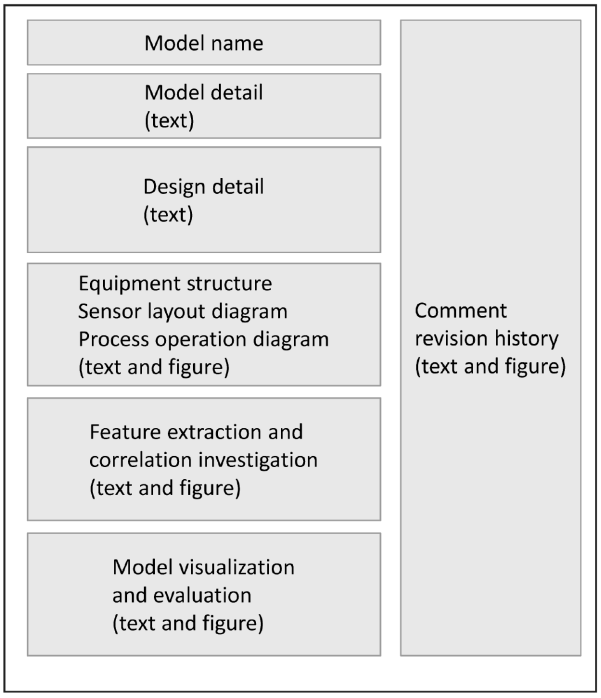

Fig. 5 Schematic image of Airtable

4. Developing an anomaly detection system

We developed the MONAD system (Mode Oriented Novel Anomaly Detector; **Fig. 6**) based on the design procedure standardized in Section 3, "Establishing a method for model creation." MONAD enables simple, no-programming model creation and implementation via the workflow shown in Fig. 2.

MONAD has two core strengths: (1) Only two characteristics are required for anomaly detection. As such, even operators and maintenance technicians without expertise in machine learning can ascertain model behavior via scatter plots and trend graphs, enabling the design of practical anomaly detection logic that capitalizes on their operational expertise. (2) MONAD has extensive

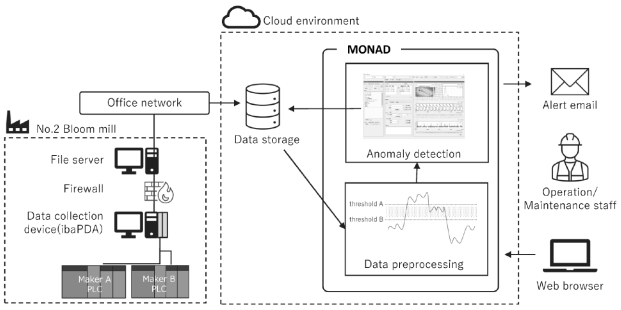

Fig. 6 MONAD system

preprocessing options, enabling simple, user-driven processing of the two variables selected. The following sections introduce MONAD's mode extraction and anomaly detection logic construction functions.

4.1 Mode extraction function

In MONAD, the regularity of data fluctuations occurring alongside operating conditions and operating patterns is called a "mode." To extract the desired mode from the data, the first step is to select up to two variables for the anomalies to be detected and the auxiliary signals, such as ON/OFF signals and command values, to be used for mode extraction. Mode extraction methods include the specification of a range of auxiliary signal values, segmentation based on fluctuation patterns within time-series data, and direct selection of the extraction range on a scatter plot. Users can combine these functions to extract the data they wish to evaluate, such as during constant-load operation, based on the knowledge they have about the equipment (**Fig. 7**).

4.2 Anomaly detection logic construction function

MONAD trains anomaly detection models such as the LOF (local outlier factor)[6] on data after mode extraction. The system then uses the trained models to calculate and graph anomaly scores for the evaluation period. The user can confirm that the model is designed as intended by graphing contour plots of anomaly scores on a scatter plot (**Fig. 8**).

Anomaly evaluation occurs via batch processing (processing of a predefined set of data in bulk) after deployment of the model. An anomaly is reported if the anomaly score exceeds the threshold at a frequency greater than the permissible frequency.

In addition to LOF, MONAD can perform anomaly detection by evaluating monotonically increasing or decreasing trends in time series data and changes in data distributions and waveforms. Users can select from these logics for anomaly

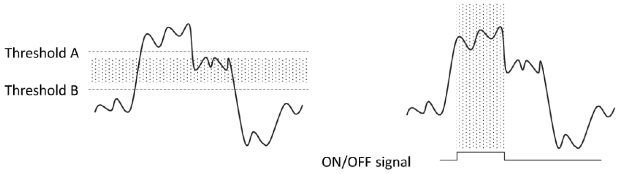

Fig. 7 Examples of mode extraction

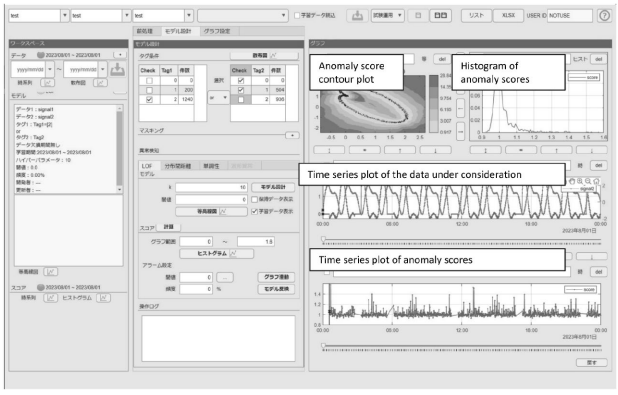

Fig. 8 Example of model design screen

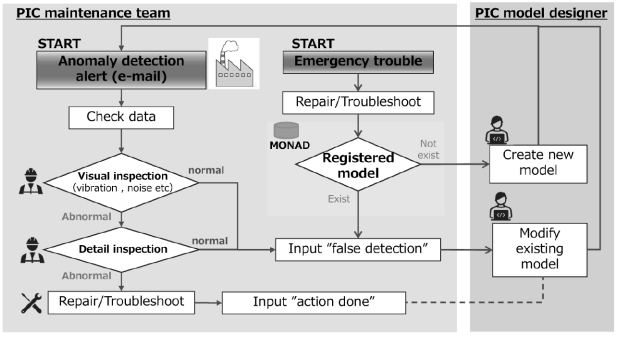

Fig. 9 Workflow of daily maintenance using MONAD

detection, and new logics will be added based on user requests and analyses of anomaly cases.

5. Application in maintenance

To use the models in MONAD for each piece of equipment as tools for anomaly detection in maintenance activities (predictive maintenance), the system must be deployed on the production line, and the models must be refined.

To support deployment on the production line, we first had to define the optimal workflow for data and situational validation following an anomaly detection alert (**Fig. 9**). We designed the interface based on this to provide maintenance technicians with the necessary information at each step when using MONAD.

MONAD automatically emails the maintenance technician when equipment is determined to be in an anomalous condition. The maintenance technician

checks how the anomaly score is trending, checks the condition at the time of the anomalous data, performs a visual inspection of the equipment, and inspects the equipment for abnormal vibration and noise. If an anomaly is suspected during the visual inspection, the technician decides whether to shut the equipment down and conduct a detailed investigation. The technician records the inspection results and actions taken on the monitoring screen so the pertinent information is available to anyone who needs it, such as the model's creator.

After establishing the framework detailed above, the system went live in production in October 2023. We are validating and improving the accuracy of each model alongside our use of the system per the process flow shown in Fig. 9 The system has already detected early indications of poor bearing lubrication in steel billet conveying equipment; as such, we anticipate similar benefits in the future. For equipment comprising multiple drive components, such as reduction drives, however, we must continue validating the accuracy of the models alongside research into suitable condition monitoring methods based on the unique parameters of each piece of equipment.

Conclusions

This paper describes the efforts to collect data from equipment and introduce an anomaly detection system that uses these data at the No.2 Bloom Mill. Operators and maintenance technicians without expertise in machine learning can use the MONAD system and model creation process introduced in this paper to create equipment-specific models using agile methods. This constitutes a new approach to anomaly detection in plants with diverse operating conditions and operating patterns. Furthermore, MONAD itself is a versatile system that can easily be deployed to other plants alongside an appropriate selection of the data required for monitoring the equipment. We will continue to validate MONAD's effectiveness at the No.2 Bloom Mill and plan to deploy it to other plants within the company.

References

1) T. Taira et al. R&D Kobe Steel Engineering Reports. 2019, Vol.69, No.2, pp.37-41.
2) T. Ide. Introduction to Anomaly Detection using Machine Learning. CORONA PUBLISHING CO., LTD. 2015.
3) K. Yamanishi. Anomaly Detection with Data Mining. KYORITSU SHUPPAN CO., LTD. 2009.
4) T. Soma. Journal of Japan Society for Safety Engineering. 2018, Vol.57, No.2, pp.107-113.
5) National Institute of Advanced Industrial Science and Technology. Machine Learning Quality Management Guidelines. 4th edition. 2023-12-12. https://www.digiarc.aist.go.jp/publication/aiqm/AIQuality-requirements-rev4.1.0.0112-signed.pdf. Accessed 2023-12-13.
6) M. Breunig et al. Proceedings of the 2000 ACM SIGMOD international conference on Management of data. 2000, pp.93-104.

Integrated Management of Machining Factory Using IoT Platform

Shinsuke ASAI*1・Kazuki KITA*2・Hideo IKEDA*3

*1 Machinery Plant, Production Division, Machinery Business (currently Kobelco Industrial Machinery India Pvt. Ltd.)
*2 Materials Research Laboratory, Technical Development Group (currently Planning & Administration Department, Technical Development Group)
*3 Digital Innovation Technology Center, Technical Development Group

Abstract

In a processing plant with a multiple-variety mixed-flow production system, a single worker handles multiple machine tools. The traditional human-dependent management method, however, is facing difficulty in efficiently operating the entire factory. As an attempt to solve such issues using process data obtained from machine tools, an IoT platform has been constructed to monitor the status of the machine tools by utilizing IoT technology. This paper details the construction of a system that analyzes process data from machine tools in real-time and detects abnormalities for automation, including the machine-stop command. It also discusses the implementation of this system on machine tools and provides examples of analysis and utilization by combining worker position information with machine operation information.

Introduction

Although manufacturing is becoming more advanced, Japan is experiencing a major issue of a severe labor shortage. The early years of the 21st century are seeing the practical application of digital technologies such as AI, IoT, and robotics, advancing automation and efficiency in numerous fields. However, there are still many manufacturing processes that rely on skilled labor, with technologies to overcome this challenge still to be desired.

The machining factory at Kobe Steel's Takasago Works runs multiple-variety mixed-flow production. Each part undergoes a large number of processes on its way to becoming a finished good, with pitch times for each process ranging widely, from a few hours to several hundred hours. In addition, the operation is made more complex because of each customer's highly specific requirements, which entails many parts with similar geometries yet few that are identical. The conventional method of improving productivity has been to automate machinery and employ a system in which each operator is responsible for multiple machine tools (hereafter, multi-machine operation). However, monitoring production operations is a challenging task because the products vary and have demanding machining needs in terms of shape, workpiece material, and tolerances. As the combination of machine operation status and worker status becomes more complex, it becomes more difficult for the supervisor to grasp the overall status of the operation, which is a major impediment to improving productivity on the shop floor.

As part of recent progress in IoT, production facilities are outfitting machine tools with communication functions to acquire real-time data. These endeavors are intended to overcome the aforementioned issues by supporting an IoT platform (hereinafter, PF) that grasps the status of the entire machine tool, or multiple machine tools, to enable data utilization.

Many attempts have been made to quantify the effects of improvement and value added in production using industrial engineering techniques, mainly in terms of increased throughput in tasks performed by humans[1]. Recent developments in sensor technologies have also driven attempts to analyze operations based on worker position information and imaging.[2] Furthermore, the field of machine tools has seen remarkable progress in terms of IoT. Computer Numerical Control systems (CNCs) and Programmable Logic Controllers (PLCs) can now provide detailed information regarding operating status. In the machining sector, for example, MTConnect has become a proven standardized protocol for obtaining operating information.[3]

These developments have led to attempts to visualize the value added behind operations incorporating people and equipment by combining worker position information with machine operation information.[4]

The PF presented in this paper supports the management of production status in a machining factory in a manner that integrates the statuses of workers and equipment.

Section 1 describes the machine tool PF central to this initiative. Section 2 provides examples of the use of process data acquired from machine tools using the PF. Finally, we report the results of evaluating the productivity of operations incorporating people and equipment by combining machine operation information acquired by the PF with worker position information.

1. Machine tool IoT platform

Kobe Steel's machine tools come from many different manufacturers, necessitating a versatile data acquisition system that can interface with a wide variety of machine tools. Many of our machine tools use FANUC CORPORATION's control panels. Because communication with other manufacturers' control panels and robots is also possible, we adopted FANUC's factory operation management software MT-LINKi. We chose MotionBoard Cloud (BI dashboard made by WingArc1st Inc.) for our visualization tool because of its high degree of flexibility and customization. The PF developed in collaboration with KOBELCO SYSTEMS CORPORATION makes it possible to run iterative cycles of data collection, visualization, analysis, and optimization.

1.1 System configuration

Fig. 1 shows the system configuration. MT-LINKi can collect equipment information not only from machine tools with FANUC CNC systems, but also from FANUC robot controllers, PLCs supporting OPC UA (open platform communications unified architecture), and machine tools compatible with MTConnect. Machine tools made by other manufacturers, such as the Yamazaki Mazak Corporation and Okuma Corporation tools in our plants, interface with MT-LINKi via MTConnect. With this system configuration, data from machines with FANUC control panels can be acquired every 0.5 seconds, and data from equipment using MTConnect can be acquired every 2.0 seconds.

1.2 Information and visualization screens

Table 1 shows a sample of the data that can be obtained from a machine tool. Information that can be collected includes machine operating status, program information, command and actual speed and feed rate, spindle load, servo load by axis, and position deviation.

We designed our visualization screen to facilitate the use of information collected from the machine tools and have begun trial operation. The following is an explanation of the visualization screen and how it is used.

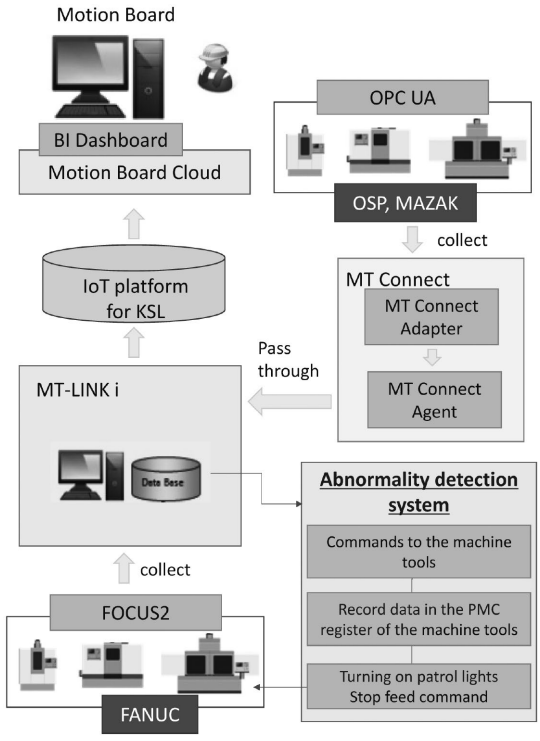

Fig. 1 System configuration

Table 1 Signal data from a machine tool

No	Signal data	Description	No	Signal data	Description
1	SigOP	Automatic operation signal	31	Override	Override of feed rate
2	SigSTL	Automatic operation starting signal	32	SigNP	In-position signal
3	SigSPL	Automatic operation stop signal	33	AbsPos	Absolute position
4	SigAL	Alarm signal	34	RelPos	Relative position
5	EMG	Emergency stop signal	35	McnPos	Machine position
6	Mode	Mode	36	SpindleLoad	Spindle load
7	MainProgram	Main program	37	SigENB	Operating spindle load signal
8	ActProgram	Running program	38	SpindleSpeed	Spindle speed
9	Sequence	Sequence no	39	SpindleTemp	Spindle motor temperature
10	MainComment	Main program comment	40	ServoSpeed	Servo speed
11	ActComment	Running program comment	41	ServoTemp	Servo temperature
12	ActS	Actual revolutions	42	ServoError	Servo position deviation amount
13	ActF	Actual feed rate	43	ServoLoad	Servo load
14	ActFdec	Measured feed rate	44	ServoCurrent	Servo current
15	ModalS	Command value of revolutions	45	ServoCurrentPer	Servo current rate
16	ModalF	Command feed rate	46	PulseCodeTemp	Servo pulse code temperatuire
	…	…		…	…

Fig. 2 shows the operation status visualization screen. The operator can use this screen to check the real-time operating status of the machines they are responsible for with a mobile device such as a smartphone. The screen also helps the operator determine which machine to attend to next, reducing machine downtime. Machines in green are in automatic operation and do not require attention. If a machine is yellow, this indicates that the programmed operation has stopped and human intervention is required. A red machine is stopped in the alarm state and requires immediate confirmation of machine status.

Fig. 2 Operation status visualization screen

Fig. 3 shows the automatic measurement result visualization screen. Specifically, in the machining process of mass production operations, a touch sensor can automatically measure workpiece dimensions after machining. The results can be viewed in chronological order, with the vertical axis containing the automatic measurement results. Entering the upper and lower tolerance limits in advance makes it possible to see at a glance whether the measurement result is within tolerance. This feature can be used to enhance traceability and manage trends in dimensional stability.

Fig. 4 shows the program operation status screen. Previously, we could only determine operating status via indicator lights for three modes: automatic operation, stop, and alarm. With this screen, we can now see not only the operating status, but also the percentage of time each mode is active. EDIT applies during program editing; HANDLE, JOG, and MDI involve different types of operator intervention; and MEMORY is an automatic operation. It is possible to increase the automatic operation ratio by first analyzing the proportion of each mode per NC program and then reducing the duration of modes other than automatic operation. In addition, comparing NC programs for similar parts makes it possible to compare automatic operation ratios by NC programmer to determine whether a program lends itself well to automatic operation.

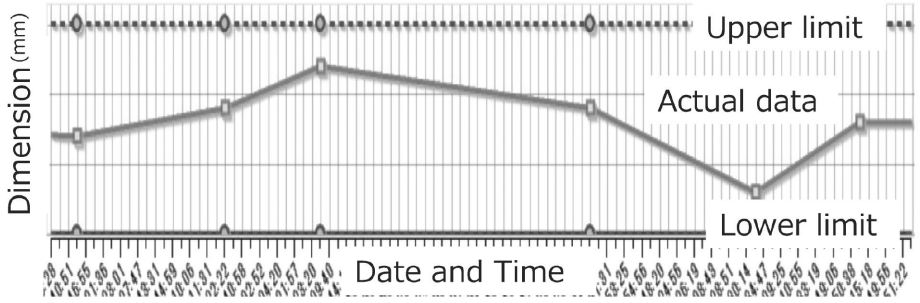

Fig. 3 Automatic measurement result visualization screen

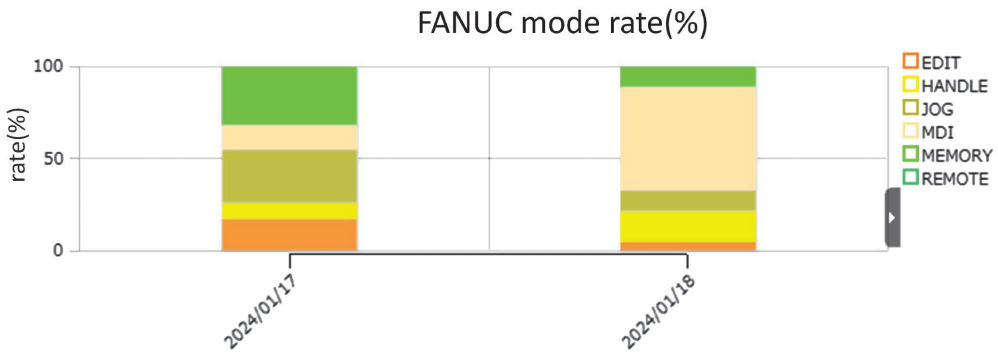

Fig. 4 Program operation status screen

2. Prediction and detection of tool abnormalities using process data

The machining process for Part A includes the cutting of a deep pocket with an end mill. The required tool has a long projection relative to the tool diameter, increasing the likelihood of tool abnormalities due to machining vibration and tool deflection. This hinders the ability to increase throughput, reduce manpower, or automate the process. To prevent tool abnormalities, Kobe Steel has developed and deployed tool abnormality prediction and detection technology and an adaptive control system using IoT-powered machining technology.

2.1 Target workpiece and machining process

Major tool damage could occur during machining, as shown in **Fig. 5**. In some cases, the workpiece must be scrapped. This led us to begin developing a system that prevents tool breakage by detecting fractures or adhesion. The system analyzes process data collected from machine tools and stops the equipment before the tool breaks completely.

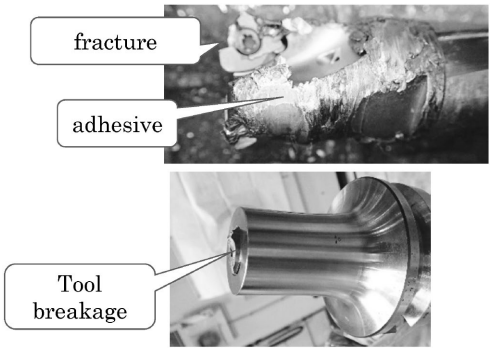

Fig. 5 Pictures of damaged tools

There is potential in techniques to detect tool abnormalities via comparison with simulations[5] and via discernment of abnormalities based only on data occurring under normal conditions, such as machining sounds, acoustic emissions, and spindle current.[6), 7)] However, the need to collect simulation data or normal data under similar machining conditions prior to actual production was an impediment to the practical application of these techniques. Therefore, we pursued a method that uses only load data collected from machines without requiring prior data for learning. We studied past tool abnormalities, as shown in **Fig. 6**, focusing on the fact that a sudden increase in spindle load (load on the spindle motor) or an increase in the vibration of the spindle and Z-axis servo motors (load swing - absolute value of the difference between data points) occurs before an abnormality. As such, we developed an abnormality detection algorithm that detects load and load fluctuations to recognize precursors to a machining abnormality. Note that spindle load and changes in load are shown as a percentage of the rated output of the drive motor of each axis.

2.2 Abnormality detection algorithm

The abnormality detection algorithm based on the spindle load data in **Fig. 7** is described next. The first 40 seconds of machining are excluded from the target of detection, as large changes in load are likely to occur before and after the start of tool rotation and before and after the start of machining during this period. Furthermore, averaging the data from the most recent 20 seconds of abnormality judgment time (hereafter, smoothed value) suppresses false positives due to sudden changes in machining load outside of intended tool

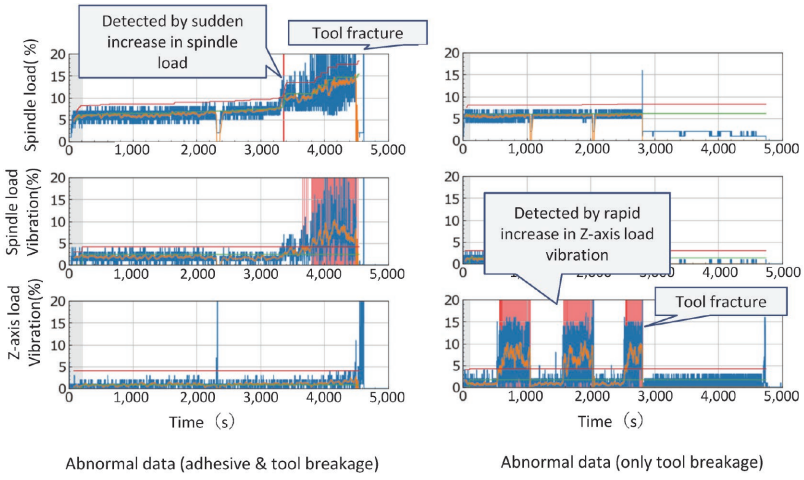

Fig. 6 Process data when an abnormality occurs

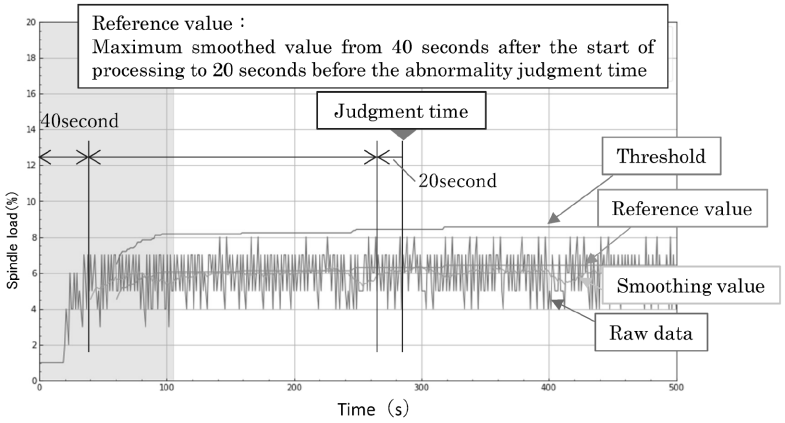

Fig. 7 Features for abnormality detection related to spindle load

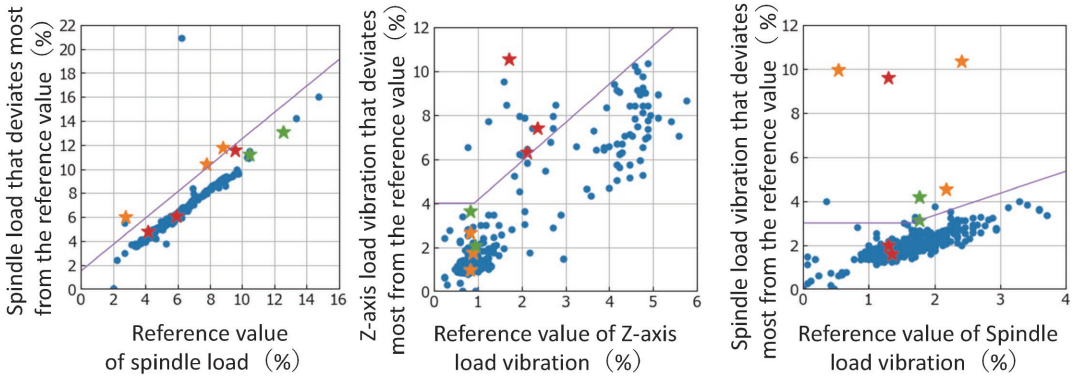

Fig. 8 Detection simulation results for past abnormal conditions

abnormalities. The maximum value of the smoothed load in each interval from 40 seconds after the start of machining to 20 seconds before the abnormality judgment time serves as the reference value per Equation 1. If the smoothed value exceeds the threshold value, obtained by adding an offset to the reference value multiplied by a coefficient based on historical results, it is judged that an abnormality is impending.

Equation 1: Smoothed value > threshold (= coefficient × reference value + offset)

To validate this abnormality detection method, its detection performance was verified using two years of historical process data. **Fig. 8** contains the results. Each graph in Fig. 8 shows the smoothed value and reference value when the ratio of the former to the latter is at its maximum, calculated sequentially for all historical machining orders (data with the highest risk of abnormality for a given machining order). The system determines that an abnormality has occurred when there is a value above the purple line, which is the threshold value. The graph on the left shows the results of discrimination by spindle load, with orange stars indicating the points detected within the abnormal machining process. The graph in the center shows the results of discrimination by Z-axis load vibration, with red stars indicating the points detected within the abnormal machining process. The graph on the right shows the results of discrimination based on the spindle load vibration. Among the plots that were not detected by the two aforementioned criteria, those detected here are indicated by green stars.

The results show that by indicating the presence of an abnormality when any of the three criteria are met, all types of machining abnormalities are flagged in the historical data without being overlooked. However, several points were detected in processes without an abnormality. But although the applicable parts were machined without issue, it appears that an abnormality nearly occurred in quite a few of these instances. Therefore, this detection method is beneficial in terms of ensuring that parts are not scrapped due to tool breakage.

When used in an actual machining process, this system must prevent tool breakage and the subsequent substantial damage. As a result of this project, we have constructed and implemented a system that automatically stops the machine tool safely when any sign of abnormality is detected, and we have enabled continuous monitoring for tool

abnormalities without requiring an operator near the machine.

3. Productivity analysis by combining machine operation information with worker position information

Progress in the automation of machines has increased the prevalence of multi-machine operation, wherein one operator is in charge of multiple machines. In the case of multiple-variety mixed-flow production, such as at Kobe Steel, setup work before and after machining and inspections during the machining of new or complex parts are processes that occur at irregular intervals. How to weave human intervention into multi-machine operation is a defining factor affecting productivity. However, there was previously no mechanism for a comprehensive and continuous analysis of this concept.

Therefore, we developed a system to visualize productivity (wasted time) by combining machine operation information with worker position information.

3.1 System overview

Our system visualizes the status of a machine based on the machine's operating status and worker position. Machine operation information is acquired from sources including MT-LINKi and the operating status visualization system. Worker position information is obtained from BLE (Bluetooth low energy) beacons on the control panel and in the setup area of the machine. The operator carries a smartphone, and worker position is estimated based on the strength of the BLE beacon signal received.

The site of the experiment is shown in **Fig. 9**. 27 beacons were installed around 12 machines in an area of about 1,800 m^2 (32 m east/west × 56 m north/south). Data were collected from nine total operators with smartphones on the day and night shifts.

3.2 Analytical methods and experiment results

Fig.10 shows a example of operational status visualization. The machine's status is organized based on the combination of machine operation status ("operation," "stop," and "abnormality") and worker position status ("absence," "control panel," and "setup location"). For example, when a worker is absent and the machine is stopped, the situation status is defined as "waiting for worker," which means that the equipment may be ready for machining if a worker arrives, and therefore that there could be potential for improvement. As another example, when a worker is absent and the machine is running, the situation is defined as "automatic operating," which means productivity is at its maximum. **Fig.11** shows the results of the visualization experiment. Machines A and B have high automatic operation rates and are usually either operating automatically or waiting for human operators. Improving the throughput of these machines likely lies in how to keep them running without interruption. Machines C and D require significant operator attention for operation and setup, so the challenge here is clearly to optimize the manual processes.

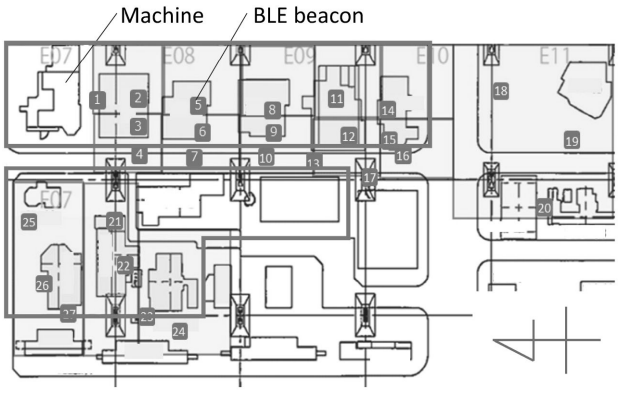

Fig. 9 Experiment site

Machine operation status	Worker position status	Situation status
Stop	Absence	00_Waiting for worker
Operation	Absence	01_Automatic Operating
Operation	Control panel	02_Operating while Control
Operation	Setup location	03_Operating while Setup
Stop	Control panel	04_Waiting for control
Stop	Setup location	05_Waiting for setup

Fig.10 Example of visualizing operational status

Machine	Operating rate	(Automatic op. rate)	Worker waiting rate	Other (setup, etc.)
A	76%	(100%)	21%	3%
B	59%	(100%)	41%	0%
C	28%	(66%)	48%	24%
D	72%	(21%)	7%	21%

Fig.11 Example of visualization experiment

Conclusions

This paper introduced the challenge of multi-machine operation necessary for multiple-variety mixed-flow production at Kobe Steel. It presented an example of how we successfully addressed this challenge by using IoT technology to develop and implement an adaptive control system that uses data from machine tools to detect abnormalities and automatically stop machine tools. We have shown that a more detailed analysis into the productivity of multi-machine operation is possible by combining machine operation information with worker position information, although a future improvement is to provide timely information to operators. Multiple-variety mixed-flow production will become increasingly prevalent alongside an increasing difficulty in securing labor. The issue of how to ensure the stable operation of a large number of machines with a small number of workers is therefore expected to gain importance. As such, we intend to broaden the scope of application of this PF to yield an integrated system that provides a holistic view of the production line, including personnel and equipment. This system will be able to guide workers regarding the optimal next steps in a timely manner, with the aim of achieving DX (systematization = D, workflow transformation = X) that will transform manufacturing.

References

1) S. Hiiragi et al. The Journal of Cost Accounting Research. 2017, Vol.41, No.1, p.76.
2) H. Ishida et al. Information Processing Society of Japan, Transactions on Consumer Devices and Systems. 2019, Vol.9, No.3, pp.10-19.
3) S. Enomoto. Shogaku Ronsan (The journal of Commerce). 2018, Vol.60, No.3-4, pp.391-474.
4) Y. Tsumatori et al. The Proceedings of Manufacturing Systems Division Conference. 2019, p.611.
5) I. Nishida et al. Transactions of the JSME. 2018, Vol.84, No.857, p.17.
6) T. Murakoshi. 2022 JSPE Spring Conference, Proceedings of Semestrial Meeting, p.408.
7) K. Nishikawa. 2021 JSPE Autumn Conference, Proceedings of Semestrial Meeting, p.235

Business Process Re-engineering of Production Management Applying Agile Principles

Keiichi FUKUDA*1・Takaaki IMOTO*1
*1 Digital Innovation Technology Center, Technical Development Group

Abstract

In a changing business environment, it is necessary to promote Digital Transformation (DX) by utilizing digital technology. Additionally, for DX business transformations, which are highly uncertain, it is recommended to apply agile principles. On the basis of this recommendation, Kobe Steel has implemented a business transformation in the production management operations of its titanium plant. This has been achieved through the application of simple business support tools and the Plan-Do-Check-Act (PDCA) cycle for continuous improvement. As a result, it has been confirmed that agile principles are valid for the business transformation of legacy production management operations, which still have numerous constraints and accumulated know- how.

Introduction

Digital technology, external factors such as pandemics and SDGs, and corporate globalization all constitute areas of extreme and rapid change. Against this backdrop, many companies across all industries are promoting business transformation using digital technology - that is, digital transformation (hereafter, DX) - as a critical initiative in maintaining and improving competitiveness. According to a 2022 survey conducted by the Japan Management Association, 55.9% of companies have already started taking measures toward DX, an increase over the previous year. However, a rather small proportion of companies reported achieving good or very good results - only 16.9%.[1)] Challenges reported in promoting DX include a shortage of DX experts, insufficient management strategies for DX, and challenges with developing DX into specific businesses, with the methodology for promoting DX cited as a main hurdle.

Much of the literature, such as 2023 DX White Paper published by Information-technology Promotion Agency, Japan suggest that a process in line with the Twelve Principles of Agile Software[2)] is needed to promote DX.[3)] Business transformation through DX often entails a high degree of uncertainty surrounding the ultimate goal and whether the technologies can be used as intended. Therefore, rather than devising a detailed plan and simply executing it as written, companies must begin the transformation based on assumptions and pivot as necessary. In system development as well, companies must consider agile development in addition to conventional waterfall methodology.

This paper introduces a case study in which we applied agile principles to our business transformation initiative and to the development of its supporting systems in the business process re-engineering of production management within Kobe Steel's materials business. Section 1 describes the basic principles for applying agile methodology to the business process re-engineering of production management. Section 2 presents a specific use case.

1. Approach to applying agile methodology to the business process re-engineering of production management

1.1 Challenges in production management operations at Kobe Steel

Kobe Steel's materials business is known for responding flexibly to customer requests in providing a broad spectrum of high-quality products. Although many of our businesses operate on a smaller scale than that of our competitors, our accumulated expertise in production management enables us to efficiently produce a wide variety of products with minimal equipment by skillfully combining production resources, including those of our partners.

However, recent years have seen an increase in customer demand for improvements not only in product quality, on-time delivery, and supply chain security, but also in value creation based on new metrics such as low-CO_2 operation. As such, the degree of complexity in manufacturing, particularly in terms of production management, grows by the day. Furthermore, changes to the business environment, particularly following major capital expenditure or an expansion of production capacity, necessitate a restructuring of business processes in a way that capitalizes on the production management expertise cultivated. Responding to these challenges without delay requires the transformation of production management operations using digital data - in other words, the DX of production management.

1.2 Using agile methods in business transformation

Agile development is characterized by a team sharing a main goal, defining an incremental development process, and repeating iterations of small development cycles over a short period.[4] In traditional waterfall development, the entire project is divided into phases such as defining requirements, planning, and implementation. Standards are defined for each phase, and the project is advanced in a stepwise manner. Conversely, in agile development, PDCA cycles are repeated over a period from a few weeks to a few months to cover the project from determining the functions to be developed (e.g., by defining requirements) to implementation and testing.

Fig. 1 shows the process for re-engineering production management based on this information.

(1) Define the new production management business process policy
- Define goals and policies for the production management business process for the business model
- Draft a workflow

(2) Develop a new production management business process workflow
- Develop a workflow based on agile principles and supporting tools

(2-1) Make the operating procedure
- Make the operating procedure and identify work areas to be systematized

(2-2) Develop business support tools
- Develop and improve business support tools in the work areas to be systematized

(2-3) Trial operation
- Trial operation using business support tools based on the workflow

(2-4) Operating procedure reviews
- Identify challenges, modify workflow/procedures, develop a plan for improving business support tools

Step (1) involves defining policies and workflows for the entire business. Step (2) is a cyclical process with the objectives of developing specific operating procedures, identifying and systematizing core tasks with a high burden, conducting trial operations, and identifying challenges and formulating improvement plans. This process entails multiple benefits: new operations are introduced at an early stage, production management personnel have time to comprehend and develop proficiency in the new operations, challenges associated with operations and tools are revealed early, and the entire business transformation is implemented in a stepwise manner.

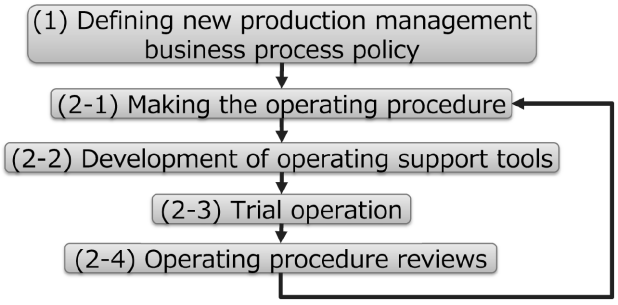

Fig. 1 Construction process of new production management

2. Business process re-engineering of production management at our titanium plant

2.1 Overview of the production management business process at our titanium plant

Kobe Steel is the only integrated manufacturer in Japan that processes titanium from melting to the finished product. Kobe Steel's Takasago Works titanium plant manufactures rolled ring forged products of various shapes and materials, from pure titanium to titanium alloys, for domestic and international fuselage and engine manufacturers.

Numerous manufacturing processes are involved in producing titanium products from the raw material to the finished product. First, ingots are manufactured from titanium sponge, which is the raw material. The ingots are then forged into billets, which serve as the starting material for the end product. Billets undergo rolled ring forging, heat treatment, and machining on their way to becoming end products.[5]

Because of the nature of this manufacturing process, rather than dedicated production lines for each product, Kobe Steel uses shared equipment for mixed-flow production to achieve efficient lot-size-one production of a range of products. The production management department has many practices that support this methodology. Beyond cultivating expertise in production management, it supports interdepartmental sharing of information, such as by devising production plans based on customers' manufacturing parameters and the available bandwidth of each manufacturing process and partner company. The department also manages the production plan's progress and revisions.

However, the landscape must change in response to the recovery in demand for aircraft components and similar products following COVID-19. Operations must expand to accommodate the large increase in volumes, meaning the production management business processes must be

transformed. In contrast to the previous approach of flexible production on a relatively small scale, operations must center around efficient and stable mass production. As such, we launched an initiative in 2021 to transform our operations based on data.

2.2 Plan for business process re-engineering of production management

Increasing throughput in a mixed-flow production process generally increases not only the workload, but also the inventory of intermediate products serving as a buffer between processes, extending manufacturing lead time; these phenomena occurred at the titanium plant.

Therefore, we established the guidelines below before introducing the new production management business process.

- Information related to production management should be shared among operations/departments, including sales, production management, and manufacturing.
- Manufacturing load and capacity per process must be more accurate.
- Bottleneck processes and the associated production planning must be optimized.

In addition to designing a workflow and data model based on the guidelines above, we also established policies for three major areas: master scheduling, operation scheduling, and surplus material management. **Fig. 2** shows a schematic diagram of the workflow and data model.

[Master scheduling]

- All processes required for long-term manufacturing load and capacity management can be computed centrally based on the sales plan prepared by the sales department for budgeting. Management aspects are divided up by process, product, and month, as appropriate. This provides a representation of the manufacturing load and enables the manufacturing department to visualize material resource fluctuations. This prevents surplus intermediate product inventory and extended manufacturing lead time caused by operating above capacity.

[Operation scheduling]

- Production planning is based on sales-related data such as orders and inquiries to support make-to-order manufacturing, which entails producing only what is needed, when it is needed. This prevents the production of surplus intermediate product inventory.
- Scheduling is based on the theory of constraints (TOC)[6]. Specifically, the plan is initially devised so as to maximize the manufacturing capacity of the bottleneck process. The processes upstream and downstream of the bottleneck process are then planned, working outward from the bottleneck process. This prevents extended manufacturing lead time caused by operating above the capacity of the bottleneck process and the production of surplus intermediate products.
- Scheduling accounts for all necessary processes to manage the overall progress of the entire process. The plan is presented to the manufacturing departments responsible for important processes regularly, even if the manufacturing load is low. In addition, management records and presentation materials are updated to visualize fluctuations in the manufacturing load. This makes it possible to grasp the required manufacturing capacity by time period. This prevents surplus intermediate product inventory and extended manufacturing lead time caused by operating above capacity.

[Surplus material management]

- The plant's production capacity and conditions are also shared with the sales department. Part of the production planning workflow when considering inquiries includes evaluating whether minimum lot sizes are met and whether volumes can be adjusted to prevent

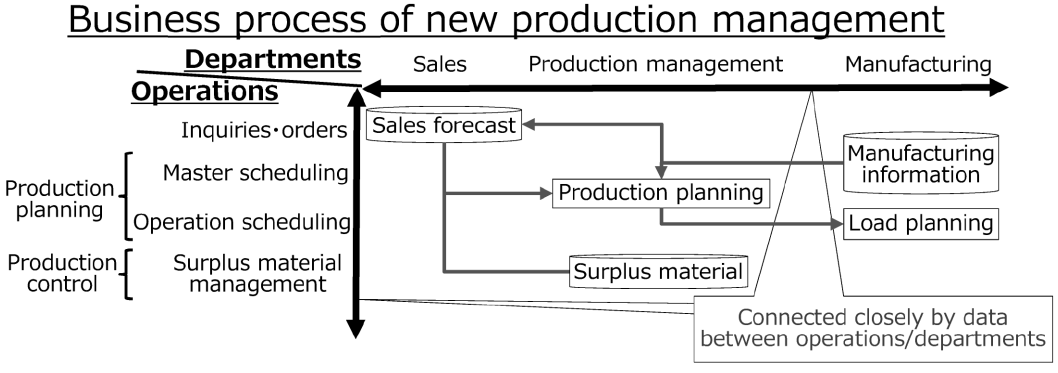

Fig. 2 Proposed production management business process

the production of surplus intermediate product inventory. The production management plan also prioritizes the use of intermediate products for orders and inquiries so as to minimize surplus intermediate product inventory. This prevents the production of surplus intermediate product inventory.

Specific business processes were designed based on the guidelines above. **Fig. 3** illustrates the process for operation scheduling, which is described next.

(1) Calculate the production quantity based on the sales information. Next, allocate intermediate products based on surplus material data, calculate the quantity of each product that must undergo new production, and confirm the customer delivery date for the order or inquiry. This minimizes production to only the volume necessary and prevents the production of surplus intermediate product inventory.

(2) Draft a plan for each product's bottleneck process. First, the standard process delivery date of the bottleneck process is calculated based on the standard manufacturing lead time between the bottleneck process and the customer delivery date. A load-balancing plan is then developed based on the standard process delivery date and the manufacturing capacity information provided by the manufacturing department. This prevents the bottleneck process from extending the lead time because of a delay in the start of manufacturing.

(3) Calculate the production quantity of the manufacturing processes upstream and downstream of the bottleneck process, as well as the standard process delivery date based on the schedule of the bottleneck process. The standard process delivery dates of the upstream and downstream processes are then calculated by backward/forward progression, starting from the standard process delivery date of the bottleneck process and using the standard manufacturing lead time between each process. This makes it possible to load balance among the upstream and downstream manufacturing processes based on the bottleneck process.

(4) Hold regular meetings with the manufacturing department to coordinate the plan for each process and the manufacturing load calculated based on the plan. If the manufacturing load exceeds the manufacturing capacity for a given process, determine appropriate measures to balance the load or increase capacity. This secures the necessary manufacturing capacity and prevents an extended manufacturing lead time caused by a delay in the start of manufacturing within any process.

2.3 Applying agile methodology to new operations and improvements

It would be impossible to perform each of the new business processes described in the previous section manually. However, designing and developing a single management system would take extensive time and introduce a high risk of the system not meeting the varying requirements inherent to each manufacturing operation.

In this initiative, we selected core operations with high workloads and developed simple business support tools using agile methodology to support business operations while establishing and improving the new business processes.

Specifically, we developed support tools to devise plans for bottleneck processes (item (2)), calculate process-specific delivery dates based on the bottleneck process plans and progress management (item (3)), and manage the manufacturing load and capacity for each process (item (4)). We also organized the data necessary for production management (shipping plans based on sales information, intermediate product inventories, manufacturing results by process, etc.)

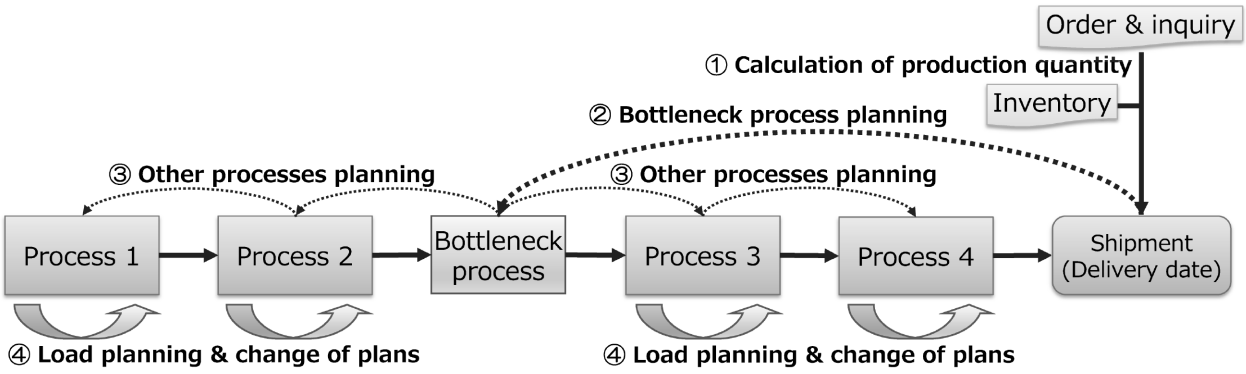

Fig. 3 Proposed operation scheduling process

and shared them throughout the plant alongside the manufacturing load and planning information calculated by the tool.

Members of the project developed each tool in house inside of about 2-3 months. After go-live, production management leadership communicated issues revealed through operation. We conducted PDCA cycles to release an improved version once per month.

Item (2), bottleneck process planning, is described next by way of example. Specific aspects covered include the application to new operations and the kaizen process for operation scheduling of the rolled ring forging process.

Most orders placed with Kobe Steel for rolled ring forging parts are manufactured by mixed-flow production. However, improving throughput necessitates lot production, in which the same product is rolled continuously.

The associated production plan must incorporate a massive amount of data (several thousand to tens of thousands of items) to cover the medium to long term; performing this task manually would be impractical. Therefore, we decided to use a support tool to automatically formulate a monthly production plan once the sales department provides sales information. Detailed below were our basic requirements for the tool's functionalities.

i Sales and intermediate product information feed the calculations for the quantities of each product that must be produced and the delivery dates for orders and inquiries, which can then be confirmed.

ii The standard process delivery time for the rolled ring forging process is calculated by subtracting the standard manufacturing lead time for the rolled ring forging process from the customer delivery date.

iii Standard process delivery dates are prioritized, and orders and inquiries are sequenced accordingly. The standard lot size is set with productivity being the main factor, orders and inquiries are consolidated into lots, and the sequence of lot production is determined.

iv The manufacturing date and time for each lot are calculated based on manufacturing capacity information (takt time) linked from the manufacturing department.

Table 1 shows a sample automated operation scheduling plan. Multiple orders and inquiries are consolidated into lots. The manufacturing date and standard process delivery date are indicated for each lot to reveal the margin to the manufacturing date in days. The production planning manager evaluates the risk of late delivery based on the margin and can take the following actions if necessary:

- Develop a plan to make up for lost time in downstream processes
- Extend equipment operating hours (overtime support)

The production planning manager can also investigate other measures to mitigate the risk of delayed delivery.

We designed and deployed the initial version of the tool to operations at an early stage. We then initiated the kaizen cycle shown as steps (2-1)

Table 1 An example result of operation scheduling planning

Order				Bottleneck process					
No	Types	Delivery date	Qty	①Standard delivery date on the process	②Start date	End date	Margin (①-②)	Lot ID	Takt time
1	A	**2023/08/31**	7	2023/07/12			2		
2	A	**2023/09/14**	2	2023/07/26	2023/07/10	2023/07/19	16	L1	57
3	A	**2023/09/30**	3	2023/08/11			32		
4	B	**2023/09/06**	5	2023/07/18			-1		
5	B	**2023/09/14**	5	2023/07/26			7		
6	B	**2023/09/21**	5	2023/08/02			14		
7	B	**2023/09/28**	5	2023/08/09	2023/07/19	2023/07/24	21	L2	37
8	B	**2023/09/30**	5	2023/08/11			23		
9	B	**2023/10/07**	5	2023/08/18			30		
10	B	**2023/10/14**	2	2023/08/25			37		
11	C	**2023/09/12**	4	2023/07/24	2023/07/24	2023/07/24	0	L3	5
12	D	**2023/09/15**	5	2023/07/27	2023/07/24	2023/07/25	3	L4	5
13	E	**2023/09/20**	10	2023/08/01			7		
14	E	**2023/12/20**	10	2023/10/31	2023/07/25	2023/08/02	98	L5	47
15	E	**2024/02/20**	5	2024/01/01			160		
3	A	**2023/09/30**	12	2023/08/11	2023/08/02	2023/08/11	9	L6	57
10	B	**2023/10/14**	3	2023/08/25			14		
17	B	**2023/11/14**	10	2023/09/25	2023/08/11	2023/09/17	45	L7	37
18	B	**2023/11/21**	9	2023/10/02			52		

through (2-4) in Fig. 1 to improve operations and the tool in tandem. Around 25 issues surfaced during this period. We prioritized improvement plans and released new versions in conjunction with monthly planning activities.

These efforts made it possible to quickly formulate monthly production plans that maximize the throughput of bottleneck processes (the original objective). They also spurred kaizen-related communication and activities initiated by personnel throughout the organization.

We successfully transformed the entire production management business process - a feat that would normally span several years - in one year: three months for planning, three months to develop the tools, and six months for agile-guided improvement. As a result of this initiative, we reduced the manufacturing lead time for rolled ring forged products, a core product line, by two-thirds and cut the related inventories by half. We also reduced warehousing costs and unexpected shipping costs by mitigating delays in production, resulting in concrete economic benefits beyond expectations.

Conclusions

This paper describes the usefulness of agile principles in the promotion of DX, explains the process of using agile methodology in the business process re-engineering of production management, and describes the implementation and effects of these initiatives by means of the case study of Kobe Steel's titanium plant.

We have thus confirmed the applicability of agile principles for the business transformation of legacy production management operations, which have numerous constraints and rely on accumulated know-how.

Production management connects customers to manufacturing and ensures that customers receive the full potential value of products. We will use this initiative as a starting point to promote DX initiatives and thereby deliver even greater value to our customers.

References

1) Japan Management Association. Corporate Management Issues 2022. https://www.jma.or.jp/img/pdf-report/keieikadai_2022_report.pdf. Accessed 2022-12-12.
2) K. Beck et al. Manifesto for Agile Software Development. https://agilemanifesto.org/iso/en/manifesto.html. Accessed 2020-06-10.
3) Information-technology Promotion Agency, Japan. 2023 DX White Paper. Executive Summary. 1st edition. pp.5-14.
4) T. Sato. Proposal of Interdisciplinary Cooperation and Agile Program Management Framework for DX. Journal of International Association of P2M. 2022, Vol.17, No.1, pp.171-189.
5) T. Suzuki et al. The Tale of Titanium, Revised. Japanese Standards Association. 2023. pp.51-61.
6) E. Goldratt. Theory of Constraints. North River Press. 1990.

Development of Fuel Supply and Demand Planning Simulator at Kobe Power Plant

Dr. Toyohiro UMEDA*1 · Yuki FUJII*2 · Yusuke TAKIZAWA*2 · Hideyuki TAKI*2 · Takahisa HAMANO*2 · Yotaro HIRAIDE*3

*1 Digital Innovation Technology Center, Technical Development Group
*2 No.1 Power Generation Department, Kobe Power Plant, Electric Power Business
*3 Department of Technological Administration, Electric Power Business

Abstract

This study focuses on the logistics planning of fuel for thermal-power generation from its unloading to being supplied for boilers. A new concept simulation system has been developed and implemented, which utilizes both logistics models and human judgment bidirectionally. This system utilizes diverse historical and planned information such as ship allocation, silo inventory, power generation, fuel composition, and process data. Its core is a simulator that calculates the logistics of storage from ships to silos, transportation from silos to boilers, and circulation among silos in a time series manner. Additionally, this system can incorporate human judgment in switching logistics during simulation. Furthermore, it is possible to backtrack to any chosen point in time after execution and modify or add judgments for switching, enabling re-simulation. These capabilities allow for the seamless incorporation of irregular operations that are difficult to model, while basing logistics planning on standard conditions derived from data and models.

Introduction

Following the 1995 amendment to the Electricity Business Act, Kobe Steel built a coal-fired power plant to make maximum use of our existing infrastructure and in-house power generation expertise in the ironmaking business. The plant has two 700,000 kW power generation units. Unit 1 began operation in April 2002, and Unit 2 in April 2004.

Following the suspension of upstream operations at Kobe Works in 2017, we constructed a power plant with two 650,000 kW units on the former site of a blast furnace - Unit 3 began commercial operation in February 2022, and Unit 4 in February 2023.

During capital expenditure planning for Units 3 and 4, we recognized that our procurement of coal, the fuel for power generation, would nearly double. We leveraged our knowledge in ironmaking logistics[1] to develop a simulator[2] designed specifically for power plant coal logistics. We used the simulator to study coal carrier configurations and the number of additional coal storage silos required.

Maintaining our manual supply and demand planning process, which requires in-depth experience, would be challenging because of the increase in complexity of logistics between the loading port and the berths, silos, and boilers in the power plant.

This challenge drove us to leverage our experience using simulators for production planning and similar operations.[3), 4)] Using the simulator for Units 3 and 4 capital expenditure planning as a foundation, we developed a support system for coal logistics supply and demand planning on the scale of several days to months.

This system supports supply and demand planning given the increased coal volume and complexity in coal logistics following the introduction of Units 3 and 4. Its output is implemented directly into live operations, including for irregular conditions.

As such, we focused on not only the accuracy of the simulator's logic, but also on linking it seamlessly and efficiently with human judgment.

This paper describes the configuration and features of the simulation system developed to address these issues.

1. Overview of target processes and operations

1.1 Power plant coal logistics

Fig. 1 shows an overview of the logistics at Kobe Power Plant. Coal for power generation comes from Australia, Indonesia, and other foreign countries by

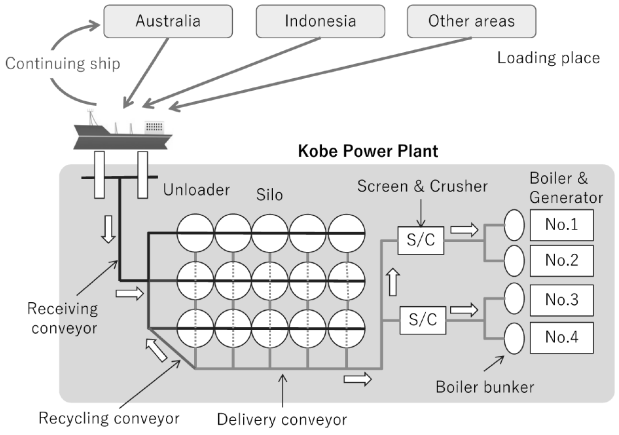

Fig. 1 Outline of Kobe Power Plant logistics

ships with capacities in the tens of thousands of tons. Unloaders at the plant's dedicated wharf unload the coal for storage in 15 silos with an approximate capacity of 30,000 tons.

Because coal composition varies by place of origin and because different brands are procured, each incoming lot is allocated to a designated silo. Four steam turbines are each connected directly to a generator, each of which has a boiler to supply steam. Coal from the silos is pulverized and prepared in the screens and crushers, sent to the bunkers upstream of the four boilers, and then fed into the boilers. Coal transport handling downstream of the unloader is performed by a conveyor. All unloaders and conveyors are sealed for environmental health and safety.

The flow described to this point represents the basic transport path; described next are the logistical factors of coal for power generation.

(1) It is common practice to mix coal brands with different compositions to satisfy various parameters such as combustibility in the boiler, the control of soot after combustion, and the quality assurance of by-products such as ash and gypsum (for reuse as raw materials, e.g., in cement). This practice, called "coal mixing," involves adjusting ratios adjusted based on operating conditions and brands.
(2) Exposure to air activates some of the coal while in storage, generating heat. Coal can ignite if stored for a long time, so it is moved to another empty silo depending on the gas concentration inside the silo, the temperature of the stored coal, how long the coal has been stored, and brand-specific heat generation characteristics. This practice, called "recycling," interferes with regular coal logistics because it uses the same conveyors and pathways.
(3) Long-term coal storage is undesirable from the perspective of disaster prevention, as described above. Additionally, sufficient coal storage capacity is a challenge due to space constraints at urban power plants. Therefore, it is not at all implausible to have no silos available for unloading, creating delays for coal carriers (demurrage and detention).

1.2 Supply and demand planning operations

Coal supply and demand planning in a power plant involves determining the rate and route of coal transport from unloading to storage and to the boiler, as described above. An appropriate route must be selected from the many possibilities based on silo inventory and the status of coal carriers. Transport rates depend on coal consumption at the boiler (i.e., the end of the route) as well as the capacities of the equipment and conveyors. Therefore, the key to coal supply and demand planning is to set the routes based on a timeline, which can be thought of as a task of deciding when and how to switch logistics operations. Detailed below are the three logistics switching functions.

(1) Unloading: Decide when to start unloading and which silo to unload to based on coal carriers' voyage information and the maintenance schedules of the unloaders and conveyors.
(2) Coal mixing: Determine brands (1 to 3 types), brand ratios (coal mix ratio), and silos based on the power generation schedule of each boiler. Switching to coal mixing usually occurs when the silo is emptied.
(3) Recycling: The start time of coal transfer, supplying silo, and empty receiving silo are based on the number of days the coal has been stored, the temperature of the stored coal, and forecast silo availability. This process is also used to move coal to another silo in preparation for silo servicing.

Real-world coal logistics switching requires consideration of many different conditions, posing the challenges below.

i) Recycling uses conveyors on both the receiving and delivery sides of the silos, which can interfere with unloading and with feeding coal to the boiler. Prioritizing recycling to prevent ignition could interrupt or delay unloading or restrict the routes available for feeding coal to the boilers.
ii) There is an abundance of possibilities in coal logistics switching, each of which has spatial and temporal ripple effects; it is very difficult to accurately predict the effects of switching at the time of switching. Logistics planning hence, ultimately involves a degree of trial and error.
iii) Supply and demand plans must be revised daily to compensate for variables unknown during planning, such as the arrival times of coal carriers, temperatures of stored coal, and equipment malfunctions. Moreover, the entire plan must be evaluated, not just a part of the plan created the previous day (see the logistics propagation in reference ii).
iv) While there are standard logistics switching rules and constraints, circumstances may require irregular operations that run counter to these. For example, when running trials with new brands, switching processes involving coal mixing may be performed many times before a silo is empty. As another example, when a particular coal type

must be prioritized, coal carriers may have to wait for coal carriers that arrived later to unload.

A simulation model based on parameters, rules, and logic is effective for factors through i) to iii), which are within the standard scope of logistical control (regular operation).

Factor iv), however, falls outside this scope (i.e., irregular operation) and is difficult to model logically. As such, human judgment is required. Because regular and irregular operations are temporally linked, one challenge in developing a system for supply and demand planning is to support bidirectional interaction between the simulation model and human judgment.

2. Coal logistics simulation model

2.1 Components

Fig. 2 shows the configuration of the simulation system for supply and demand planning. This system can compute coal movement in a power plant given varying conditions and assumptions by incorporating information such as historical data, plans, and constraint parameters. Below is an overview of the system's components.

-Logistics elements model:

There are three types of elements, the equipment and facilities that form the basis of logistics: buffers, equipment, and transportation. Buffers hold a volume, equipment and transportation elements have capacity in terms of the weight they can handle per unit time, and transportation elements have routes with buffers or equipment as endpoints.

-Actual data:

Actual data on silo inventory and ship allocation link the plan with actual results. Further data points include composition inspection information for each coal lot, which is used for coal mixing calculations, and coal storage temperature and gas chromatography data, which are used to determine when recycling should occur.

-Preliminary planning data:

Information on ship allocation, power generation, equipment maintenance, etc. is entered for preliminary supply and demand planning.

-Masters:

Parameters for standard constraints are established, including capacities of logistics components, brand combinations, and coal mixing ratios, and the maximum number of storage days per brand.

-Simulation engine:

This simulator calculates changes in the logistics status at regular intervals. It has a component that determines whether logistics switching is necessary upon each update and a component that calculates changes in physical quantities over the interval. The system has a user interface to reflect human judgment in logistics switching.

-Simulation log:

Logistics switching operations and transition times of each element's status are stored as data for the simulation process. The former is output at the time of switching and the latter at regular intervals. These are used for backward re-simulation, a feature that will be described later.

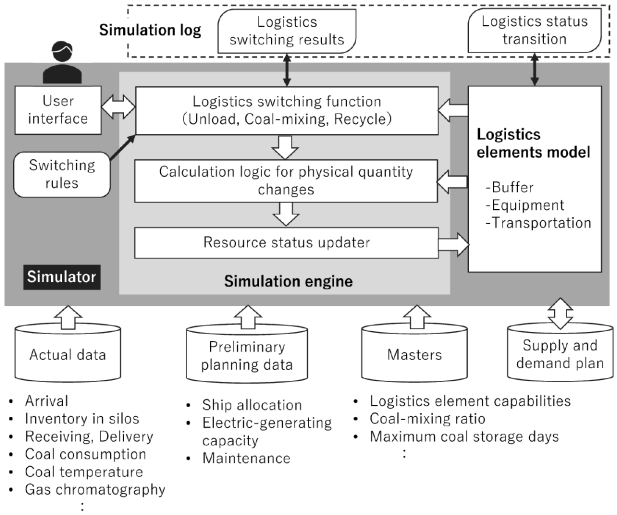

Fig. 2 System configuration

2.2 Simulator operation

This section covers the operational features of the simulator based on the simulator's operational flow shown in **Fig. 3**.

- Since the system operates in conjunction with updates to the time, the time updates at regular intervals (ΔT: variable), with changes in physical quantities over an interval being calculated to provide discrete updates to the quantity. The smaller the ΔT is set, the greater the resolution of calculated changes; however, this increases the calculation time, so we set it to one hour based on preliminary testing.
- The simulator decides whether to switch logistics at each point in time and calculates the change in physical quantities based on the result of the decision. There are two modes of logistics switching decisions: a mode based on the standard rules of the simulator and a mode that can reflect user judgment. The next section covers the latter.
- To reuse user decisions upon the next day's simulations or backward re-simulation, the

previous logistics switching decision is retrieved at each point in time and adopted if possible.

2.3 Verification of accuracy

Although the simulator is characterized by its ability to reflect user judgment in the simulation process, it must be able to accurately reproduce realistic logistics operations using standard simulation logic as a foundation for supply and demand planning. Therefore, we compared historical logistics results with the simulator's logistics calculations, with the conditions below set for the simulator.

- Ship allocation information: coal brands, weights, and port arrival times of coal carriers
- Inventory information: brands and inventories in each silo on the first day
- Coal demand: coal consumption per boiler per day
- Number of coal storage days: coal storage days of each silo as of the first day

In addition, standard operating conditions were established for coal mixing and recycling rules.

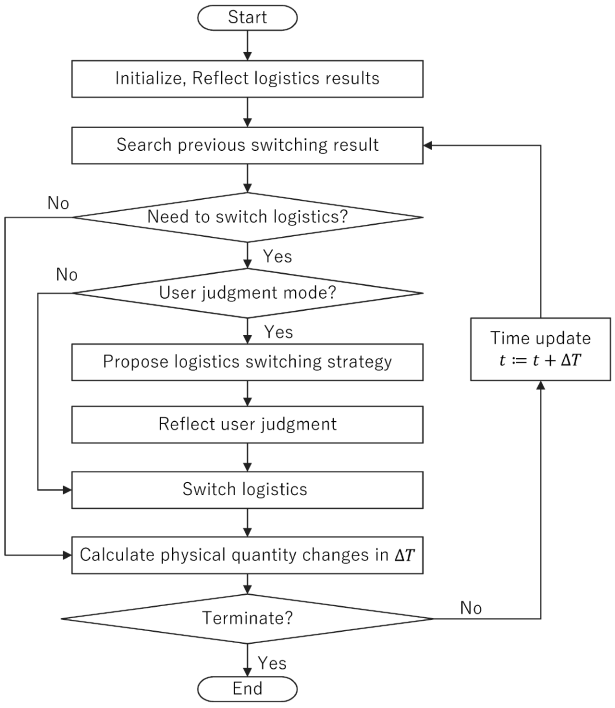

Fig. 3 Simulation flow

Fig. 4 shows a comparison between the actual and simulated change in silo inventory over three months, with the simulator being provided the parameters above.

This figure reflects the composition of the inventory when brands are classified into one of four coal types based on their characteristics. Although there are idiosyncrasies in the simulator's decisions regarding logistics switching, it clearly reproduces actual changes in the composition of the inventory over time well. The difference in the total inventory in the first month is due to unloader issues.

We also confirmed that the amount of coal transferred by recycling and the average coal carrier waiting time differed from actual results by only a few percent, leading to our decision to use this simulator as the basis for supply and demand planning.

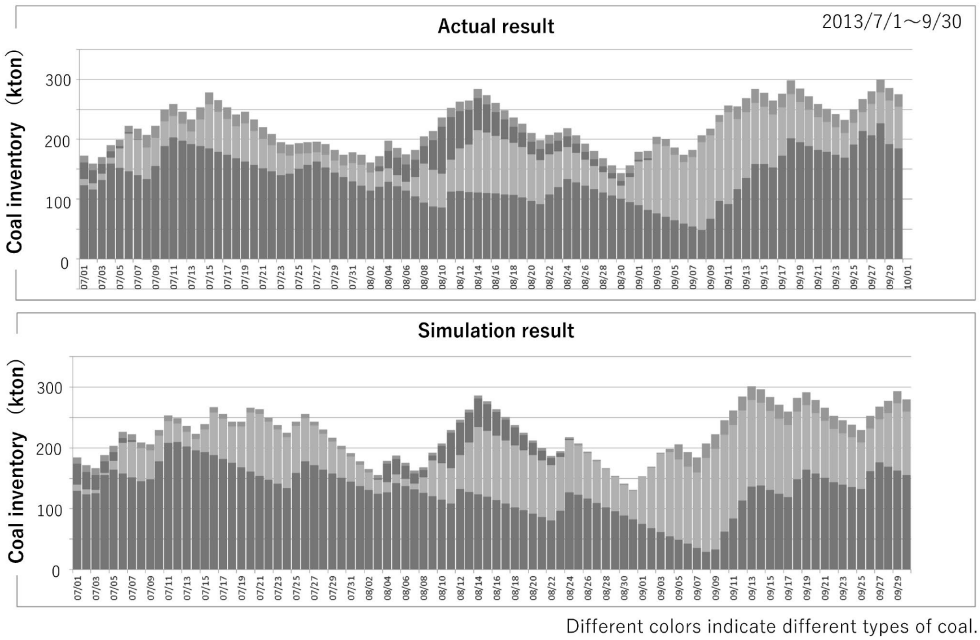

Fig. 4 Comparison between simulation results and actual results (changes in coal inventory)

3. Linking human judgment

3.1 Interactive execution mode

As described above, this simulation system features the ability to reflect user judgment in terms of logistics switching in the simulation process. An execution mode enables the user to override a decision the simulator makes based on standard rules, add a new decision, or change the time of execution of a decision. The characteristics of this feature are as follows.

- When the simulator deems logistics switching necessary, it stops and presents the decision. The user can confirm or change the decision. For example, the user can change the silo used for coal mixing, the coal mixing ratio, or the silo used for recycling or unloading.
- The user can push back the simulator's suggested timing for a logistics switching operation. It might be necessary, for example, to postpone unloading to change the unloading sequence of coal carriers, or to postpone recycling in a silo that is currently being unloaded.
- By combining this feature with the backward re-simulation function (next section), the user can set a new logistics switching process for any time during the execution period after running a simulation once. For example, logistics switching can be set for a time at which it would not occur under standard rules, such as switching the coal mixture before the silo is emptied or starting recycling early.

All logistics switching decisions are saved to a decision log with timestamps that can be read and reused in the next execution. This way, the user does not have to repeatedly enter the same inputs. Additionally, the previous input can be modified to set a different logistics switching operation. **Fig. 5** shows an example of a case in which re-simulation is performed using the results of an earlier logistics switching decision. The first simulation was started at 0:00 on April 1, after which five logistics switching operations were performed (numbered (1) to (5)). Three of the five switching operations ((2), (3), and (5)) were user decisions. The five logistics switching decisions and their time stamps were saved to a log.

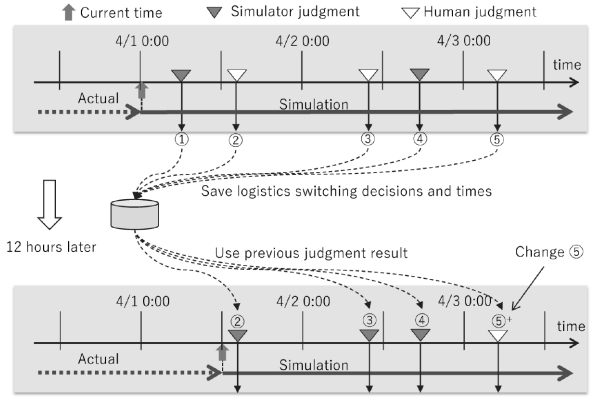

Fig. 5 Simulation using results of previous logistics switching decision

Upon re-simulation 12 hours later (12:00 on 4/1), the previous user decisions are reflected by retrieving logistics switching decisions (2) to (5) from the log. In this example, the logistics plan changes starting on 4/3 following a modification to the original logistics switching decision number (5).

3.2 Backward re-simulation function

The simulation is run and modified (logistics switching modifications) several times to arrive at a more suitable supply and demand plan. As mentioned in the previous section, a requirement for this process is the ability to revert the simulation status to that of any given time and add or change logistics switching decisions. One method for returning to any given time is to reverse the logistics operation log and stop it at a specified time[5]. Another is to save the logistics status (silo and bunker inventories, coal destinations, postponement decisions, etc.) at each point in time and replace the logistics status at a specified time. Both methods are impracticable. The reverse playback for the first method consumes the same amount of time as the forward simulation. In the second method, the state must be saved for every time interval, amounting to thousands to tens of thousands of data points for supply and demand planning.

Therefore, we developed a function for this system to save the logistics status at a coarse interval (e.g., daily) and perform pre-simulation from a given save time to a specified backtracking time. This function enables the system to quickly return to any specified time. **Fig. 6** depicts an example of returning to a backtracking time. In this example, the logistics status is stored every two days, and a pre-simulation of 39 hours is performed by resetting to the logistics status at 0:00 on 4/5 (the most recent save before 15:00 on 4/6). The logistics switching decision from the previous execution during this period at 12:00 on 4/5 is retrieved, making it possible to accurately reproduce the logistics status even if a user decision is made.

The simulator pauses when the scheduled time is reached. A new logistics switching decision can be set or the previous decision can be changed, making it possible to simulate different conditions from any point as many times as desired.

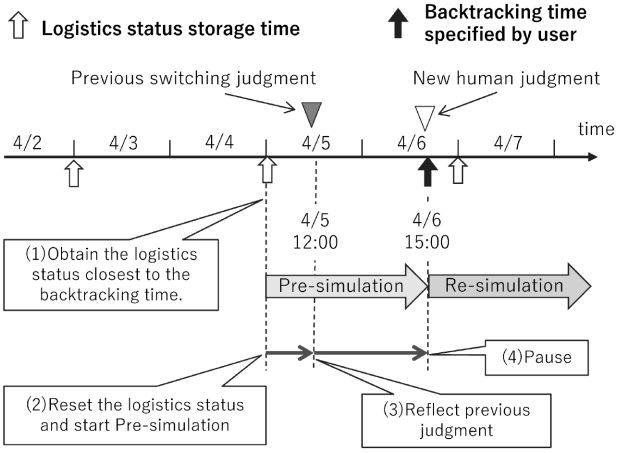

Fig. 6 Return to backtracking time and reproduction of logistics status

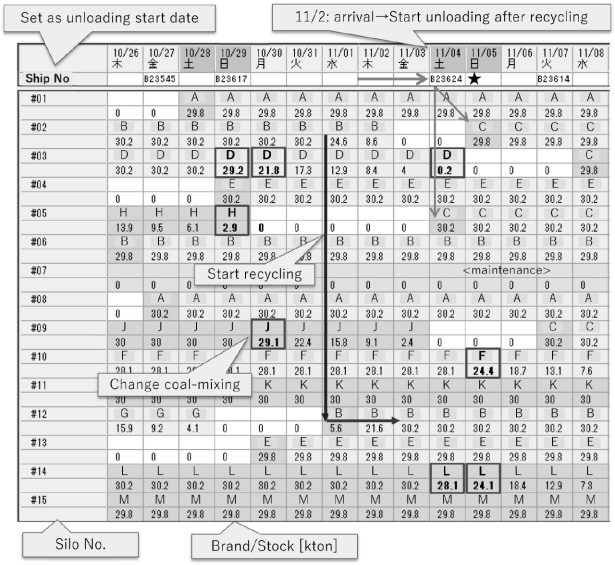

Fig. 7 Example of supply and demand planning screen (unloading and silo inventory)

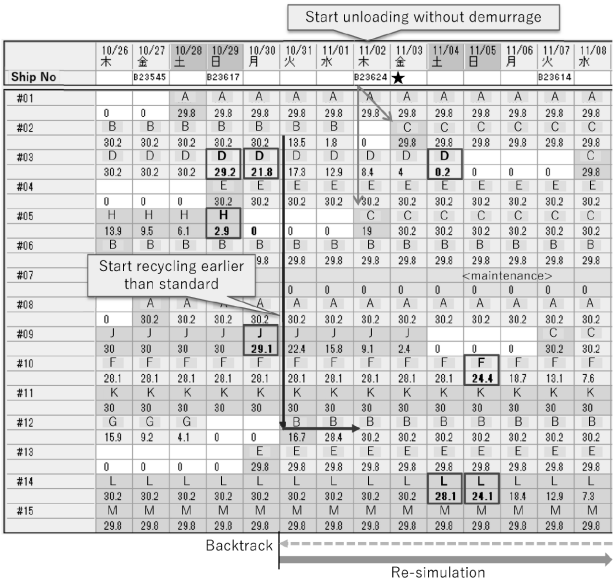

Fig. 8 Backward re-simulation example (case of starting recycling 40 hours earlier)

3.3 Execution example

We prepared data replicating actual conditions and used the backward re-simulation function described above to simulate planning operations. **Figs. 7** and **8** show the resulting supply and demand planning screens, which show the daily inventory (across the table) for each silo (top to bottom). The top row shows the voyage number of the coal carrier on the start date of unloading. A-L indicates the coal brand. The numbers below each of these letters indicate the inventory in the silo in kton.

Fig. 7 shows the daily supply and demand planning screen simulated based on the rules for unloading and recycling set in the master, with only the coal mixing set by the user. In this simulation, the inventory in Silo 2 reaches the coal storage deadline at 16:00 on 11/1. Therefore, recycling was started using Silo 12, which was empty. A coal carrier (indicated by ★) arrives during the recycling process on 11/2. Because recycling has priority and the carrier cannot enter the port at night, unloading begins at 8:00 on 11/4, when the carrier can enter the port after recycling is complete.

Fig. 8 shows the supply and demand planning screen after re-simulation. To start recycling earlier, the user set the recycling of Silo 2 to occur at 0:00 on 10/31 and the simulator's decisions to occur thereafter. As a result, the coal carrier that arrived on 11/2 could start unloading on 11/2, without waiting for recycling to finish as had occurred in Fig. 7. The coal mix switching operation on 11/4 and 11/5 is the same in Figs. 7 and 8, indicating that the original logistics switching decision was reused. It would be challenging to execute a plan such as the one presented, in which the timing of logistics switching had to be moved earlier than standard, using the simulator alone. As such, the incorporation of human judgment and the backward re-simulation functions are critical.

4. Application to operations

We linked our simulator to power plant operating and process data, ran trials in tandem with supply and demand planning operations, and made improvements to functionality and operability. In doing so, we confirmed that the system can create plans that can be used in actual operations. Following are specific details regarding use of the system.

- For the approximately one-month period after ship allocation is almost finalized, a detailed plan that incorporates human judgment and irregular operations is created. The results are incorporated into coal logistics operating instructions, and plans are revised daily to reflect changes in operations and coal carrier movement.
- After a detailed one-month plan is developed, the simulator's automatic decision mode automatically generates a plan for the subsequent five months based on ship allocation and maintenance schedules, yielding a six-month forecast. The simulated plan is linked to the most recent plan to reflect the effects of plan modifications. The results are used to adapt ship allocation (procurement).
- The amount of ash and gypsum generated by combustion is predicted based on the coal mixing plan for each boiler, in turn based on supply and demand planning. This information is used for inventory management and to plan shipping operations for reusing these materials.

Below are some of the long-term accomplishments we achieved through this system.

- The project's initial objective was met, which was to enable supply and demand planning that accommodates the additional coal volume and additional logistical complexity associated with increasing the number of boilers from two to four.
- An accelerated planning process makes it possible to compare scenarios with different coal mixes, unloading and recycling times, etc., in turn reducing vessel delays and stabilizing operations.
- The ability to simulate changes in ship allocation enables the power plant to request ship allocation and coal procurement changes at an early stage, thereby reducing operational risk by stabilizing inventories.
- Planning know-how that has been hidden in the minds of skilled employees can be visualized and shared, expanding the pool of experts capable of supply and demand planning.

Conclusions

Kobe Steel has applied its simulation technology to numerous in-house manufacturing and logistics processes. Application has been especially strong in the materials business (e.g., steel and nonferrous metals), which is responsible for an increasingly wide variety of products, to enhance and expand the simulation models' functionality and expressive power. These systems were offline, operating independently from actual operations. In tasks such as comparing production patterns or researching capacities to support capital expenditure decisions for equipment or logistics, results were not reflected directly in live operations. Therefore, a certain degree of inaccuracy was acceptable. However, if this simulator is connected directly to live operations, a level of accuracy that can faithfully reproduce actual operations would clearly be necessary. Real-world operations, however, are always subject to anomalies involving information a simulator cannot be cognizant of. We achieved a level of accuracy sufficient for connection to live operation by developing a new guiding model based on data- and logic-driven simulation technology that incorporates human judgment at logistics switching points.

Continued, reliable use in day-to-day operations requires a mechanism to continually update master settings to reflect changes in coal procurement and operating methods. This can be achieved by detecting inconsistencies between actual data and master settings and issuing alarms. Another opportunity for improvement is a more intuitive user interface for enhanced operability. In support of comprehensive coal logistics, we will link supply and demand planning at the power plant with ship allocation planning in the coal procurement department to achieve integrated supply and demand planning for power generation from the loading area to the boilers.

The simulator's distinctive technologies, such as interactive execution mode and backward re-simulation can be applied broadly not only to power plant logistics but also to simulations of production and transport operations even outside of the factory. We intend to solve a wide range of logistical challenges throughout our group using this technology.

References

1) T. Iwatani et al. R&D Kobe Steel Engineering Reports. 2018, Vol.68, No.2, pp.29-35.
2) Kobe Steel, Ltd, T. Umeda. Coal logistics status management equipment and methods. Patent No.7011570. 2022-1-18.
3) K. Matsuda et al. R&D Kobe Steel Engineering Reports. 2001, Vol.51, No.3, pp.28-35.
4) A. Horio et al. Transactions of the Institute of Systems, Control and Information Engineers. 2018, Vol.31, No.10, pp.347-355.
5) Hitachi, Ltd. K. Maeda et al. Simulation method. Japanese patent 1-270164. 1989-10-27.

MI Technology in Developing and Utilizing Materials

Takashi WADA*1 · Masahiro INOMOTO*2 · Keita NAKAYAMA*2 · Dr. Chiharu KURA*3 · Takufumi KOBAYASHI*4

*1 Digital Innovation Technology Center, Technical Development Group (currently Planning & Administration Department, Technical Development Group)
*2 Materials Research Laboratory, Technical Development Group
*3 Applied Physics Research Laboratory, Technical Development Group
*4 Application Technology Center, Technical Development Group (currently Aluminum Sheets & Coils Development Department, Moka Works, Steel & Aluminum Business)

Abstract

Materials Informatics/Materials Integration (MI) technology is gaining attention as a method to advance the development of new materials efficiently. Kobe Steel is actively utilizing MI technology, exemplified by AI and simulations, in developing and utilizing a wide range of metal materials and their associated technologies. This article explains some representative cases: one involves using AI to predict material properties based on experimental data for welding materials and thin steel sheets, enabling the discovery of materials that achieve target properties by exploring chemical composition and heat treatment conditions. The other case explains how MI was used to obtain a material patent with few embodiments. Also explained is a case where simulations were constructed to evaluate the atomic-level material structure, properties, and processability into parts for thick steel plates and copper alloys. This allowed the development to be conducted on the desk. Finally, this article discusses the outlook for broadly utilizing MI to its fullest potential.

Introduction

Circumstances surrounding environmental issues are undergoing drastic change, for example, in the relatively new objective of carbon neutrality. Alongside this phenomenon, the requirements for materials and components are growing in terms of variety, complexity, and performance, with competition in the area of development intensifying. Working against these parameters are a declining birthrate and a population that is shrinking in number and advancing in age. Because these factors will likely make experts in the requisite areas of development scarcer, it is critical to be able to develop new materials more efficiently.

Conventional materials development has primarily relied on experiments, theory, and the experience and intuition of researchers, often requiring a massive amount of time and effort. Recently, however, materials informatics/materials integration (MI) has been attracting attention as a new materials development methodology that can overcome this challenge. Research into MI in the United States began in 2011 with the Materials Genome Initiative. In Japan, such research began in the mid-2010s with nationally run projects such as the Materials Research by Information Integration Initiative (MI^2I) for functional materials, and SIP-MI[1), 2)] (Cross-ministerial Strategic Innovation Promotion Program, materials integration) for structural materials. This propagated the use of MI in industry, with materials manufacturers using MI in the development process and suppliers of IT products beginning to offer a variety of related services.[3)] Kobe Steel, in particular, is working to reform materials development using MI as part of the company's DX strategy.

MI refers to two innovation methodologies: materials informatics and materials integration. Materials informatics involves applying information science (AI, machine learning) to materials science. Materials integration denotes the blending of information science with experimentation, theory, and computation/simulation (promoted by, e.g, SIP-MI). Further, there are two primary techniques for using MI in materials development. The deductive approach is theory-based and involves developing physical models to capture actual phenomena via simulation. In the inductive approach, data from experiments and simulations are analyzed by AI to find relationships between design data (e.g., chemical composition) and material properties.

Simulation techniques are selected based on the scale of the phenomenon being studied and include micro-scale (atomic-level) calculations using first-principle calculations and molecular dynamics, mesoscale calculations of material structures and properties using metallurgical theory and phase-field methods, and macro-scale calculations using the finite element method (FEM) to evaluate the workability and strength of components. One established subset of AI technologies uses regression methods such as linear regression, Gaussian process regression, and neural networks to learn from design data to create material property prediction models (forward problem analysis). Another subset uses optimization techniques (e.g., Bayesian optimization) to search for the design data most likely to achieve the desired material properties (inverse problem analysis)[4), 5)].

Kobe Steel has a deep understanding of chemical

composition and manufacturing process conditions related to a wide range of metal materials such as steel, aluminum alloys, copper alloys, and welding materials. This expertise is how the company develops materials that meet the desired material properties. We are also well versed in materials utilization, as proven in our components made of carefully designed materials, as well as our structural designs that rely on component performance. Further, we use MI technology in an exceptionally precise manner in developing the various metal materials we specialize in, as well as their applications (**Fig. 1**).

Examples of materials development covered in this paper describe the use of AI to predict material properties and explore chemical composition and heat treatment conditions using experimental data. Covered as well are examples of the use of AI in combination with micro- and macro-scale simulations. The areas of focus are welding materials (Section 1), thin steel plates (Section 2), thick steel plates (Section 3), and copper alloys (Sections 4 and 5).

1. Welding material development using experimental data and AI

This section introduces a case study in which AI was taught experimental data in a material property prediction model for flux-cored wire, a welding consumable used in arc welding. AI was used to research chemical composition to arrive at a material

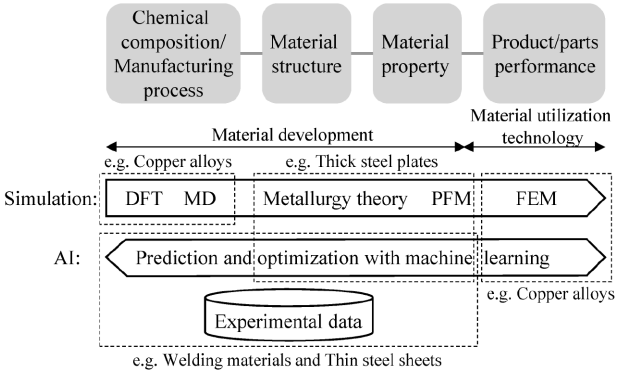

Fig. 1 Application of MI technology for material development and utilization

with an excellent balance of strength and toughness.

Fig. 2 shows a diagram of the AI-based prediction and search technology developed for this initiative. Conventional welding material development accounts for relationships between (1) raw material composition, (2) the chemical composition of welding materials made up of multiple raw materials (weld material composition), (3) the chemical composition of the weld metal after welding (weld metal chemical composition), and (4) the mechanical properties of the weld metal (weld metal properties). We developed MI technology that accounts for these hallmarks of welding material development in the form of AI prediction and search technology that connects every element, from (1) through (4), from both the forward and reverse perspectives.[6] The models within our prediction technology compute in the forward direction from (1)→(2), (2)→(3), and (3)→(4). Chaining the results of the individual models yields the overall prediction of (1)→(4). Our search technology also uses the prediction models for computations in the reverse direction, that is, (4)→(3)→(2)→(1). Described next are the details of the prediction and search technologies.

First, we modeled the prediction of (2) weld material composition from (1) raw material composition by taking advantage of the associated linear relationships. Next, we searched for (1) raw material composition from (2) weld material composition based on a convex optimization method that is effective for linear models. Gaussian process regression, a machine learning method, was then applied to experimental data to construct the prediction models for (2) weld material composition to (3) weld metal chemical composition and for (3) weld metal chemical composition to (4) weld metal properties. We chose this method because it is still difficult to define clear relationships based on theoretical physics due to complex welding phenomena and material microstructure morphology. The prediction model contains dozens of types of explanatory variables for weld material composition and weld metal chemical composition. As such, it is difficult to achieve high prediction accuracy simply by applying machine learning

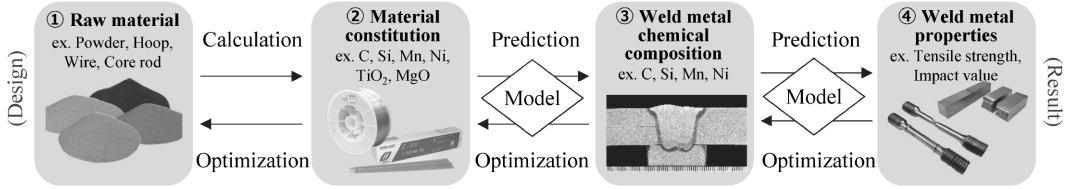

Fig. 2 Concept of MI application for welding material designing

methods to limited experimental data. We reduced the number of explanatory variables by excluding constituents known to have little effect based on our expertise in materials. We also incorporated the relationship between test temperature and brittle fracture rate into the model to predict toughness, a weld metal property. Through these measures, we improved the accuracy of our unique prediction model. Bayesian optimization, which is compatible with the Gaussian process regression used in the prediction model, was selected to search for (3) weld metal chemical composition and (2) weld material composition based on (4) weld metal properties. We applied this technology to flux-cored wire for arc welding of high-strength steel used in structural components.

First, we collected thousands of experimental data points in a range of strength classes for teaching to a prediction model. Next, we searched for raw material compositions predicted to achieve the weld metal's verification metrics of a tensile strength (TS) of ≥ 830 MPa and a 0℃ toughness (vE0℃ - energy absorbed upon Charpy impact test at 0℃) of ≥ 90 J. We made a prototype wire based on the results and evaluated its weld metal properties. Verification results were incorporated into the experimental data, and the process was iterated several times. **Fig. 3** shows the results based on conventional methods (white points) and based on MI (black points). Through MI, we uncovered a bold new design involving several composition changes compared with designs stipulated by conventional methods. One material satisfied the target properties by optimizing the balance between tensile strength and vE0℃. In short, we used MI to efficiently pinpoint a material that achieves the target properties, thereby revealing the value of using compositions different from those recommended by conventional design guidelines.

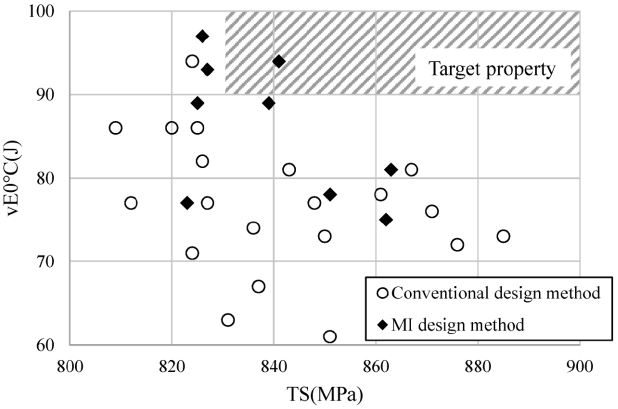

Fig. 3 Comparison of material properties between conventional design method and MI design method

2. Materials development using AI and experimental data on thin steel sheets

This section introduces a case study in which we used the experimental data Kobe Steel has amassed through developing ultra-high-tensile strength steel for vehicles to develop an AI-based property prediction model, which we then used to search for candidate materials, find a material that satisfies target properties, and obtain a patent with few embodiments.

Ultra-high-tensile strength steels for automotive applications must have high tensile strength for collision safety alongside mechanical properties in opposition to this, such as good total elongation (EL) and hole expandability (λ), which ensure formability. Although mechanical properties tend to improve with an increase in added elements, steel composition cannot be endlessly modified without sacrificing weldability and machinability. The cost and labor expenditure to develop and test ultra-high-tensile strength materials with excellent mechanical properties, given these constraints, is enormous. Our objective was therefore to find a suitable material using MI technology and few trials.

First, we constructed an AI-based property prediction model using 369 experimental data points accumulated by Kobe Steel on ultra-high-tensile strength steels. In addition to steel composition and heat treatment conditions, explanatory variables include the difference between the Ae_3 point and the uniform heat treatment temperature (T_1), and the difference between the Ms point and the cooling stop temperature (T_2). These parameters were introduced to capture changes in the material structure more directly and to improve the accuracy of mechanical property predictions. The Ae_3 point and Ms point can be calculated from composition information using the thermodynamics calculation software Thermo-Calc.[7] The objective variables were TS, EL, and λ, and Gaussian process regression was used as the prediction method. **Fig. 4** shows the relationship between the predicted and experimental values for TS and EL; both parameters were predicted with high accuracy.

Then, using the prediction model and Bayesian optimization, we searched for materials that satisfy the target properties of TS ≥ 950 MPa, EL ≥ 22%, and λ ≥ 20% within the composition ranges of C, Si, and Mn established for the verification material. We used Bayesian optimization to identify compositions and heat treatment conditions predicted to have the highest probability of achieving the desired properties. We then produced prototype materials and evaluated their properties. The first search

revealed 18 materials. We added the experimental data obtained based on this search to the training data and ran a second search, which revealed two additional materials. Materials satisfying the target properties were discovered via the second search.

Subsequently, we initiated the process to obtain a patent with a few embodiments for the composition and heat treatment conditions discovered via our AI-based property prediction model. The exact flow is described next. (1) We constructed an AI model that uses a large amount of experimental data to predict properties based on composition and heat treatment conditions. Further, we demonstrated the reliability of the model's predictions by comparing predicted and experimental values. (2) We used the AI model to create virtual data predicting properties based on composition and heat treatment conditions within and outside the scope of patent claims, and defended the validity of the claims. (3) We provided an embodiment and a comparative example using experimental data. **Table 1** shows the experimental and virtual data reported in the patent application. A circle in a property column of the virtual data section indicates that the target property was met; an 'x' indicates that it was not met. The embodiments of a patent claim must typically be based on a large amount of experimental data with great variation within each parameter. However, by substituting most of the required experimental data with virtual data predicted by AI, we were able to secure a patent, granted in October 2022[8], with only two sets of actual experimental data.

3. Materials development using metallurgical and fracture mechanics models and AI in thick steel plates

Large structures such as vessels and architectural steel frames are made up of welded thick steel plates. The heat-affected zone (HAZ) of a steel plate is generally less tough than the base metal, so ensuring the toughness of the HAZ is critical to the structure's safety. Evaluating the effects of compositions and welding conditions on HAZ toughness via experimentation is a complex process. The steel plate must be melted and rolled, and a simulation of heat treatment or thermal history during welding must be made available, entailing costly prototype production. Therefore, instead of using AI to predict HAZ toughness based on a vast repository of experimental data, we developed technology to predict HAZ toughness based on physical models and used inverse problem analysis to design the composition of the HAZ of thick steel plates. These projects are detailed next.

Inverse problem analysis requires a forward

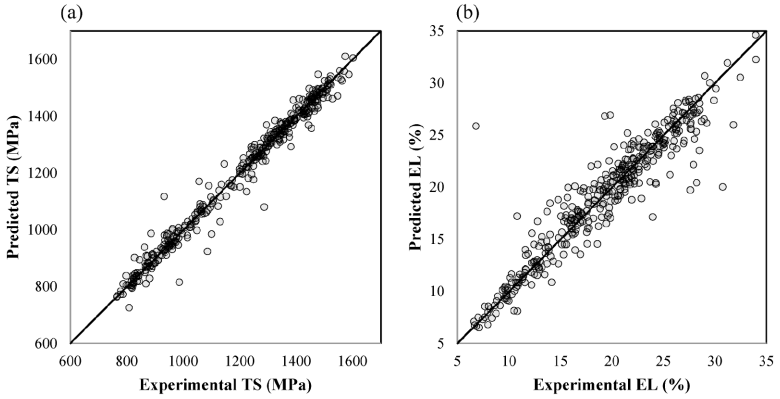

Fig. 4 Relationship between predicted and experimental values of each property - (a) Tensile strength, (b) Total elongation

Table 1 Experimental data and virtual data used for patent acquisition

Data No	Chemical compositions of materials								Annealing condition parameters						Mechanical properties		
	C	Si	Mn	Al	Ti	Ni	Mo	Cr	T_1-Ae_3	T_{preAT}	Ms-T_2	T_{postAT}	t_{preAT}	t_{postAT}	TS	EL	λ
	(mass %)								(℃)				(s)		(MPa)	(%)	(%)
Experimental-Data 1	0.20	0.8	2.0	0.04	0.00	0.0	0.0	0.5	-9	500	180	400	10	300	983	24.2	39.0
Experimental-Data 2	0.24	0.6	2.4	0.60	0.00	0.0	0.0	0.0	24	450	218	460	90	20	933	19.1	42.2
Virtual-Data1	0.20	0.8	2.0	0.04	0.00	0.0	0.0	1.0	130	500	50	400	10	300	○	×	○
Virtual-Data2	0.20	0.8	2.0	0.04	0.08	0.0	0.0	0.0	110	500	100	400	10	300	×	○	○
Virtual-Data3	0.40	2.0	2.0	0.04	0.00	0.0	0.0	0.0	48	380	5	380	100	450	○	×	×
Virtual-Data4	0.20	0.8	2.0	1.2	0.00	0.0	0.0	0.0	-12	450	200	400	23	300	×	○	○
Virtual-Data5	0.20	0.8	2.0	0.04	0.00	0.5	0.0	0.0	130	450	100	400	5	300	×	×	○
Virtual-Data6	0.20	0.8	2.0	0.04	0.00	0.0	0.2	0.0	110	500	50	400	5	300	×	×	○

※○: achieve target property. ×: not achieve target property

prediction model that predicts HAZ toughness from the composition and thermal history. Two models were linked together for forward prediction. One model calculates phase transformations based on composition and thermal history as well as structural characteristics, such as the hard second-phase microstructure that is the origin of fracture, based on transformation temperature information. The other model determines the occurrence of a brittle fracture based on the weakest link theory.[9] The model reproduces the phase transformation behavior of the HAZ at various cooling rates in thick low-carbon steel plates with different chemical compositions. It enables the use of the microstructure's characteristics in the HAZ to calculate the energy absorbed upon Charpy impact testing in the temperature range where brittle fracture is most likely to occur.[9] The predicted strength and toughness of the base metal corresponding to the quenching and tempering process are also modeled.[2]

To reduce the time required for optimization calculations during inverse problem analysis, more than 10,000 forward calculations with random chemical compositions were performed using our forward problem model, and an approximate function was learned by a neural network. Using this AI model to perform optimization calculations under specified constraints automates the design of steel composition and welding conditions (one pass). As a verification metric for inverse problem analysis, we researched the composition and process conditions (welding heat input) for steel plates with a strength of 980 MPa and low-temperature toughness in both the base metal and HAZ. Lower limits for base metal strength and base metal toughness and upper limits for alloy cost and equivalent carbon content were specified as optimization constraints. Given these constraints, we searched for the chemical composition that maximizes HAZ toughness in the heat input range of 4 - 8 kJ/mm. **Table 2** shows the steel plate composition for the verification test that was output by inverse problem analysis. Steel plates corresponding to the target composition in Table 2 were produced by melting, rolling, quenching, and tempering. These plates then underwent tensile and Charpy impact testing. HAZ toughness was evaluated using material subjected to a recreated HAZ thermal cycle. The toughness evaluation index is the transition temperature at which the absorbed energy upon the Charpy impact test reached 50 J. **Table 3** shows the results of the experimental verification and the properties obtained by inverse problem analysis.[2] Although the difference between the predicted and experimental HAZ toughness values was relatively large, the experimental verification results were satisfactory for each property. While it is impossible to completely eliminate the need for prototyping, the method used appears to be effective for defining material design guidelines. Our models will improve the efficiency of developing steel plates that meet various specifications and constraints.

Table 2 Chemical composition of steel plate for verification test

(mass%)

C	Si	Mn	Ni	Cr	Mo
0.06	0.4	1.6	2.0	1.0	0.5

Others Cu, Nb, V, Al

4. Materials development using molecular dynamics in copper alloys

Copper alloys exhibit excellent thermal and electrical conductivity, making them ideal for applications such as electronic devices, terminals in automotive electronics, and machinery cabling. However, the demand for lighter and smaller products is driving the need to develop copper alloys with higher strength and electrical conductivity. Solid solution strengthening is one way to increase the strength of a copper alloy. One of the many theories proposed as the mechanism of solid solution strengthening is the size effect theory[10]. The size effect theory starts with the explanation that when an element (solute) is dissolved in a solid material of another single element (solvent), the difference in atomic radii (solute vs. solvent) causes lattice distortion.

Table 3 Inverse problem analysis verification test results

	Base material		HAZ
	Tensile strength (MPa)	50 J transition temperature (℃)	50 J transition temperature (℃)
Predicted value	1,090	-44	-91※
Experimental result	1,011	-45	-58～-70
Target property	> 980	< -40	< -50

※Worst value in the heat input range for calculating HAZ toughness

Dislocations then adhere to the solute atoms (pinning), suppressing the movement of dislocations and thereby increasing strength. Experimental data show that the larger the difference between the atomic radii of the solute and solvent, the greater the effect of solid solution strengthening. However, the atomic-level mechanism of the size effect theory is not well understood. Therefore, we developed a simulation model for a binary copper alloy to calculate the force required to depin a dislocation from a solute atom using the molecular dynamics (MD) method, which can analyze the dynamics of a large number of atoms[11]. Furthermore, we extracted factors closely related to depinning force and developed a prediction formula to easily calculate depinning force. An example[12] is detailed next.

First, we created models to which we could apply MD methods. Specifically, we created Cu-Ni and Cu-Mo models with crystalline structures containing Cu as the solvent, one Ni or Mo atom as the solute, and one edge dislocation. Dislocations in a face-centered cubic lattice (FCC), such as those exhibited by Cu can expand into two partial dislocations and stacking faults, a phenomenon that can be reproduced. We used the MD method to determine the depinning force required for the partial dislocation to detach from the solute atom by increasing the force applied in the slip direction of the model. Results showed that the depinning force required for the Cu-Mo model was about 10 times higher than that of the Cu-Ni model (**Fig. 5**). The atomic radius of Mo is greater than Ni, which is similar in size to Cu. The results therefore line up with the tendency that the larger the difference in atomic radii between solute and solvent, the more intense the solid solution strengthening, making it possible to compare the depinning forces.

However, to calculate via the MD method, the interatomic potential must be known for each element. This entails enormous computational costs,

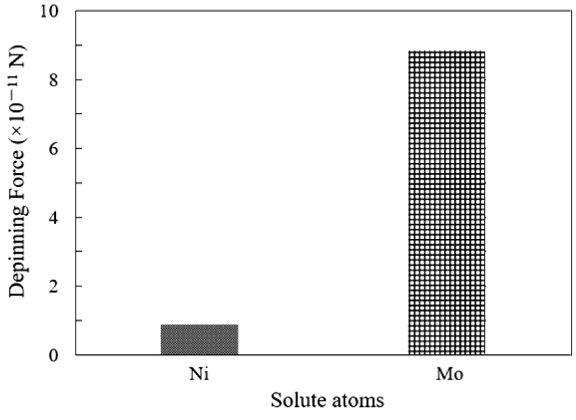

Fig. 5 Depinning force required for partial dislocation to move away from solute atom

making it difficult to simulate solid solutions of a large number of different elements. We therefore set out to develop a simple equation for prediction. The results of the MD method indicated that the maximum volumetric strain around the solute atom and the misalignment between the solute and solvent atoms calculated by first-principle calculations are related to the depinning force. As such, we developed Equation (1) to predict the depinning force F_V.

Equation (1): $F_V = \alpha|\Omega|Gb^2|\varepsilon_V^{max}|$

Here, α is a fitting parameter, Ω is the alignment between the solute and solvent atoms calculated by first-principle calculations, G is the shear modulus, b is the Burgers vector, and ε_V^{max} is the maximum volumetric strain. These parameters are element specific and can be determined via a simple simulation. In using this prediction equation to calculate the depinning force F_V when elements undergo solid dissolution, it is possible to screen for added elements that are highly effective for solid-solution strengthening via theoretical calculation. We anticipate that this will serve as a new guideline for designing high-strength copper alloys.

5. Developing materials application technology using finite element analysis and AI in copper alloys

This section introduces a case study in which AI and simulation via finite element analysis were jointly applied to optimize a multi-stage bending process for copper alloy sheets used in terminals for automotive electronics[13].

Conductivity is an essential property in terminals used for automotive electronics. When the pin-shaped male terminal is inserted into the female terminal, the leaf spring inside the female terminal deforms, generating counterforce from the contact pressure and thus ensuring conductivity. Terminals in automotive electronics have been made smaller in recent years to conserve space, entailing shorter leaf springs and therefore lower spring constants. To maintain the same contact pressure as before, spring deformation must be increased to compensate for the decrease in spring constant. However, if the leaf spring deforms to the point of plastic deformation, the desired contact pressure will not be achieved. Therefore, the material of the leaf spring must be strong enough to preclude plastic deformation. The stronger a material, though, the lower its bend formability, with breakage and creasing being more likely to occur during manufacturing. One way to improve bend formability is to

ensure manufacturing conditions are conducive to effective bending processes. However, there are many relevant process condition parameters, and determining the appropriate set of conditions through experimentation is costly. This drove us to develop a technique for efficiently exploring optimal bending conditions by combining optimization techniques with technology for evaluating bending formability through simulation.

Fig. 6 shows an FE model for contact bending as a simulation to evaluate bend formability. Contact bending is a four-stage bending process (1st through 4th stage) with six main process condition parameters: 1st bending radius R_1, 1st bending angle θ_1, 2nd bending clearance C, 2nd bending radius R_2, 2nd bending punch radius R_p, and 3rd bending angle θ_3. Experience shows a correlation between bending strain and the degree of breakage and creasing on the plate surface. Therefore, the maximum bending strain ε_{max} generated on the plate surface after the 4th bending stage was used for the simulation to evaluate bend formability. We used the explicit dynamics software LS-DYNA[14] for FEA. CATIA V5[15] (CAD software) and HyperMesh[16] (mesh creation software) were used to modify the FE model in response to changes in the process condition parameters.

This simulation was used to search for process condition parameters that would reduce the maximum bending strain ε_{max} via optimization techniques. Since a simulation takes about 30 minutes, we chose Bayesian optimization for its greater likelihood of obtaining an optimal solution within fewer runs of the simulation. The overall calculation flow was to acquire initial data by running a simulation with process condition parameters based on experimental design, search for process condition parameters using Bayesian optimization, modify the FE model, and rerun the simulation. The search process involves adding newly acquired data and repeating the calculations in an iterative process.

To verify the effectiveness of this technology, we ran experiments using dies for contact bending under three different conditions: (a) conventional condition, (b) manually adjusted condition, and (c) optimized condition. **Fig. 7** shows the contact bending surface under each condition. The copper alloy sheets in this experiment were tin plated. Under the conventional and manually adjusted conditions, the tin plating peeled off, exposing a large area of copper substrate. The optimized condition suppressed exposure of the copper substrate, confirming that this bending condition is favorable. This technology is a promising solution for quickly providing optimal bending conditions for copper alloy sheets with varying properties.

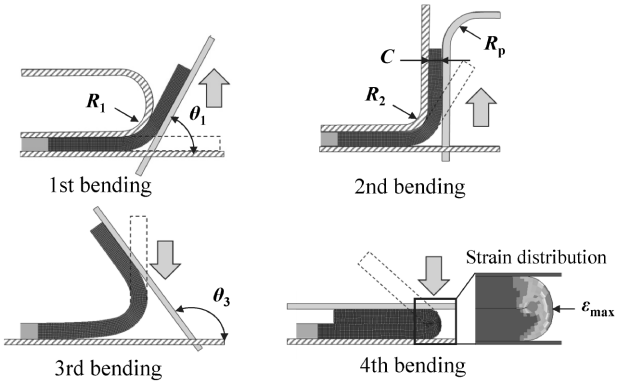

Fig. 6 FE model for contact bending evaluation

Conclusion

This paper describes examples of materials development and utilization as applied to various metal materials using MI technologies such as AI and simulation models. To use MI effectively in the discovery of new materials, we gathered extensive experimental data (from experiments conducted by Kobe Steel, patents, and publications), constructed physical models that capture physical phenomena on each scale, produced data through theoretical simulations of various conditions to overcome barriers to experimentation, and used AI to explore this large amount of high-dimensional data

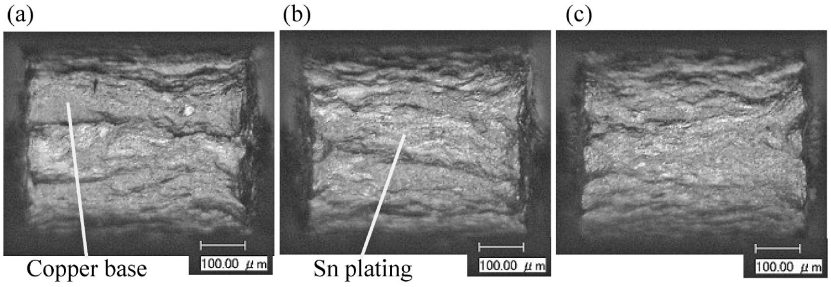

Fig. 7 Observation of contact bending outside surface experimented under each condition - (a) Conventional condition, (b) Manually adjusted condition, (c) Optimized condition

to an extent beyond human capabilities. We are continuing to develop our cloud-based platform DataLab® to foster the comprehensive utilization of MI, as this requires a platform with a database for storing experimental data and tools that enable materials engineers to use AI and simulation technologies without programming expertise. For details regarding DataLab®, see "Building and Utilizing Company-wide Data Analytics Platform, DataLab®" (pp.4-8 of this issue). While our application of DataLab® began with the development of welding materials[6], we will expand its scope by creating a development system that can respond quickly to the varying needs of our customers.

Our research was conducted in part under the Cross-ministerial Strategic Innovation Promotion Program (SIP) "Materials Integration for Revolutionary Design System of Structural Materials" of the Council for Science, Technology and Innovation, Cabinet Office, Government of Japan (managed by JST, Japan Science and Technology Agency).

References

1) M. Demura. Tetsu-to-Hagane. 2023, Vol.109, No.6, pp.490-500.
2) Cross-ministerial Strategic Innovation Promotion Program (SIP) Materials Integration for Revolutionary Design System of Structural Materials Final Results Report. https://www.jst.go.jp/sip/dl/p05/p05_results-report2023_1.pdf. Accessed 2023-12-15.
3) Sumitomo Mitsui Banking Corporation. Report on Economic and Industry Trends. https://www.smbc.co.jp/hojin/report/investigationlecture/resources/pdf/3_00_CRSDReport090.pdf. Accessed 2023-12-15.
4) H. Hino et al. Materia Japan. 2019, Vol.58, No.1, pp.7-11.
5) K. Matsui et al. Materia Japan. 2019, Vol.58, No.1, pp.12-16.
6) G. Taniguchi et al. R&D Kobe Steel Engineering Reports. 2023, Vol.72, No.1, pp.91-96.
7) Thermo-Calc Software AB. https://thermocalc.com/. Accessed 2024-01-29.
8) Kobe Steel, Ltd. K. Nakayama et al. Method for manufacturing high strength steel sheet. Patent No.7146127 (P7146127). 2022-10-3.
9) M. Inomoto et al. R&D Kobe Steel Engineering Reports. 2021, Vol.71, No.1, pp.31-36.
10) Z. Huda. Mechanical Behavior of Materials Fundamentals, Analysis, and Calculations, 1st ed. Springer, 2021, pp.63-79.
11) K. Tsuzuki et al. Journal of the Japan Institute of Metals and Materials. 2002, Vol.66, No.7, pp.728-734.
12) C. Kura et al. Materials Today Communications. 2024, Vol.38, No.108242.
13) T. Kobayashi et al. The proceedings of 74th Japanese Joint Conference for the Technology of Plasticity. 2023, pp.303-304.
14) Ansys LS-DYNA. https://www.ansys.com/products/structures/ansys-ls-dyna. Accessed 2024-01-29.
15) Dassault Systèmes. CATIA V5. https://www.3ds.com/products/catia. Accessed 2024-01-29.
16) Altair HyperMesh. https://altair.com/hypermesh. Accessed 2024-01-29.

Digital Transformation (DX) Technology Contributing to Further Automation of Robotic Welding

Yuji KIMURA*1・Kazuki HIDAKA*1・Takaya HIGASHIRA*1・Fumiaki SAWAKAWA*2・Atsushi ARAI*1・Kohei KOMUKAI*1

*1 Welding System Department, Technical Center, Welding Business
*2 Welding System Department, Technical Center, Welding Business（currently Digital Innovation Technology Center, Technical Development Group）

Abstract

Information and communication technologies, as well as DX technologies, are advancing, raising expectations for the acceleration of automation and labor-saving in production sites. Kobe Steel has been focusing on the development of various functions, including welding robots, aiming at automating welding operations. However, the introduction of welding robot systems has created new tasks requiring manual work such as teaching and maintenance. Using DX technology to reduce this manual labor can further enhance the effectiveness of introducing welding robot systems, contributing to increased productivity for our customers. Combining the ARCMAN™ Offline Teaching System with DX technology, Kobe Steel has developed new functions for automatically generating welding programs and simulating cable behaviors to reduce manual teaching work. Furthermore, connecting laser sensors, interpass temperature sensors, and cameras linked with ARCMAN™ View to the robot system has automated the measurements required for welding.

Introduction

Kobe Steel has an extensive background in developing and marketing welding robot systems for welding medium-to-thick plate, which is widely used in a variety of industries and applications such as architectural steel frames, construction machinery, bridges, and shipbuilding. In this way, we improve our customers' productivity by automating and reducing labor needs in the welding process. Components in these industries and applications are composed of large workpieces. Gaps between components from misalignment during assembly are common, and the repeated application of heat for multi-pass welding can cause thermal distortion. This can shift the target position of the weld joint, precluding a sound joint. Industry requirements for welding architectural steel frames include standards for thermal input and interpass temperature control, necessitating manual temperature measurement between passes.

To meet these requirements, our welding robot system has a laser sensor and a non-contact temperature sensor to measure and automatically control shape and temperature, thereby furthering automatic welding. The laser sensor sends out a beam that measures the root gap for automatic selection of optimal welding conditions. This enables automated narrow-gap welding, which was previously only a semiautomatic welding performed by skilled technicians. Two types of measurement methods are available; production cycle time can be minimized by using the appropriate method for the measurement point. Temperature sensors foster automation of the measurement and control of interpass temperature, improving throughput by reducing cycle time and manual labor.

This combination between the welding robot system and measurement technology promotes automation. However, welding robot systems require their own set of manual tasks not required with conventional manual welding, such as robot teaching, robot operation, and recovery from certain temporary stoppages (e.g., sensor failures, wire jams). To help eliminate these manual processes, we developed the ARCMAN™ Note 1) Offline Teaching System (hereafter, KOTS™ Note 2)) to support teaching and ARCMAN™ View to visualize robot-guided production and reduce temporary stoppages.

In Section 1 of this paper, we describe a case study in which we reduced teaching time by incorporating DX technology into KOTS™. Sections 2 and 3 contain examples of how we have further automated and optimized robot welding using various sensors.

1. ARCMAN™ Offline Teaching System

This section introduces use cases involving KOTS™, an offline simulator designed for the ARCMAN™ welding robot system. KOTS™ can reproduce the movements of peripheral equipment and mounted workpieces in addition to the main ARCMAN™ body. This software is an effective solution for a variety of situations, including preliminary application studies.[1)]

Note 1) ARCMAN is a trademark of Kobe Steel (1715437).
Note 2) KOTS is a trademark of Kobe Steel.

1.1 Automatic welding program generation function

Welding robots achieve high throughput in the mass production of identical workpieces because they operate in accordance with data points taught in advance. Producing workpieces of different shapes, however, necessitates individualized teaching data, making it difficult to achieve high throughput.

Kobe Steel developed an automatic welding program generation function to overcome this challenge. This function turns the teaching methods of skilled technicians into rules and automatically generates welding programs based on factors including such rules, the system configuration, and welding process execution information. With this function, even operators with limited teaching experience can easily create welding programs, with teaching time reduced from two days to one day.

1.2 Cable simulation

KOTS™ has an optional cable simulation function. With this function, the operator can use the KOTS™ interface to check the behavior of the torch cable via ARCMAN™ as well as how the cable is wound around the manipulator and the interference between the workpiece and the cable when entering a confined space.[2)] Particularly when checking cable behavior in a confined space, interference between the cable and workpiece may place an unexpected load on the robot and damage the robot or workpiece. Previously, it took about two days to model the cable curvature via CAD for each robot pose and check for the presence of interference. With KOTS™, it is possible to evaluate the risk of movements that may cause interference in advance (**Fig. 1**), reducing the evaluation time to only about half a day.

1.3 Using robots in multiple-variety mixed-flow production

The automatic welding program generation function makes it possible to automatically create welding programs from workpiece models and welding process execution information. Thus, operators do not need to perform teaching operations for every workpiece in multiple-variety mixed-flow production. Our current focus in developing this function centers around the construction machinery sector. We will later expand the scope of development to include further applications, such as the welding of steel segments to prevent bridge collapse (**Fig. 2**). Kobe Steel is developing a function for the welding robot system to compensate for machine error as well as additional sensing functions to make the simulated environment more similar to the production environment and reduce the need for teaching corrections. Our ultimate goal is to fully automate the welding process by using CAD data to automatically create welding programs, which in turn will be used to automatically create teaching programs, all of which will be linked to the robot system.

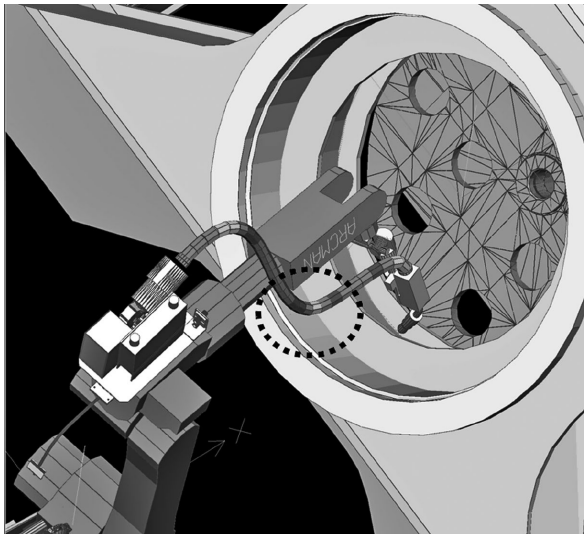

Fig. 1 Cable simulation and curvature display

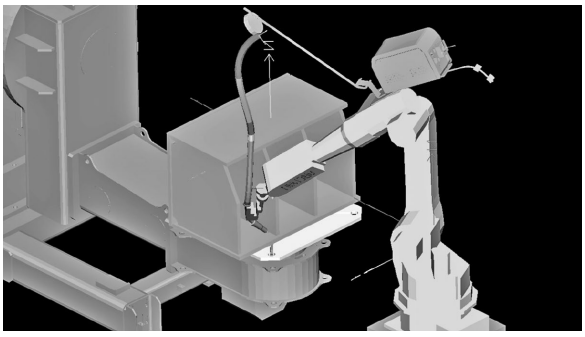

Fig. 2 Feasibility study for application to anti-collapsing devices for bridges

1.4 Efficiency improvement via KOTS™

At Kobe Steel, we work to understand the customer's situation before proposing the optimal welding robot system. We select robots, sliders, positioners, and other equipment based on their suitability for the dimensions of the target workpiece. We also determine how this equipment is structured and laid out, which requires an enormous amount of time for validation. Creating a teaching program to determine the feasibility of robot welding accounts for a considerable proportion of

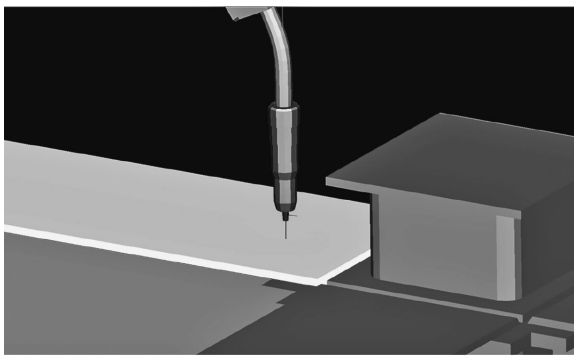

Fig. 3 3-way sensing simulation

the configuration design time. To overcome this challenge, we used the automatic welding program generation function to shorten the welding program creation time and standardize the quality of the welding programs created, reducing validation time and improving quality.

In addition, Kobe Steel's welding software for architectural steel frames can automatically generate teaching programs in advance based on workpiece dimensions, such as columns and joints.[3] Operators can use KOTS™ to verify the suitability of the teaching programs the software creates, making it possible to validate operations without preparing workpieces of various sizes or setting up actual systems. KOTS™ also includes functionality for touch sensing, a robot function that could not previously be simulated, enabling sensing that accounts for workpiece misalignment. This reduces the workload of developing software related to the automatic generation of welding programs as well as the cost of workpiece procurement (**Fig. 3**).

These technologies make it possible to propose to our customers the optimal system for welding automation.

2. Sensing technology

Kobe Steel's welding robots have sensing technologies, such as touch sensing, that eliminate the need for special measuring equipment. They also have arc sensors to compensate for groove irregularities and distortion. However, these sensing technologies cannot measure complex groove shapes. Additionally, certain workpieces are subject to temperature control requirements, hindering robot welding. The following sections detail how our system achieves automated welding of complex grooves using laser sensors and automated welding of architectural steel frames using temperature sensors.

Fig. 4 Welding torch with laser sensors

2.1 Laser sensors

Laser sensors strike the groove and weld zone for high-speed measurement of grooves of various shapes, a function that touch sensing cannot accomplish. Unlike touch sensing, laser sensing can accurately measure a wide range of joints, including flare bevel grooves and T-joints. Additionally, a small-profile laser sensor enables stable sensing even where there is little clearance[4] (**Fig. 4**).

2.1.1 Automating difficult welds

Large structures are often constructed of welded medium-to-thick plate, where distortion and misalignments can cause unintentional gaps in the weld line. Conventionally, human operators had to fill these gaps using semiautomatic welding before robot welding. Now that the gap can be measured via laser sensing, a robot can fill the gap, thereby reducing the operator's workload. This function automates the process, as the robot selects the optimal welding conditions from a database of welding conditions based on the gap width measured by the laser sensor (**Fig. 5**).

2.1.2 Cycle time reduction using laser sensors

Laser sensing involves striking the groove with a laser line to gather abundant data in a single measurement, unlike touch sensing, which requires multiple measuring operations to capture the same data. Conventional root gap measurement using a wire requires three measurement operations, which takes about 10 seconds. Laser sensing takes one second, or one-tenth of the measurement time. Our laser sensing system offers two measuring

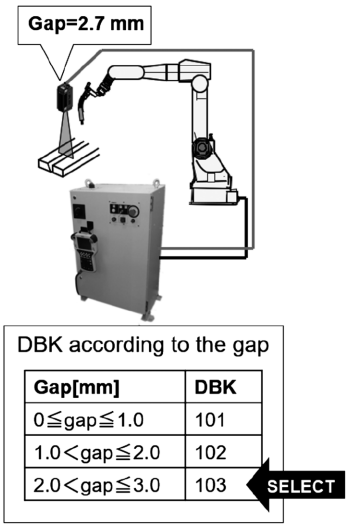

Fig. 5 Switching welding conditions using laser sensors

methods: scanning and one-shot. In the scanning measurement, the laser sensor scans a fixed distance in the direction of the weld line to collect multiple data points, which are then averaged. This reduces the influence of measurement error caused by scratches from machining or assembly, or by fumes or spatter in the groove or on the surface of the workpiece from the welding process. One-shot measurement measures a single point rather than scanning a line and is therefore faster. Custom commands can be set up to define the appropriate measurement method based on the measurement point.

2.2 Overview of interpass temperature sensors

There are standards for interpass temperature control in the welding of architectural steel frames. Common practice is for an operator to measure the temperature at a specific location using a thermometer or temperature-indicating marker just before welding the next pass. The operator then starts the next pass after confirming that the interpass temperature is below the set value.

Our interpass temperature measurement function for welding robot systems that process steel frames automates the measurement and control of interpass temperature. This function eliminates the need for operators to measure the temperature between passes. As such, this time can be reallocated to other tasks to reduce cycle time. Additionally, reliably controlling interpass temperature ensures weld joint quality.[5] This function also improves safety because the operator no longer needs to enter the safety fence to measure the temperature between passes.

This function has already been integrated at steel fabrication shops with S-grade certification.

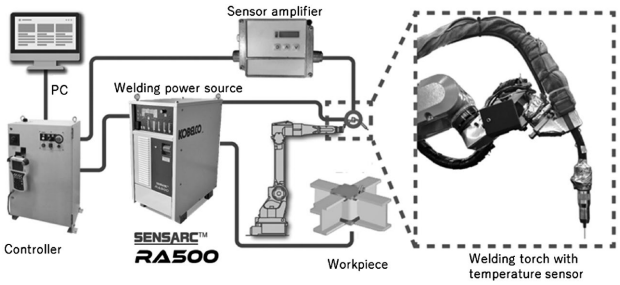

Fig. 6 System using temperature sensors

(Japanese factories can become certified by the Ministry of Land, Infrastructure, Transport and Tourism, an agency of the Japanese government, based on standards of quality control and technology. “S” stands for “Super” and is the highest grade achievable.)

2.2.1 System configuration

Fig. 6 shows the configuration of a system with the interpass temperature measurement function. The non-contact temperature sensor is near the wrist of the robot in a location that does not interfere with welding, precluding the need to switch between the temperature sensor and the torch. The sensor amplifier and controller transmit data from the temperature sensor to the computer. The temperature can be viewed on the monitor and the teaching pendant.

2.2.2 Process flow of interpass temperature measurement

Fig. 7 shows the process flow of the interpass temperature measurement function. Just before welding, the robot moves to the measurement point and measures the temperature. If the temperature is higher than the set value, the robot waits to start welding until the temperature drops below it. The temperature can be observed on the monitor during this process. This process is repeated until the final pass.

2.2.3 Interpass temperature log

This welding robot system can automatically record data, including welding current, arc voltage, and thermal input to create a welding procedure report. Previously, an operator had to record interpass temperature on paper or into a computer program. With this function, interpass temperature is automatically entered into the welding procedure report, eliminating the work of manual entry and the possibility of reporting errors (**Fig. 8**).

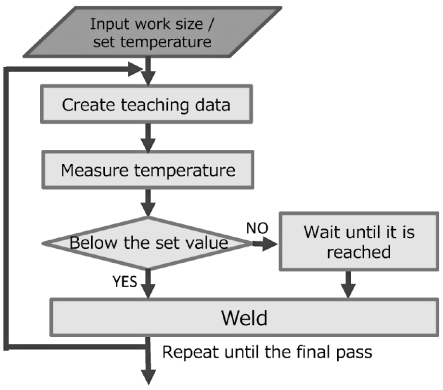

Fig. 7 Temperature measurement workflow

工事名称				作業日	2022/06/30
柱番号				ロボット名称	
継手名				オペレータ	
母材		部位	コラム	記録者	
板厚	32mm	ルート間隔	8.9mm	積層図	
開先角度	35°	溶接姿勢	下向姿勢		
溶接材料	規格				
	ワイヤ径				
	メーカー				
	銘柄				
管理	パス間温度	250℃			
	溶接入熱	30000J/cm		11層16パス	

パス	区間	溶接電流(A)	アーク電圧(V)	溶接速度(cm/min)	溶接入熱(J/cm)	パス間温度(℃)
1	直線	318	34.8	24.0	27666	100℃以下
	コーナ	301	33.3	24.0	25058	
2	直線	295	35.8	26.8	23644	100℃以下
	コーナ	289	34.4	26.2	22767	
3	直線	280	36.0	26.3	22996	100℃以下
	コーナ	269	35.1	25.2	22480	
4	直線	283	35.7	25.3	23959	102
	コーナ	280	35.1	24.1	24468	
5	直線	282	34.8	32.7	18006	100℃以下
	コーナ	270	34.2	32.1	17259	
6	直線	288	35.1	30.7	19756	113
	コーナ	270	34.7	31.1	18075	
7	直線	286	35.1	29.7	20280	134
	コーナ	281	34.4	29.6	19594	
8	直線	286	35.1	28.2	21358	136
	コーナ	259	34.8	28.0	19313	
9	直線	290	35.2	30.1	20348	116
	コーナ	269	34.7	29.9	18731	
10	直線	282	35.2	28.5	20897	137
	コーナ	259	34.5	27.6	19425	
11	直線	283	34.9	30.0	19753	157
	コーナ	274	34.6	30.0	18960	
12	直線	277	35.2	27.1	21587	152
	コーナ	264	34.6	26.4	20760	
13	直線	256	33.6	32.4	15928	126
	コーナ	247	33.6	30.0	16598	
14	直線	270	33.3	31.3	17235	132
	コーナ	231	33.4	27.9	16592	
15	直線	264	33.6	31.6	16842	145
	コーナ	235	33.6	27.8	17041	
16	直線	254	33.9	29.7	17395	143
	コーナ	245	33.7	26.3	18836	

Fig. 8 Example of a welding procedure report generated by the system

3. ARCMAN™ View

This section describes use cases involving ARCMAN™ View, an optional function of ARCMAN™ PRODUCTION SUPPORT[6]. This function supports production management and the analysis of temporary stoppages and welding defects by collecting operating data from the welding robot system and visualizing welding and production data.

3.1 Overview of ARCMAN™ View

ARCMAN™ View is an optional function that enables real-time display and recording of robot operation via cameras connected to the network (**Figs. 9** and **10**).

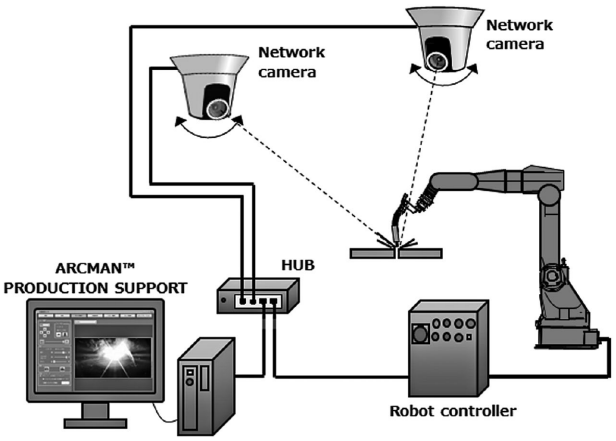

Fig. 9 ARCMAN™ View system configuration

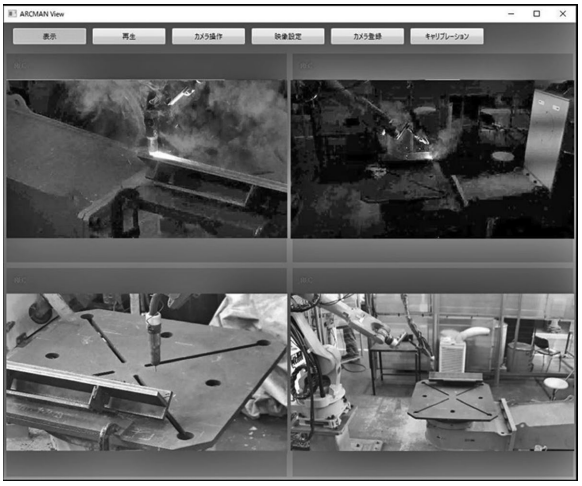

Fig.10 Sample image of ARCMAN™ View

3.2 Safety improvement with ARCMAN™ View

One feature of ARCMAN™ View is the ability to have the camera track the tip of the welding torch on the robot so it is constantly in view.

With this function, the operator can use the monitor for robot operation and to continuously observe the area around the tip of the welding torch without moving the camera manually.[7]

Remote operation via the monitor makes it possible to safely operate the robot from outside the safety fence, even in situations where it is conventionally necessary to enter the safety fence for operation via line of sight (**Fig.11**). A manufacturer of rolling stock reported a case in which the ARCMAN™ View monitor was used to perform recovery operations from outside the safety fence when a temporary stoppage occurred during welding at height.

Fig.11 Sample of remote operation outside the Fence

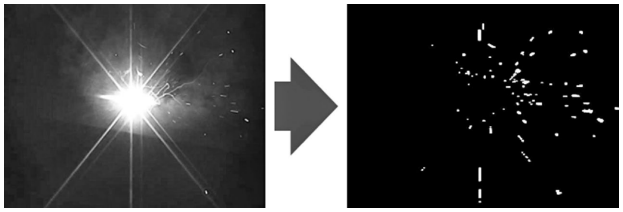

Fig.12 Image of spatter detection

3.3 Weld evaluation with ARCMAN™ View

We developed a spatter measurement function for ARCMAN™ View. This module identifies areas corresponding to spatter in images taken during welding, provides a real-time indication of the number of pixels as a numerical value, and saves it to a log (**Fig.12**). This function makes it easy to quantify the change in spatter volume based on welding conditions. As such, welding defects can be detected sooner, and the process for evaluating the effects of changing conditions is faster (**Fig.13**).

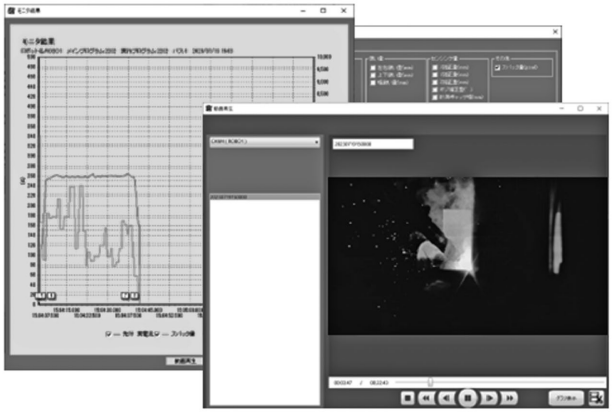

Fig.13 Image of spatter measurement display

Conclusion

This paper introduces teaching functions and measurement technologies for welding robot systems utilizing DX technology. Japan's declining birthrate and aging population are projected to intensify the need for automation and workforce reduction in production. Given this backdrop, we aim to alleviate the challenges of labor shortages and heavy manual labor by automating welding processes and improving quality, thereby improving productivity and safety in our customers' operations.

References

1) T. Izumi et al. R&D Kobe Steel Engineering Reports. 2013, Vol.63, No.1, pp.94-98.
2) A. Fukunaga et al. R&D Kobe Steel Engineering Reports. 2023, Vol.72, No.1, pp.21-26.
3) H. Matsumura. R&D Kobe Steel Engineering Reports. 2009, Vol.59, No.3, p.67.
4) T. Higashira. Boudayori Technical Guide, Technical Report. 2019, Vol.60, 2019-5.
5) A. Arai. Boudayori Technical Guide, Technical Report . 2023, Vol.64, 2023-2.
6) A. Fukunaga et al. R&D Kobe Steel Engineering Reports. 2013, Vol.63, No.1, pp.99-103.
7) T. Koike et al. R&D Kobe Steel Engineering Reports. 2018, Vol.68, No.2, pp.59-62.

User-Centered Design of K-D2PLANNER® Crane Construction Planning Support Software

Masanori OKAMOTO*1 · Satoshi OKADA*2 · Nobuhiro TAKAMATSU*1 · Hiroo TATAKAWA*1

*1 Business Development Department, KOBELCO CONSTRUCTION MACHINERY CO., LTD.
*2 Business Development Department, KOBELCO CONSTRUCTION MACHINERY CO., LTD. (currently Advanced Technology Engineering Department, Product Development Engineering Division, KOBELCO CONSTRUCTION MACHINERY CO., LTD.)

Abstract

In April 2023, the Ministry of Land, Infrastructure, Transport and Tourism announced its guidelines for the application of Building Information Modeling (BIM). In response, general contractors and others are accelerating their efforts to connect all the processes of design, construction, and maintenance to improve efficiency. Based on user feedback, Kobelco Construction Machinery has developed K-D2PLANNER®, software to support crane- construction planning, focusing on connecting the design and construction processes and aiming to solve the challenges of that process. The expected results include preventing interference between cranes and structures during the construction process, confirming the required crane capacity and ground pressure, and commonizing construction procedures to prevent the need for reworking at the site, as well as suppressing construction delays and the incurrence of additional cost. It is also presumed that streamlining model creation can reduce the costs of construction planning, and selecting the optimal crane can reduce execution costs, contributing to increased productivity.

Introduction

In 2019, the Ministry of Land, Infrastructure, Transport and Tourism established the BIM/CIM Promotion Committee to promote the use of BIM (building information modeling) in construction. The agency has also released guidelines for the use of BIM in all mid-scale and larger public-sector projects, effective April 2023. Although BIM is seeing increasing use in the construction sector, it remains underutilized in the crane construction planning process for steel structures. General contractors and others have established specialized departments to promote the use of BIM, connecting all processes of design, construction, and maintenance, and are accelerating efforts to make these processes more efficient.

Kobelco Construction Machinery developed the crane construction planning support software K-D2PLANNER® Note 1) with a focus on construction planning for crane-built steel structures. This software connects the design and construction processes and helps manage and solve challenges throughout the construction planning process. This paper introduces the functions of this software and describes how it supports construction planning.

Note 1) K-D2PLANNER® is a trademark of Kobelco Construction Machinery.

1. Challenges in crane construction[1)]

Among general architectural design firms, the rate of BIM application is about 80% in the design process and about 50% in the construction process. However, the use of BIM in construction planning, connecting the design and construction processes, has not progressed. The following are detailed challenges in construction planning for crane-built steel structures that can be addressed using BIM.

1.1 Site reworking

Certain issues could arise during construction that necessitate a major procedural revision and scheduling delay alongside site reworking. For instance, it could be discovered during site work that the crane boom or superstructure will interfere with part of the steel structure already built, necessitating temporary removal of structural members.

As another example, if the bearing capacity of the soil under a crane is inadequate, construction must stop for the installation of steel plates or other reinforcement. These reworking processes delay construction and result in additional costs.

1.2 Construction planning efficiency

Document preparation is a particularly time-consuming element of the construction planning process, such as in the creation of execution drawings as well as construction work plans as required by Article 88 of the Japanese Industrial Safety and Health Act.

Construction work plans require crane construction plans. To compile such documentation, experienced, knowledgeable professionals must spend considerable time referencing cross-sectional views and capacity figures to provide crane specifications and capacities.

On-site construction review meetings serve as a forum to discuss construction procedures and important agenda items. However, a great deal of explanation is required when only two-dimensional drawings are available to supplement the conversation, which can ultimately still result in misunderstandings.

1.3 Challenges to implementing BIM in construction planning

Using BIM in the construction planning process can reduce the reworking needs described previously. However, while architectural CAD is specifically intended to improve the design process of steel structures, it is not necessarily easy to use for crane construction planning. To use architectural CAD in the construction planning process, the planner must have experience and expertise not only in architectural CAD, construction planning, and construction, but also in crane operation and application (e.g., crane specifications and capacities).

Cultivating the requisite training and development in all areas necessary to use BIM in the construction planning process demands extensive time.

2. Overview of K-D2PLANNER®

K-D2PLANNER®, an add-in for the 3D architectural CAD program Autodesk Revit (trademark Autodesk), supports crane construction planning. The program's BIM models include 3D crane data, crane specifications and capacities, and functions to improve the efficiency of construction planning using cranes.

The sections below describe the software's main features and functions.

2.1 Intuitive operation

3D construction plans are used in the construction planning process for buildings.

They contain information related to the building structure, heavy machinery such as cranes, requisite crane capacities, building material weights, and more.

When using Revit to create 3D crane construction plans, it is usually necessary to change each individual parameter of the crane BIM model in **Fig. 1** and adjust the crane's posture based on the material being lifted. The suitability of the posture must be verified each time, which is a complex task.

When using K-D2PLANNER® in Revit, simply clicking the material to be lifted automatically

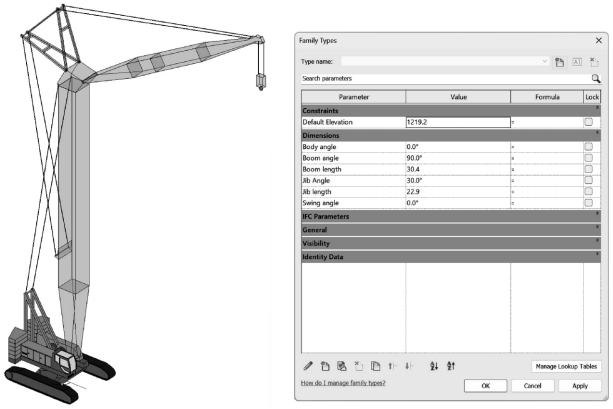

Fig. 1 Crane BIM model

changes the crane posture. The hook position is then determined with the wire rope sling at the recommended angle of 60° based on the shape of the material. The program indicates the distance from the top of the material to the hook as the interference area (**Fig. 2**).

This function makes it possible to visually confirm whether materials will contact structures during lifting operations (**Fig. 3**).

The interference area can also be expressed as a cylinder whose radius is the distance from the material's center point to its furthest edge in plan view (**Fig. 4**). This representation makes it possible to determine whether the material will contact another object if it rotates while suspended.

The working radius, maximum working radius, and minimum working radius (circles and cylinder in **Fig. 5**) can be displayed for a given crane posture. The tail swing radius (circle and cylinder in **Fig. 6**) can also be displayed, making it possible to check for interference when the crane enters a structure and is used in construction operations.

Further, the user interface has icons for the different functions and key numerical values accompanied by a representative image of a crane. In this way, users can operate the architectural CAD program intuitively even if they are unfamiliar with the names of crane parts (**Fig. 7**).

2.2 Simulation

To ensure safe crane operations, construction planners check the load factor and ground pressure of the cranes and determine whether there could be interference between cranes and structures. The load factor indicates how much load the crane can handle. Lifting a load that exceeds the load factor could result in an accident, such as the crane tipping. Ground pressure indicates the pressure exerted by the crane on the ground. Excessive ground pressure could cause ground subsidence, followed by the

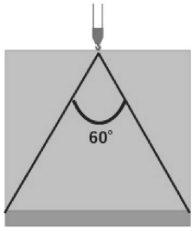

Fig. 2 Area of wire

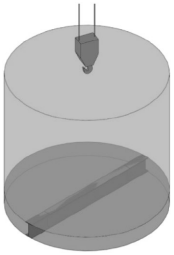

Fig. 4 Cylinder expression

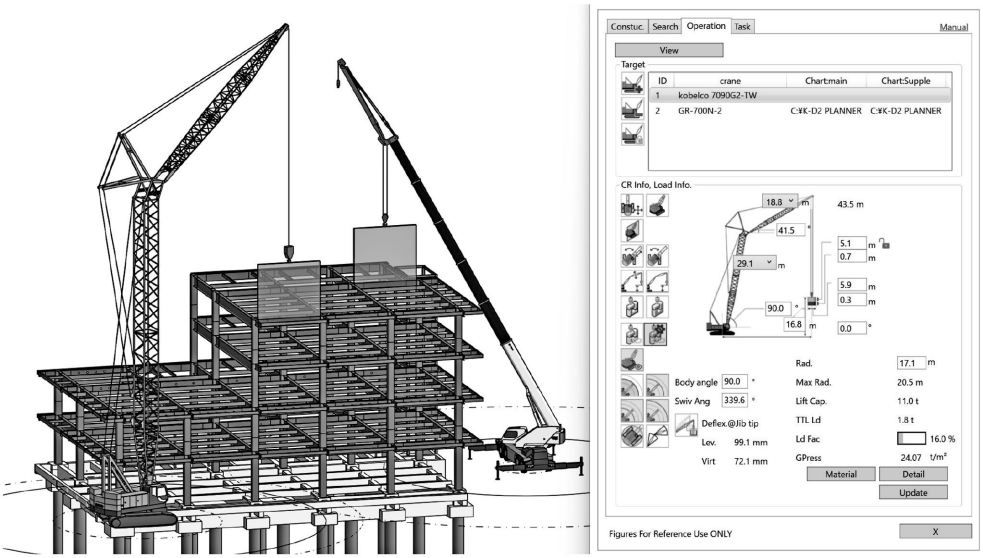

Fig. 3 Lifting image on K-D2PLANNER®

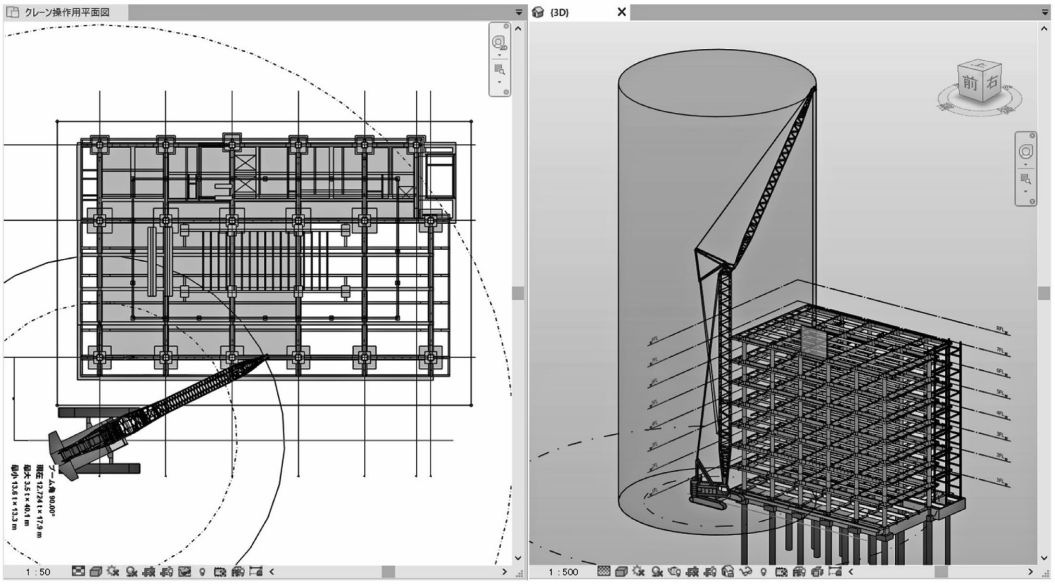

Fig. 5 Maximum or minimum working radius

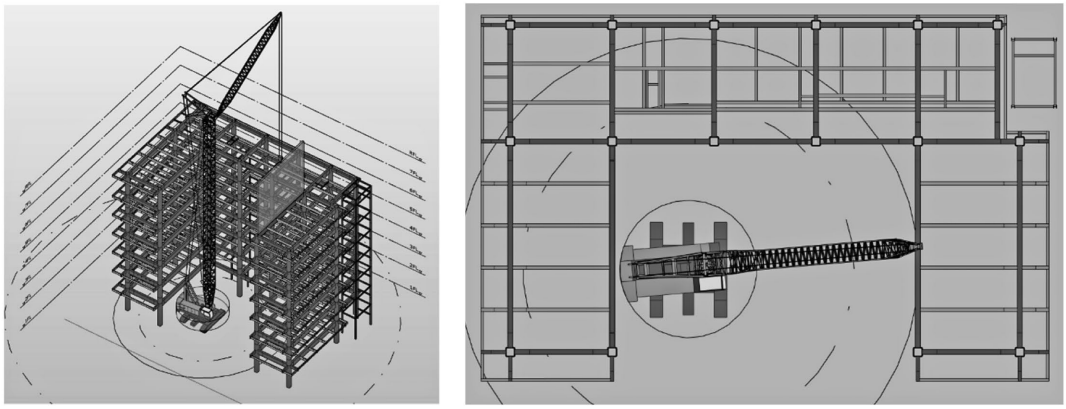

Fig. 6 Turning area view

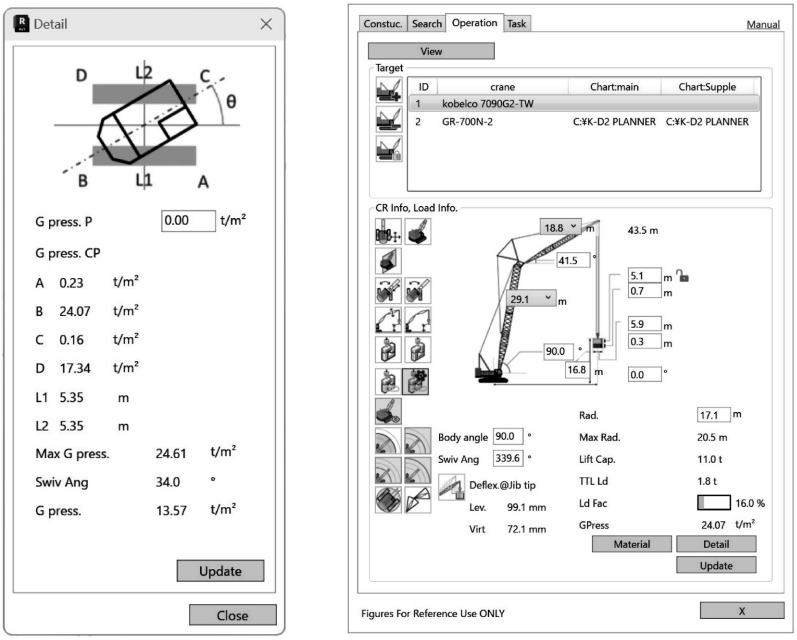

Fig. 7 User interface

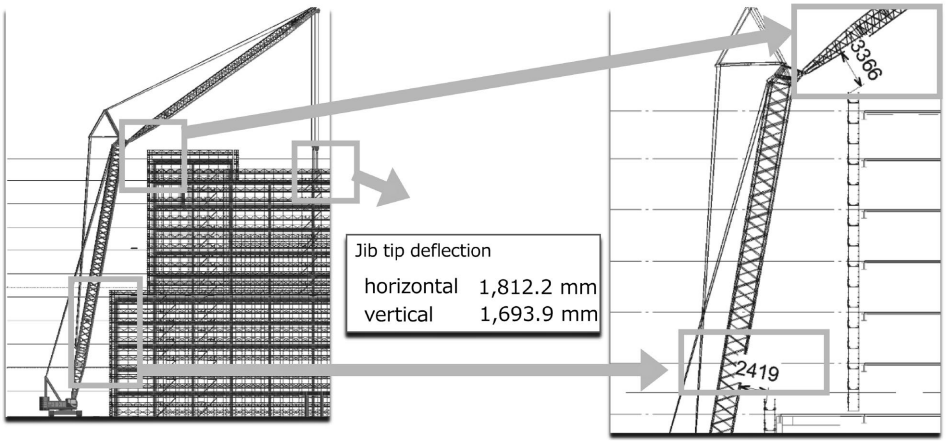

Fig. 8 Interference check with deflection

crane tipping.

K-D2PLANNER® automatically calculates and displays the load factor and ground pressure when the user simply selects the material to be checked in the BIM model of the steel frame. This makes it easy to evaluate the feasibility of parameters during construction planning through iterations of trial and error based on differing conditions such as crane type and specifications, target materials, and lifting conditions. The program can also be used to calculate the required ground reinforcement and steel plate thickness at the crane's operating location, substantially reducing time and improving accuracy in construction planning in comparison with capacity charts or 2D CAD.

Recent years have seen an increase in the use of precast concrete materials as well as the use of heavier materials. These factors are significant because crane boom deflection is based on the weight of the material being lifted. If the crane boom will be near the building, yet boom deflection is not considered during planning, the boom could contact the structure during operations.

K-D2PLANNER® can visually display crane deflection based on the load to be lifted. **Fig. 8** shows an example of a simulation that accounts for deflection. The jib tip deflection is 1812.2 mm in the horizontal direction and 1693.9 mm in the vertical direction, yielding approach distances of 2419 mm between the boom and the structure and 3366 mm between the jib and the structure. In this way, it is possible to check interferences and separation distances between temporary scaffolding and the crane boom in a way that accounts for deflection and

does not rely on expert knowledge.

Tracking the details of each step of the construction process chronologically also provides key verification capabilities. For instance, it is possible to visually check whether there is interference between the steel structure and the crane boom or superstructure as the building structure is assembled.

2.3 Preparing construction drawings

Construction drawings contain key information such as boom length, working radius, and the location of the crane in relation to the structure. These drawings facilitate team communication to ensure smooth, error-free construction. With K-D2PLANNER®, the user can create an automatically generated cross-section along the length of the boom by simply selecting the material to be lifted and clicking the icon to create a cross-sectional view. In addition, a crane operating range diagram can be superimposed, which is useful when drafting construction work plans as required by Article 88 of the Japanese Industrial Safety and Health Act (**Fig. 9**).

2.4 Compatibility with numerous cranes

K-D2PLANNER® comes pre-registered with BIM models of Kobelco Construction Machinery's main crawler cranes (50 to 500t class) (**Fig.10**) for loading into this CAD software. The pre-registered crane BIM models have capacity information, enabling operators to simply view the results of load factor calculations.

The full selection of pre-registered crane BIM models satisfies the needs of many construction sites in Japan. These models include rough terrain cranes and all terrain cranes manufactured by Tadano Ltd. (13 to 700t class) and KATO WORKS CO., LTD. (13 to 400t class) as well as crawler cranes manufactured by Sumitomo Heavy Industries Construction Cranes Co., Ltd. (55 to 500t class) (**Fig.11**).

Other cranes, such as tower cranes, must also be accounted for in construction planning. With some processing, it is possible to import crane BIM models prepared by construction machinery manufacturers under the initiative of the Japan Federation of Construction Contractors and by general contractors and other companies that provide construction planning services. Ground pressure and deflection

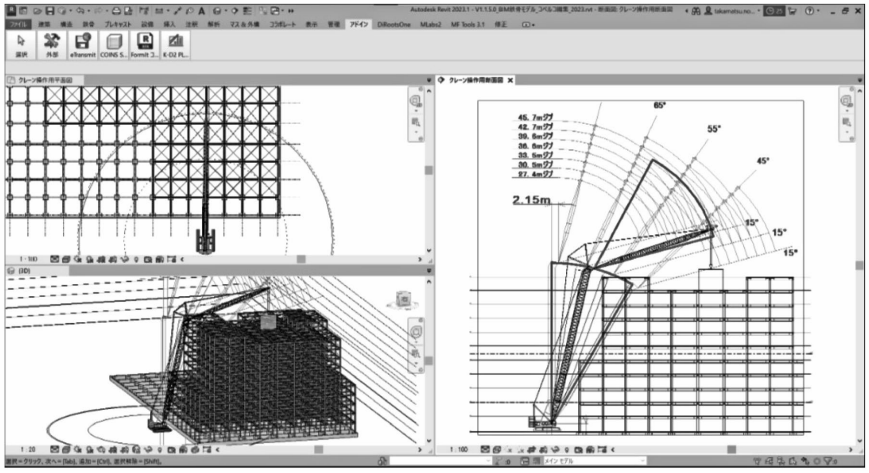

Fig. 9 Crane operating range on cross-section view

Fig.10 KOBELCO models

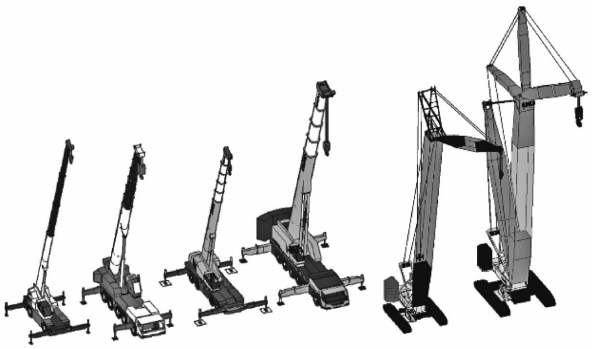

Fig.11 Other models

can only be automatically calculated for Kobelco Construction Machinery's crane BIM models, though.

2.5 Crane selection support

If the capacity of a crane is insufficient during construction, it must be swapped out, extending the construction timeline. Conversely, if the capacity of a crane is too high, this increases the cost of construction. As such, selecting cranes appropriately is important.

After the user enters the crane location and the material to be lifted in Revit, the system determines the material's position to enable searching for appropriate cranes and specifications. It is also possible to stipulate multiple conditions for the search. **Fig.12** shows such an example, in which the crane can be selected from three models (200t old model, 200t latest model, and 350t model) based on load factor and whether there is interference between the crane and the structure. This functionality supports the selection of the optimal class of crane, minimizing the footprint required for equipment and for dismantling and construction, and thereby minimizing construction costs.

2.6 Use in presentations

K-D2PLANNER® can register 3D construction plans as four-dimensional information by adding data arranged chronologically by construction step, enabling on-demand visualization of the results of construction plan reviews. In the project shown in **Fig.13**, space constraints prevent the positioning of cranes around the building, so the proposed procedure is to construct the building from the interior at the rear, working in the forward direction. In such a situation, it is beneficial to present a visual representation of the construction procedure at construction planning meetings. Such images make it possible to efficiently share information regarding the layout and construction plan, which prevents reworking due to misunderstandings. In addition, the construction procedure can be output to Navisworks, an Autodesk viewer program. This program makes it possible to view the entire project using Autodesk's architectural 3D CAD, facilitating the sharing of construction plans based on four-dimensional information at the construction site.

3. Effectiveness in construction planning

General contractors and similar parties using K-D2PLANNER® in the crane construction planning process reported the benefits below.

- Benefit 1: A model of the crane itself is necessary for crane construction planning using 3D CAD. This requires the services of a specialist, and the cost of creating a model is approximately 1500

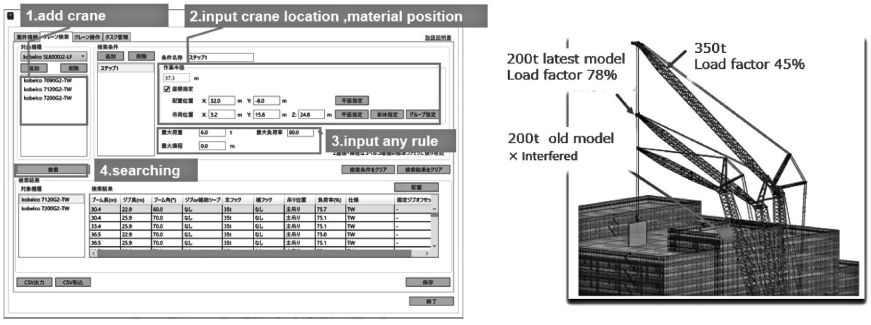

Fig.12 Crane search interface and result

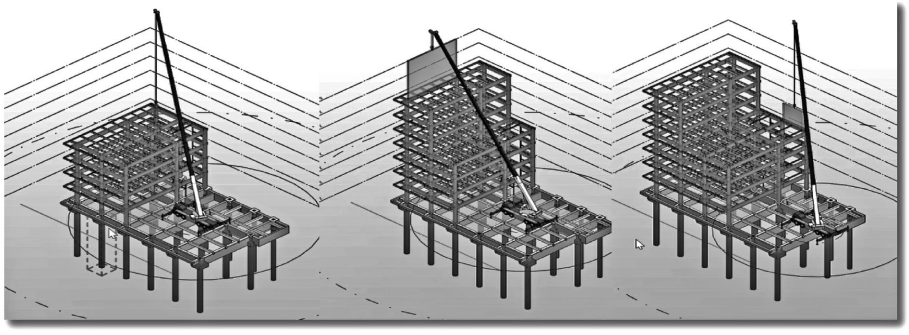

Fig.13 Construction procedure

USD per model. Maintenance is also required for new and discontinued models. However, K-D2PLANNER® contains models sold by major Japanese construction equipment manufacturers such as Kobelco Construction Machinery, Tadano Ltd., Sumitomo Heavy Industries Construction Cranes Co., Ltd., and KATO WORKS CO., LTD. With a total of 57 models, this software eliminates about 11.4 million JPY (80,000 USD) in model creation and maintenance costs (**Fig.14**).

- Benefit 2: By selecting optimally sized cranes using K-D2PLANNER®, rental fees for mobile cranes plus operator can be reduced from, for example, about 2.4 million JPY (17,000 USD)/unit/month for a 120t crane to about 2 million JPY (14,000 USD)/unit/month for a 90t crane, based on the February 2023 issue of construction material pricing report published by the Construction Research Institute. For a site that is active for 10 months, the total savings amounts to 4 million JPY (28,000 USD) (**Fig.15**).
- Benefit 3: K-D2PLANNER® eliminates modeling time and reduces construction review time by 40%, resulting in a 66% reduction in construction planning time (**Fig.16**).

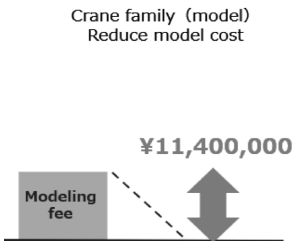

Fig.14 Benefit 1

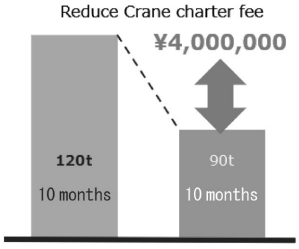

Fig.15 Benefit 2

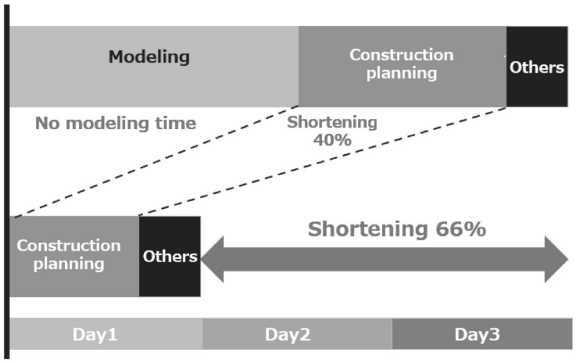

Fig.16 Benefit 3

A further benefit is the ability to verify the quality of the construction plan without relying on the expertise of the construction planner. As such, the quality of the construction plan and the construction project itself improve, and costs are reduced by preventing reworking.

In addition, the use of add-in software such as K-D2PLANNER® facilitates the use of BIM construction planning. General contractors and adjacent professionals anticipate that this will promote the use of BIM by eliminating barriers to incorporating BIM into the construction planning process.

Conclusions

The future of building construction will change drastically through the use of BIM for everything from design and construction to maintenance and management. K-D2PLANNER® is an intuitive program that unites design and construction in crane construction planning using architectural CAD by providing easy access to all information needed in a way that does not necessitate extensive expertise. We have incorporated numerous functions into the program in response to feedback from our wide range of users, from general contractors to plant and bridge engineering companies. We are developing new functionalities based on the further requests of our users and anticipate that additional needs will surface as the number of users increases. Our continuous improvements, added functionalities, and establishment of and research into standards for effectiveness will further promote BIM utilization in construction work.

References

1) Japan Construction Machinery and Construction Association. Construction Machinery and Construction 2023, Vol.75, No.1, pp.41-44.

Construction of MBD Models from xEV Vehicle Disassembly Benchmark Data and their Engineering Utilization

Hiroshi SHIMIZU*1 · Dr. Kenichi ISHIHARA*1 · Motohiro ITADANI · Akira NAKAYAMA*1
*1 Computational Science Center, Technology Unit, KOBELCO RESEARCH INSTITUTE, INC.

Abstract

Many automakers are focusing on developing electric vehicles (EVs). In this effort, benchmarking research, which focuses on the automobiles of competitors and leading companies, is an important process for understanding the latest technology and market trends. Utilizing computer-aided engineering (CAE) in benchmark research allows for various investigations without compromising the research subject. An exemplary CAE model has been created from 3D-shape measurement data of an EV battery pack to perform several evaluations (e.g., impact crushing, thermal runaway, and durability.) The durability issue, herein identified, has been addressed by improving the cross-sectional shape of the components on the basis of the results of topology optimization. As a result, both durability and impact safety have been enhanced.

Introduction

With automakers' focus on developing electric vehicles (EVs), benchmarking research centering around the automobiles of competitors and leading companies reveals our own products' advantages and opportunities for improvement in comparison with others on the market. Ultimately, this information helps us improve our competitiveness. This research is key to understanding other companies' latest technologies and products and to developing products that are in line with market trends and customer requirements.

One challenge, though, is that destructive testing processes (e.g., durability and crush testing) limit the number of devices under test because of high procurement costs. However, by using computer aided engineering (CAE) for reverse engineering, it is possible to run multiple tests without causing wear to parts.

In 2021, Kobelco Research Institute, Inc. began conducting disassembly benchmarking research into the latest EV vehicles made outside Japan. Data on performance, structural, and physical properties for each of the vehicles' components are compiled into reports available for commercial purchase. As part of the process, we create model-based development (MBD) models, CAD models, and finite element analysis (FEA) data based on the research data. This paper describes how 3D models based on disassembly benchmarking data for battery packs can be used in engineering design. Use cases covered include the durability evaluation of battery packs, collision safety, and thermal runaway evaluation, and topology optimization of the internal structure of battery cases.

1. Battery pack modeling

3D data of component geometry (CAD data) is needed to create the numerical analysis model of a battery pack for collision safety evaluation. We used a handheld non-contact scanner (accuracy up to 0.050 mm) to measure geometry while disassembling the battery pack of an EV produced by a non-Japanese manufacturer. We used these data to model the surface for the CAD model. **Fig. 1** shows the actual battery packs, their scanned shapes, and the surfaced CAD data. The scope of the CAD data was limited to structural components that contribute to collision safety performance. We used the CAD

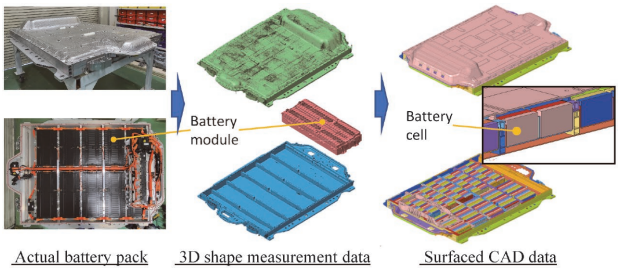

Fig. 1 Creating CAD data for the actual battery pack

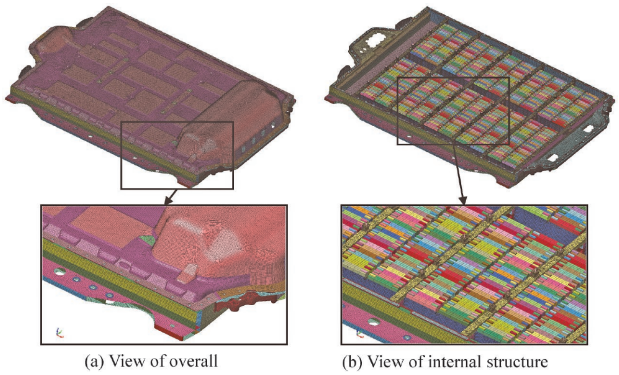

Fig. 2 Mesh model for the numerical simulation

data to create a mesh model for CAE, as shown in **Fig. 2**, and performed numerical analysis to evaluate safety and durability. The model comprised about 1.3 million nodes and 1.5 million elements.

2. Durability evaluation via CAE

ISO 12405 specifies standard tests for the durability evaluation of battery packs.[1), 2)] One of the reliability tests in this standard is a vibration test, which determines whether battery damage or faulty electrical contact could result from random oscillations caused by vehicle travel or drivetrain vibration. **Fig. 3** shows a power spectral density (PSD) chart per ISO 12405. Although the ISO 12405 vibration test method is based on vibration data from driving in Germany, it has been validated as applicable to road conditions in Japan.[3)] Alternatively, random response analysis is an efficient and relatively quick method for running simulated testing for vibration caused by random waves.[4)] We used this method for the durability evaluation of battery packs because of its reasonable computational cost and applicability to design. MSC Nastran, a multidisciplinary vibration and structural analysis program, was used as the analysis solver. **Fig. 4** shows the analysis conditions for random response analysis. Since the battery pack is bolted to the side sill and floor, this is the transmission path for vibration. Therefore, the bolted joints were rigidly coupled with rigid 1D elements, and all bolted joints were vibrated simultaneously. Fig. 3 shows the PSD results upon simultaneous excitation in the three axes of front-back, side-to-side, and up-down. **Fig. 5** shows the stress RMS (root mean square) contour plot from the random response analysis. Stress RMS indicates the average variation in stress in terms of a random response and is an index for statistically evaluating a structure's response to random load.[5)]

Results show that the stress is at its maximum at the bolted joint, with a stress RMS of 133 MPa. This exceeds the fatigue strength σ_w (10^7 cycles) of extruded 6N01-T5, which is 108 MPa[6)]. There is a distinct peak in stress PSD at 43 Hz. Stress PSD is an index for the power distribution of random stress acting on a structure for a given frequency.[7)] Specifically, it represents the spectral density obtained by Fourier transformation of the time-history data of stress. **Fig. 6** shows the results of natural vibration analysis performed to determine the vibration mode of 43 Hz. The first-order vibration mode of the battery pack occurs at 43 Hz, coinciding with the frequency of the peak stress PSD.

Although this vibration mode causes bending

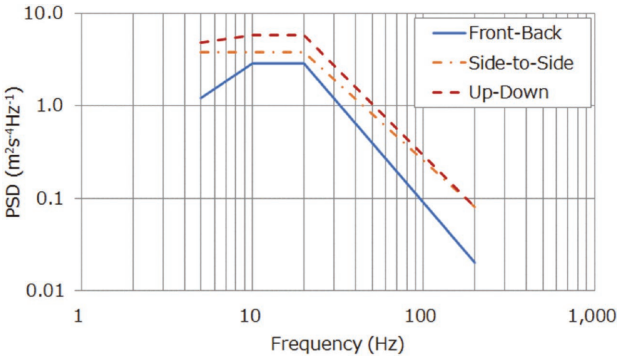

Fig. 3 PSD on 3 axes with ISO 12405

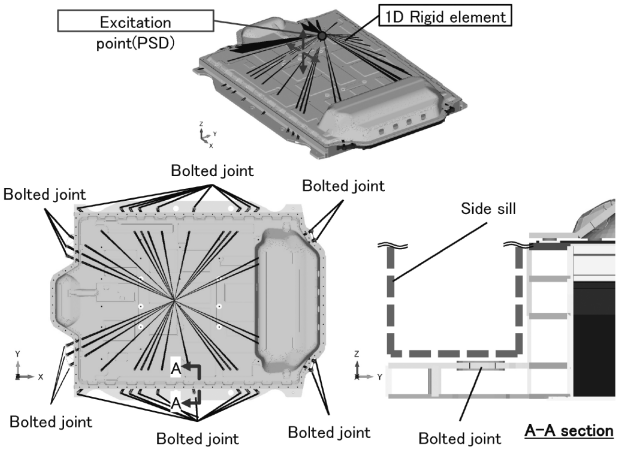

Fig. 4 Analysis conditions for random response analysis

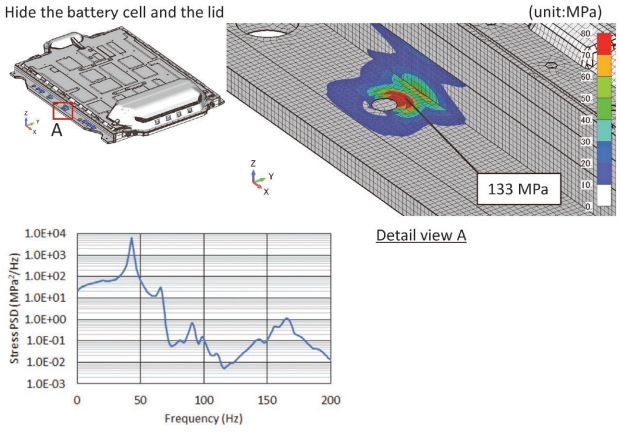

Fig. 5 Stress RMS value contour for random response analysis

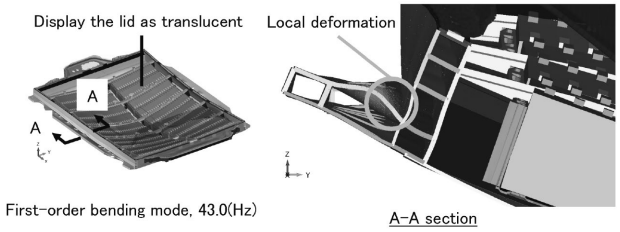

Fig. 6 Natural vibration modes of first-order bending

deformation throughout the entire battery pack, the degree of local deformation is particularly high near the bolted joints. As such, increasing surface rigidity at the bolted joints should be an efficient way to reduce stress.

3. Using CAE for collision safety evaluation

Standards for vehicle collision safety evaluation vary by country and region. Collision safety minimizes harm to pedestrians and vehicle occupants in the event of an automobile accident. Impact tests are typically performed for three main directions: front, side, and rear. However, with EVs, there is a risk of fire due to thermal runaway of the lithium-ion battery, meaning it is vital to account for the collision safety of the battery pack itself. This led us to use numerical analysis to validate the collision deformation performance, specifically of the battery pack. We used the side impact test to validate performance, as this is the direction in which collision deformation is most likely to be transmitted to the battery pack. **Fig. 7** shows the impact conditions simulating the impact of a pole on the side of the battery pack.

Although the original intention behind collision safety applies to the frame, we analyzed the collision phenomena of the battery pack in isolation to understand this component's design in terms of collision resistance. In this study, we evaluated whether safety is maintained upon absorbing the kinetic energy generated by the mass of the battery pack.

Impact speeds were 32 km/h as referred to in UN Regulation (UN-R135), "pole side-impact protection," and approximately twice this value as an excessive condition, at 60 km/h. We used the multidisciplinary program Ansys LS-DYNA (hereafter, LS-DYNA) as the analysis solver.

Fig. 8 shows the deformation condition of the battery pack at an impact speed of 32 km/h. The side frame of the battery pack curves toward the interior at the pole's area of impact. Deformation is confined to the area between the side frame and the battery module and does not affect the battery module. This result indicates that this location was intended as a crumple zone to ensure safety by preventing frame deformation from reaching the battery cells upon side impact.

Next, we tested the impact conditions beyond those stipulated by UN-R135. **Fig. 9** shows the deformation condition of the battery pack at an impact speed of 60 km/h. In a 60-km/h impact, deformation of the side frame reaches the battery module, compressing cells at the edge. Therefore, the crumple zone does not fully absorb the deformation.

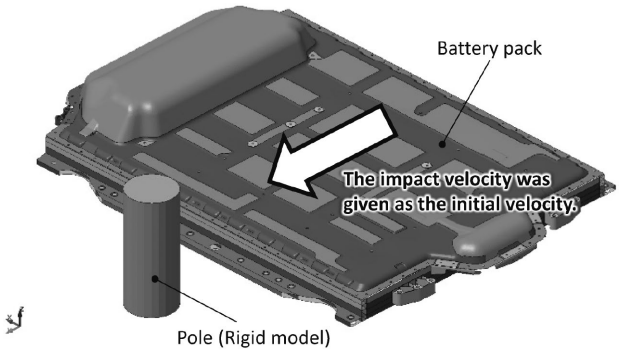

Fig. 7 Battery pack side impact conditions

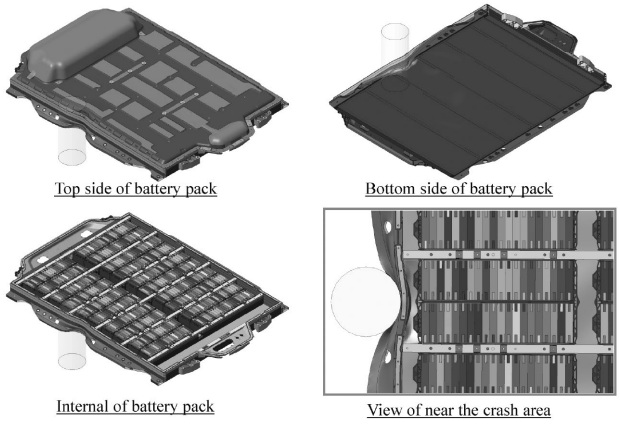

Fig. 8 The deformation condition at an impact speed of 32 km/h

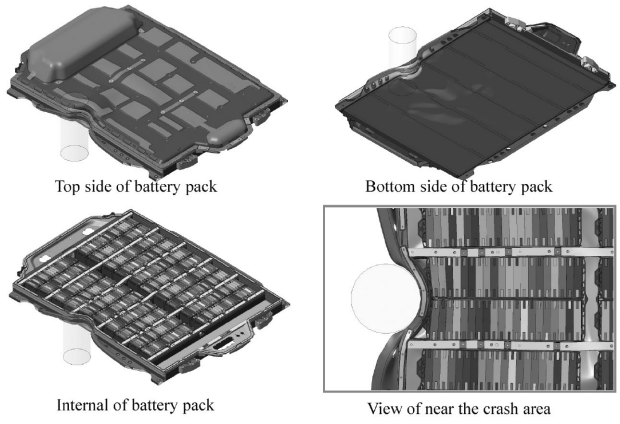

Fig. 9 The deformation condition at an impact speed of 60 km/h

The kinetic energy of a 60 km/h impact is approximately four times that of a 32 km/h impact. The resulting compression could cause a short circuit in the battery cells, resulting in thermal runaway. This battery pack has spaces between each module in the center of the pack, similar to the spaces on the sides, distributed in the side-to-side direction of the frame. Therefore, the design appears to be such that deformation that reaches a module from

the side is absorbed by the rigid body movement of the module itself (sliding movement - Fig. 9, lower right), reducing load on the cells.

4. Evaluating thermal runaway due to short circuiting via CAE

We used LS-DYNA's coupled solver for structure, heat transfer, and electromagnetic (EM) analysis to simulate thermal runaway caused by a short circuit. A short circuit occurs in the battery when the cathode and anode come in direct contact with each other following impact or insulation damage. This causes a sharp rise in current flow inside the battery and therefore an increase in temperature. Thermal runaway is a phenomenon in which the temperature inside the battery rises rapidly and uncontrollably. It can be caused by overcharging, an internal short circuit, or excessive external heat. As thermal runaway progresses, the stored energy is released all at once, causing the battery to overheat, which can lead to a fire or explosion.

Conventional simulations for evaluating battery performance and safety require detailed modeling of each layer of the cell; analyzing such large models is costly. However, there is a method that uses what is called the Battery Macro model (BatMac model[8]). This model represents battery cells with very few meshes, which is beneficial when analyzing many cells or the entire battery. In the BatMac model, a Randles-type equivalent circuit[9] (**Fig.10**) is accounted for at each node. We used the BatMac model because it can efficiently represent phenomena such as internal short circuits and thermal runaway.

As explained, short circuits and thermal runaway are complex phenomena caused by reactions in a cell. Because heat transfer/EM analysis takes longer than a general quick impact analysis, running a series of coupled analyses is costly. Therefore, for this simulation, we set the deformation and strain conditions from the impact analysis as the initial conditions for the heat transfer/EM analysis. Further, we modeled the short circuit based on the initial strain distribution, and the thermal runaway based on the temperature change after the short circuit. In this way, we were able to run the simulation in a practical time frame.

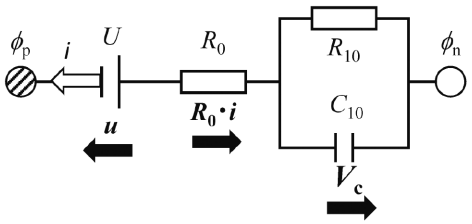

Fig.10 Randles-type equivalent circuit

4.1 Analyzing individual cells

We simulated thermal runaway due to short circuiting in an individual cell using the BatMac model. We applied the same mechanical properties as in the impact analysis and used typical physical property values for each component for the heat transfer and electrical properties. Measured values were used for the cell capacity (57 Ah) and the relationship between voltage and State of charge (hereafter, SOC) (**Fig.11**). The parameters of the Randles-type equivalent circuit were established as $R_0 = R_{10} = 0.001$ and $C_{10} = 1000$ based on charge/discharge curves. As it is not possible to confirm the exact short circuit threshold via testing or other methods, this was assumed to be 10% of the strain of the cell, based on the strain distribution from the impact analysis. We assumed a threshold value of 200℃ for thermal runaway based on the temperature at which a typical lithium-ion battery experiences thermal runaway[10].

Fig.12 shows the initial strain distribution and Joule heat distribution. The figures show that in the region where strain exceeds 10%, short circuiting occurs, causing high current to flow throughout the cell. This leads to high Joule heating throughout the entire cell, including in the non-short-circuited region.

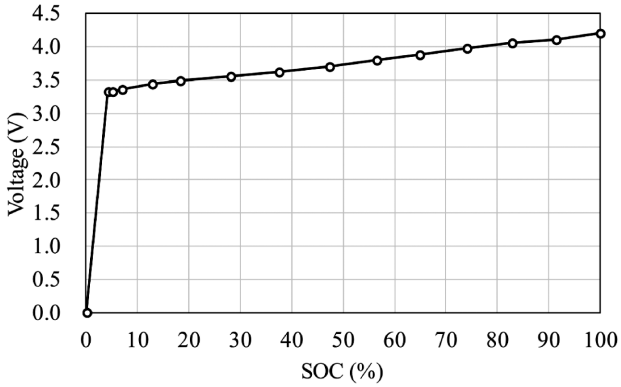

Fig.11 Relationship between voltage and SOC

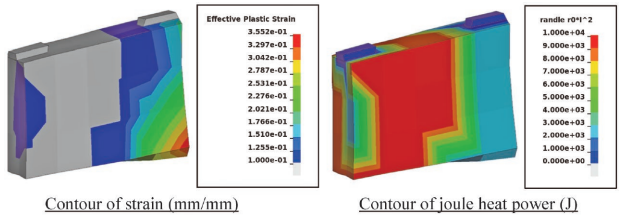

Fig.12 Initial strain distribution and joule heat power distribution of cell

Fig.13 shows the temperature history between the tabs on top of the cell. Deformation causes a short circuit, causing the temperature to rise suddenly, surpassing 200℃ just under 40 seconds later due to thermal runaway. The temperature increase stops after a certain amount of heating, ending the thermal runaway. In this way, it is possible to use the BatMac model to simulate the phenomenon of thermal runaway due to short circuiting.

4.2 Analyzing battery packs

We simulated thermal runaway due to short circuiting based on the analysis results for an impact speed of 60 km/h in Section 3, using the parameters set in Section 4.1 for the battery pack. We considered heat transfer by conduction within the cells and between each component as well as heat transfer by convection with the air around the battery pack.

The initial strain and current distributions in **Fig.14** show that the strain induced by the impact extends to the second cell from the impact zone (②, left side of the figure). Just like in the analysis of an individual cell, this indicates high current flow in the short-circuited region.

Fig.15 shows the temperature history between the top tabs of the representative cells (①, ⑤, ⑩, ⑮, ⑳). The temperature of the first cell from the impact zone (①) increased immediately after the start of the short circuit, and thermal runaway occurred when the temperature exceeded 200℃. The temperature of the fifth cell (⑤, dash-dotted line) started to increase about 120 seconds after the impact and rapidly increased about 150 - 160 seconds after the impact. When thermal runaway due to short circuiting occurred in a cell at the impact zone, the phenomenon cascaded to cells far from the impact zone by thermal conduction. 480 seconds later, the thermal runaway was occurring in an entire module.

Fig.16 shows the temperature distribution for specified elapsed times from the start of the short circuit. 50 seconds after the start of the short circuit, the temperature increased in the first and second cells from the impact zone. 473 seconds after the start of the short circuit, the temperature increase affected nearly the entire module. Since the temperature increased only in one module, it is assumed that the structure of the battery pack studied prevents heat transfer between modules.

As described previously, the BatMac model makes it possible to analyze thermal runaway due to short circuiting for the entire battery pack at a practical cost.

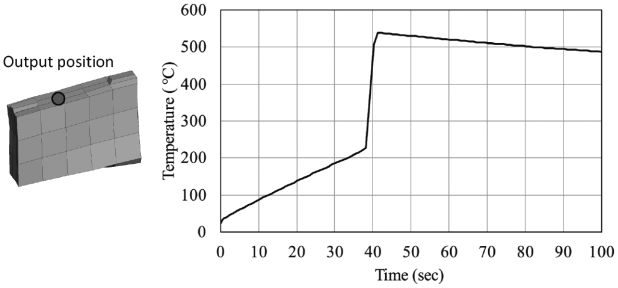

Fig.13 Temperature history between cell top tabs

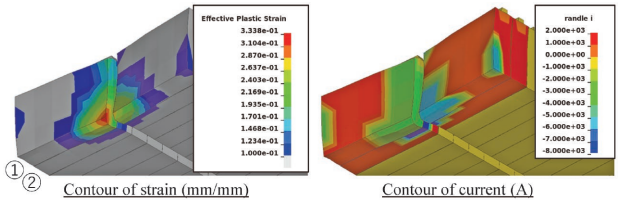

Fig.14 Initial strain distribution and current distribution of module

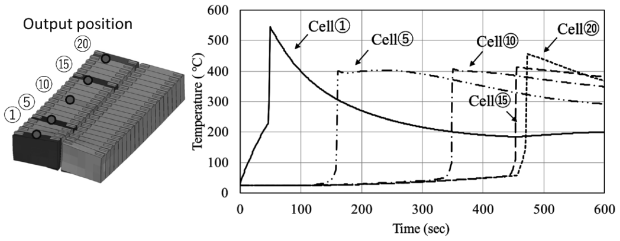

Fig.15 Temperature history between top tabs of representative cells

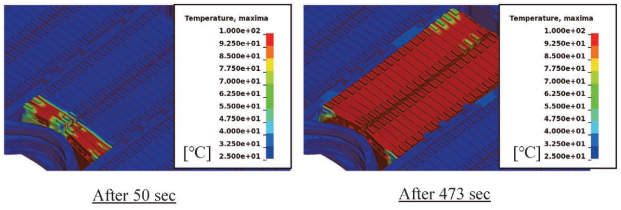

Fig.16 Temperature contour of the module at representative time

5. Optimizing design via CAE

5.1 Optimizing extrusion shape

Section 2 covered the occurrence of stresses exceeding the fatigue strength of constituent materials in the durability evaluation. We performed a topology optimization analysis to investigate countermeasures to these stresses. Topology optimization is a structural optimization method that determines the optimal layout while reducing material from the design region given structural constraints, loads, and restraint conditions. To perform this analysis, we used Altair OptiStruct, a general-purpose solver for optimization analysis.

We focused on the side frames and cross members as optimization regions. These are the main structural members with a major influence on the first-order vibration mode of the battery pack. **Fig.17** shows the substructure model for topology optimization. The analysis model was created by partially extracting the side frame and cross member and applying geometric symmetry to create a 1/4 symmetrical model. **Fig.18** shows the design region (pale blue), boundary conditions, and topology optimization results. The design region is the area inside the external surface of the original structure. The original rib arrangement was maintained, and the minimum remaining plate thickness was set to 1 mm, with exceptions where necessary for functionality. As constraint conditions, the areas near bolted joints were fixed, and a load was applied to the top surface of the cross member to express the first-order bending deformation mode. The constraints for the side frame and cross member were that the mass should be the same or lower and that rigidity should be maximized (deflection of the cross member should be minimized).

Topology optimization indicated that a rib should be added to the side frame to connect the upper and lower plates near the bolted joint, that the bolted joint that was previously only on the top surface should also be incorporated on the bottom surface, and that the two lower ribs of the cross member should be thicker. The structural modification shown in **Fig.19** was made based on these results. After the structural modification, the mass of the battery case increased by only 120 g, which is remarkably close to the mass of the original structure.

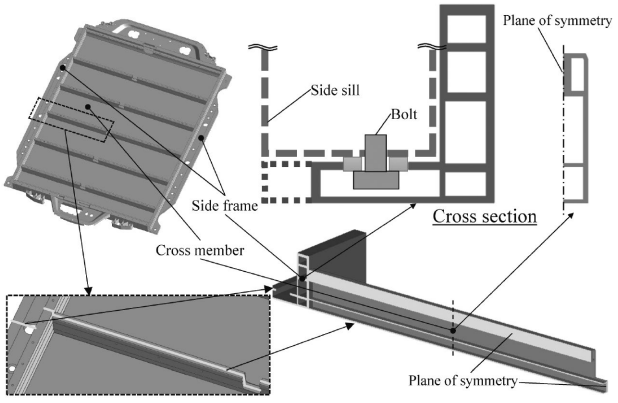

Fig.17 Substructure model for topology optimization

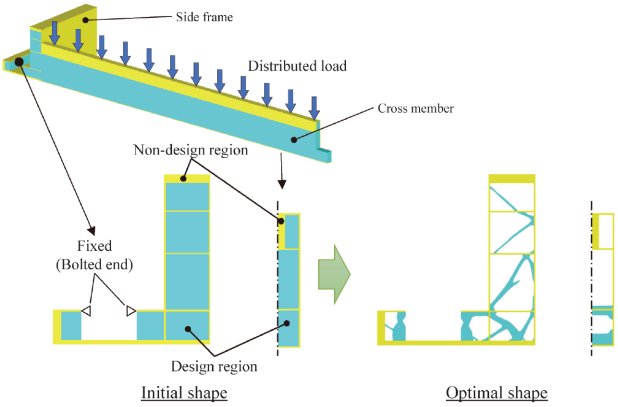

Fig.18 Design region, boundary conditions, and optimization results

5.2 Durability evaluation

Fig.20 shows the results of random response analysis applied to the optimized shape from Section 5.1. The maximum stress RMS at the bolted joint was 87 MPa. This constitutes a 35% reduction from the original shape and is below the fatigue strength σ_w (10^7 cycles) of extruded 6N01-T5, which is 108 MPa[5]. By changing to the optimized shape, the peak stress PSD decreased and shifted to the high-frequency side. **Fig.21** shows the results of natural frequency analysis for the optimized shape. The natural vibration of first-order bending of the battery pack increased by 10%, from 43.0 Hz to 47.3 Hz. The optimized shape suppresses local deformation by the joining of two plates. These results suggest that there are two reasons the optimized shape

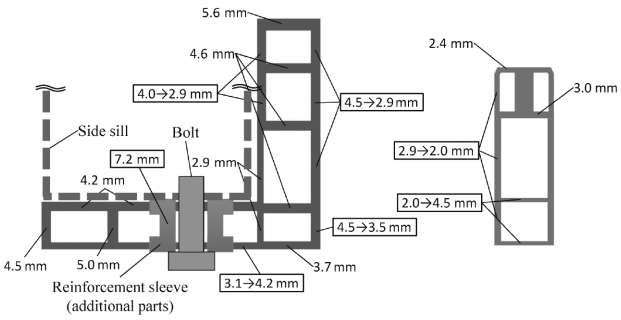

Fig.19 Structural modification proposal based on topology optimization results

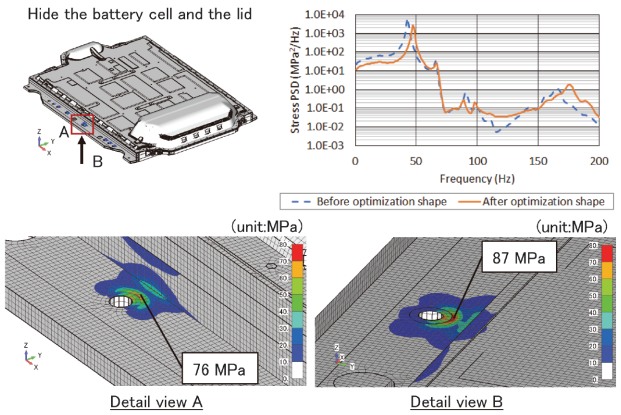

Fig.20 Contour plot of stress RMS values after optimization

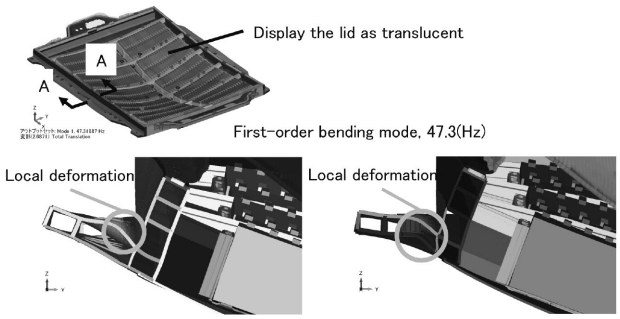

Fig.21 Natural vibration modes of first-order bending after optimization

reduces the stress RMS. The first is the increased rigidity of the bolted surfaces from bolting the two plates together, and the second is the reduced input excitation PSD due to the increase in the natural vibration. Above 20 Hz, PSD decreases as frequency increases (Fig. 3), meaning that as natural frequency increases, input excitation PSD decreases, reducing stress.

This study proves that it is possible to efficiently optimize cross-section geometry in terms of durability without relying on an individual's expertise.

5.3 Collision safety evaluation

Fig.22 shows the results of the same impact analysis as in Section 3 (impact speed 32 km/h) applied to the optimized shape from Section 5.1. Increasing the thickness of the plate under the bolted joint from 3.1 mm to 4.2 mm significantly increased impact absorption capacity and decreased side frame deformation. Therefore, this structural modification improved collision safety.

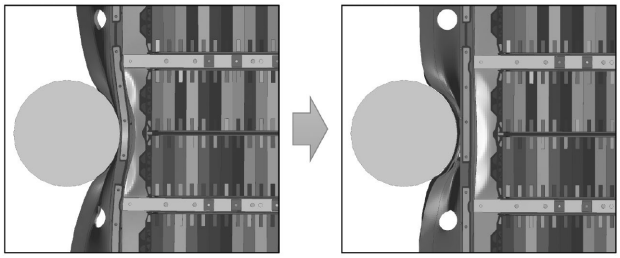

Fig.22 The deformation condition at an impact speed of 32 km/h after optimization

Conclusions

This paper describes engineering design considerations for battery packs in terms of durability evaluation, collision safety evaluation, evaluation of thermal runaway due to short circuiting, and design optimization using CAE. Using CAE in disassembly benchmarking research is very effective for comparing performance with other companies' products and understanding design trends. It enables quick feedback during the design phase and improves efficiency within the development process.

References

1) ISO 12405-1:2011: Electrically propelled road vehicles - Test specification for lithium-ion traction battery packs and systems. Part 1: High-power applications.
2) ISO 12405-2:2012: Electrically propelled road vehicles - Test specification for lithium-ion traction battery packs and systems. Part 2: High-energy applications.
3) K. Maeda et al. Proceedings of the Society of Automotive Engineers of Japan, Inc. 2015, Vol.46, No.1, pp.109-114.
4) M. Itadani et al. Kobelnics. 2023, Vol.31, No.57, pp.23-29.
5) S. Fujita et al. FUJITSU TEN Technical Journal. 2016, Vol.33, No.1, p.45.
6) Japan Aluminum Association. Aluminum Handbook. 7th edition. shoeisha Co. Ltd. 2007, p.57.
7) N. Takeda et al. Journal of the Society of Materials Science, Japan. 2012, Vol.61, No.10, p.853.
8) LST, an Ansys company. LS-DYNA Keyword User's Manual Volume III. Multi-Physics Solvers. LS-DYNA R13.
9) P. L'Eplattenier et al. 12th European LS-DYNA Conference. 2019.
10) T. Mukai et al. Journal of The Surface Finishing Society of Japan. 2019, Vol.70, No.6, pp.301-307.

Soft Magnetic Iron Wire Rod and Sheet: Estimation of Their Benefit for Electromagnetic Components

Yukihiro HISAI*1 · Shinya KAWASHIMA*2 · Dr. Masamichi CHIBA*1 · Kenshi IKEDA*3 · Shinya MORITA*4

*1 Wire Rod & Bar Products Unit, Steel & Aluminum Business
*2 Materials Research Laboratory, Technical Development Group
*3 Wire Rod & Bar Products Unit, Steel & Aluminum Business (currently Wire Rod & Bar Products Development Department, Research & Development Laboratory, Steel & Aluminum Business)
*4 Applied Physics Research Laboratory, Technical Development Group

Abstract

Electrification and decarbonization in the automotive field are raising the demand for higher-performance electromagnetic components. The pure iron-based soft magnetic wire rod (ELCH2 series), which features high magnetic flux density and cold forgeability, is a newly developed material that has contributed to the downsizing of electromagnetic components and energy saving. Furthermore, development is underway on pure iron-based soft magnetic wire rod (ELAC series) with improved responsiveness and alternating current properties to meet diversifying demands. An electromagnetic pure iron steel sheet (KELMOS) is also being developed. This paper introduces the magnetic properties and processability of pure iron-based soft magnetic materials. Also introduced are the results of the magnetic field analysis of electromagnetic relay components, which confirm that the magnetic force and responsiveness have been improved by using pure iron-based soft magnetic material and electromagnetic pure steel sheets instead of typical low-carbon steel in electromagnetic components.

Introduction

Progress in the EV (electric vehicle) sector and the shift toward carbon neutrality in the automotive field have increased the demands placed on automotive electronics.[1)] EVs are complex systems that rely heavily on the performance and specifications of the battery. Alongside the recent industry developments imposing changes regarding EVs, the requirements for electromagnetic components such as motors, solenoids, and relays incorporated in automotive electronics are becoming more varied and sophisticated. Such components must be more responsive for quicker operation, smaller to reduce weight and space, and more efficient to reduce load on the battery. In addition, inverters increase the number of components subjected to superimposed AC magnetic fields, and eddy current losses must be minimized. Low-carbon steel with a carbon content of 0.1% has been widely used for these electromagnetic parts. However, to meet the demands for more advanced components, it is essential to use higher-performing materials.

Kobe Steel's pure iron-based soft magnetic wire rod ELCH2 Note) (extra-low-carbon cold heading wire rod) has excellent magnetic properties and has been used in valve parts (solenoids) of electronic transmission control systems, helping satisfy the need for high-performance electromagnetic parts. Kobe Steel is also pursuing further developments to propose pure iron-based soft magnetic materials suitable for a broad range of needs.

Fig. 1 shows examples of the operating frequency ranges and magnetic flux densities of Kobe Steel's pure iron-based soft magnetic materials.

Our developments beyond the ELCH2 series designed for DC components include the ELAC Note) series, which has added elements to improve responsiveness and suppress eddy current; KELMOS Note), an electromagnetic pure iron steel sheet that builds on expertise gained from ELCH2; and MAGMEL Note), a magnetic iron powder featuring low iron loss and high efficiency that is also suitable for three-dimensional magnetic circuit design. These products constitute a sample of our magnetic material solutions developed in conjunction with magnetic field analysis technology and secondary processing technology. This paper introduces the main characteristics and applications of Kobe Steel's ELCH2 series and ELAC series of pure iron-based soft magnetic wire and KELMOS electromagnetic pure iron steel sheets.

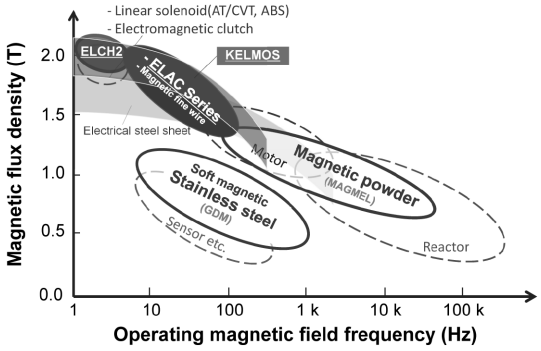

Fig. 1 Examples of operating frequency range and magnetic flux density

Note) ELCH, ELAC, KELMOS, and MAGMEL are trademarks of Kobe Steel (4812504, 6788096, 6668543, 4669506).

1. ELCH2 and ELAC series

1.1 Chemical composition and magnetic properties

Kobe Steel develops advanced steels by designing the chemical composition and material microstructure based on the desired properties. Soft magnetic materials used in electromagnetic components must have high magnetic flux density and low coercive force to ensure sufficient magnetic force and output control. At the same time, high electrical resistivity is desirable in support of time response and AC characteristics. **Table 1** shows the chemical compositions of the ELCH2 series (ELCH2 and ELCH2S), ELAC series (ELAC20 and ELAC30), and S10C, a conventional general-purpose steel. **Table 2** shows the magnetic properties and electrical resistivity of each steel. The ELCH2 series and ELAC series are characterized by their high magnetic flux density and low coercive force. While the ELCH2 series has a particularly high maximum magnetic flux density, the ELAC series exhibits both high magnetic flux density and high electrical resistivity.

We achieved a high saturation magnetic flux density in the ELCH2 series by eliminating factors that adversely affect the magnetic properties of soft magnetic materials. The magnetic properties of soft magnetic materials depend on the material structure and the magnitude of the magnetic moment in the material. The extremely low carbon content of the ELCH2 series yields a single-phase structure of highly pure ferrite, resulting in a high magnetic moment and saturation magnetic flux density (which corresponds to the magnetic force of an electromagnetic component). Additionally, this series has a reduced content of Al and N, which act as pinning sources for grain growth. This decreases the area of the grain boundaries that inhibit domain wall migration. The resulting low coercive force facilitates the control of electrical current.[2)]

The ELAC (ELectromagnetic wire rod for AC application) series has a higher electrical resistivity than the ELCH2 series due to the addition of elements to a degree that preserves the target magnetic properties and forgeability. This suppresses the generation of eddy currents that interfere with the magnetization of materials, improving the time response to changes in the external magnetic field and reducing eddy current loss (power consumption) in AC applications. The ELAC series offers steel materials with different electrical resistivities, such as ELAC20 and ELAC30 (approximate electrical resistivity 20 $\mu\Omega$cm and 30 $\mu\Omega$cm, respectively), making it possible to propose materials based on the characteristics needed. The saturation magnetic flux density of this series is slightly lower than that of the ELCH2 series as a trade-off for the addition of elements. However, as shown in the *B1* column of Table 2, the ELAC series has good magnetic properties in the low magnetic field region, making it suitable for AC applications and components that require a fast response speed.

1.2 Cold forgeability

ELCH2 has high cold forgeability due to the minimized concentration of added elements. Even in the as-rolled state, it has a lower flow stress and

Table 1 Characteristics and example of chemical composition of steels

Characteristic	Steel	Elements (mass%)				
		C	Si	Mn	P	S
Magnetic properties and forgeability	ELCH2	0.005	0.004	0.25	0.009	0.008
Cutting workability	ELCH2S	0.005	0.004	0.26	0.010	0.025
Responsivity and energy efficiency for AC use	ELAC20	0.006	Added a little	0.27	0.005	0.005
	ELAC30	0.008	Added	0.26	0.005	0.005
Conventional steel	S10C	0.08 / 0.13	0.15 / 0.35	0.30 / 0.60	≤ 0.030	≤ 0.035

Table 2 Example of magnetic properties and electrical resistivity of steels

Steel	Magnetic flux density (T)				Coercive force (A/m)	Electrical resistivity (μΩcm)
	B1	*B5*	*B10*	*B50*		
ELCH2	1.35	1.60	1.65	1.90	37	12
ELCH2S	1.33	1.46	1.64	1.89	47	12
ELAC20	1.46	1.57	1.62	1.80	35	22
ELAC30	1.40	1.51	1.55	1.72	31	30
S10C	0.45	1.40	1.54	1.74	86	16

a higher critical upset rate before cracking occurs in comparison with the spheroidized annealed general-purpose carbon steel S10C.[3] **Fig. 2** shows the flow stresses of ELCH2, ELAC20, and ELAC30 as determined by cold upset testing.

Cylindrical specimens of ϕ10 mm × 15 mm were prepared and compressed at a strain rate of 10/s and a compression rate of 60%. ELCH2 has lower flow stress and is superior in terms of tool life. Because the ELAC series has added elements to increase electrical resistivity, it has a higher flow stress than the ELCH2 series; however, at less than 600 MPa, this value is low. Additionally, the cold forgeability of the ELAC series is superior to that of spheroidized annealed S30C and S45C (both at least 600 MPa flow stress).[4] As described above, the ELCH2 and ELAC series have excellent magnetic properties and cold forgeability, enabling reduced manufacturing and component costs through, for example, single-piece forgeability.

On the other hand, high cold forgeability runs counter to high ductility, increasing the likelihood of adhesion to tool edges and increased burr height during cutting. An effective method of improving the machinability of pure iron-based soft magnetic materials is to add sulfur to disperse an appropriate amount of MnS.[5] As such, Kobe Steel developed ELCH2S and ELAC20S for enhanced machinability and can propose materials and solutions that not only account for the required magnetic properties of electromagnetic parts, but also account for the manufacturing process.[6]

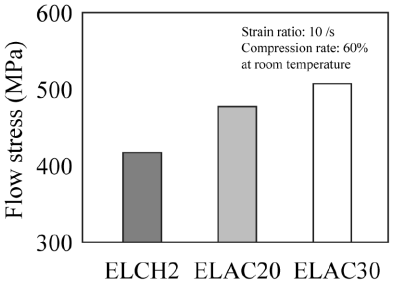

Fig. 2 Flow stress of steels at room temperature

2. KELMOS

2.1 Chemical composition and mechanical properties

By using soft magnetic materials with appropriate component-specific geometries and processing characteristics, it is possible to develop electromagnetic components that meet targets in both magnetic properties and manufacturing cost. As such, Kobe Steel is applying the expertise gained from ELCH2 wire rod to steel sheets in developing KELMOS (Kobe extra-low-carbon electro-magnetic of steel), an electromagnetic pure iron steel sheet with magnetic properties equivalent to those of ELCH2.

Soft magnetic materials must have (1) high saturation magnetic flux density and (2) low coercive force. **Table 3** shows example chemical compositions of KELMOS and conventional mild steel. In line with the ELCH2 series, KELMOS has improved magnetic properties owing to the ultra-low carbon content, which increases the magnetic moment to yield a high saturation magnetic flux density. In addition, this new material has a reduced proportion of Al and N. This composition suppresses the formation of grain boundaries, which inhibit magnetic responsiveness, and the formation of aluminum nitride, which reduces the uniformity of grain growth.[2] As such, this design achieves low coercive force.

With these features, KELMOS will improve control functionality and reduce size, weight, and energy consumption in electromagnetic components.

In addition to its excellent magnetic properties, KELMOS is also characterized by excellent processability. **Table 4** shows examples of the mechanical properties of KELMOS and SPCC, a

Table 3 Example of chemical composition of KELMOS

Steel	Elements (mass%)				
	C	Si	Mn	P	S
KELMOS	≤ 0.02	≤ 0.03	0.20 / 0.30	≤ 0.030	≤ 0.030
JIS SUY-0	≤ 0.030	≤ 0.20	≤ 0.50	≤ 0.030	≤ 0.030

Table 4 Example of mechanical properties of steels

Steel	YS (MPa)	TS (MPa)	Elongation (%)	Hardness (HV)
KELMOS	236	332	44	98
SPCC #1	215	340	42	103
SPCC #2	262	350	41	109

conventional mild steel. SPCC has a wide range of composition specifications, so its mechanical properties can vary. KELMOS has low hardness, high elongation, and excellent processability because the alloying elements and impurities have been reduced to the extent possible, as described above.

2.2 DC magnetic properties

Figs. 3 and **4** show examples of the DC magnetic properties of KELMOS and conventional mild steel. One sheet each (60 mm x 60 mm, 1.0 mm thickness) of the steels tested was annealed for magnetic properties in hydrogen at 850℃ for 3 hours. The initial magnetization curve and hysteresis curve were developed in accordance with JIS C 2556, and the magnetic flux density and coercive force were determined at various specific magnetic field strengths. Fig. 3 shows that KELMOS exhibits a rapid rise in magnetic flux density starting from the low-field strength side and a high saturation magnetic flux density at the high-field strength side.

Fig. 4 shows that only some SPCC materials satisfy the upper limit for coercive force of 60 A/m per JIS SUY-0 (SUY: steel use for yoke) due to compositional variations, analogous to the mechanical properties of these materials. KELMOS, on the other hand, has a sufficiently low coercive force; its magnetic properties meet or surpass the specifications in SUY-0. Therefore, this material will improve the performance of electromagnetic components such as relays and linear solenoids.

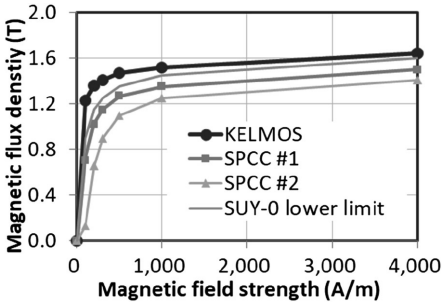

Fig. 3 Example of magnetization curves of steels

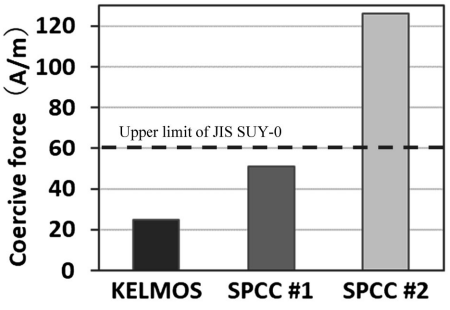

Fig. 4 Example of coercive force of steels

2.3 AC magnetic properties

Fig. 5 shows a sample of the AC magnetic properties of KELMOS. We annealed for magnetic properties 12 samples measuring 30 mm × 300 mm, 0.8 mm thickness in hydrogen at 850℃ for 3 hours. The samples were subjected to testing via an Epstein frame per JIS C 2550, and the iron loss of each magnetic field was evaluated at the frequencies from 50-1,000 Hz shown in Fig. 5. Curve fitting was performed at each frequency using Equation (1) below. **Fig. 6** shows the results converted to indicate the AC magnetic properties for a sheet thickness of 0.5 mm.

$$P=K_h f B_m^{1.6}+K_e \frac{(tfB_m)^2}{\rho} \quad \cdots\cdots (1)$$

Here, f is the frequency, B_m is the maximum magnetic flux density, t is the thickness of the steel sheet, ρ is the electrical resistivity of the magnetic material, and K_h and K_e are proportionality constants. For example, 50A700 per JIS C 2552, a non-oriented magnetic steel sheet, has an iron loss of 7 W/kg (0.5 mm thickness) at 1.5 T and 50 Hz. The iron loss of KELMOS is about 7 W/kg under the same conditions, implying that this material can also be used in low-frequency (50-60 Hz) applications.

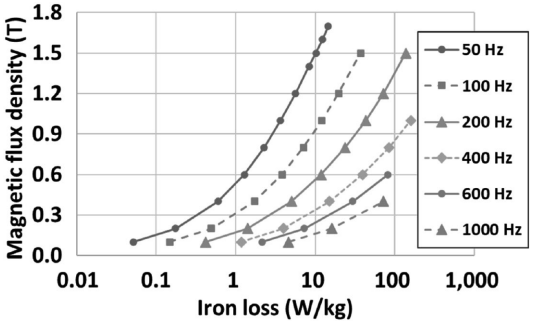

Fig. 5 AC magnetic properties of KELMOS (thickness 0.8 mm)

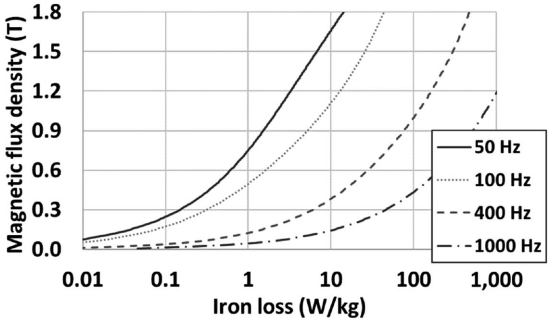

Fig. 6 AC magnetic properties of KELMOS (converted to 0.5 mm thickness)

3. Research into the application in electromagnetic components

We used magnetic field analysis to study the effectiveness and suitability of pure iron-based soft magnetic materials in electromagnetic components. JMAG (Ver. 22.3), made by JSOL Corporation, was used as the electromagnetic field analysis software. **Fig. 7** depicts the model of the relay component used in this study. It is an electromagnetic component consisting of an excitation coil, core, armature, and yoke. A magnetic circuit is formed when an excitation current flows through the coil, generating a magnetic force. For this study, we analyzed and compared the electromagnetic force and response time with S10C, ELCH2, or ELAC20 as the material of the core, and SPCC or KELMOS as the material of the armature and yoke. The number of coil turns was 5,400, and the excitation voltage was 24 VDC. The response time was defined as the time it takes for the angle θ of the armature to move from 5° to 0°. We analyzed the electromagnetic force when the armature was at 0°, that is, when the iron core and armature were in contact and the relay was held, and calculated the maximum torque (corresponding to the magnetic force of the relay components) **Table 5** shows the results of the analysis. When the core material was changed from S10C to ELCH2 (Case 2), the maximum torque increased, reflecting the higher magnetic flux density. Furthermore, when the core material was ELCH2 and the armature and yoke were made of KELMOS (Case 3), this yielded the highest torque, which was 12.4% higher than with general-purpose steel (S10C and SPCC, Case 1). The response times of Cases 2 and 3 were almost the same as Case 1. Although eddy currents hinder magnetization due to low electrical resistance in pure iron-based soft magnetic materials, the high magnetic flux density strongly attracted the armature, which is thought to have a compensatory effect on response time. Thus, ELCH2 is effective in applications in which torque is a priority. The greater capacity to generate a higher torque means that the same torque can be achieved with a lower excitation current. Beneficial results include reductions in power consumption, heat generation, copper usage, and size.

The core made of ELAC20 (Cases 4 and 5) also achieved a higher torque than did the core made of general-purpose steel (Case 1). In addition, the response time was about 2% faster than with S10C and ELCH2 as core materials (Cases 1 to 3). **Fig. 8** shows the eddy current distribution 4 ms after the circuit was energized, with ELCH2 and ELAC20 as core materials (Cases 2 and 4). Because the electrical resistivity of ELAC20 is higher than that of ELCH2, the current density is lower on the surface of the

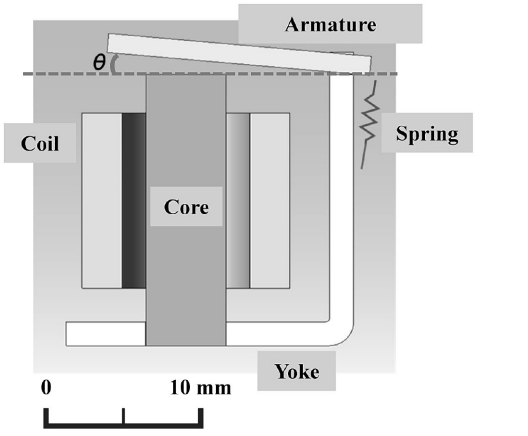

Fig. 7 Calculation model of electromagnetic relay for electromagnetic field analysis

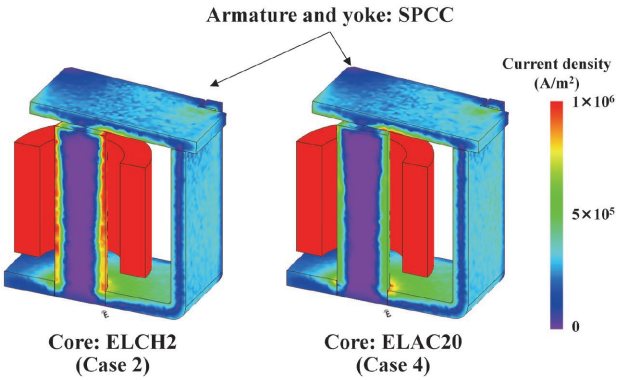

Fig. 8 Eddy current distribution in electromagnetic relays

Table 5 Estimated torque and response time of electromagnetic relay

	Core	Armature	Yoke	Maximum torque (mN·m)	Response time (ms) ON
Case 1	S10C	SPCC	SPCC	90.7	5.094
Case 2	ELCH2	SPCC	SPCC	98.1 (+8.1%)	5.088 (−0.1%)
Case 3	ELCH2	KELMOS	KELMOS	101.9 (+12.4%)	5.088 (−0.1%)
Case 4	ELAC20	SPCC	SPCC	95.8 (+5.6%)	4.998 (−1.9%)
Case 5	ELAC20	KELMOS	KELMOS	99.3 (+9.5%)	5.000 (−1.8%)

ELAC20 core. This is thought to have suppressed the generation of eddy currents that interfere with the magnetization of the material, resulting in a shorter response time. In addition, an excitation coil with fewer turns results in a lower inductance, intensifying the effect of eddy current on response time. As such, the effect of using ELAC20 is further enhanced.

As described above, selecting the material based on the required performance improves the performance of relay components and reduces power consumption.

Conclusions

As the shift toward EVs progresses, electromagnetic components will need to fulfill new requirements in aspects such as compactness, reduced power consumption, and diversity of AC applications. This paper introduces the main characteristics of the ELCH2 series, which features high magnetic flux density and cold forgeability; the ELAC series, which features excellent response time and a high capacity for suppressing eddy current generation; and KELMOS, which applies the findings of ELCH2 to thin sheets. These pure iron-based soft magnetic materials not only meet the required characteristics of electromagnetic components, but also can be used in combination to achieve even higher performance. Kobe Steel will continue to develop and propose pure iron-based soft magnetic materials suitable for various requirements to support higher-performing, more economical electromagnetic components, thereby contributing to the resolution of societal challenges.

References

1) Ministry of Economy, Trade and Industry et al. Mobility Digital Transformation (DX) Strategy. 2024.
2) M. Chiba et al. R&D Kobe Steel Engineering Reports. 2002, Vol.52, No.3, pp.66-69.
3) M. Sakata et al. R&D Kobe Steel Engineering Reports. 2015, Vol.65, No.2, pp.6-11.
4) T. Hoshino et al. KAWASAKI STEEL GIHO. 1991, Vol.23, No.2, pp.21-27.
5) M. Chiba. R&D Kobe Steel Engineering Reports. 2011, Vol.61, No.1, pp.57-61.
6) S. Kasai et al. R&D Kobe Steel Engineering Reports. 2011, Vol.61, No.1, pp.3-6.

Martensitic Steel Sheets of 1,700 MPa-Grade

Atsuhiro SHIRAKI*1 · Michiharu NAKAYA*1 · Ryuji MORIHARA*2

*1 Steel Sheet & Plate Products Development Department, Research & Development Laboratory, Steel & Aluminum Business
*2 Materials Research Laboratory, Technical Development Group (currently Steel Sheet & Plate Products Development Department, Research & Development Laboratory, Steel & Aluminum Business)

Abstract

The application of high-strength steel sheets to automotive parts is being considered to improve the collision safety of automobiles and reduce CO_2 emissions through weight reduction, and further strengthening is expected in parts that already use 1,470 MPa-grade steel sheets. The 1,700 MPa-grade steel sheet developed by Kobe Steel utilizes continuous annealing equipment with water quenching and has a martensite single-phase structure despite being a low alloy. This solves the application challenges associated with strengthening, such as bending workability, weldability, and delayed fracture resistance. One issue with water quenching is the deterioration of flatness due to thermal distortion during rapid cooling. This, however, has been improved by straightening with a powerful tension leveler, achieving flatness equal to or better than that of the 1,470 MPa-grade. This report introduces the concept of material design and the characteristics of steel sheets.

Introduction

High-strength steel sheets are seeing increasing use in automotive parts to improve collision safety and reduce emissions through weight reduction. Forming methods for automotive parts made of high-strength steel sheets include hot forming (e.g., hot stamping) and cold forming (e.g., press forming, roll forming). Roll-formed 1,470 MPa-grade high-strength steel sheet is used in components such as bumper reinforcements, cross members, and roof racks. This grade is also increasingly being used in press-formed parts such as A-pillars and car body parts that are more complex and require greater dimensional accuracy. Further, the need for steel sheets with even higher strength than 1,470 MPa is also now on the horizon.

To fulfill this projected demand for higher-strength components, Kobe Steel has developed a 1,700 MPa-grade martensitic steel. This steel uses a continuous annealing line with a water quenching system for rapid cooling. Further, it has the necessary workability, weldability, and delayed fracture resistance, which are the main issues in increasing strength. This paper introduces the design concept and main characteristics of the developed material. It also covers how we improved flatness, as this parameter affects the dimensional accuracy of parts, which is particularly crucial in car body applications.

1. Design concept of the developed steel

In roll-formed parts such as bumper reinforcements and roof racks, steel sheets are fed through multiple rolls to form the cross-sectional shape of the part through successive bending processes. As such, these steel sheets must exhibit bending workability. Delayed fracture due to residual stresses generated in the part during forming is also a concern. Therefore, it is necessary to design the material such that it has these characteristics on top of merely having a higher strength rating.

The proposed method of achieving these properties was to use a martensite single-phase microstructure that can achieve high strength with low alloying. The martensitic structure is formed by austenitizing the material via uniform heat treatment and then rapidly cooling it. Kobe Steel uses a continuous annealing furnace with a water quenching system. This inhibits the formation of soft microstructures such as ferrite and bainite during rapid cooling while precluding the need to add a high alloy content. This makes it possible to reduce elements with adverse effects in terms of weldability and delayed fracture, and it yields a composition with highly favorable properties. Details of the concept for achieving such properties are described next.

1.1 Strength

To protect vehicle occupants, parts such as bumper reinforcements must not undergo plastic deformation during a collision. As such, they must have a high yield strength as well as a tensile strength of at least 1,700 MPa.

Martensite structures are very hard because carbon is supersaturated in the interstitial sites of the solid solution.[1)] However, martensite exhibits low toughness and a low yield ratio in the as-quenched state.[2)] To ensure toughness and high yield strength, the developed steel was tempered at a relatively low temperature to achieve a tempered martensite single-phase structure.

1.2 Bend formability

The microstructural changes associated with tempering greatly influence bend formability, so appropriate processing is necessary. As the tempering temperature increases, the number density of needle-like cementite formations increases, reducing bending workability.[3] We therefore selected the temperature range for tempering so as not to deteriorate workability, thus achieving a design that ensures bending workability. Additionally, we adapted the steel composition to combat the issue that inclusions on the surface of the steel sheet act as stress concentration points during bending, which can initiate cracks and reduce bending workability.[4]

1.3 Delayed fracture

Delayed fracture, a phenomenon known to result from hydrogen embrittlement, occurs when a material subjected to tensile stress suddenly fails after some amount of time. The stages of delayed fracture are (1) hydrogen ingress, (2) hydrogen diffusion, (3) crack initiation, and (4) crack propagation.[5] We applied countermeasures against each of the stages from (1) to (4) to inhibit delayed fracture.

One countermeasure, designed to combat hydrogen ingress (stage 1), was to add elements that improve corrosion resistance[6] as implemented in a 1,470 MPa-grade steel sheet. To suppress hydrogen diffusion (stage 2), we increased the tempering temperature to form hydrogen traps created by carbides. And to suppress crack initiation and propagation (stages 3 and 4), we took measures to increase the formation of alloy carbides to inhibit grain growth and thus refine the crystalline grains. Laboratory studies confirmed the effects of these measures on delayed fracture resistance (**Table 1**).

We added alloying elements and adjusted manufacturing conditions to increase the tempered carbide in steels A and B and to refine the γ particle size in steels B and C. The delayed fracture resistance of the three steels was tested via the method shown in **Fig. 1** of U-bending, followed by immersion in hydrochloric acid.

Test specimens were steel strips with machined end faces and dimensions of 150 mm perpendicular to the rolling direction × 30 mm in the rolling direction. The strips were U-bent to a bending radius of 10 mm, with the bending ridge in the rolling direction. Stress was applied to each test specimen through a bolt such that multiplying Young's modulus by the amount of strain measured via strain gauge equals the specified stress. The specimens were immersed in 0.1N HCl for 200 hours and evaluated for fracture. Table 1 shows the results. Load stresses of 1,500 MPa and 2,000 MPa were applied to N=3 test samples for each condition. Those that did not exhibit fracture are indicated by ○, and those exhibited fracture are indicated by ×. Steel B has a finer original γ particle size than steel A and a higher carbide ratio than steel C. Delayed fracture occurred in steels A and C but not B, indicating that steel B has superior delayed fracture characteristics. These findings, which validate an improvement in delayed fracture resistance upon

Table 1 Effects of tempered carbide and grain refinement on delayed fracture resistance

Steel type	Corrosion resistance element	Tempered carbide	Prior gamma particle size	Thickness (mm)	TS (MPa)	Delayed fracture evaluation results	
						Bending radius : 10R Applied stress : 1,500 MPa	Bending radius : 10R Applied stress : 2,000 MPa
A	addition	increase	-	1.0	1,785	○×○	×××
B	addition	increase	fine	1.0	1,757	○○○	○○○
C	addition	-	fine	1.0	1,744	××○	-

○ : No fracture × : Fracture

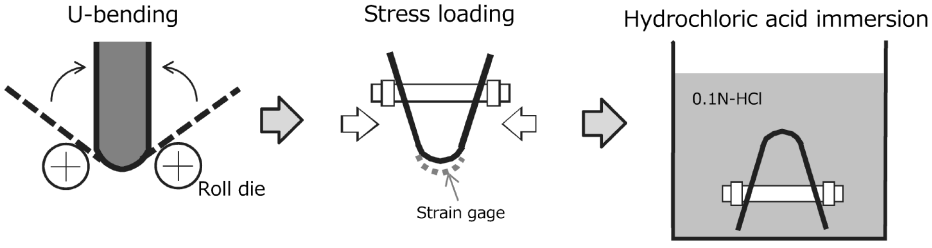

Fig. 1 Delayed fracture evaluation method using U-bending test pieces

increasing the tempered carbide ratio and refining the γ particle size, are reflected in the design of the developed steel.

2. Key properties of the developed steel

2.1 Mechanical properties and proper welding current range

Fig. 2 shows representative microstructures of the developed and conventional steels. The developed steel has a fine needle-like microstructure, indicating a uniform martensite single-phase microstructure. Further, the developed steel has a finer microstructure than the conventional steel, which testing confirmed as the superior microstructure in terms of delayed fracture resistance.

Table 2 shows a comparison of the mechanical properties of the developed and conventional steels.

We evaluated the tensile strength properties by preparing JIS No. 5 test pieces and performing tensile testing per JIS Z 2241. Stretch-flangeability was evaluated via the hole expanding test specified in JIS Z 2256, and bending workability via the 90° V-bend test specified in JIS Z 2248.

The specimens were bent with the bending edge in the rolling direction. The smallest bending radius at which the bent surface did not fracture was divided by the sheet thickness (R/t) to serve as an index of bendability.

The developed steel has a high yield ratio, similar to the 1,470 MPa-grade steel. In addition to a tensile strength of at least 1,700 MPa, it also has a high yield strength, making it suitable for high-strength parts. The total elongation (El.), hole expandability (λ), and bending workability (R/t) are nearly the same as those of 1,470 MPa-grade steel, indicating that the application of the developed steel where 1,470 MPa-grade steel is used should be unproblematic in terms of formability.

Fig. 3 shows the appropriate welding current range. Spot weldability is a requirement for car body applications. As such, we performed spot welding using a 1.4 mm test sheet under the conditions in **Table 3** and evaluated the current range from the current at which the nugget diameter was $4\sqrt{t}$ (t: sheet thickness) to the current at which expulsion occurred. Although the expulsion limit current decreases with increasing strength, the developed steel has a wide current range of 7 to 10 kA. This is equivalent to the 1,470 MPa-grade steel, and it was confirmed that the same welding conditions could be used to ensure the specified nugget diameter.

2.2 Delayed fracture

Plastic strain and residual stress contribute to delayed fracture. As such, in automotive parts, there is concern about the occurrence of delayed fracture in cut edges machined during blanking and in formed parts, where a high degree of plastic strain is introduced. To confirm the resistance of the developed steel to delayed fracture in these locations, we applied U-bending and shearing processes to test samples to simulate the production of an automotive part.

Test specimens for testing U-bent parts were steel strips with machined end faces and dimensions of 150 mm perpendicular to the rolling direction × 30 mm in the rolling direction. The strips were U-bent

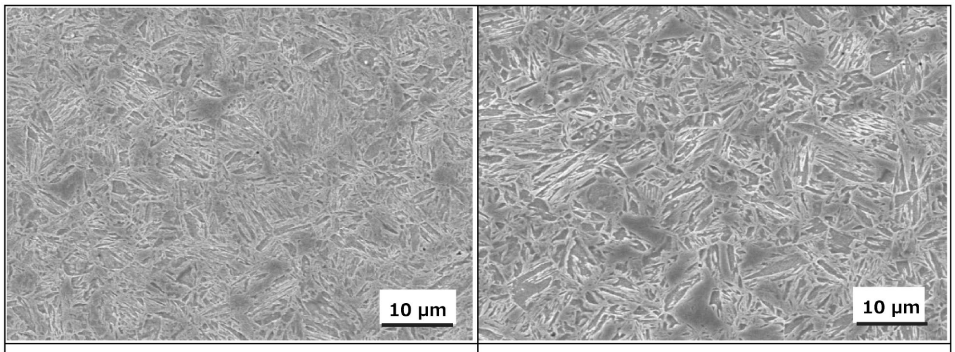

Fig. 2 Microstructure of developed steel and conventional steel

Table 2 Mechanical properties of developed and conventional steels

	YS(MPa)	TS(MPa)	El.(%)	λ (%)	R/t
1,700 MPa-grade (Developed steel)	1,503	1,768	6	39	3.6
1,470 MPa-grade (Conventional steel)	1,332	1,544	6	47	3.5

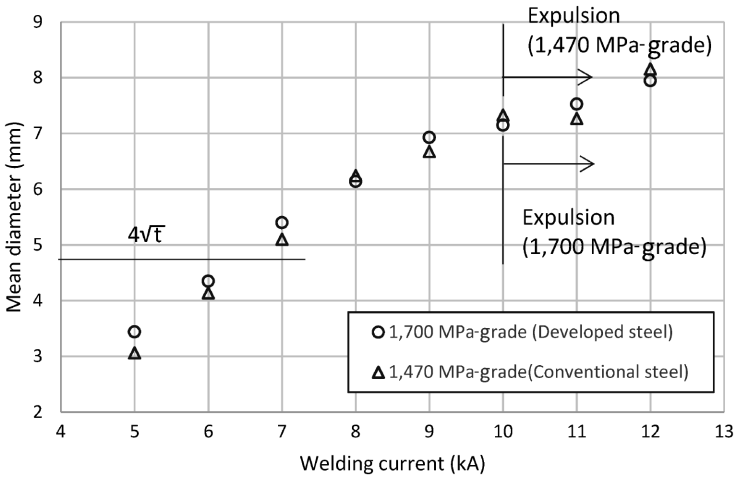

Fig. 3 Relationship between welding current and nugget diameter

Table 3 Spot welding condition

Electrode tip	1%Cr-Cu dome radius type
Tip diameter	6 mm
Electrode force	5.0 kN
Welding time	18 cycles/60Hz
Squeeze time	60 cycles/60Hz
Hold time	1 cycle/60Hz
Welding current	5-12 kA

Table 4 Delayed fracture test results for U-bending part

Steel	Grade	TS (MPa)	Thickness (mm)	Applied stress (MPa)	Evaluation results
Developed steel	1,700 MPa	1,798	1.2	1,700	○○○
Conventional steel	1,470 MPa	1,488	1.4	1,500	○○○

○：No fracture ×：Fracture

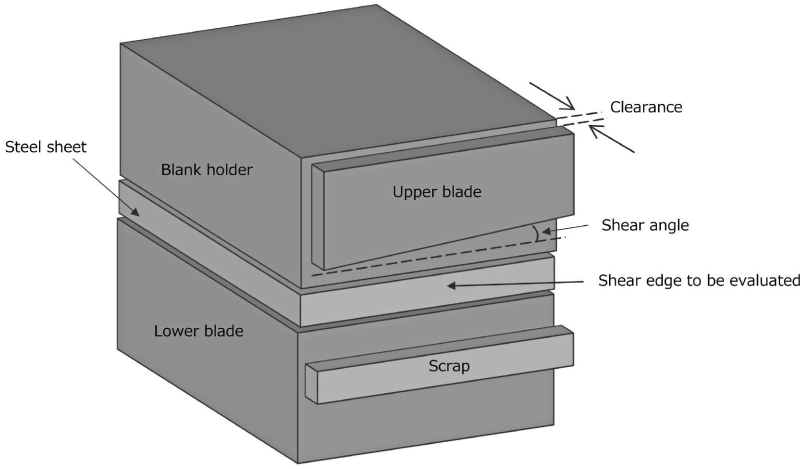

Fig. 4 Schematic diagram of shear processing

to a bending radius of 5 mm, with the bending ridge in the rolling direction. Stress was applied to each test specimen through a bolt such that multiplying Young's modulus by the amount of strain measured via strain gauge equals the specified stress. The specimens were immersed in 0.1N HCl for 300 hours and evaluated for fracture. **Table 4** shows the results; no fracture occurred at a stress of 1,700 MPa, or when strain was applied beyond the elastic limit.

The test specimens for evaluating the delayed fracture resistance of sheared ends were sheared to 15 mm × 30 mm, with the longitudinal direction perpendicular to the rolling direction. The test pieces were immersed in 0.1 N HCl for 24 hours, after which the end faces were inspected for fracture via visual inspection or a microscope. **Fig. 4** depicts the shearing setup. To evaluate the end face perpendicular to the rolling direction, we examined the end of the steel sheet sandwiched between the lower blade and the blank holder after cutting. The shear angle was 0°, and clearances were 5, 10, 15, 20, and 25%. **Table 5** shows the evaluation results. Three tests were performed for each condition. No fractures were observed under any of the conditions, confirming that the specimens had good resistance to delayed fracture.

Table 5 Delayed fracture evaluation results for sheared ends

Steel	Grade	TS (MPa)	Thickness (mm)	Evaluation results				
				CL=5%	CL=10%	CL=15%	CL=20%	CL=25%
Developed steel	1,700 MPa	1,755	1.0	○○○	○○○	○○○	○○○	○○○

○ : No fracture × : Fracture

3. Improving the flatness of steel sheets

Water quenching reduces the flatness of martensitic steels due to the thermal strain caused by rapid cooling. Flatness is an issue with car body parts such as pillars, which must exhibit high dimensional accuracy. As such, we cover Kobe Steel's flatness correction method at the end of this paper.

Kobe Steel has introduced a tension leveler with high correcting capacity that can correct the poor flatness of high-strength steel sheets after annealing. We have already established correction technology that ensures both favorable material properties and good flatness in 1,470 MPa-grade martensitic steel sheets for car body parts, which require exceptional dimensional accuracy. Since it is anticipated that 1,700 MPa-grade steel sheets will also be used for car body parts, the correction technology developed for 1,470 MPa-grade steel was applied to 1,700 MPa-grade steel to improve flatness. **Figs. 5** and **6** depict the change in flatness and appearance after correction using the tension leveler. The maximum warpage height of a steel sheet, cut to a length of 500 mm in the rolling direction, when placed on a flat surface, was used as a flatness index.

The results confirm that shape correction using the tension leveler reduced the warpage height and achieved good flatness. The flatness of our developed steel and the 1,470 MPa-grade steel is approximately equal in the longitudinal direction. Furthermore, water quenching causes deformation and large residual stresses in the sheet surface. This residual stress causes a high degree of deformation when blanks are cut from the coil. We confirmed that this residual stress can be sufficiently reduced through correction via a tension leveler. Further, the 1,700 MPa-grade steel developed is characterized by low deformation when cut.

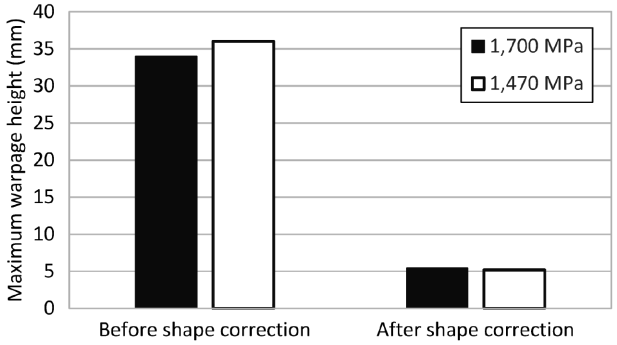

Fig. 5 Flatness measurement results

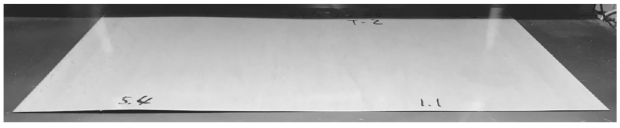

Fig. 6 Appearance of steel sheet after shape correction

Conclusions

Kobe Steel has developed a 1,700 MPa-grade martensitic steel to meet the need for even higher strength in demanding applications. This paper introduces the composition, microstructure control concept, main properties, and flatness correction method of this new steel. This steel features excellent bend formability, delayed fracture resistance, and flatness after shape correction.

Kobe Steel will continue developing materials that meet the expanding needs of car body applications, including demands for even higher strength.

References

1) T. Maki. Materia Japan. 2015, Vol.54, No.11, pp.557-563.
2) O.Izumi et al. Lectures on Modern Metallurgy. Materials, Vol.4., Iron and Steel Materials. The Japan Institute of Metals and Materials. 1985, p.99.
3) Y. Nagataki et al. Tetsu-to-Hagane. 2013, Vol.99, No.3, pp.245-253.
4) K. Morinaga et al. Tetsu-to-Hagane. 1966, Vol.52, No.4, pp.304-306.
5) T. Shirakami. Corrosion Engineering. 2011, Vol.60, No.5, pp.236-240.
6) M. Kowaka. Bulletin of the Japan Institute of Metals. 1973, Vol.12, No.8, pp.533-545.

Hydrogen Evaluation Technology and Material Design Technology for Suppressing Hydrogen Embrittlement of High-Tensile-Strength Steels

Dr. Makoto KAWAMORI*1 · Takuya HIRAMATSU*1 · Dr. Junichiro KINUGASA*2 · Takayuki YASUI*3 · Takuya KOCHI*3 · Yosuke FUJITA*4

*1 Materials Research Laboratory, Technical Development Group
*2 Application Technology Center, Technical Development Group
*3 Wire Rod & Bar Products Development Department, Research & Development Laboratory, Steel & Aluminum Business
*4 Corrosion & Protection Evaluation Department, Material Solution Center, KOBELCO RESEARCH INSTITUTE, INC.

Abstract

Increasing the tensile-strength of steel is an effective means of reducing the weight of automobiles and the environmental burden. Kobe Steel has developed high-tensile-strength steel for bolts, springs, thin steel sheets, and other products and provided them to society. To meet the demands for even higher-tensile-strength and applications in severe corrosion and hydrogen environments, it is important to understand the factors influencing hydrogen embrittlement, which may be a challenge for high-tensile-strength steels, and to create material design technology. This paper introduces hydrogen evaluation technologies to clarify the effects of the environment, material, stress, and strain on hydrogen embrittlement, including hydrogen entry monitoring using hydrogen permeation technique, hydrogen evaluation technology in materials using thermal desorption spectrometry, and slow strain rate tensile technique, as well as hydrogen visualization technology using secondary ion mass spectrometry. In addition, examples of material design technology, such as hydrogen entry suppression by elemental addition and hydrogen embrittlement suppression utilizing microstructure control and compressive residual stress, are explained.

Introduction

Increasing the tensile-strength of steel is an effective way to reduce environmental burden by supporting lower material consumption and reduced weight of vehicles and other transportation equipment, curtailing CO_2 emissions. However, steel's susceptibility to hydrogen embrittlement tends to increase with increasing tensile-strength, making the suppression of hydrogen embrittlement an issue that must be addressed. Postulated mechanisms of hydrogen embrittlement include hydrogen-enhanced localized plasticity (HELP)[1), 2)], hydrogen-enhanced decohesion (HEDE)[3)], hydrogen-enhanced strain-induced vacancies (HESIV)[4), 5)], and combinations of these mechanisms[6)]. **Fig. 1** shows a schematic diagram of the process leading to crack initiation by hydrogen embrittlement. Hydrogen from the environment enters a material and is trapped, diffuses, and accumulates based on the material microstructure and stress/strain. Crack initiation and propagation then occur, resulting in fracture. When the amount of hydrogen that enters the material from the environment (hydrogen concentration entered from the environment H_e) exceeds the maximum hydrogen concentration that will not result in fracture (critical hydrogen concentration H_c), a value specific to each steel, cracking occurs due to hydrogen embrittlement.[7), 8), 9)] Hence, the environment, material, and stress affect each other. Furthermore, it is necessary to consider the effects of plastic strain in, for example, automotive parts (frame parts) made of stamped high-tensile-strength steel sheet or cold-headed non-heat-treated bolts. **Fig. 2** shows a schematic diagram of the factors affecting hydrogen embrittlement as well as hydrogen evaluation material design technologies. Suppressing hydrogen embrittlement and developing materials with excellent resistance to this phenomenon requires two main developments. First, it requires hydrogen evaluation technologies that uncover the effects of material, environment, and stress and strain. Second, it requires material design technologies centered around the mechanisms behind hydrogen embrittlement as revealed by such hydrogen evaluation technologies.

Fig. 3 shows a schematic diagram of hydrogen evaluation technologies organized by spatial and temporal resolution. This paper describes examples of the technologies we developed for suppressing hydrogen embrittlement in high-tensile-strength steel: evaluation technology of hydrogen entry from the environment, evaluation technology of hydrogen in materials, stress and strain evaluation technology, and material design technology coordinated to these technologies.

1. Evaluation and control technologies of hydrogen entry from the environment

When planning to use high-tensile-strength steel for automotive components, it is important

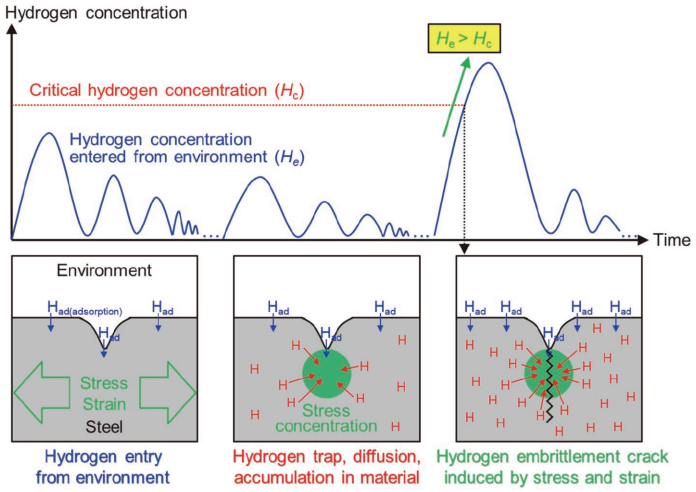

Fig. 1 Schematic illustration of process of hydrogen entry and crack initiation due to hydrogen embrittlement

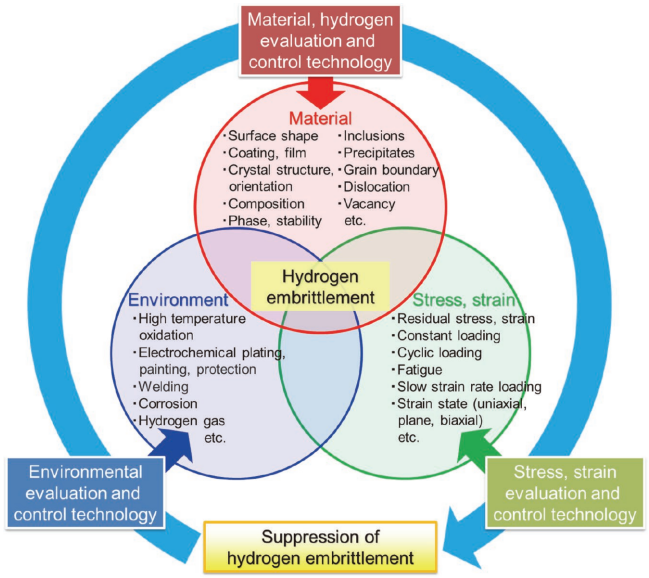

Fig. 2 Schematic illustration of factors affecting hydrogen embrittlement, hydrogen evaluation technology, and material design technologies

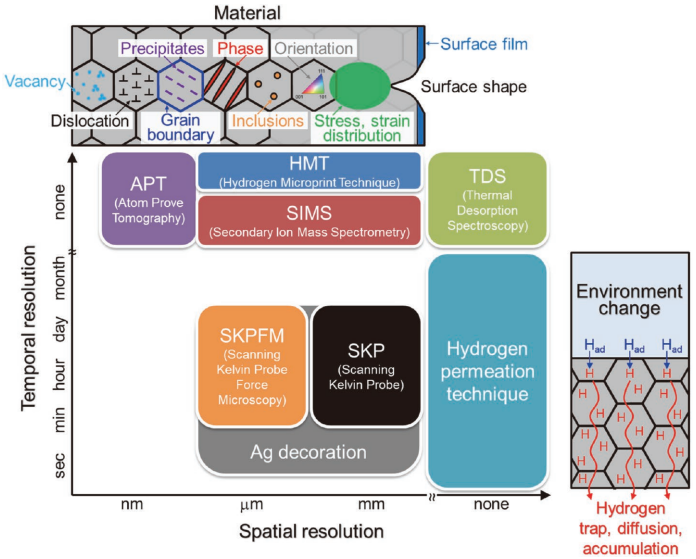

Fig. 3 Schematic illustration of spatial and temporal resolution of various hydrogen evaluation technologies

to understand the hydrogen concentration entered from the environment and the critical hydrogen concentration of the material, and to consider its applicability. As shown in Fig. 2, environmental factors that affect hydrogen entry are wide ranging and include manufacturing processes such as electrodeposition coating, and welding, as well as the vehicle operating environment. This section covers hydrogen entry in operating environments (corrosion environments) for which there is little understanding. It is difficult to determine the hydrogen concentration entered from a corrosion environment because hydrogen moves readily even at room temperature, so how the amount of hydrogen in steel changes over time is complex. Material samples that have fractured due to hydrogen embrittlement provide limited information of value because the exact time of fracture and the hydrogen concentration at that time are lost. Understanding the influence of the actual environment requires an in-depth grasp of hydrogen entry, the corrosion environment, and how fracture due to hydrogen embrittlement changes over time. Kobe Steel is developing various monitoring technologies accordingly. The hydrogen permeation technique is effective for long-term monitoring of hydrogen because, as shown in Fig. 3, it has a broader temporal resolution range than most other techniques. Further, this technique enables simple in-situ measurement. In the hydrogen permeation technique, hydrogen that has entered the steel is oxidized and detected as current. **Fig. 4** shows examples of how we use evaluation technology of hydrogen entry from the environment. Kobe Steel has improved the hydrogen permeation technique such that long-term evaluation is possible even in particularly adverse corrosion environments. The use of temperature, humidity, and ACM (atmospheric corrosion monitoring) sensors for in-situ readings related to the environment and corrosion behavior in a corrosion environment elucidates the relationships between these factors and hydrogen entry. It is also possible to monitor the onset of hydrogen embrittlement by applying the strain gauge method to specimens replicating automotive parts (e.g., U-bend specimens to test bending workability). This test relates to actual vehicle operating environments and atmospheric corrosion environments. Here, we describe the application of this test to hydrogen entry into steel and hydrogen embrittlement behavior in an atmospheric corrosion environment.[9), 10)]

Japan covers many latitudes and thus many different climate zones, from subarctic Hokkaido in the north to subtropical Okinawa in the south. This makes the country suitable for testing how an atmospheric corrosion environment affects hydrogen embrittlement in a broad sense. To investigate hydrogen embrittlement behavior in high-tensile-strength steel in subarctic, temperate, and subtropical climates, we conducted atmospheric exposure tests in Hakodate, Hokkaido; Choshi, Chiba Prefecture; and Miyakojima, Okinawa Prefecture, as shown in Fig. 4. For the hydrogen embrittlement evaluation, SCM435 steel sheets with a tensile-strength of 1,500 MPa and a thickness of 1.6 mm were used. U-bend specimens were prepared with a bending radius of 10 mm. To understand the material's behavior in terms of hydrogen embrittlement under stress, a bolt was threaded through the specimen, and a nut tightened down such that the strain measured by a strain gauge at the top of the bend was 4.9%.

Fig. 5 shows an analysis of the hydrogen embrittlement behavior through a comparison of the time-dependent change in the hydrogen concentration entered from the environment into the steel H_e with the critical hydrogen concentration H_c. The hydrogen concentration entered from the environment was calculated by the current from the hydrogen permeation technique using the steel's hydrogen diffusion coefficient using Fick's law.[9)] The U-bend specimens were immersed in aqueous solutions of varying pH values to study crack formation due to hydrogen embrittlement and determine the maximum amount of hydrogen at which cracking does not occur (critical hydrogen concentration H_c) - see Fig. 5.[9)] In Miyakojima, which has abundant deleterious factors including high temperature and humidity, solar radiation, and sea salt, cracks due to hydrogen embrittlement were confirmed in the early stage of corrosion after the start of testing. By combining hydrogen embrittlement monitoring using the strain gauge method, hydrogen entry monitoring using the hydrogen permeation technique, and environmental monitoring using ACM sensors, it is possible to accurately determine the time of cracking, the amount of hydrogen that entered, and the specifics of the corrosion environment at that time. High ACM currents thought to be caused by rainfall were measured during the early stage of corrosion when cracking occurred due to hydrogen embrittlement. The corrosion reaction accelerated, resulting in increased hydrogen entry and cracking of the U-bend test specimen. The corrosion reaction accelerates and hydrogen entry increases not only in the early stage of corrosion, but also upon the deposition of airborne salt due to strong winds and typhoons that bring heavy rainfall. Choshi has

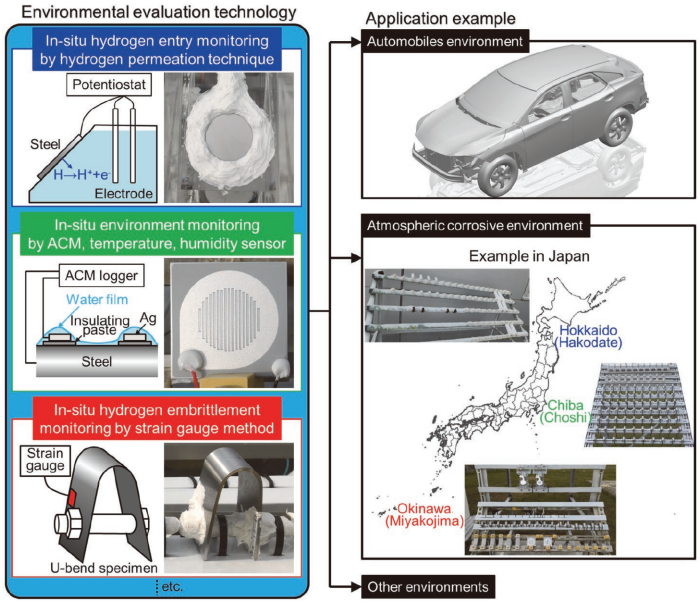

Fig. 4 Evaluation technology of hydrogen entry from the environment and monitoring technology of the environment and hydrogen embrittlement

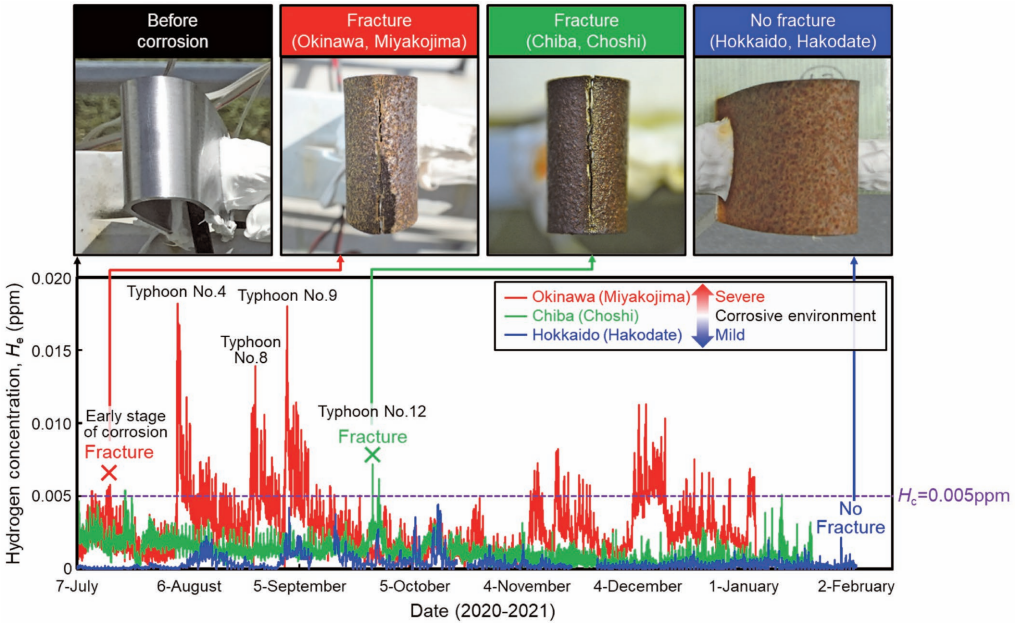

Fig. 5 Analysis of hydrogen embrittlement behavior based on comparison of time-dependent changes in hydrogen entry into steel in an atmospheric corrosion environment and the critical hydrogen concentration

a warm and humid climate and is representative of environmental exposure in Japan. In this test location, although the degree of hydrogen entry was insufficient to cause cracking under everyday conditions, the corrosion reaction accelerated upon the approach of a typhoon, increasing hydrogen entry as well as cracking due to hydrogen embrittlement. By contrast, Hakodate has a lower airborne salt content and lower temperature and humidity. Here, the amount of hydrogen entry was low because of the low amount of corrosion, and cracking due to hydrogen embrittlement did not occur. As such, our monitoring and evaluation technology validated that the amount of hydrogen entry from the environment, H_e in an atmospheric corrosion environment, increases with an accelerated corrosion reaction due to airborne salt, rainfall, high temperature, and humidity. This technology also validated that when the amount of hydrogen entry from the environment H_e exceeds the critical hydrogen concentration H_c, cracking due to hydrogen embrittlement occurs. This technology can precisely evaluate hydrogen entry and hydrogen embrittlement behavior in actual environments and

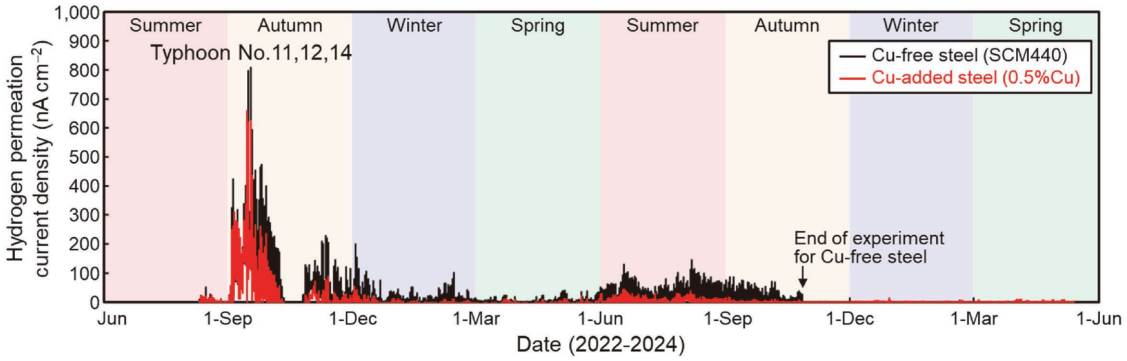

Fig. 6 Effect of Cu addition on hydrogen entry into steel in atmospheric corrosion environment

can be applied not only to the atmospheric corrosion environments described here, but also to vehicle operating environments, for example.

There is concern that hydrogen entry suppression methods that are not based on data from an actual environment might not be as effective as expected when used in an actual environment. Establishing and using the hydrogen environment evaluation technology described above enables the development of material design technology to suppress hydrogen entry in an actual environment.

As an example of hydrogen entry suppression technology in the form of adding elements to steel, **Fig. 6** shows the effect of Cu on hydrogen permeation current density in an atmospheric corrosion environment. The hydrogen entry behavior of steel with 0.5% added Cu was compared with that of Cu-free SCM440 steel. Long-term hydrogen monitoring shows that adding Cu suppresses hydrogen entry in an actual environment. Furthermore, adding Ni reduces the hydrogen concentration entered from the environment[11], and adding Cu and Ni suppresses hydrogen embrittlement[12]. Mechanisms behind these phenomena include improving the corrosion resistance of the base metal itself[13]; suppressing the corrosion reaction through densification of rust[12], thereby reducing the generation of hydrogen; and inhibiting the driving force behind hydrogen entry caused by a higher electrical potential. Our hydrogen entry suppression technology has been applied to the development of high-tensile-strength steels for applications such as high-tensile-strength bolts and thin steel sheets[14), 15]. We will continue to advance the development of countermeasures against hydrogen embrittlement in actual environments.

2. Evaluation and control technologies of hydrogen in materials

Vacancies, dislocations, grain boundaries, and

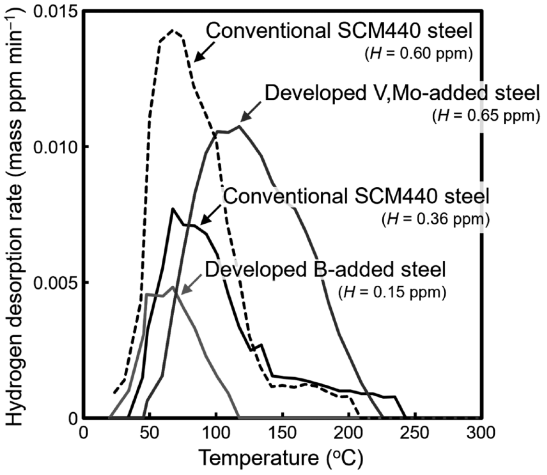

Fig. 7 Hydrogen desorption profile of conventional SCM440 steel, developed V, Mo-added steel, and developed B-added steel

precipitates are trapping sites for hydrogen entering a material from the environment. Additionally, the state of hydrogen changes with factors such as stress, strain, and material microstructure. It is important to evaluate and control the state of hydrogen in a material to suppress hydrogen embrittlement.

Thermal desorption spectroscopy (TDS) has become one of the most widely used methods for evaluating hydrogen in materials. TDS can quantitatively measure the concentration of hydrogen on the order of 0.01 ppm and yield a hydrogen desorption profile for evaluating the state of hydrogen. **Fig. 7** shows an example of TDS results indicating the differing states of hydrogen for varying steel microstructures. Hydrogen was added to steel via cathodic charging method. The solid lines depict the hydrogen desorption profiles for different grades of steel upon hydrogen charging under the same conditions. The dotted hydrogen desorption profile is the result of charging more hydrogen at a higher current density than with the solid lines. The hydrogen desorption profiles for SCM440 steel with different hydrogen concentrations (0.36 ppm and 0.60 ppm) show that hydrogen is

trapped by relatively stable desorption sites on the high-temperature side and that as the hydrogen concentration increases, more desorption sites on the low-temperature side are occupied. Increasing the hydrogen concentration increases the amount of hydrogen that corresponds to desorption sites on the low-temperature side and that easily diffuses even at room temperature (diffusible hydrogen), accelerating hydrogen embrittlement.

Fig. 7 shows the hydrogen desorption profile of high-tensile-strength developed steel in which fine carbides containing V and Mo are dispersed by adding V and Mo and tempering at a high temperature of about 600℃. Compared with SCM440 steel, the peak is shifted toward the high-temperature side, indicating an increase in the number of stable, strong hydrogen trapping sites. Hydrogen was charged via cathodic charging method to annular notched specimens (Kt = 3.5) of each steel grade with varying hardness as preparation for evaluating maximum nominal stress via the slow strain rate technique (SSRT)[16] (results in **Fig. 8**). As the hardness of SCM440 steel increases, the maximum nominal stress after hydrogen charging decreases. The higher the tensile-strength, the more susceptible the steel is to hydrogen embrittlement.

In addition, intergranular fracture occurred near the crack initiation point, suggesting that this phenomenon was caused by hydrogen accumulation at the grain boundaries. However, the maximum nominal stress of V, Mo-added steel being higher than that of SCM440 steel of the same hardness indicates that the former has improved hydrogen embrittlement resistance. As shown in the hydrogen desorption profiles in Fig. 7, this may be due in part to the trapping of hydrogen by fine carbides containing V and Mo[17], suppressing hydrogen accumulation at the grain boundary. In addition to the hydrogen trapping effect, tempering at a high temperature reduces the number and mobility of dislocations, suppressing the transport of hydrogen to grain boundaries through dislocations. The spheroidization of grain boundary carbides further contributes to hydrogen embrittlement resistance.[18] The use of V, Mo-added high-tensile-strength steel for bolts with excellent hydrogen embrittlement resistance reduces the size of automotive parts, thereby reducing vehicle weight and environmental burden, and enhances design flexibility.

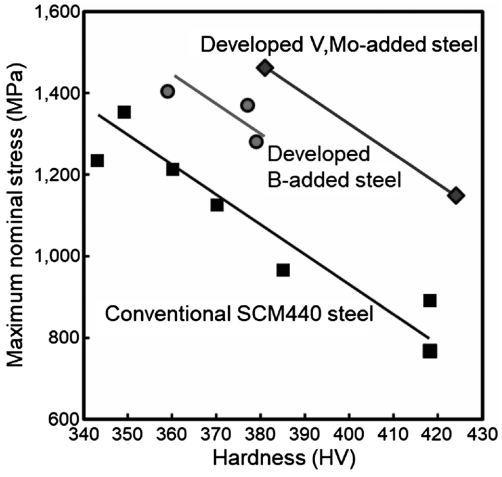

Fig. 8 Effect of hardness on the maximum nominal stress of conventional SCM440 steel, developed V, Mo-added steel, and B-added steel evaluated by SSRT after cathodic hydrogen charging method

Fig. 7 also shows the hydrogen desorption profile of the developed B-added steel. B-added steel is designed for high hardenability and high-tensile-strength grain boundaries through the replacement of relatively expensive Cr and Mo with B. The peak of B-added steel's hydrogen desorption profile is toward the low-temperature side in comparison with SCM440 steel, meaning that its hydrogen trapping power is less than or equal to that of conventional steel. However, at 0.15 ppm, the hydrogen concentration of the B-added steel is less than that of the SCM440 steel (0.36 ppm). As shown in the hydrogen embrittlement test results in Fig. 8, the B-added steel has a higher maximum nominal stress than SCM440 steel of the same hardness. It also has superior hydrogen embrittlement resistance, owing in part to the lower concentration of added elements such as Cr and Mo, which reduces the number of hydrogen trapping sites (amount of hydrogen entry), such as carbides. A further mechanism behind this benefit is the segregation of B to grain boundaries, which suppresses hydrogen accumulation at grain boundaries subjected to stress. Because the B-added steel is a lower alloy than SCM440 steel, it has better cold heading capacity. When used as steel for bolts, for example, the spheroidize annealing process before forming can be omitted, reducing costs and carbon emissions.

Our research validates TDS as an effective method for understanding the state of hydrogen to elucidate the mechanisms behind hydrogen embrittlement and develop material design guidelines for suppressing hydrogen embrittlement. We will improve the accuracy of our technology for determining the concentration of hydrogen via TDS alongside computational methods that can simulate the resulting hydrogen desorption profiles. This will improve the state of the art of technology for evaluating hydrogen in materials and support material design technology based on said technology.

3. Evaluation and control technologies of the effects of stress and strain

Hydrogen embrittlement is strongly influenced not only by the environmental and material factors mentioned above, but also by stress and strain. Hydrogen entering the material from the environment accumulates at stress concentration sites, promoting hydrogen embrittlement. In addition, dislocations and vacancies introduced by strain act as hydrogen traps and affect embrittlement through their interaction with hydrogen.[19] Formed steel can have localized areas of high stress and strain. Therefore, to understand the parameters surrounding hydrogen embrittlement, it is necessary to understand how the localized hydrogen distribution changes based on the distribution of stress and strain. Although TDS is effective for determining the state of hydrogen in materials, it is ineffective for identifying the location of hydrogen in the material because it lacks spatial resolution (see Fig. 3). Hydrogen visualization techniques include atom probe tomography (APT), which has high spatial resolution at the atomic level[20], and the hydrogen microprint technique (HMT), which has superior sensitivity and resolution[21] (Fig. 3). Hydrogen visualization techniques with both spatial and temporal resolution include the scanning Kelvin probe (SKP)[22], scanning Kelvin probe force microscopy (SKPFM)[23], and Ag decoration[24]. Kobe Steel's research group is working to advance hydrogen visualization technology using secondary ion mass spectrometry (SIMS), which offers high spatial resolution covering the sub-μm to sub-mm range as well as high sensitivity in the ppm to ppb range for mass analysis.

As an example of hydrogen visualization technology for evaluating the effects of stress and strain, we introduce the results of an investigation into the hydrogen embrittlement mechanism of the U-bend test specimens.[8), 25)] **Fig. 9** shows the fracture of the U-bend test specimen that underwent hydrogen embrittlement in the atmospheric corrosion environment (Miyakojima) shown in Fig. 5. The fracture near the outer surface of the bend was a quasi-cleavage fracture, whereas the fracture relatively farther from the surface was an intergranular fracture. We used SIMS to investigate the hydrogen distribution in the U-bend test specimen to understand the mechanism behind fracture development, the results of which are shown in **Fig.10**.[8), 25)] Here, deuterium (D) was used

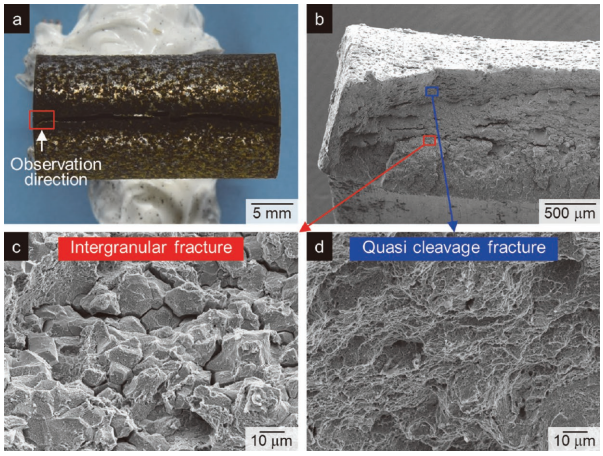

Fig. 9 (a) Photographic image and (b-d) SEM images of hydrogen embrittled U-bend specimens in atmospheric corrosion environment at Miyakojima, Okinawa

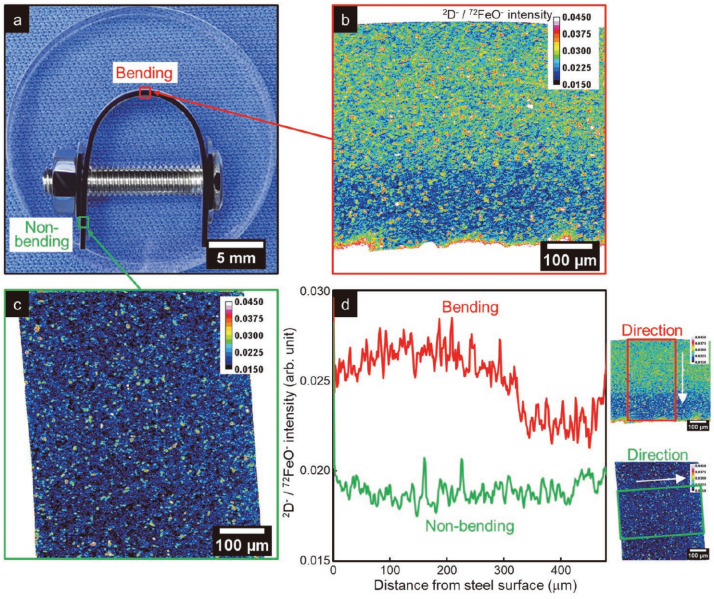

Fig.10 Deuterium visualization images of the U-bend specimen evaluated by SIMS

instead of hydrogen (H) as a tracer for hydrogen trapping sites. Isotope labeling using deuterium, a rare isotope, as a tracer makes it possible to differentiate hydrogen initially present in steel from deuterium introduced from the environment and to determine the locations of these isotopes. Furthermore, since it is possible to distinguish hydrogen in the sample from background hydrogen, the evacuation time required to reduce the background hydrogen can be shortened. This makes it possible to start evaluating the hydrogen visualization before the hydrogen in the specimen dissipates. More hydrogen was detected in the bending area of the U-bend specimen (Fig.10(b)) than in the non-bending area (Fig.10(c)). This was because the number of hydrogen trapping sites increased due to dislocations and vacancies introduced by the strain caused by bending. In the bending area, the hydrogen concentration was high on the front, where there is tensile stress, and low on the rear, where there is compressive stress. Further, the hydrogen concentration was highest about 0.1-0.2 mm into the outermost layer. This is because the highest compressive stress in the outermost layer occurs when the material is left as is in the spring-back state after bending, and when stress is then applied by tightening the bolt, the load is reduced by the compressive stress in the outermost layer, and the area inside the outermost layer becomes the area with the highest stress.

As shown in Fig. 9, intergranular and quasi-cleavage fractures were observed in the U-bend specimen. It has been reported that intergranular fracture occurs in areas of high local stress and hydrogen concentration.[26] Quasi-cleavage fracture occurs readily in the presence of plastic deformation.[27] It is believed that intergranular fracture occurred in the U-bend specimen with hydrogen embrittlement because of the high local hydrogen concentration resulting from the high localized stress some distance in from the surface. Because plastic deformation occurred near the surface, the dislocations and vacancies introduced interacted with hydrogen, resulting in quasi-cleavage fracture.

In the U-bend specimens, tensile stresses caused localized hydrogen accumulation and promoted hydrogen embrittlement. Described next is a case study in which shot peening was used to apply compressive stress to control the hydrogen distribution and suppress hydrogen embrittlement.[28] Shot peening is a method of introducing plastic deformation. There is a concern that strain remaining on the surface of the steel after this process will increase the hydrogen concentration by creating traps in the form of dislocations and vacancies. Therefore, low-temperature annealing was performed after shot peening to an extent that did not reduce compressive residual stress, with the objective of reducing the hydrogen concentration by stabilizing dislocations via Cottrell interaction with carbon and eliminating vacancies. In other words, the method was to suppress hydrogen embrittlement by reducing the amount of hydrogen trapped by strain while the surface of the steel is under compressive residual stress. Hydrogen visualization was then performed for the surface of the steel. A round bar test specimen of tempered martensitic steel with a tensile-strength of 2,000 MPa was subjected to cathodic hydrogen charging method on the surface that had been shot peened. **Fig.11**(a) shows the resulting hydrogen distributions as revealed via SIMS; Fig.11(b) shows the line profiles of hydrogen in the center and on the surface within a width of 50 μm. In the non-shot-peened steel, the concentration of hydrogen in the surface layer is similar to that in the center, and hydrogen is trapped relatively uniformly inside the steel. Conversely, in the shot-peened steel, the concentration of hydrogen in the surface layer is less than that in the center, and there is no increase in hydrogen trapping due to the plastic strain introduced by shot peening. Hydrogen in the shot-peened steel decreases as the distance from the center to the surface layer increases, in parallel with the distribution of compressive residual stress.

We researched hydrogen embrittlement suppression technology using SIMS in conjunction with technology for evaluating the influence of stress and strain on hydrogen distribution. We evaluated the effects of shot peening on hydrogen embrittlement behavior by applying SSRT to hydrogen-charged round bar tensile test specimens. **Fig.12** shows the findings, namely that shot peening increases the maximum nominal stress and hydrogen embrittlement resistance both when relatively large amounts of hydrogen were charged via cathodic charging method (Fig.12(a)) and when relatively small amounts of hydrogen were charged via the combined cyclic corrosion test (CCT) (Fig.12(b)). This is thought to be due to the relief of tensile stress via the compressive residual stress on the surface and due to reducing the concentration of hydrogen in the surface layer. In other words, it was revealed that the hydrogen embrittlement resistance can be improved by introducing compressive residual stress by shot peening and controlling the hydrogen distribution on the steel surface to a low level.

It will be increasingly important to reduce the

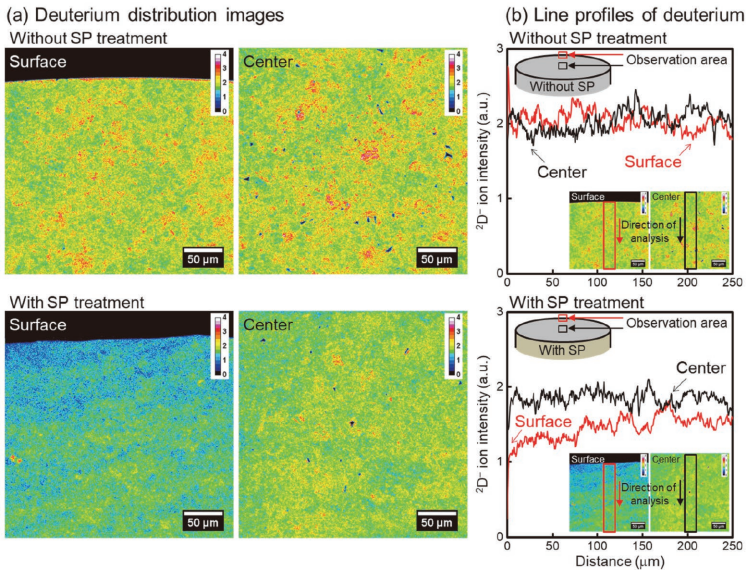

Fig.11 Effects of shot peening and subsequent low-temperature annealing on (a) deuterium distribution and (b) deuterium line profile in the surface and interior of steel

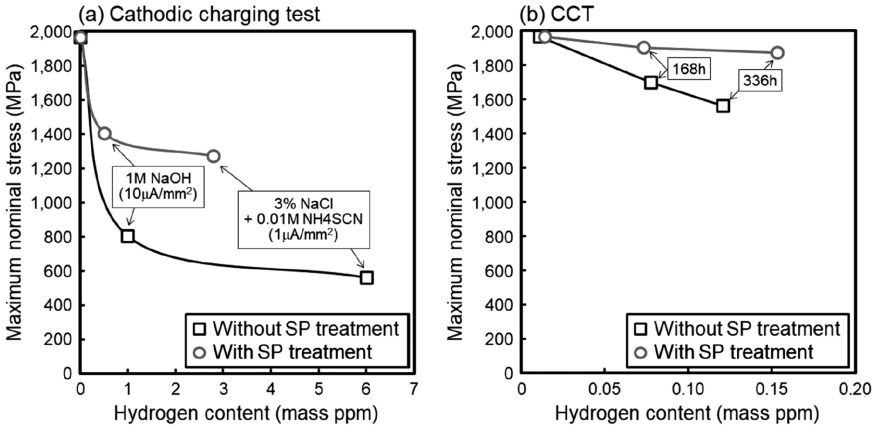

Fig.12 Effect of hydrogen concentration on the maximum nominal stress evaluated by SSRT of steels hydrogen-charged by (a) cathodic charging test and (b) combined cyclic corrosion test

need for heat treatment processes that release CO_2 emissions and to use high-tensile-strength steels formed by cold working to reduce environmental burden and processing. The technologies described here can be used to evaluate hydrogen embrittlement in high-tensile-strength materials under stress and strain after intense working. Further, these technologies support the development of guidelines for material design and production methods to suppress hydrogen embrittlement.

Conclusions

This paper describes hydrogen evaluation and material design technologies for suppressing hydrogen embrittlement in high-tensile-strength steels. Materials that are designed for use in vehicles, conserve resources, and reduce environmental burden are a necessity for fostering a safe, secure, low-carbon, recycling-oriented green society. To combat hydrogen embrittlement, it is critical to elucidate poorly understood aspects such as the effects of microstructure, residual stress, and processing strain on hydrogen entry and on the state and distribution of hydrogen in complex vehicle parts. We will improve environmental evaluation technologies for understanding and simulating the actual environments, technologies for evaluating hydrogen in materials with excellent spatial and temporal resolution, and technologies for measuring and controlling stress and strain. Such developments alongside our forthcoming prediction technologies rooted in computational science will advance hydrogen-resistant design technologies for materials. Through these technologies, we will foster the development of high-tensile-

strength steels such as bolt steels for automotive applications and ultra-high-tensile-strength thin steels to reduce environmental burden. In doing so, we will also develop materials for a hydrogen society, thereby contributing to a green society and to safe and security in community development and manufacturing.

References

1) C. Beachem. Metallurgical Transactions. 1972, Vol.3, pp.441-455.
2) H. Birnbaum et al. Materials Science and Engineering: A. 1994, Vol.176, pp.191-202.
3) R. Oriani et al. Acta Metallurgica. 1974, Vol.22, pp.1065-1074.
4) M. Nagumo. Materials Science and Technology. 2004, Vol.20, pp.940-950.
5) K. Takai et al. Acta Materialia. 2008, Vol.56, pp.5158-5167.
6) T. Neeraj et al. Acta Materialia. 2012, Vol.60, pp.5160-5171.
7) N. Suzuki et al. Tetsu-to-Hagane. 1993, Vol.79, No.2, pp.227-232.
8) S. Yamasaki et al. Tetsu-to-Hagane. 1997, Vol.83, No.7, pp.454-459.
9) M. Kawamori et al. Corrosion Science. 2023, Vol.219, 111212.
10) M. Kawamori et al. ISIJ International. 2022, Vol.62, No.8, pp.1731-1740.
11) S. Takadate et al. Proceedings of the 70th Japan Conference on Materials and Environments. 2023-10-30/11-1. Japan Society of Corrosion Engineering. 2023, C-307.
12) J. Kinugasa et al. ISIJ International. 2016, Vol.56, No.3, pp.459-464.
13) T. Takimoto et al. Collected Abstracts of the 2023 Autumn Meeting of the Japan Inst. Metals and Materials. 2023-9-19/26. 2023, p.61.
14) T. Yasui et al. Materia Japan. 2024, Vol.63, No.1, pp.63-65.
15) M. Takeda et al. R&D Kobe Steel Engineering Reports. 2024, Vol.72, No.2, pp.33-37.
16) W. Urushihara et al. R&D Kobe Steel Engineering Reports. 2002, Vol.52, No.3, pp.57-61.
17) K. Hokazono et al. IOP Conference Series: Materials Science and Engineering. 2019, Vol.461, 012024.
18) K. Kagiya et al. CAMP-ISIJ. 2024, Vol.37, p.157.
19) J. Kinugasa et al. ISIJ International. 2021, Vol.61, No.4, pp.1071-1078.
20) J. Takahashi et al. Scripta Materialia. 2010, Vol.63, pp.261-264.
21) T. Pérez et al. Scripta Metallurgica. 1982, Vol.16, pp.161-164.
22) S. Evers et al. Science and Technology of Advanced Materials. 2013, Vol.14, 014201.
23) W. Krieger et al. Acta Materialia. 2018, Vol.144, pp.235-244.
24) M. Koyama et al. Scripta Materialia. 2017, Vol.129, pp.48-51.
25) J. Kinugasa et al. ISIJ International. 2021, Vol.61, No.4, pp.1091-1098.
26) M. Wang et al. Corrosion Science. 2007, Vol.49, pp.4081-4097.
27) A. Shibata et al. Acta Materialia. 2021, Vol.210, 116828.
28) M. Kawamori et al. ISIJ International. 2021, Vol.61, pp.1159-1169.

Welding Process Enhancing Electrodeposition-coating Performance for Ultra-High-Tensile-Strength Steel Sheet

Naohide FURUKAWA*1・Kazuya IKAI*1
*1 Welding Process Department, Technical Center, Welding Business

Abstract

In gas-shield arc-welded joints of ultra-high-tensile-strength steel sheets, there is an issue of increased slag generation, which inhibits electrodeposition-coatability. To address this issue, a welding technology has been developed to reduce the amount of slag generated and improve corrosion resistance after electrodeposition-coating. A welding process has been adopted in which the argon gas ratio in the shielding gas has been increased to 95% (high-argon welding process). The welding consumable has been designed to increase the strength of the welding joint by adding alloying elements that have low affinity with oxygen. In addition, the productivity of welding consumables has also been taken into consideration, and practical application has been sought using composite wires rather than the solid wires that are generally used in the automotive field. This paper describes a welding technology that combines electrodeposition-coatability and fatigue strength, realized by a combination of the welding process and welding consumables.

Introduction

In recent years, the automotive field has seen a growing need for stronger and lighter materials in response to more stringent environmental and collision safety standards. Steel is generally used for automotive suspension parts that support the weight of the chassis. These parts must simultaneously exhibit high fatigue strength, rigidity, and corrosion resistance. To improve the fatigue strength and rigidity of parts with complex shapes, it is necessary to increase the strength of not only the steel sheet but also the welds. Although the thickness of a steel sheet can be reduced if its tensile-strength is increased, a thinner sheet would lead to reaching the fatigue limit sooner if corrosion resistance is not increased. In addition, damage caused by gravel while driving, salt in the atmosphere in coastal regions, and de-icing agents in cold regions necessitate even greater corrosion resistance.

Gas-shield arc welding with solid wire is the typical practice for joining automotive suspension parts. When welding consumables for ultra-high-tensile-strength steel sheets are manufactured using solid wire, the wire strength tends to be high. This is due to work hardening during wire drawing and to the increase in wire hardness from the addition of alloying elements. As a welding consumable, it is necessary for the wire strength to be appropriate for the size of the part for good wire feeding and workability during welding. For wires with a high alloy content, annealing is necessary during drawing to ensure appropriate strength.

Furthermore, multiple stages of annealing may be necessary if the wire strength is not suitable after annealing once. As a result, the wire's productivity is greatly reduced, increasing the cost. Therefore, Kobe Steel set out to develop a welding consumable designed for 980 MPa-grade steel sheet using composite wire. The design of the material accounts for formability during wire manufacturing, with a mild steel outer layer and flux with alloying elements as the core. **Table 1** shows the advantages and disadvantages of composite versus solid wire. For high-strength materials that are difficult to draw, composite wire is advantageous because it is both economical and has a higher deposition rate.

One disadvantage of composite wire is low rigidity, which tends to reduce the straightness of the wire slightly. This aspect was evaluated by testing weldability at a part manufacturer's facility. This paper introduces welding technology that results in welding joints with excellent corrosion resistance and fatigue strength, even in the welding of ultra-high-tensile-strength steel by using the composite wire and welding process described above.

Table 1 Advantages and disadvantages of composite wire against solid wire

		Solid wire	Composite wire
Typical cross section			
Formability	Mild steel	○	○
	High tensile steel	○	◎
Production cost	Mild steel	○	△
	High tensile steel	○	◎
Deposition rate		○	◎
Wire stiffness		○	△

[Judge standard] ◎: Better - ○:Standard - △:Poor - ×:Bad

1. Underlying technology

1.1 Concept behind improving corrosion resistance

Our concept behind improving corrosion resistance is divided into the welding process and the subsequent electrodeposition-coating process, as shown in **Fig. 1**. In gas-shield arc welding, typical shielding gas compositions are 100% CO_2 or an 80/20 blend of Ar with CO_2 to prevent the incorporation of atmosphere into the molten metal. CO_2 dissociates into CO and O under the arc. Oxygen stabilizes the arc but is an active gas that combines with Si, Mn, and other alloying elements, producing slag. Oxide slag containing silicon as the main constituent is highly insulative, so if this composition of slag is on the surface of the weld bead, a coating film will not form during the electrodeposition-coating process after welding. Therefore, the amount of slag on the weld bead must be minimized to improve electrodeposition-coatability.

To overcome this challenge, we employed a high-argon welding process that uses a shielding gas of a 95/5 blend of Ar with CO_2 to stabilize the arc during welding while reducing active gas, thereby suppressing slag formation[1]. There is an established method for the subsequent electrodeposition-coating process in which the viscosity of the electrodeposition-coating is decreased to increase fluidity during baking, thereby coating the insulative material[2].

Our concept is to minimize slag using a high-argon welding process and then thicken the electrodeposition-coating to increase the amount of fluid coating and cover the slag in the uncoated areas.

1.2 Welding consumables

It is possible to reduce slag by using a high-argon welding process with a higher inert gas ratio. Various related efforts have been pursued to reduce slag and improve electrodeposition-coatability in welding consumables[3)~5)].

Two approaches have been proposed for welding consumables used in combination with a high-argon welding process to achieve low-slag welding. The optimal conditions for each approach are a point of study. **Table 2** shows the approaches to reducing slag in a high-argon welding process by coordinating the welding consumables to processing conditions.

The first approach is to suppress slag formation by increasing the ratio of inert gas, concentrate, and recover the slag, and transport the slag to the weld end. Concentrated slag detaches easily; as a mechanism to concentrate slag, the welding wire contains 0.020% sulfur. Adding sulfur changes the convection of the molten pool, causing microscopic slag particles to aggregate in the crater during welding and be transported along with the arc. Another factor, aside from molten pool convection, that influences slag behavior is the flow rate of the shielding gas. Reducing the gas flow rate helps concentrate slag and transport it to the weld end in a stable way[5]. Therefore, it is best to use a nozzle with a larger diameter than normal. Wire for gas-shield arc-welding that imparts the above-mentioned characteristics to slag is called "slag-concentrating wire" in this paper. The second approach to reducing slag is to transport slag to the rear of the molten pool and actively incorporate it into the Fe-based oxide film in a deconcentrated state. Welding consumables for this approach contain Ti, which forms oxides with higher liquidus temperatures than those of Si and Mn oxides. Compared with Si and Mn, Ti forms molten slag that is higher in temperature and therefore more strongly affected by the flow of the plasma, providing the driving force for the molten slag to move rearward in the molten pool. To incorporate slag transported to the rear of the molten pool into the Fe-based oxide film, it is best to expose slag to the atmosphere from the area near the solid-liquid interface at the rear of the molten pool. According to Yamasaki et al.[5], a high welding speed or a nozzle diameter smaller than a certain value results in a region of the weld bead without slag after welding. Changing these two parameters

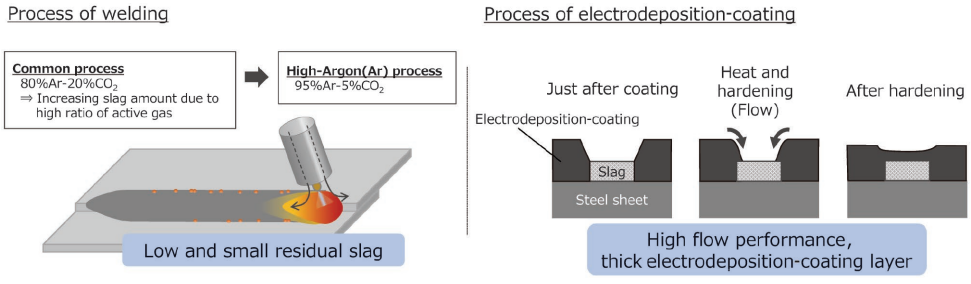

Fig. 1 Basic idea to improve corrosion resistance

Table 2 Two approaches for slag reduction method

Welding process	High−Ar process	
Shielding gas	95%Ar-5%CO_2	
Wire type	Slag concentrating	Slag deconcentrating
Unique chemical composition in wire	S add.	Ti add.
Gas flow rate	20 (Liter/min.)	
Size of nozzle	Φ19 (mm)	Φ13(mm)
Welding speed	Normal	Faster
Schematic drawing	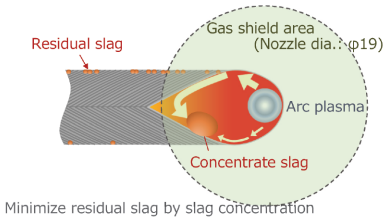 Minimize residual slag by slag concentration	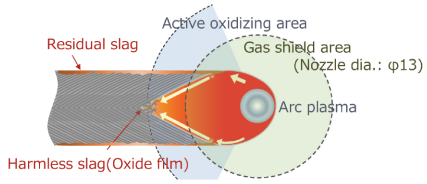 Creating harmless slag by active oxidizing in the rear molten pool
Observation by HSV	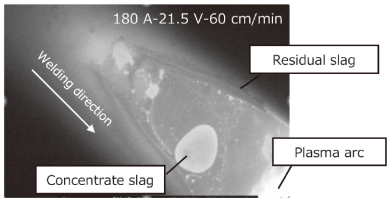	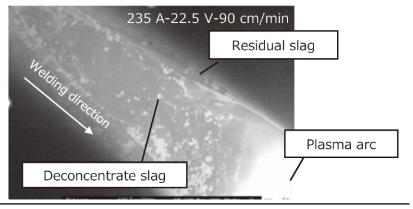

Table 3 Corrosion resistance performance of lap weld joint

Welding process	Conventional MAG	High −Ar process	
Shielding gas	100%CO_2 or 80%Ar-20%CO_2	95%Ar-5%CO_2	
Wire type	Normal YGW12	Slag concentrating	Slag deconcentrating
Base metal	440 MPa-grade steel, 2.0 mm^t		
Bead appearance after electrodeposition-coating	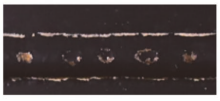	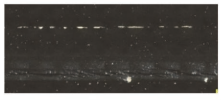	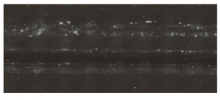
Bead appearance after 10 cycles of corrosion test	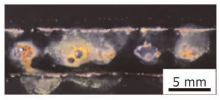		
Judge*	3	4	5

* [Judge standard] 5(Good) − 4(better) − 3(Standard) − 2(poor) − 1(Bad)

accordingly increases the area of the molten pool exposed to the atmosphere and promotes more aggressive coating by the Fe-based oxide film. This is a more sensible approach, as the welding speed can be increased without increasing porosity due to air entrainment or reducing mechanical performance. In this paper, gas-shield arc welding wire that deconcentrates slag as described above is called "slag-deconcentrating wire."

Table 3 shows welding joints in 440 MPa-grade steel after electrodeposition-coating and corrosion testing as described below. Compared with conventional metal active gas (MAG) welding, welding joints produced using the high-argon welding process exhibit significantly better electrodeposition-coatability. Additionally, in comparing the two approaches to reducing slag, the slag-concentrating wire shows some rusting from residual slag that could not be fully concentrated. By contrast, the slag-deconcentrating wire has good corrosion resistance if the slag is properly deconcentrated and rendered harmless.

Since an increase in slag is expected in welding wire for ultra-high-tensile-strength steel, we decided to design a welding wire based on slag-deconcentrating wire because of its demonstrated higher corrosion resistance.

2. Welding technology for ultra-high-tensile-strength steel

2.1 Welding consumables

In developing a welding wire for ultra-high-tensile-strength steel sheet, we investigated a composite wire that combines a mild steel strip with excellent formability as the outer layer and a mixed flux with alloying elements as the core.

Table 4 shows the target chemical compositions of the trial wires when fully melted. Alloys are added to 980 MPa-grade steel sheet to achieve the required strength. The weld metal is affected by the base metal composition and the alloy composition of the wire. A high alloying content inevitably increases slag when welding ultra-high-tensile-strength steel sheet. To minimize slag in the welding wire, we considered using carbon or Cr to improve the strength of the weld metal instead of Si, which has a high affinity with oxygen. Carbon has little effect on the amount of slag because it combines with oxygen and vaporizes as CO_2. Cr has a relatively low affinity with oxygen. When alloying elements with a higher affinity are present, Cr is not readily oxidized and consumed in the slag-metal reaction. Therefore, Cr will bond with oxygen only to a limited degree and will mostly remain in the weld metal.

2.2 Experiment conditions

2.2.1 Welding and electrodeposition-coating

For the trials, we lap welded 980 MPa-grade steel sheets provided by Mazda Motor Corporation in a horizontal welding position. **Table 5** and **Fig. 2** show the welding conditions. The image of slag on the weld bead was binarized for calculation of the area ratio of slag. The welding joints were cleaned, degreased, prepared, conversion coated (zinc phosphate), and cleaned again before coating with black cationic electrodeposition-coating (target thickness 20 μm). Images of the coated surfaces were binarized for calculation of the non-coated area.

2.2.2 Combined cyclic corrosion test (CCT)

CCT is a method for accelerated testing of the corrosion resistance of metal materials, coatings, and platings. This test method involves repeated corrosion cycles of salt spray, drying, and wetting in a test chamber. We evaluated the corrosion resistance of lap weld joints, selecting specimens from joints using trial wires A-F for their low slag and good electrodeposition-coatability. Specimens were subjected to up to 50 cycles of the testing conditions stipulated in JASO M609 (Japanese Automotive Standards Organization) to definitively reveal the difference in corrosion resistance between trial wires. We took images of the specimens to record their corrosion status after removing them from the test chamber.

2.2.3 Fatigue testing of welding joints

Specimens were prepared by performing electrical discharge machining on pieces welded under the conditions in Table 5. Bending fatigue tests were performed on the specimens with a stress ratio R = 0. The benchmark was wire of specification JIS Z 3312 G43A2M 16, which is commonly used as a welding consumable for 440 to 780 MPa-grade steel sheets. **Table 6** shows the fatigue test conditions.

Table 4 Typical chemical compositions of trial wires for 980 MPa-grade steel

Wire	C	Si	Mn	Cr	Ti	Ni, Mo	Ceq.
Wire A	0.08	0.29	1.45	0.10	0.14	Add.	0.54
Wire B	0.09	0.14		0.13			0.55
Wire C	0.09	0.04		0.13			0.54
Wire D	0.08	0.29		0.10	0.10		0.54
Wire E	0.09	0.14		0.13			0.55
Wire F	0.09	0.04		0.13			0.54

[JIS/WES] Ceq.: C+Mn/6+Si/24+Ni/40+Cr/5+Mo/4+V/4

Table 5 Welding condition for lap weld joint

Welding robot	DAIHEN Almega AX-V6
Power source	DAIHEN Digital Pulse DP400R
Shielding gas	95%Ar-5%CO_2, 20 ℓ/min
CTWD	15 mm
Nozzle inner dia.	13 mmφ
Torch angle	45°
Base metal	980MPa-grade steel, thickness : 2 mm
Current (Voltage)	240 A (24.5 V)
Welding speed	110 cm/min

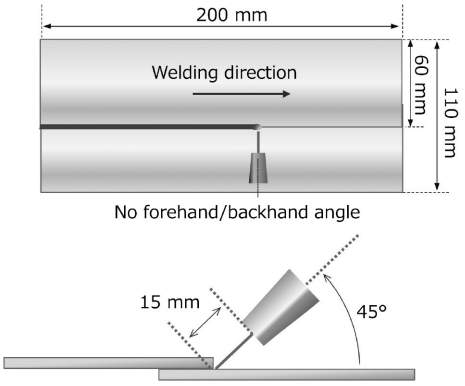

Fig. 2 Wire aiming position when lap weld joint done

Table 6 Bending fatigue test condition

Test temperature	RT
Stress ratio	R≒0 (pulsating fatigue test)
Frequency	25 Hz
Number of cycles to failure	2×10^6 cycles or 10% less than initial torque

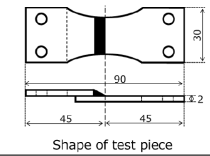

Shape of test piece

2.2.4 Hardness testing of welding joints

Vickers hardness testing was performed on cross-sectional macro specimens of welding joints from the same specimens from which the fatigue test samples were taken. Hardness was measured at the lower side weld toe, an area that can affect the fatigue strength of the welding joint, in an area spanning the weld metal, heat-affected zone, and base metal. The load for hardness measurement was 3 N.

2.3 Experiment results and explanation

2.3.1 Results of evaluating slag generation and electrodeposition-coatability

Table 7 shows the weld beads after lap welding and electrodeposition-coating. **Figs. 3** and **4** show quantitative results as calculated by image analysis in the form of the area ratio of slag and the non-electrodeposition-coated area. These results show that there is less residual slag on the bead with a lower ratio of Ti and Si, which are strong deoxidizing elements. A comparison of the beads after electrodeposition-coating confirms that most of the bead, including the residual slag, was electrodeposition-coated. Wires A-C (0.14% added Ti) exhibited good electrodeposition-coatability even on the upper side of the bead where there was residual slag. Conversely, wires D - F (0.10% added Ti), which had a relatively low amount of slag, exhibited poor electrodeposition-coatability in some areas. In summary, although good electrodeposition-coatability was achieved even with a high amount of residual slag, there were cases in which electrodeposition-coatability was insufficient even with a low amount of slag.

2.3.2 Results of slag analysis

We examined the cross-sections of the slag, focusing on the residual slag on the upper side of the beads, which exhibited differing degrees of electrodeposition-coatability. Specifically, we used electron probe microanalysis (EPMA) to perform elemental mapping and COMPASS multivariate image analysis software (Thermo Fisher Scientific Inc.) to perform phase separation analysis.

Fig. 5 shows the ratios of the main oxides that make up the slag as calculated based on the elements

Table 7 Bead appearance after welding and after electrodeposition-coating

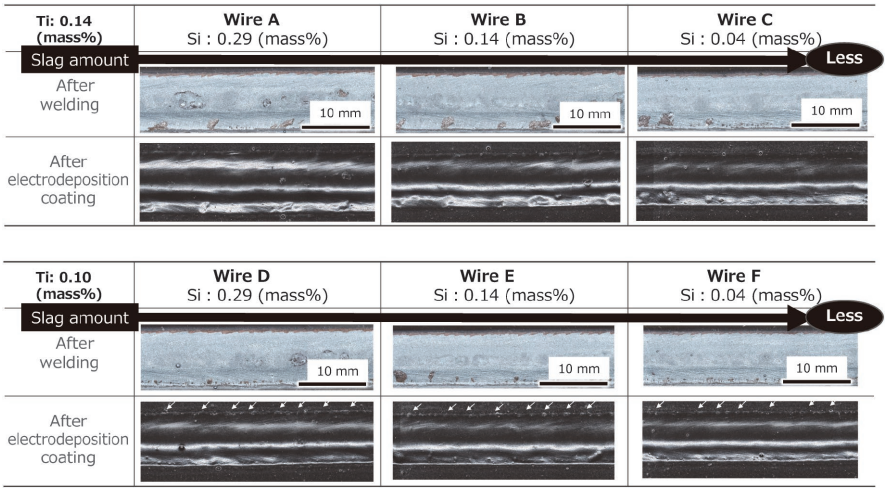

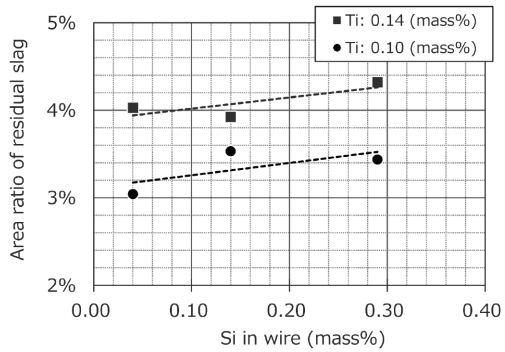

Fig. 3 Area ratio of residual slag

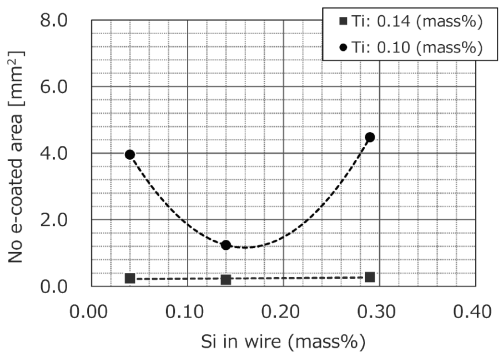

Fig. 4 Non- electrodeposition-coated area

and mass ratios identified by element mapping. While the ratio of SiO_2 in the slag tends to decrease as the ratio of Si in the wire decreases, no significant differences were observed in the ratios of TiO_2, MnO, or other components.

Table 8 shows the distribution of the oxide phase as output by COMPASS. Phases with a ratio of 20% or more in the slag were extracted. Components constituting 10% or more of a phase were deemed representative components of those phases. The Mn-Ti-Si oxide and Mn-Ti oxide phases were found to be main phases of the slag in every case. As the Si content in the wire decreases, the Mn-Ti oxide phase tends to precipitate in the form of dendrites from the bottom of the slag (steel ground side) to the top (electrodeposition-coating ground side). Additionally, the boundary between phases is generally distinct. This tendency is stronger in the slag of wires A - C (0.14% added Ti), which have good electrodeposition-coatability.

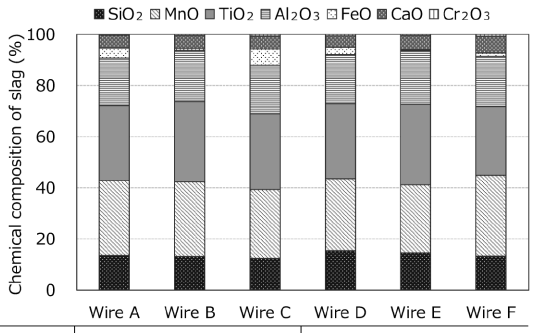

Ti in wire (mass%)	0.14			0.10		
Si in wire (mass%)	0.29	0.14	0.04	0.29	0.14	0.04

Fig. 5 Percentage of slag elements taken from upper side in the welding bead

This can be explained by assuming that the Mn-Ti oxide phase is more conductive than the Mn-Ti-Si oxide phase. It seems that the conductive pathways take a complex three-dimensional path from the bottom of the slag up, fostering good electrodeposition-coatability despite an increase in the area ratio of the slag. Quantitative analysis of the conductivity of each oxide phase is a potential future research area to elucidate the mechanisms behind improving electrodeposition-coatability.

2.3.3 Results of the CCT

Table 9 shows the CCT results for 980 MPa-grade steel sheet upon application of a cationic electrodeposition-coating to a lap weld fillet joint created with wire B. This joint exhibited superior

Table 8 Phase analyzed results at cross-sectional slag

Wire	Wire A	Wire B	Wire C	Wire D	Wire E	Wire F
Ti in wire (mass%)	0.14			0.10		
Si in wire (mass%)	0.29	0.14	0.04	0.29	0.14	0.04
Composition image	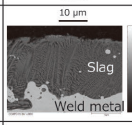	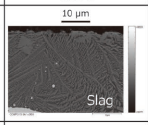	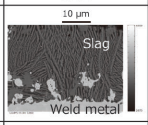	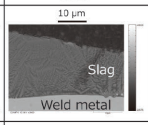	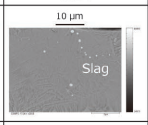	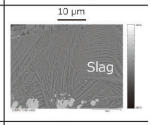
Mapping image	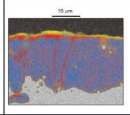	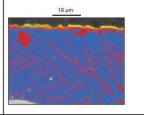	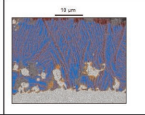	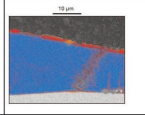	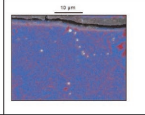	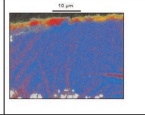
Slag component phase	Mn-Ti-Si Mn-Ti Fe-Mn-Ti Others (Fume etc.)	Mn-Ti-Si Mn-Ti Others (Fume etc.)	Mn-Ti-Si Mn-Ti Fe-Mn-Ti	Mn-Ti-Si Mn-Ti Fe-Mn-Ti	Mn-Ti-Si Mn-Ti	Mn-Ti-Si Mn-Ti Others (Fume etc.)

Table 9 CCT results of weld joint prepared with Wire B

Welding process	High-Ar process	
Wire type	Conventional wire for high-tensile-strength-steel (Slag concentrating)	Wire B for ultra-high-tensile-strength-steel (Slag deconcentrating)
Base metal	440 MPa-grade steel, 2.0 mm^t	Wire B 980 MPa-grade steel, 2.0 mm^t
After welding	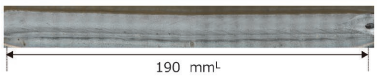 190 mm^L	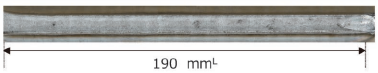 190 mm^L
AFter electrodeposition coating	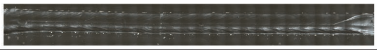	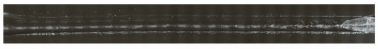
After 30 cycle of CCT		
After 50 cycle of CCT	N/A	

*Conventional wire: G43A2M 16

electrodeposition-coatability in comparison with the joint created using conventional wire and 440 MPa-grade steel sheet. Furthermore, after 50 cycles of the CCT, no rust originating from the residual slag on the weld bead was observed, confirming that the material has good corrosion resistance.

2.3.4 Results of fatigue testing of welding joints

Fig. 6 shows the fatigue test results of lap fillet weld joints. Introduced here are the fatigue properties of wire B, which balances electrodeposition-coatability and weld metal strength in the welding of 980 MPa-grade steel sheet.

Testing shows improved fatigue properties of the welding joint when conventional wire is paired with 980 MPa-grade steel sheet in comparison with 440 MPa-grade steel sheet.

The combination of wire B and 980 MPa-grade steel sheet is shifted toward a higher number of cycles to failure compared with conventional wire under the same stress amplitude. Further, the fatigue strength of the former at 2 million cycles is about 1.5 times higher.

Table 10 shows the macro-level cross-sections of the lap weld fillet joints and the toe radii and flank angles. While the geometry of the weld toe greatly affects the fatigue properties of the lap fillet weld joint, there were no significant differences in this feature with the trial wire used in this study. Therefore, it is concluded that the increase in the tensile-strength of the steel sheet and weld metal increases the load-bearing capacity of the welding joint itself, thus increasing fatigue strength.

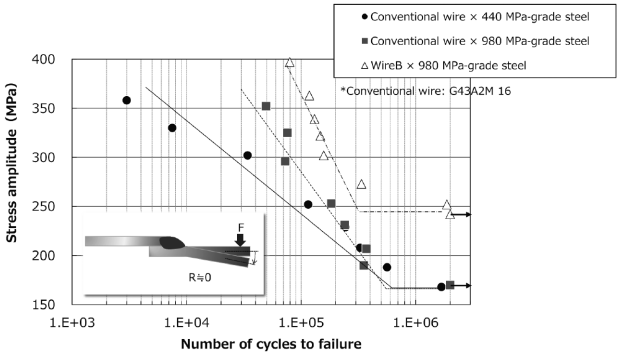

Fig. 6 Fatigue strength of lap fillet weld joint

2.3.5 Results of hardness testing of the weld metal

Fig. 7 shows the results of the Vickers hardness test near the lower-side weld toe of the welding joint. The weld metal of the welding joint using conventional wire is harder in combination with the 980 MPa-grade steel sheet in comparison with the 440 MPa-grade steel sheet. This could be because the base metal is diluted by alloying elements added to the 980 MPa-grade steel sheet. The hardness of

Table 10 Cross-section of lap fillet weld joint

	Conventional wire × 440 MPa-grade steel	Conventional wire × 980 MPa-grade steel	WireB × 980 MPa-grade steel
	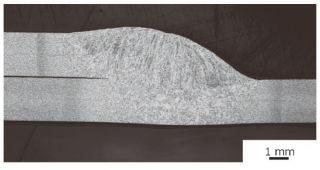	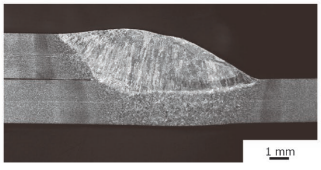	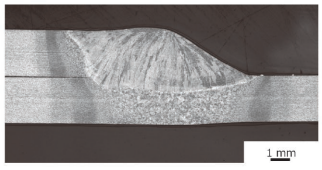
Frank angle (°)	150	149	152
Toe radius (mm)	2.0	1.6	2.1

*Conventional wire: G43A2M 16

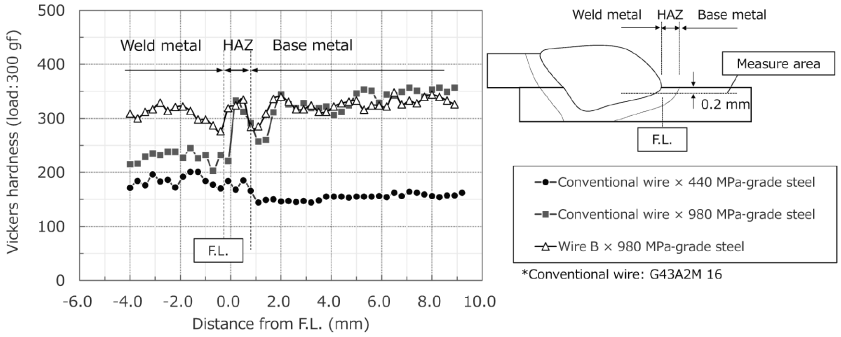

Fig. 7 Vickers hardness around lower side weld toe

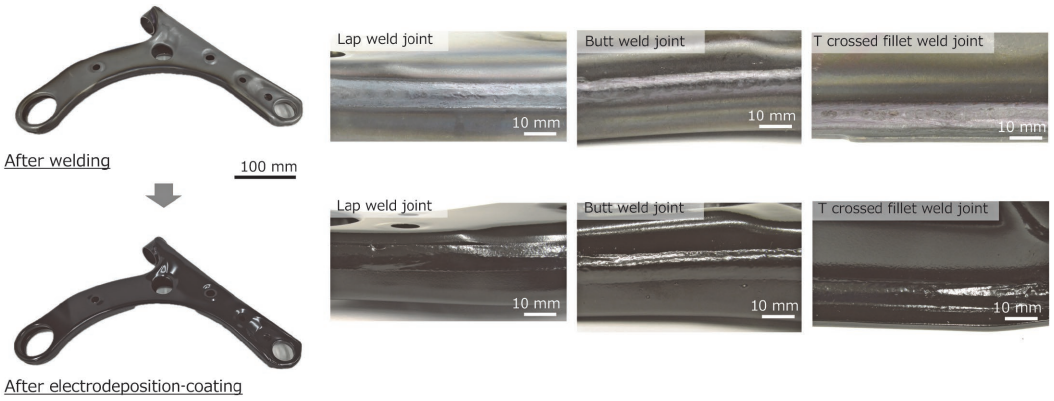

Fig. 8 Trial Lower Control Arm and bead appearance at unique welding position

the weld metal of the welding joint using wire B, which exhibited the best results in the plane bending fatigue test, is approximately HV 300.

In summary, increasing the hardness of the weld metal near the toe, which is subject to concentrated stress, is an effective means of improving the fatigue properties of lap fillet weld joints.

3. Application to actual parts

Since wire B exhibited excellent corrosion resistance and fatigue strength in laboratory tests, we evaluated its weldability and electrodeposition-coatability on actual parts. Specifically, we conducted testing on a lower control arm made from 980 MPa-grade steel sheet (thickness 2 mm^t). This steel, produced by Mazda Motor Corporation, reduces component weight by approximately 25% compared with parts made from conventional 780 MPa-grade steel sheet.

Fig. 8 (top) shows the lower control arm and its main welds, created using wire B. Good weldability was confirmed for the three types of joints required for this part, namely, butt welds, lap welds, and T-crossed fillet welds. One drawback of composite wire is its low rigidity, causing concerns regarding wire target performance during robot welding; however, defect-free weld beads were achieved. Fig. 8 (bottom) shows the lower control arm after cationic electrodeposition-coating. The wire has good electrodeposition-coatability, and the expected effects of combining slag-deconcentrating wire with a high-argon welding process have been confirmed in actual parts.

Conclusions

Ultra-high-tensile-strength steel sheets are being developed to reduce the thickness of automotive suspension parts and thereby reduce vehicle weight. Adding alloys to steel sheet to increase tensile-strength also increases slag, which interferes with electrodeposition-coatability. Perforation caused by rust reduces the functional life of thin steel sheet. To overcome these challenges, we developed a high-argon welding process technology that increases strength while reducing slag and improves corrosion resistance through alteration of the slag. In selecting welding consumables for high-tensile-strength steel, we chose composite wire for its productivity and procurement cost. In the automotive field, although stainless steel composite wire has been used for exhaust system parts, it is almost never used for suspension parts. The component manufacturers that made application of our composite wire possible rated it highly in terms of weldability and productivity. We anticipate that this development will be recognized as a solution technology for reducing the weight of vehicle bodies in the automotive field and that the scope of use will expand. We will continue to bring a green society to fruition through our joining technology.

Finally, we would like to express our sincere appreciation to Mazda Motor Corporation and Yorozu Corporation for their collaboration in this joint development, including in the evaluation of corrosion resistance, weldability, and durability of actual parts.

References

1) M. Tanaka et al. Mazda Technical Review. 2017, No.34, pp.123-124.
2) M. Tanaka et al. Mazda Technical Review. 2018, No.35, pp.27-28.
3) R. Suzuki et al. R&D Kobe Steel Engineering Reports. 2017, Vol.66, No.2, pp.64-66.
4) H. Kinashi et al. R&D Kobe Steel Engineering Reports. 2023, Vol.72, No.1, pp.81-82
5) R. Yamasaki et al. R&D Kobe Steel Engineering Reports. 2019, Vol.69, No.1, pp.98-104.

Dissimilar Metal Joining Technology, SP-ray™, for Realizing Circular Economy

Dr. Kyohei MAEDA*1

*1 Application Technology Center, Technical Development Group (currently Technology Strategy & Planning Department)

Abstract

The industrial sector has recently placed increasing importance on material recycling to realize a circular economy. Mechanical fastening is the mainstream joining method for dissimilar metals in automobiles. Although this method assures high joint strength, disassembly of these joints is complicated. It is not the optimal joining method from the viewpoint of the material separation required for recycling. Against this backdrop, a laser joining technology, SP-ray™, which uses cold-spray coating as an intermediate layer, has been developed as a dissimilar metal joining method that achieves high joint strength together with assuring ease of disassembly. This paper presents the results which show that SP-ray™ joints can achieve joint strength equivalent to that achieved by mechanical fastening, and that heat treatment renders the steel and aluminum parts separable.

Introduction

Efforts toward a decarbonized society are being promoted worldwide, with Western countries, and Japan aiming for carbon neutrality by 2050.[1] Vehicles emit more CO_2 per unit volume of cargo transported in comparison with rail and vessel transport and account for about 15% of Japan's total emissions.[2] As such, vehicles have a significant impact on global warming, and carbon emissions from this mode of transport must be reduced. Against this backdrop, vehicle electrification has been progressing in recent years, with electric vehicles (EVs) that run only on a motor rapidly gaining popularity. EVs reduce the environmental burden of vehicle operation but require high-capacity batteries of around 60 to 100 kWh to ensure the same driving range as conventional internal combustion engine vehicles.[3] Since high-capacity batteries are heavy and thus reduce efficiency, one of the challenges in EV design is to reduce the overall weight of the vehicle, including the battery.[3), 4]

Most of a vehicle's parts are steel, so attempts to reduce weight have often centered around increasing the tensile-strength of steel sheets to reduce part thickness. Multi-material parts combining lightweight materials such as aluminum alloys with high-tensile-strength steel sheets have started becoming more common, especially in luxury vehicles in Europe and the United States. For example, aluminum alloy sheets are used for exterior panels such as hoods and doors, extrusions are used for reinforcing parts such as bumper reinforcements and door intrusion beams, and die castings are used for components with complex shapes such as strut towers and subframes.[5), 6] In EVs, aluminum extrusions and die castings are used for battery boxes.[7), 8]

One challenge in manufacturing multi-material vehicle bodies is joining dissimilar metals. Resistance spot welding and laser welding were the traditional methods for assembling steel vehicle bodies. However, weak intermetallic compounds (IMCs) such as $FeAl_3$ and Fe_2Al_5 are produced when steel and aluminum alloys are welded together, making it difficult to achieve high joint strength. Therefore, mechanical fastening, which does not involve melting the joint, is generally used nowadays. The most widely used joining methods are SPR (self-piercing rivets) and FDS® (flow-drill screws, trademark EJOT GmbH & Co. KG), shown in **Fig. 1**. A given vehicle model may require several thousand SPR joints and several hundred FDS® joints on a single vehicle body. SPR, which involves the use of a punch and die to drive rivets into the parts to be joined, has recently become feasible for sheet

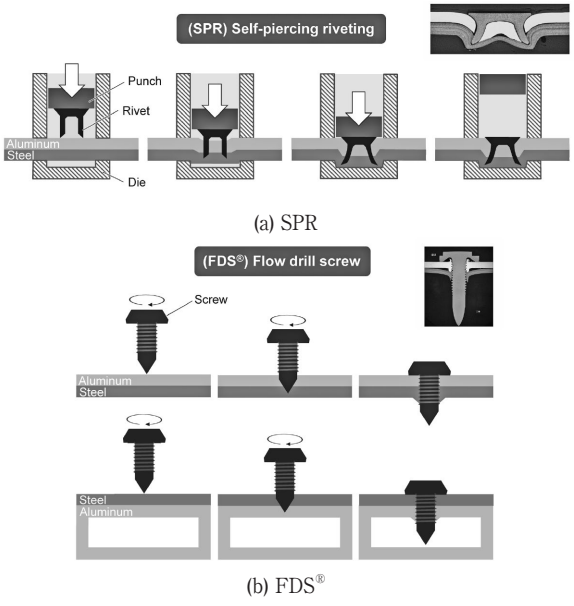

Fig. 1 Schematic illustrations of (a) SPR, (b) FDS®

assemblies including high-tensile-strength steel sheets.

However, it can be difficult to insert a punch and die into the cavity of hollow parts such as aluminum extrusions, invalidating this as a potential method. FDS®, a joining method employing single-side access, is used for such materials. FDS® is highly robust and maintains strength.[3] However, it has as a relatively long joining time of about 2 to 3 seconds,[9] requires pilot holes for high-tensile-strength steel sheets, and precludes a flat surface at the joint because the head and shaft of the screw protrude. However, there is a limited number of automated joining methods employing single-side access; FDS® is currently the mainstream method for joining high-tensile-strength steel sheets and hollow aluminum alloy parts.

Reuse and recycling are also major issues with multi-material components. Key concepts pertinent to vehicle carbon emissions include tank-to-wheel (TtW) emissions, which comprises only emissions from driving, and well-to-wheel (WtW) emissions, which include emissions from fuel production as well. Another concept that has recently gained popularity is that of the life cycle assessment (LCA). This assessment evaluates carbon emissions from the entire process, including the procurement of raw materials and the production, disassembly, and disposal of parts and vehicle bodies. Depending on the method of power generation, the production of a new aluminum alloy ingot can generate up to 4 - 5 times more carbon emissions than steel ingot. Furthermore, the production of recycled aluminum alloy reduces carbon emissions by more than 90% compared with the production of new ingot.[10] Therefore, the reuse and recycling of aluminum alloy is crucial in terms of LCA. There are already some car models that make use of recycled aluminum.[6]

In such cases, it is necessary to have a method for disassembling joints of dissimilar metals to retrieve the aluminum alloy from the multi-material vehicle body. The aforementioned mechanical fastening methods would require the laborious task of disassembling one joint at a time. Although it seems viable to consider soluble adhesive as a joining method[11], vehicle manufacturing conditions are usually not conducive to adhesive for assembly because of rust-preventive oil and oil from hydraulic presses adhering to surfaces. Adhesive must also be kept cool to maintain performance, complicating storage and logistics.[12]

To overcome these challenges, we developed SP-ray™ Note 1), an indirect laser joining method for steel and aluminum alloys. This dissimilar metal joining method uses a cold-spray coating as an intermediate layer. It yields excellent strength and ease of disassembly, can be used with high-tensile-strength steel sheets, is a single-side access technique, and supports high-speed assembly. This paper describes the basic concept of SP-ray™, including its joint strength and disassembly properties.

1. Basic concept of SP-ray™

Fig. 2(a) depicts the SP-ray™ process. First, a steel coating is deposited on the aluminum alloy by cold-spraying, a type of thermal spraying method. A steel sheet is then layered over the steel coating and laser welded to that coating. Fig. 2(b) depicts the structure. The steel coating is firmly joined to both the steel sheet and the aluminum alloy by different mechanisms for high joint performance without unnecessary melting of the aluminum alloy during laser welding. Unlike other thermal spraying methods, cold-spraying occurs at a temperature at which the powder does not melt, resulting in a coating suitable for welding with almost no oxidation. The resulting adhesion strength is about 50-100 MPa, depending on the material and process conditions, which is higher than the conventional thermal spraying method of plasma spraying.[13]

Although there is no consensus regarding the mechanism of adhesion in cold-spraying, a leading

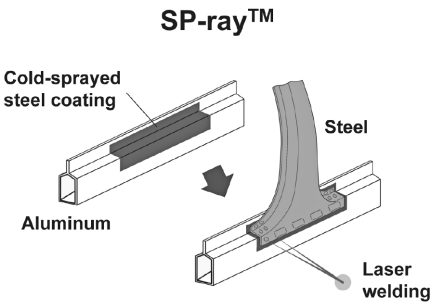

(a) schematic illustration of whole process

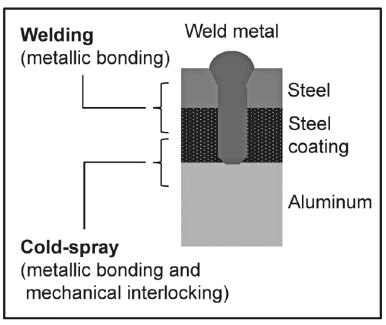

(b) joining mechanism

Fig. 2 (a) Schematic illustration of whole process, (b) joining mechanism of SP-ray™

Note 1) SP-ray is a trademark of Kobe Steel (6738793).

hypothesis is that there is solid-state bonding or mechanical interlocking (anchor effect) at the interface.[14] Another dissimilar metal joining technology that uses welding, like SP-ray™, is weld bonding. This method combines the use of welding and adhesive. However, as stated previously, adhesives are difficult to manage and result in a bond strength of about 30 MPa[15], which is less than that of cold-spraying. Hence, Kobe Steel's research centers around SP-ray™.

2. SP-ray™ joint properties and effect of cold-spray intermediate layer

Fig. 3(a) shows the cross-section of an SP-ray™ joint fabricated by laser welding a 1.5 GPa-grade steel sheet (thickness 1.4 mm) and a cold-spray sample. For comparison, Fig. 3(b) shows the cross-section of a direct-laser-welded joint without cold-spray coating. The cold-spray sample comprises AA7204-T6 (thickness 3 mm) with a 2 mm thickness steel coating made from pure iron powder. Nitrogen at 1,273 K and 5 MPa was the process gas for cold-spraying. The direct-laser-welded joint was created using a 5 mm thickness sheet of AA7204-T6 to match the total sheet thickness at the SP-ray™ joint. Welding was performed under the conditions in **Table 1** using a fiber laser with a wavelength of 1,070 nm as the laser oscillator. Whereas the weld metal of the direct-laser-welded joint has pits

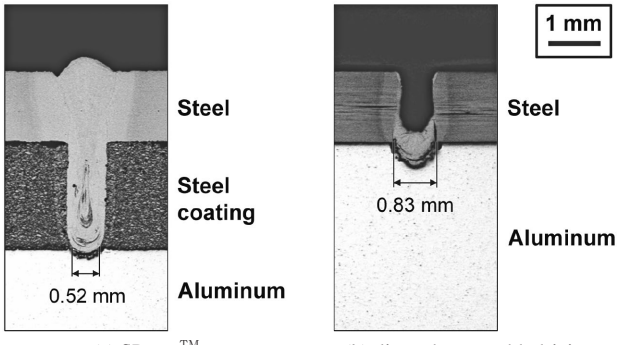

(a) SP-ray™ (b) direct laser welded joints

Fig. 3 Cross-section image of (a) SP-ray™, (b) direct laser welded joints

Table 1 Laser welding conditions

Spot size (μm)		330
Power density ($\times 10^6$ W/cm^2)	Without coating	2.6
	With coating	4.4
Scanning speed (mm/s)		67
Bead shape		Circle
Weld diameter (mm)		ϕ12

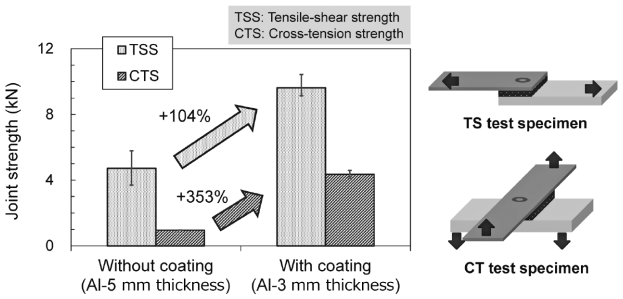

Fig. 4 Comparison of joint strengths between SP-ray™ and direct laser welding

and cracks, the SP-ray™ joint has a sound weld nearly free of weld defects. **Fig. 4** compares the joint strengths of the SP-ray™ and direct-laser-welded joints. SP-ray™ yields significantly greater joint strength in comparison with direct laser welding in terms of its tensile-shear strength (TSS), at approximately two times greater, and its cross-tension strength (CTS), at approximately 4.5 times greater. A previous study showed the TSS of an FDS® joint in a sheet assembly of high-tensile-strength steel (1.0 to 1.6 mm thickness, 0.6 to 1.5 GPa-grade high-tensile-strength steel sheet as base metal) and aluminum alloy (3.0 mm thickness) to be 6 to 10 kN.[16] Notably, SP-ray™ can provide the same TSS as FDS®.

3. Ease of disassembly of SP-ray™

3.1 Disassembly by heating using an atmospheric furnace

The cold-spray sample used in the SP-ray™ joint has an aluminum alloy substrate and a steel coating, so a thick IMC layer on the order of several dozen micrometers forms at the interface upon heating to a high temperature, as shown in **Fig. 5**. This characteristic can be exploited to separate the joined steel and aluminum alloy. **Fig. 6** shows images of the surface and cross-section of the SP-ray™ joint fabricated with the same sheet assembly as in Section 2 after heat treatment at 600℃ for 15-60 minutes in an atmospheric furnace. Heating for 30 minutes or more causes peeling at the interface between the steel coating and the aluminum alloy, making it possible to separate the joint into the steel and the aluminum alloy. **Fig. 7** shows a mapping analysis of the coating side of the peeled interface using an electron probe microanalyzer (EMPA). An extensive amount of Al was detected, suggesting fracture in the IMC layer. Furthermore, point analysis via EPMA reveals a weak IMC layer with a higher composition ratio of Al than Fe, such as in $FeAl_3$ or Fe_2Al_5. Since Al diffuses into Fe at

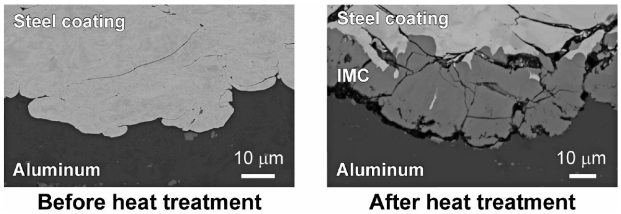

Fig. 5 SEM images of interface between cold-spray coating and aluminum before and after heat treatment

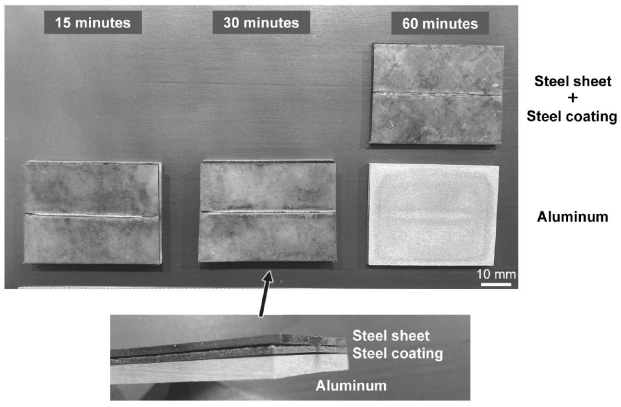

(a) surface

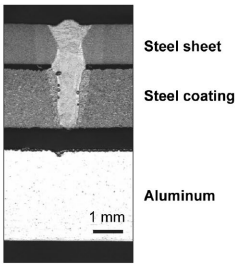

(b) cross-section images

Fig. 6 (a) surface, (b) cross-section images of SP-ray™ joint after heat treatment

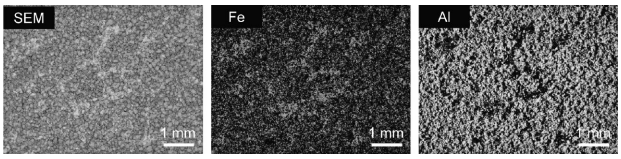

Fig. 7 Result of mapping analysis at surface of cold-spray coating, peeled from aluminum

temperatures above about 400℃,[17] IMCs should not form at the interface between the coating and the aluminum alloy during paint baking at around 170℃ for a few dozen minutes (typical parameters in vehicle manufacturing).

Based on the information above, when an SP-ray™ joint is heat treated at a high temperature, a weak IMC layer develops over time, and thermal stress caused by differing coefficients of linear expansion at the interface between the steel coating and aluminum alloy causes fracture in the IMC layer, enabling separation of the steel and aluminum

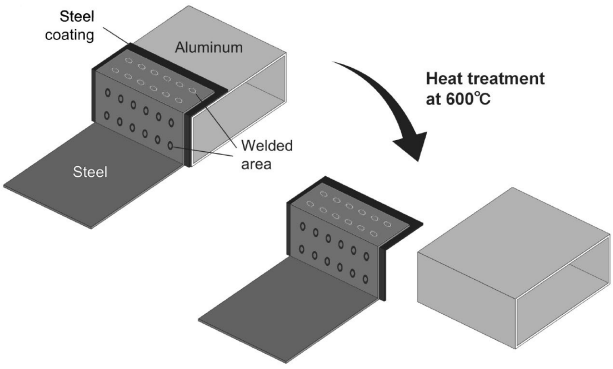

(a) schematic illustration

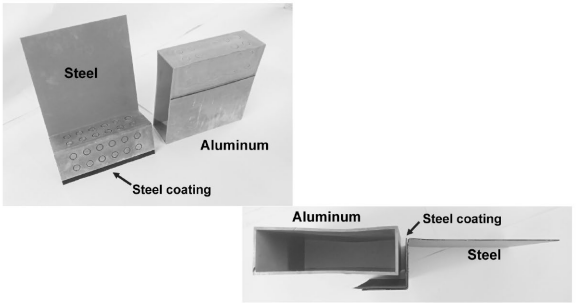

(b) surface view after heat treatment

Fig. 8 Disassembly of SP-ray™ joint with 24 laser welded areas: (a) schematic illustration, (b) surface view after heat treatment

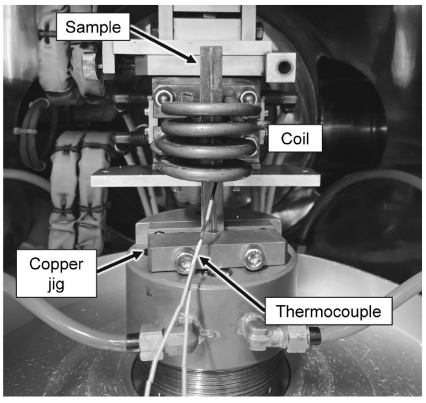

Fig. 9 Appearance of high-frequency induction heating machine

alloy. This method is also effective for disassembling multiple weldments in a sample in a single round of heat treatment (e.g., **Fig. 8**).

3.2 Disassembly using high-frequency induction heating

The previous section described how the SP-ray™ joint can be disassembled upon heat treatment. However, it is best to minimize heat treatment time from the perspective of reducing cost and environmental burden.

This led us to research the feasibility of a high-frequency induction heater (**Fig. 9**), which heats

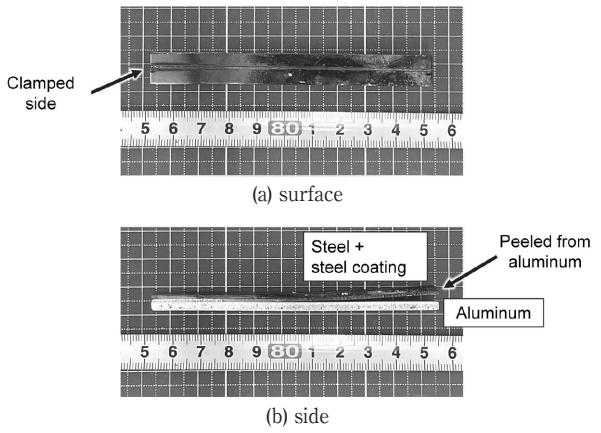

Fig.10 Surface view of SP-ray™ joint after high-frequency induction heating: (a) surface, (b) side

specimens much faster than an atmospheric furnace. We tested the same sheet assembly with the SP-ray™ joint as in Section 2. All specimens were 100 mm × 20 mm. We placed a 35 mm section at the center of the joint in the longitudinal direction into the coil and subjected it to high-frequency induction heating. For temperature control, a thermocouple was centered in the longitudinal direction on the 1.5 GPa-grade steel sheet. One end of the joint was clamped in place by a copper jig, and it is assumed that the temperature in that area did not rise to the specified level due to heat dissipation by the jig. **Fig.10** shows the sample after heat treatment at 600℃ for 15 minutes. The coating peeled off the aluminum alloy a substantial distance from the jig, indicating that high-frequency induction heating may enable faster disassembly than furnace heating.

Conclusions

Since the 1990s, automakers around the world have been working to improve engine efficiency, reduce vehicle weight, and develop electric and fuel cell vehicles to mitigate global warming. Such efforts are projected to intensify to foster carbon neutrality. Multi-material components will be a key pathway toward further weight reduction while safeguarding collision safety, necessitating an understanding of the advantages and disadvantages of both steel and aluminum alloys so each may be used as effectively as possible. As one of the few manufacturers offering both steel and aluminum alloys, Kobe Steel will contribute to reducing carbon emissions through developments not only in materials but also in automobile design. SP-ray™, the joining method introduced in this paper, is a highly reliable dissimilar metal joining method that enables ease of disassembly. This technology will support safety and weight reduction in vehicles and will foster a circular economy, in turn advancing the objective of a carbon-neutral society.

References

1) Ministry of the Environment. https://ondankataisaku.env.go.jp/carbon_neutral/about/. Accessed 2023-04-21.
2) Ministry of Land, Infrastructure, Transport and Tourism. https://www.mlit.go.jp/sogoseisaku/environment/sosei_environment_tk_000007.html. Accessed 2023-04-21.
3) T. Tarui. State of the arts multi material technologies in automotive industry. Journal of Japan Institute of Light Metals. 2022, Vol.72, No.3, pp.99-106.
4) T. Sakurai. Transformation of automotive electrification and aluminum technology. Journal of Japan Institute of Light Metals. 2022, Vol.72, No.12, pp.713-716.
5) J. Naito et al. R&D Kobe Steel Engineering Reports. 2019, Vol.69, No.1, pp.60-64.
6) Y. Ureshino. Journal of The Surface Finishing Society of Japan. 2022, Vol.73, No.8, pp.380-383.
7) S. Enderle et al. Audi e-tron. Euro Car Body, 2019.
8) M. Rössinger et al. Volkswagen ID.4, Euro Car Body, 2020.
9) J. Skovron et al. Journal of Manufacturing Science and Engineering. 2015, Vol.137, No.5, 051019.
10) S. Aoki. Journal of Japan Institute of Light Metals. 2013, Vol.63, No.7, pp.260-270.
11) C. Sato. Journal of the Adhesion Society of Japan. 2008, Vol.44, No.4, pp.136-141.
12) K. Himuro et al. Journal of the Adhesion Society of Japan. 2017, Vol.53, No.8, pp.283-289.
13) Y. Shimizu. Journal of The Surface Finishing Society of Japan. 1990, Vol.41, No.10, pp.968-973.
14) K. Sakaki. Journal of The Surface Finishing Society of Japan. 2008, Vol.59, No.8, pp.490-494.
15) C. Sato. Journal of Network Polymer, Japan. 2018, Vol.39, No.2, pp.91-96.
16) L. Kim et al. Journal of Manufacturing Processes. 2020, Vol.57, pp.400-408.
17) M. Kutsuna et al. QUARTERLY JOURNAL OF THE JAPAN WELDING SOCIETY. 2003, Vol.21, No.2, pp.282-294.

A portion of this article was published in Journal of Society of Automotive Engineers of Japan Vol.77, No.7, No.20234354, July 2023 (Society of Automotive Engineers of Japan, Inc.) and has been reprinted (with some revisions and additions) with permission from the journal.

Structure and Characteristics of Highly Durable Fuel Cell Bipolar Plate Material, NC Titanium

Toshiki SATO*1 · Jun SUZUKI*2

*1 Materials Research Laboratory, Technical Development Group
*2 Titanium Plant, Titanium Unit, Advanced Materials Business

Abstract

Bipolar plates are vital elements of fuel cell vehicles which are expected to be a key technology for reducing CO_2 emissions. They are required to have many functions and properties, such as acting as flow channels for fuel gas and acting as current collectors, also resisting corrosion, and possessing thinness for downsizing and lightening. Since several hundred bipolar plates are installed in each fuel cell vehicle, their productivity and cost reduction are also essential. Hence, Kobe Steel has developed NC (nano-carbon composite-coated) titanium, the world's first pre-coated bipolar plate material that meets the above requirements. NC titanium is installed in vehicles such as the fuel cell vehicle MIRAI, which Toyota Motor Corporation launched in 2020. This paper explains the development concept, structure, and characteristics of NC titanium.

Introduction

The transportation sector accounts for 20% to 25% of carbon emissions, making it a primary source of global warming,[1] and thus reducing carbon emissions a key issue for the industry. This has led to a shift from internal combustion engine vehicles toward electric vehicles, including fuel cell vehicles. Fuel cell vehicles run on electricity produced by the reaction between hydrogen and oxygen. Because they only emit water, these are clean vehicles free of carbon emissions. There are several types of fuel cells, but the ones used in vehicles are polymer electrolyte membrane fuel cells (PEMFC), which are characterized by low-temperature operation, low size and weight, and quick startup.

One of the core components of a PEMFC is the bipolar plate. Automotive fuel cells contain hundreds of bipolar plates, each about the size of a sheet of A4 paper. They must be thin to minimize size and weight, yet strong enough to withstand shock during vehicle operation, which is why they are most commonly made of metal. The bipolar plate serves not only as a flow channel for hydrogen, oxygen, and the water generated, but also as a current collector, which collects and conducts electrons generated by the reaction through its surface. Metal bipolar plates have a surface treatment that ensures both conductivity and corrosion resistance. High productivity and low cost are further important issues for bipolar plates. The pre-coating method of production, in which the metal foil coil undergoes continuous surface treatment and is then press-formed into a bipolar plate, supports these factors.[2), 3)] However, pre-coated bipolar plates have not been incorporated into a vehicle released to market because press-forming damages the surface treatment, degrading performance.

In response, Kobe Steel developed the world's first pre-coated titanium material for bipolar plates: NC (nano-carbon composite-coated) titanium, which exhibits both surface conductivity and corrosion resistance.[4)] This material is used in vehicles such as the Mirai fuel cell vehicle, which Toyota Motor Corporation released in 2020.[5)] This paper covers the development concept, structure, and features of NC titanium.

1. PEMFC structure and key characteristics of metal bipolar plates

To achieve high output in PEMFCs for vehicles, hundreds of layers of cells, the foundational unit of a fuel cell, are stacked. **Fig. 1** shows a schematic illustration of a cell. The center of the cell is a polymer electrolyte membrane (PEM), which is a proton conductor, with a Pt catalyst layer on both sides. On either side of the PEM is a gas diffusion layer (GDL) made of carbon fiber. Outside each GDL is a bipolar plate sandwiching the entire assembly. Since one cell uses two bipolar plates, the fuel cell module of a vehicle in turn uses several hundred bipolar plates. Bipolar plates must therefore be lightweight and thin to fit in the limited space inside the vehicle, yet strong enough to withstand shock during vehicle operation. In addition, as shown in Fig. 1, the bipolar plate serves as a flow channel for fuel gas and the water generated, so this component must be able to be press-formed into the shape of the flow channel. Furthermore, the bipolar plate acts as a current collector, collecting and discharging through its surface the electrons generated by the hydrogen decomposition reaction on the catalyst on the hydrogen gas side. As such, it must have high surface conductivity, or in other words, low surface resistance (called contact

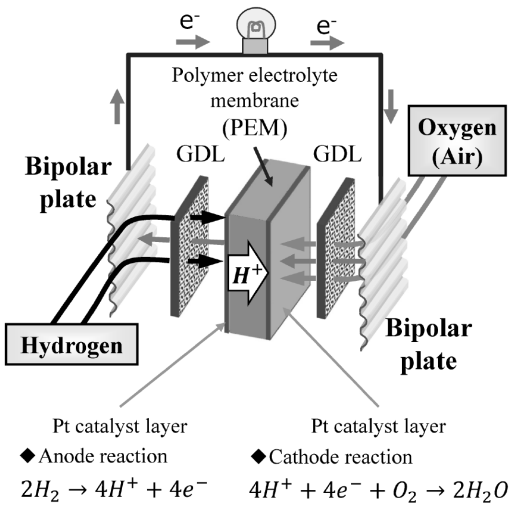

Fig. 1 Schematic structure of a PEMFC[9]

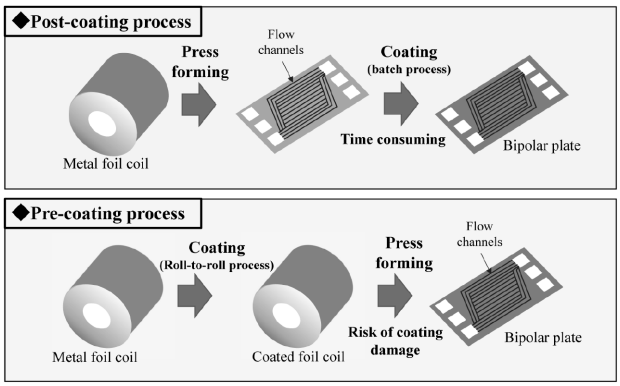

Fig. 2 Two typical production processes for metal bipolar plates[9]

resistance). The bipolar plate must also be corrosion resistant because the inside of the fuel cell is an acidic corrosion environment where the fluorine and sulfonic acid ions of the polymer electrolyte membrane are released. Corrosion of the bipolar plate not only reduces surface conductivity, but also causes the release of metal ions that contaminate the catalyst and inhibit the conduction of hydrogen ions in the polymer electrolyte membrane.[6] In particular, iron ions act as a catalyst to decompose the by-product hydrogen peroxide and generate hydroxyl radicals. Hydroxyl radicals destroy the polymer electrolyte membrane and reduce fuel cell performance.[7] This is why corrosion-resistant metals such as stainless steel and titanium are used for metal bipolar plates.[4), 8)] Corrosion-resistant metals have this property because they form a passive layer, which is a natural oxide film several nm to several dozen nm thickness, on their surfaces. However, the conductivity of the passive layer decreases in an acidic corrosion environment, making surface conductivity and corrosion resistance mutually exclusive. Therefore, a surface treatment with high conductivity and corrosion resistance is required even for corrosion-resistant metals.

Additionally, fostering more widespread acceptance of fuel cells requires greater productivity and reduced cost of bipolar plates, of which hundreds are used in a single vehicle.

As shown in **Fig. 2**, there are two types of manufacturing methods for metal bipolar plates: the post-coating method, in which surface treatment occurs after flow channel press forming, and the pre-coating method, in which flow channel press forming occurs after continuous surface treatment of the metal foil coil.[9] The post-coating method is the mainstream method, but it is characterized by low productivity. Each piece of metal foil formed into a bipolar plate must be set up, processed, and retrieved individually for surface treatment - this one-by-one process is time consuming. Conversely, the pre-coating method has higher productivity and lower cost because there is no need to set up and retrieve individual bipolar plates for surface treatment. The disadvantage of this method, however, is that the surface treatment can be damaged during press forming. This leads to peeling, reducing electrical conductivity and corrosion resistance. As such, this method has not yet been implemented in live products.

2. Concept behind the development of surface-treated titanium for bipolar plates

Titanium is characterized by high corrosion resistance, meaning it is less likely to be released in an environment with high electrical potential; however, it is more expensive than stainless steel. W. Li et al.[10] tested the corrosion resistance of SUS316L and Grade 2 titanium, each coated with a conductive amorphous carbon film using titanium as an intermediate film. Testing conditions were designed to simulate start-up and shutdown conditions, which are the most severe corrosion environments in fuel cell vehicles. Specifically, a potential of 1.4 V (vs. SCE) was applied for 1 hour in a 0.5 kmol/m^3 sulfuric acid aqueous solution containing 2 ppm fluoride ions at 70℃. The authors reported pitting in the pinholes of the coating on SUS316L, but not on titanium. This means that defects such as pinholes in the coating are acceptable with titanium. As such, the surface treatment time can be reduced because there is no need to form a thick film to eliminate pinholes, and cracks in the surface treatment from press forming the flow channels are tolerable even if the base material is exposed. Therefore, the pre-coating method could be feasible. To summarize,

although using titanium increases the cost of the base material, curtailing surface treatment time and using the pre-coating method improve bipolar plate productivity, potentially yielding an overall cost reduction for the bipolar plate when considering everything from the base material to production.

However, pre-coating requires that the adhesion properties of the surface treatment support press forming. Hence, the concept behind developing surface-treated titanium for bipolar plates is to make pre-coating feasible by developing a coating with high corrosion resistance, high electrical conductivity, and adhesion properties that support press forming. NC titanium is the surface-treated titanium we developed in line with this concept. The next section covers the structure and features of NC titanium.

3. Structure, formation process, and features of NC titanium

3.1 Structure of NC titanium

Fig. 3 shows a cross-sectional SEM image of NC titanium.[11] The NC layer consists of a titanium oxide film 40 to 50 nm in thickness (gray area) and carbon nanoparticles dispersed in the film (black area). The carbon nanoparticles act as a conductive path, and the titanium oxide film ensures adhesion to the titanium substrate. The high corrosion resistance of the carbon and titanium oxide lends high corrosion resistance to the NC layer.

3.2 Formation process of NC titanium

Fig. 4 shows the formation process of the NC layer and cross-sectional SEM images of the titanium substrate after each process.[9] The formation process of the NC layer consists of a coating process in which the surface of the titanium substrate is coated with carbon nanoparticles; an NC formation process in which high-temperature oxidation is performed under low oxygen pressure; and post-processing, which includes processes such as removing excess carbon nanoparticles. Cross-sectional SEM images after high-temperature oxidation under low oxygen pressure show that the carbon nanoparticles are incorporated into the titanium oxide. Upon high-temperature oxidation of titanium under atmospheric pressure, oxygen generally diffuses from the surface of the titanium inward, causing

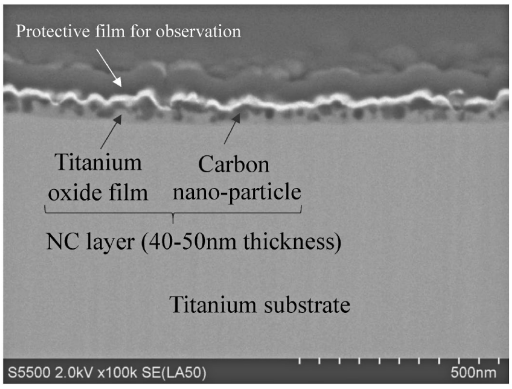

Fig. 3 Cross-sectional SEM image of NC titanium[11]

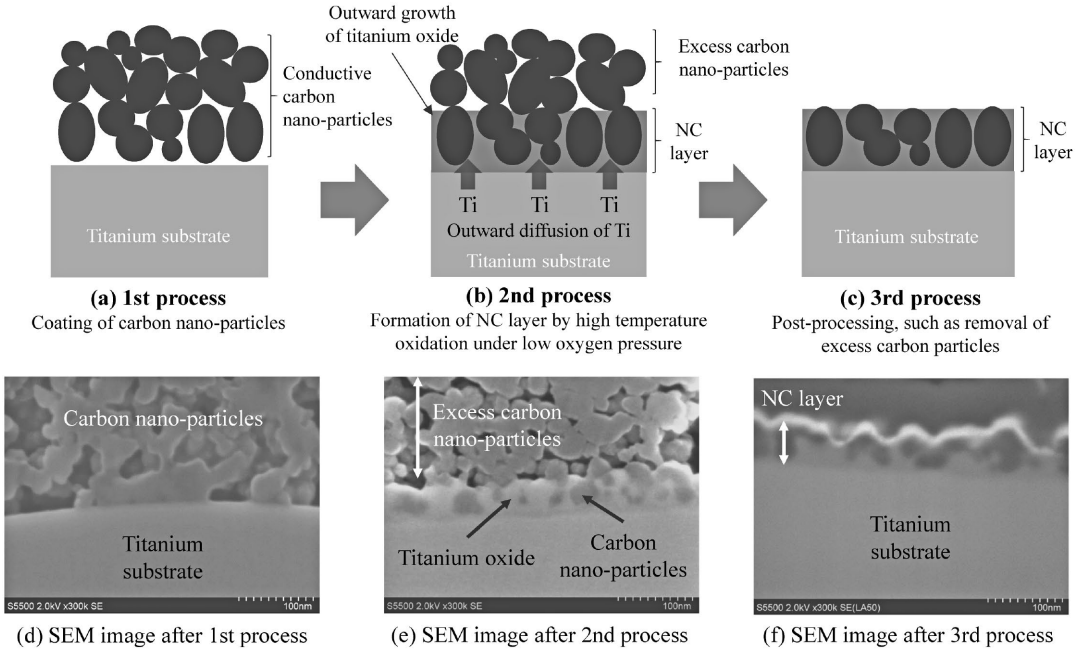

Fig. 4 NC titanium formation process (a), (b), (c) and cross-sectional SEM images after each process (d), (e), (f)[9]

titanium oxide to form in this same direction.[12)]

However, the authors had investigated the oxidation of Ti-Pd alloys pickled to precipitate Pd nanoparticles on their surfaces, from a low oxygen pressure to atmospheric pressure.[13)] At atmospheric pressure, a titanium oxide layer formed between the Pd nanoparticles and the Ti-Pd alloy due to inward oxidation, in line with conventional knowledge. However, at a low oxygen pressure, outward oxidation occurred, in which titanium oxide grew from the surface of the Ti-Pd alloy toward the Pd nanoparticles, and the Pd nanoparticles were incorporated into the titanium oxide layer. We developed an NC layer structure by exploiting the outward oxidation of titanium, which had not been reported on previously, and by replacing the Pd nanoparticles with economical carbon nanoparticles.

3.3 Features of NC titanium

3.3.1 NC titanium adhesion

Fig. 5 shows a cross-sectional TEM image of NC titanium after press forming.[11)] The NC layer remains adhered without peeling, even near the step in the surface created by the plastic deformation of titanium during press forming. This proves that NC titanium has sufficient adhesion to withstand press forming.

3.3.2 Contact resistance and durability of NC titanium

Fig. 6 compares the contact resistance of NC titanium with contact resistances measured for corrosion testing of coated stainless steel and titanium in bipolar plates of fuel cells as published in research over the six-year period from 2017 to 2022.[14)~20)] The films compared were those evaluated under the corrosion resistance test conditions most common in the research, that is, films subjected to a potentiostatic test involving immersion in an aqueous solution of 0.5 M sulfuric acid containing 2 to 5 ppm fluoride ions for 4 to 5 hours at 70 to 80℃ and the application of 0.6 V (vs. SCE). Contact resistance was measured before and after the potentiostatic test in the selected studies, and the

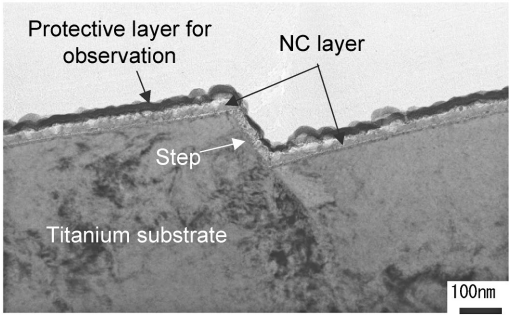

Fig. 5 Cross-sectional TEM image of NC titanium after press forming[11)]

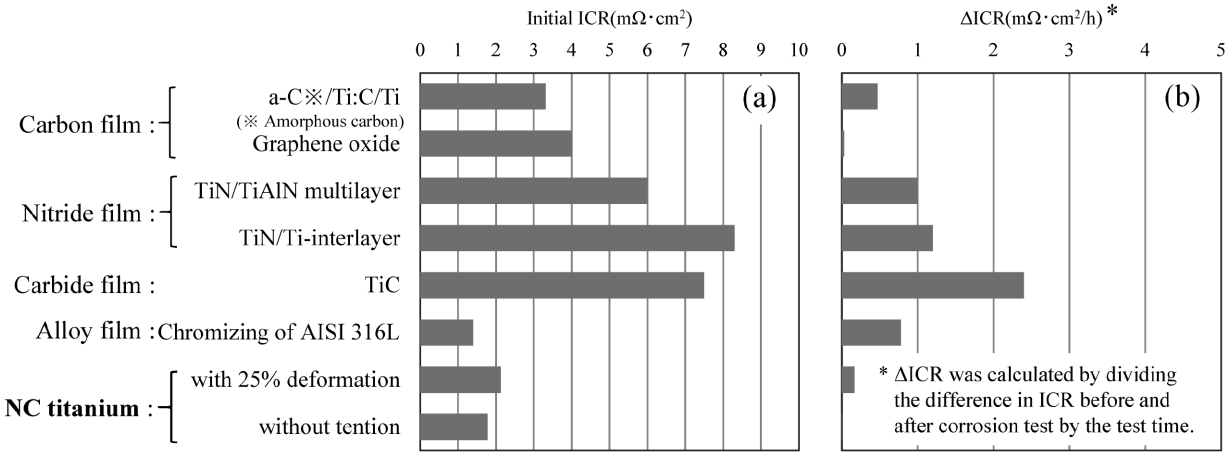

Corrosion test (potentiostatic test) conditions

	Coatings in the literature	NC titanium
Solution	0.5M H_2SO_4 +2-5ppm F^- with air or oxygen bubbling	0.5M H_2SO_4 +5ppm F^- with air bubbling
Temperature	70-80℃	80℃
Potential	0.6Vvs.SCE	0.6Vvs.SCE
Immersion time	4-5h	5h

Fig. 6 Comparison of interfacial contact resistance (ICR) before corrosion test (initial ICR) (a) and average increase rate of ICR (ΔICR) (b) of coatings studied in the literature and NC titanium[14)~20)]

comparison was limited to films whose contact resistance before the test was 10 mΩ·cm² or less, which is the target set by the U.S. Department of Energy (DOE). Corrosion resistance and conductivity testing results have been published for many different films. However, the results suitable for comparison are limited because of great variation in corrosion resistance test conditions and because most studies measure contact resistance only before corrosion resistance testing. Regardless, the types of films considered can be broadly classified into carbon, nitride, carbide, and alloy films, covering a fairly comprehensive breadth. To compare the films in the selected papers with NC titanium, the contact resistance of NC titanium was also measured in the same manner as in the papers: after immersion for 5 hours in a 0.5 M sulfuric acid aqueous solution containing 5 ppm fluoride ions at 80℃ with the application of a potential of 0.6 V (vs. SCE). To evaluate the durability of NC titanium after press forming, the same test was also performed on NC titanium subjected to 25% uniaxial tensile deformation. To compare durability, the average increase rate of contact resistance was calculated by dividing the difference in contact resistance before versus after the potentiostatic test by the duration of the potentiostatic test. The lower this value, the higher the durability. Fig. 6 shows that the initial contact resistance of NC titanium without tensile deformation and NC titanium with 25% tensile deformation is among the lowest of all the types of film, at about 1/5 or less of the contact resistance limit specified by the DOE.

Further, the average increase rate of contact resistance is lowest with NC titanium, at a value similar to carbon film. As such, NC titanium exhibits lower contact resistance and higher durability than other films, even after uniaxial tensile deformation in a way that simulates press forming.

3.3.3 NC titanium for improved bipolar plate productivity

Fig. 7 shows an NC titanium coil.[4] The productivity of NC titanium is exceptionally high because the NC layer forms quickly and because all NC titanium production processes are an integral part of the continuous manufacturing process of the titanium foil coil. In addition, the surface treatment process, which reduces fuel cell throughput, can be omitted by fuel cell manufacturers. As a result, bipolar plates can be manufactured simply by press forming NC titanium coils, improving fuel cell manufacturers' productivity and thus reducing expenditure.

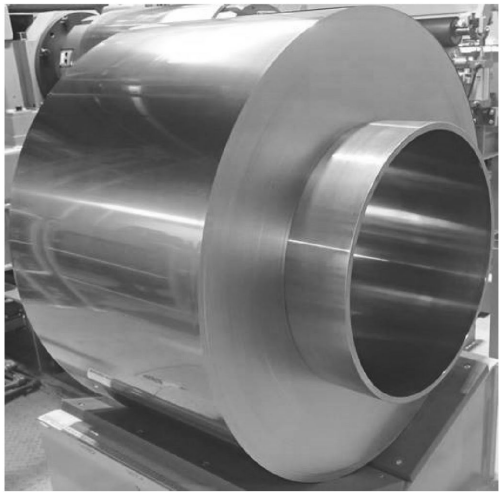

Fig. 7 Appearance of NC titanium foil coil[4]

Conclusions

The outward oxidation of titanium was discovered and exploited to develop a film used to create coated NC titanium, which has high corrosion resistance, high surface conductivity, and high adhesion, and has been implemented in the world's first pre-coated bipolar plate material. NC titanium is used in fuel cell electric vehicles such as Toyota Motor Corporation's Mirai, released in 2020, and Crown FCEV.

Since NC titanium is highly durable and lighter than stainless steel, it is expected to see application not only in passenger cars but also in equipment that must be made lighter, such as aircraft and drones, and in equipment that must be highly durable, including semi-trucks, buses, rail transport applications, and vessels.

References

1) CO_2 Emissions in 2022 - Analysis. IEA.
2) J. Huya-Kouadio et al. ECS Transactions. 2018, Vol.83, No.1, pp.93-109. doi:10.1149/08301.0093ecst.
3) S. Porstmann et al. Journal of Manufacturing Processes. 2020, Vol.60, pp.366-383. https://doi.org/10.1016/j.jmapro.2020.10.041.
4) T. Choda et al. R&D Kobe Steel Engineering Reports. 2022, Vol.71, No.2, p.78.
5) S. Mizuno et al. TOYOTA Technical Review. Mar 2021, Vol.66, pp.22-27.
6) T. Bohackova et al. Materials. 2021, Vol.14, p.2682.
7) H. Li et al. Journal of Power Sources. Vol.195, 2010, pp.8089-8093. doi:10.1016/j.jpowsour.2010.07.003.
8) [e Autopos Unboxing] # 4 World's first application of uncoated separator material, stainless Poss470FC! - Official POSCO Newsroom. Accessed 2024-06-19.
9) T. Sato et al. Handout of the Winter 2024 Fuel Cell Technology Committee Forum of the Society of Automotive Engineers of Japan, Inc.

10) W. Li et al. Diamond and Related Materials. 2021, Vol.118. https:// doi.org/10.1016/j.diamond.2021.108503.
11) T. Yamasaki et al. E&L (2023 Powertrains, Energy and Lubricants International Meeting). 2023, Proceeding.
12) K. Hauffe. Oxidation of metals. Plenum Press. 1965, pp.214-217.
13) T. Sato et al. Ti-2007 Science and Technology. Japan Institute of Metals and Materials. 2007, pp.1679-1682.
14) T. Sato. 15th World Conference on Titanium (Ti-2023), Proceeding.
15) W. Li et al. International Journal of Hydrogen Energy. 2021, Vol.46, pp.22983-22997. https://doi.org/10.1016/j.ijhydene.2021.04.132.
16) J. Wang et al. International Journal of Hydrogen Energy. 2019, Vol.44, pp.16909-16917. https://doi.org/10.1016/j.ijhydene.2019.04.245.
17) S. Mani et al. Journal of Materials Science. 2021, Vol.56, pp.10575-10596. https://doi.org/10.1007/s10853-020-05682-4.
18) J. Jin et al. Materials Chemistry and Physics. 2020, Vol.245. https://doi. org/10.1016/j.matchemphys.2020.122739.
19) J. Shi et al. International Journal of Hydrogen Energy. 2020, Vol.45, pp.10050-10058. https://doi.org/10.1016/j.ijhydene.2020.01.203.
20) Z. Dong et al. International Journal of Hydrogen Energy. 2019, Vol.44, pp.22110-22121. https://doi.org/10.1016/j.ijhydene.2019.06.099.

Tin-plated Copper Alloys for Replacing Gold-plated Terminals

Yutaro UEDA*1 · Masahiro TSURU*1 · Toshiyuki MITSUI*1
*1 Copper Rolled Products Plant, Copper Rolled Products Unit, Advanced Materials Business

Abstract

Plated copper alloys are used for automotive terminals. The terminal plating used in low-voltage circuits includes tin-plating and gold-plating. Tin is a general-purpose plating material that offers an excellent balance between cost and electrical reliability, while gold-plating is used in areas where electrical reliability is critical at low contact loads. Gold-plating, however, is subject to high manufacturing costs, and there is a need for tin-plating as a low-cost alternative. Therefore, attention has been focused on the fracture mechanism of the oxide film on a tin-plated surface, and by providing the surface with fine convex shapes of tin, low contact resistance has been obtained even under low contact loads. This paper introduces the performance of tin-plating for low contact pressure, which can partially replace gold-plating.

Introduction

The trends toward electrification and automation in vehicles entail an increase in the number of electrical components, and with this, the number of wires and terminals that connect these components.

Terminals must exhibit contact reliability to transmit electrical signals and power from the time the vehicle is manufactured until the end of its service life, which is why plated copper alloys are used for these components.

Tin and gold are the most common metals used for plating terminals in circuits with a voltage of 30 V or less and a current of 10 A or less (hereafter, low-voltage circuits).[1), 2)]

Tin-plating provides a good balance between cost and contact reliability and is used in a wide range of applications; however, it is inferior to gold-plating in terms of contact reliability. Gold-plating has good corrosion resistance, and although it is often used where contact reliability is critical,[1), 2)] it is very expensive, so there is a need for a low-cost alternative to reduce costs. As such, Kobe Steel developed a plating that is more economical than gold and has better contact reliability than tin-plating.

This paper introduces the performance of low-pressure-compatible tin-plating as an alternative to gold-plating.

1. Terminal plating and the required characteristics for terminal plating

1.1 Plating composition and structure

A comparison of reflow tin-plating and gold-plating, which are commonly used for automotive terminals, assists with describing the properties required of contact plating that can replace gold-plating. **Fig. 1** shows the cross-sections of plated copper alloys. Reflow tin-plating is a plating process in which a tin film is formed on a copper alloy by electro-plating, followed by heating above the melting point of tin (hereafter, the reflow process). This process creates an intermetallic compound layer of tin and copper (hereafter, copper-tin IMC layer) between the copper alloy and the tin film, and the surface is covered with tin.

Gold-plating is implemented as a two-layer structure of gold plated on a nickel substrate. Since gold is soft and prone to wear, plating with a small amount of hard alloy, such as cobalt or nickel, is a common practice with gold-plating to impart wear resistance.[1)]

1.2 Contact reliability

Contact reliability is one of the most important characteristics in considering substitutions for gold-plating. To ensure contact reliability, it is necessary to maintain low electrical contact resistance in the terminal contacts (hereafter, contact resistance). Contact resistance is the electrical resistance between mating surfaces. It is the sum of the film resistance, which is the electrical resistance of the film itself, and the constriction resistance due to the convergence of electric current, as expressed by Equation (1).[2), 3)]

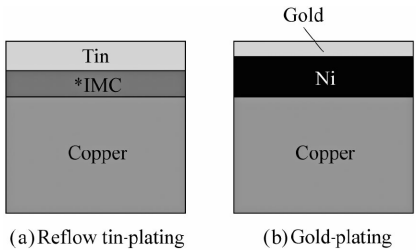

Fig. 1 Schematic images of cross section of plated copper alloys *IMC: Intermetallic compound layer of tin & copper

$$R = R_f + R_c \quad \cdots\cdots (1)$$

Here, R is the contact resistance (mΩ), R_f is the film resistance (mΩ), and R_c is the constriction resistance (mΩ).

Equation (2) expresses film resistance and constriction resistance when like metals are in contact.

$$R_f = \frac{\rho_f d}{\pi a^2},\ R_c = \frac{\rho}{2a} \quad \cdots\cdots (2)$$

Here, ρ_f is the film-specific resistance (Ωm), d is the film thickness (m), ρ is the metal-specific resistance (Ωm), and a is the radius of the contact surface (m).

Per Equation (2), film resistance decreases as film-specific resistance decreases, and constriction resistance decreases as the radius of the contact surface increases (i.e., as the contact area gets larger).

Fig. 2 shows the relationship between contact load and contact resistance for reflow tin-plating and gold-plating. Contact resistance was calculated based on the voltage drop measured by the four-terminal method applied to a flat-sheet-shaped specimen and a probe comprising a gold wire bent into a U-shape. The probe was pressed against the specimen and the voltage drop was measured while the downward force was gradually increased from 0.5 to 5 N. Although it is possible to incorporate sliding of the probe in this test,[4), 5)] we did not do so, ensuring gradual destruction of the oxide film to confirm the effect of oxide film destruction on contact resistance. Fig. 2 shows that the contact resistance of reflow tin-plating decreases significantly as the contact load increases, and that the rate of the decrease in contact resistance declines starting at 2.0 N. Gold-plating exhibits a lower contact resistance than reflow tin-plating from 0.5 to 5 N, however.

Oxide films generally exhibit higher resistance than the metal they form on, so areas with an oxide film are insulative. As a result, the conductive contact area becomes smaller and contact resistance increases due to increased concentration resistance.[2), 3)]

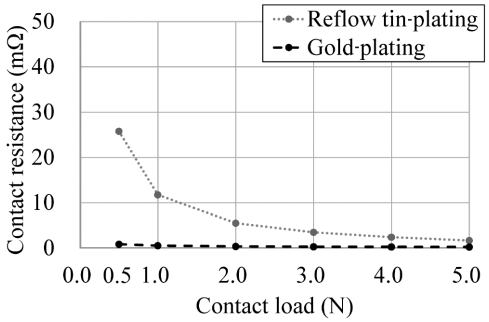

Fig. 2 Relationship between contact load and contact resistance of tin-plating and gold-plating

The surface of reflow tin-plating has a protective oxide film. In low-voltage circuits where dielectric breakdown is not a possibility, the oxide film cannot be mechanically destroyed by contact pressure alone, resulting in a higher contact resistance than with gold-plating. Gold-plating is only covered by a very thin oxide film of about a single molecule on the surface, in which case the tunneling effect ensures conduction.[2), 6)]

In reflow tin-plating, a thin, hard oxide film (Vickers hardness 16.5 GPa) forms on the soft tin (Vickers hardness 50 - 70 MPa).[7)] Here, the tin-plating deforms when a load is applied, but the oxide film cannot deform in tandem as the load increases and is broken. Thus, contact between the tin and gold is easily achieved.[4)] The destruction of the oxide film increases the contact area and decreases the concentration resistance, in turn decreasing contact resistance. Therefore, tin-plating is generally used where the contact load might be high and the oxide film can be sufficiently destroyed, whereas gold-plating is generally used in areas where contact reliability is critical and the contact load is low.[2)]

Tin-plating does not have the same contact reliability as gold-plating at low contact loads. Therefore, we developed tin-plating that can maintain contact reliability in low-voltage circuits even in terminals with low contact pressure. Here, low contact pressure is defined as the degree of load for which the contact resistance of tin-plating does not equal that of gold-plating.

2. Improving the contact reliability of tin-plating at low contact pressure

2.1 Mechanism of oxide film destruction in tin plating

As described above, tin-plating forms a highly resistive oxide film on the surface, the area covered by the oxide film becomes insulative, concentration resistance increases, and ultimately, contact resistance increases. Applying a contact load that can break the hard oxide film on the surface reduces contact resistance. Therefore, methods to reduce the contact resistance of tin-plating include suppressing the oxidation of tin and making the oxide film of the tin easier to destroy.

The oxidation of tin can be suppressed by using a precious metal that resists oxidation, such as gold or silver, or by incorporating an organic substance that inhibits oxidation. However, these methods are

not ideal because they increase costs and resource consumption in the plating process. This led us to research effective methods for mechanically destroying the oxide film of tin even under low contact load.

These include concentrating the contact load locally and increasing the contact load per unit area (surface pressure). To increase surface pressure, we developed a concept that involves creating fine convex shapes in the surface of the tin-plating.

2.2 Improving contact resistance by imparting convex shapes to the surface

To validate the concept, we developed a new tin-plating (hereafter, rough tin-plating) by creating fine convex shapes in the surface of reflow tin-plating. **Fig. 3** shows laser microscope images of the surface of the tin-plating and the arithmetical mean height Sa (ISO 25178). The reflow tin-plating is shown for comparison. The Sa of the rough tin-plating is higher than that of the reflow tin-plating, indicating a rougher surface. Sa is the arithmetical mean of the absolute values of the height from the mean plane of the surface. It extends the two-dimensional roughness parameter Ra into three dimensions.[8)]

Fig. 4 depicts the contact resistance test. It is common to plate male and female terminals with the same metal to preclude corrosion and thermal electromotive force due to contact between dissimilar metals.[9)] It is assumed that the tin-plating of the terminals will be in contact with each other. We placed the tip of the reflow tin-plating formed into a dome shape against the tin-plated sheet and measured the contact resistance.

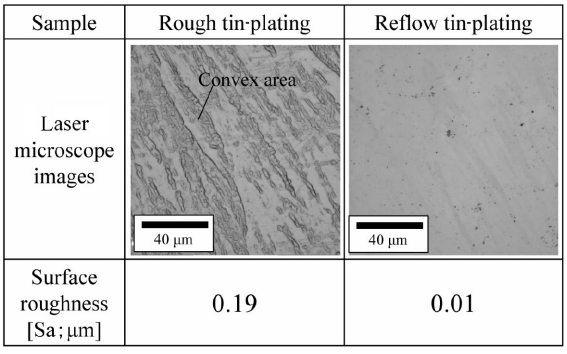

Fig. 3 Laser microscope images and surface roughness of tin-plating with different surface roughness

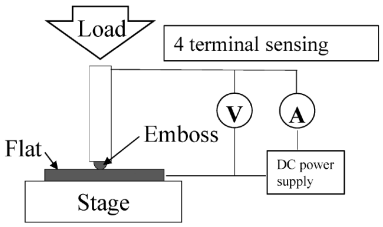

Fig. 4 Schematic image of contact resistance test

Fig. 5 shows the relationship between the contact load and contact resistance of the tin-plating. At a load of 0.2 to 0.8 N, the contact resistance of the rough tin-plating was less than that of the reflow tin-plating. At a load of 0.5 N, the contact resistance of the rough tin-plating was 4 mΩ, while that of the reflow tin-plating was 7 mΩ.

Fig. 6 shows the contact marks on the plated sample after applying a load of 0.5 N. The white circles indicate where deformation was observed by laser microscopy. We examined the cross-section near the center of the contact area, along the white dotted line. The reflow tin-plating has an overall convex shape in the contact area, whereas with the rough tin-plating, the apex of the convex tin area is lower than the surrounding area.

Fig. 7 shows the SEM images (backscattered electrons, BSE) near the center of the contact marks and outside the contact area of the plated sample. The white parts of the BSE images are tin, the gray parts tin oxide. Image processing was performed to make the tin white and the rest black. The entire surface outside the contact area of the rough tin-plating was covered with tin oxide, whereas tin and tin oxide were confirmed in the center of the contact area of the rough tin-plating and the reflow tin-plating. Additionally, the area ratio of tin was greater for the rough tin-plating. This means that the load partly destroyed the tin oxide film in the contact area, exposing tin on the surface. The contact marks show that the rough tin-plating had more dispersed islands of tin than the reflow tin-plating.

Fig. 8 depicts the contact areas. It is surmised based on the plating surfaces in Figs. 6 and 7 that with rough tin-plating, the load is concentrated in the convex area, destroying the tin oxide film on the surface and thereby reducing contact resistance.

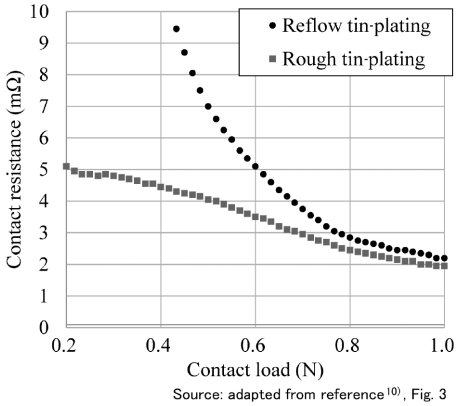

Source: adapted from reference[10)], Fig. 3

Fig. 5 Relationship between contact load and contact resistance of tin-plating with different surface roughness

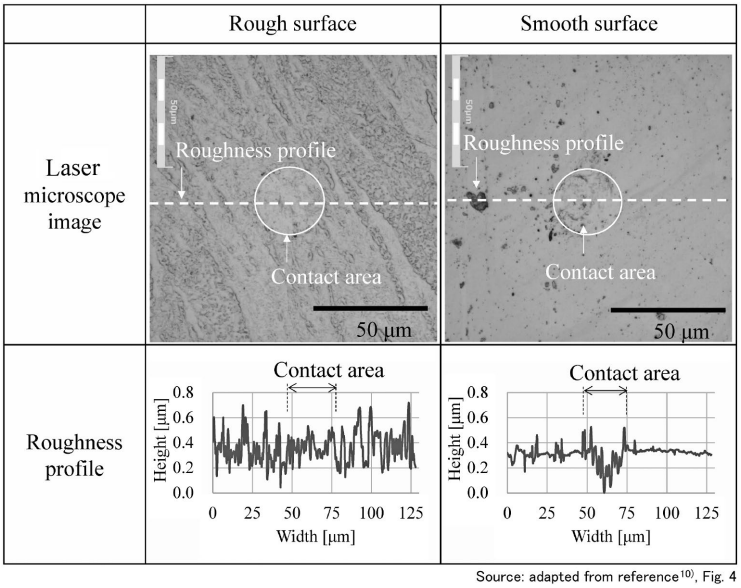

Source: adapted from reference[10], Fig. 4

Fig. 6 Laser microscope images of contact marks on the surface of test samples after applying 0.5 N load

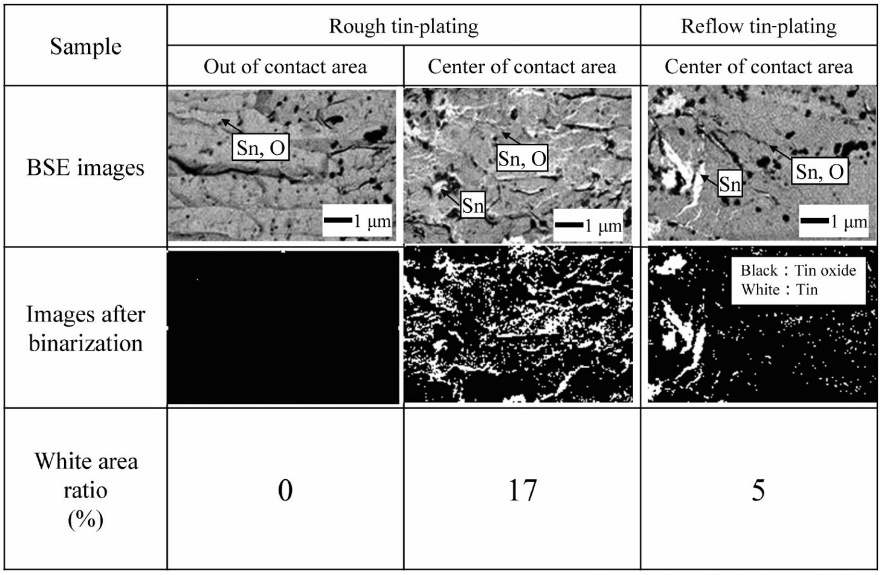

Source: adapted from reference[10], Fig. 6

Fig. 7 SEM images of contact area and outside of contact area

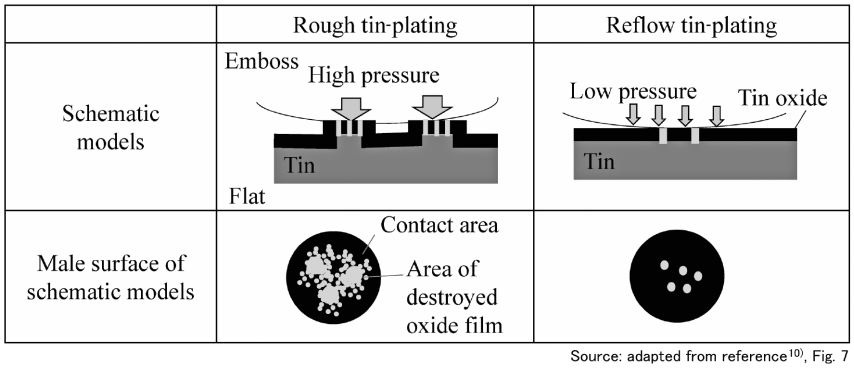

Source: adapted from reference[10], Fig. 7

Fig. 8 Schematic models of contact area

3. Low-pressure-compatible tin-plating that combines heat resistance, fretting wear resistance, and ease of terminal insertion

Automotive terminals must maintain low contact resistance even when subjected to heat and vibration. Reflow tin-plating is susceptible to forming tin oxide under such parameters, potentially increasing contact resistance. Therefore, necessities in replacing gold-plating include heat resistance to withstand high-temperature environments and fretting wear resistance to withstand temperature changes and vibration.[1), 2)]

3.1 Heat resistance

A vehicle's engine compartment usually gets hotter than its interior[11)]; accelerated life testing requires heat resistance temperatures of 150 -160℃.

Reflow tin-plating promotes mutual diffusion of the copper and tin in the material in a high-temperature environment, causing a copper-tin IMC layer to form.[3)] As such, the tin is depleted and a highly resistive copper oxide film forms on the surface, increasing resistance.[3)~5)]

An effective method of suppressing the diffusion of copper and tin and thereby improving heat resistance is to employ a three-layer structure in which there is a nickel layer under the copper-tin IMC layer of reflow tin-plating.[3)~5)]

3.2 Fretting wear resistance

Electrical contacts can become displaced due to thermal expansion and contraction caused by vibration during engine operation and vehicle travel, temperature changes in the environment, and heat generated by electricity.[3)~5)] This displacement abrades the plating, a phenomenon known as fretting wear. Soft tin is prone to fretting wear, potentially increasing contact resistance, so this phenomenon must be prevented. Exposing the copper-tin IMC layer on the surface improves fretting wear resistance.[3)~5)]

3.3 Coefficient of friction

Wire harnesses are connected manually during vehicle assembly. Therefore, efforts are underway to reduce the maximum insertion force for mating connectors to reduce physical stress on workers.[3)~5)] This means that the coefficient friction of the plating must be reduced, as this correlates to a connector's insertion force.[3)~5)] Running contrary to this objective is that reflow tin-plating is prone to wear because tin is soft. Specifically, wear of the tin could increase the coefficient of friction by presenting resistance during sliding.

Exposing the copper-tin IMC layer on the surface reduces the coefficient of friction.[3)~5)]

3.4 Low-pressure-compatible tin-plating

Fig. 9 depicts the surface and cross-section of low-pressure-compatible tin-plating, which comprises three layers to improve heat resistance: tin, copper-tin IMC, and nickel. The copper-tin IMC layer is partially exposed on the surface for fretting wear resistance and a low coefficient of friction. In addition, as described in Section 2, convex shapes were created in the topmost layer of the tin surface to improve contact reliability.

Fig.10 shows the relationship between the contact load and contact resistance of the plating before and after annealing. We studied contact resistance under a test load of up to 2.0 N to confirm the effect of an oxide film on this parameter. The contact resistance of reflow tin-plating increased significantly after annealing, whereas that of gold-plating and of low-pressure-compatible tin-plating remained low.

Exposure to high temperature accelerates the formation of the copper-tin IMC layer in reflow tin-plating. This depletes the tin, leading to the formation of a highly resistive copper oxide film on the surface and thereby increasing contact resistance.[3)~5)] As explained in Section 2, it is surmised that the convex shapes in the tin reduce initial contact resistance in the low-pressure-compatible tin-plating. It is also surmised that the contact resistance of the gold-plating and the low-pressure-compatible tin-plating remained low because the underlying nickel layer suppressed the diffusion of copper into the plated surface.[1), 3)]

Fig.11 depicts the fretting wear test equipment and conditions. A sheet-shaped specimen (Flat) and a specimen with a hemispherical protrusion with a radius of curvature of 1 mm (Emboss) were brought

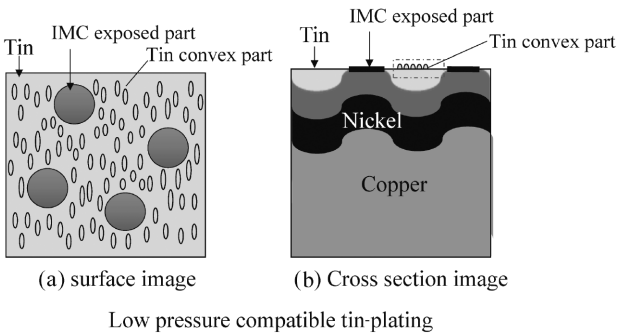

Fig. 9 Schematic models of low pressure compatible tin-plating

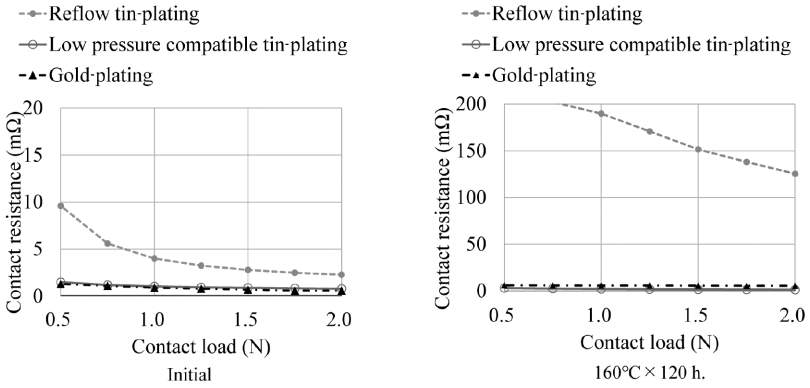

Fig.10 Relationship between contact load and contact resistance before and after 160℃×120 h. annealing

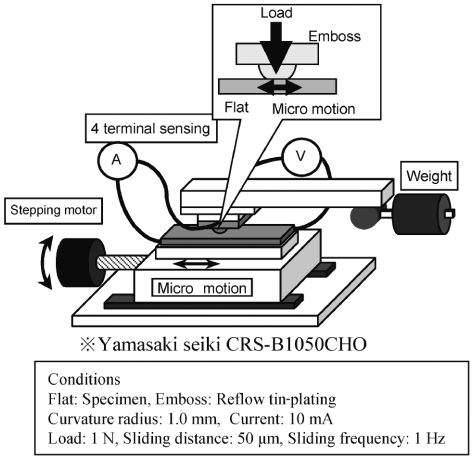

Fig.11 Schematic image of fretting test system

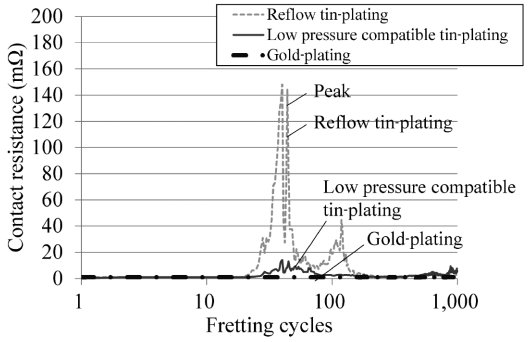

Fig.12 Changes of contact resistance of plating during fretting test

into contact, and a load of 1 N was applied. The sheet-shaped specimen was then slid repeatedly along a distance of 50 μm, and the contact resistance during sliding was measured by the four-terminal method.

Fig.12 shows the change in the contact resistance of the plating during a fretting wear test at a load of 1 N. The peak in contact resistance occurred at around 10 to 100 cycles for tin-plating, and this peak was lower for low-pressure-compatible tin-plating. Gold-plating exhibited no peak and maintained low resistance.

Soft tin particles are created when tin-plating undergoes fretting wear. Although some of the wear particles are discharged from the system, the remainder accumulate between the contacts. Oxidation of the accumulated tin wear particles increases contact resistance.[4), 5)] As wear progresses to the copper-tin IMC layer, tin depletes and more wear particles are discharged than generated, reducing the amount of wear particles accumulating at the contacts and decreasing contact resistance. Therefore, it is important to suppress the wear of tin to reduce peak contact resistance. The low-pressure-compatible tin-plating suppresses the wear of tin by exposing the copper-tin IMC layer at the surface, reducing peak contact resistance.[3)]

Gold-plating is believed to suppress a peak in contact resistance because it is hard, reducing wear particles, and because its wear particles are resistant to oxidation.[12)]

Fig.13 depicts the equipment and conditions for testing the coefficient of friction, which was measured in accordance with the Japan Copper and Brass Association technical standard JCBA T311:2002. A sheet-shaped specimen (Flat) and a specimen with a hemispherical protrusion with a radius of curvature of 1 mm (Emboss) were brought into contact, and a load of 1 N was applied normally to the surface of the sheet. The coefficient of friction was calculated based on the frictional force when the sheet-shaped specimen was slid while a load was applied.

Fig.14 shows the coefficients of kinetic friction of the different types of plating. The coefficient of kinetic friction of the low-pressure-compatible tin-plating is no greater than that of reflow tin-plating or gold-plating. Friction between two tin surfaces is regarded as adhesive wear of tin; increasing apparent hardness reduces the coefficient of friction.[3)~5)] It is thought that the copper-tin IMC layer, being harder than tin, on the surface helps suppress the wear of tin.[3)~5)]

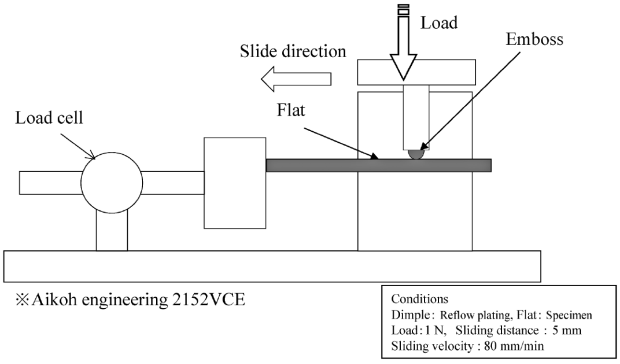

Fig.13 Schematic image of measuring apparatus of friction coefficient

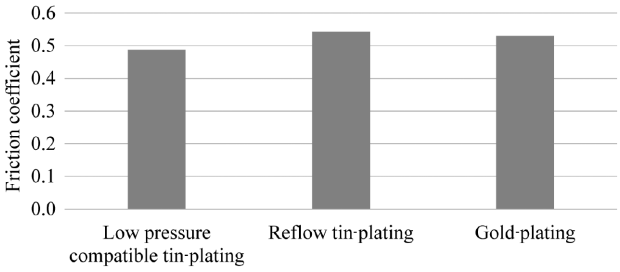

Fig.14 Friction coefficient of plating

Conclusions

To improve upon conventional reflow tin-plating, we have developed low-pressure-compatible tin-plating with superior heat resistance, fretting wear resistance, and contact reliability under low contact load. Since the fretting wear resistance of this plating is not as high as that of gold-plating, it has particularly strong potential as a substitute for high-cost gold-plating in applications where fretting wear resistance is not a concern. Mass production of this newly developed plating is the next stage in our endeavor since laboratory trials revealed strong performance characteristics.

References

1) T. Kotoda. *Precious Metal Plating*. 1st Edition. Maki Shoten. 2001, pp.119-121.
2) Latest Connector Technology '99 Editorial Committee. *Latest Connector Technology '99. 1st edition*. Japan Advanced Technology Co., Ltd., 1999, pp.1-12.
3) M. Tsuru et al. R&D Kobe Steel Engineering Reports. 2012, Vol.62, No.2, pp.59-62.
4) Y. Ueda et al. R&D Kobe Steel Engineering Reports. 2022, Vol.71, No.2, pp.22-28.
5) H. Sakamoto. R&D Kobe Steel Engineering Reports. 2019, Vol.69, No.1, pp.19-24.
6) T. Tamai. Journal of The Surface Finishing Society of Japan. 2004, Vol.55, No.12, pp.102-107.
7) T. Tamai et al. IEICE Technical Report. EMD2008-2, pp.7-12.
8) KEYENCE CORPORATION. Introduction to Measuring Surface Roughness, Surface Roughness, pp.9-18.
9) Y. Ando et al. Transactions of the IEICE, C. 1983, Vol.61, p. 11.
10) Y. Ueda et al. Journal of the Japan Institute of Copper. 2024, Vol.63, No.1, pp.221-225.
11) J. Izumi. ESPEC Technology Report. 1997, No.9, pp.5-11.
12) T. Yamanaka et al. IEICE Technical Report. EMD2012-104, pp.7-11.